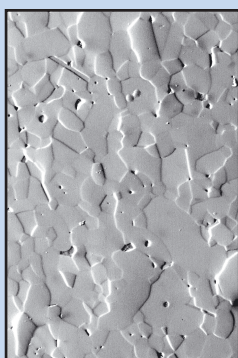
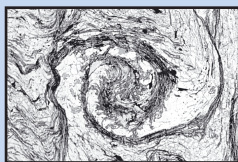


**Pierre VONLANTHEN**

## **EBSD-based investigations of upper mantle xenoliths, snowball garnets and advanced ceramics**



DÉPARTEMENT DE GÉOSCIENCES – MINÉRALOGIE ET PÉTROGRAPHIE  
UNIVERSITÉ DE FRIBOURG (SUISSE)

**EBSD-based investigations of upper mantle  
xenoliths, snowball garnets and  
advanced ceramics**

THÈSE

présentée à la Faculté des Sciences de l'Université de Fribourg (Suisse)  
pour l'obtention du grade de *Doctor rerum naturalium*

**Pierre VONLANTHEN**

de Schmitten (FR), Suisse

Thèse N° 1555

Multiprint, Fribourg, 2007

**Acceptée par la Faculté des Sciences de l'Université de Fribourg (Suisse)  
sur la proposition de:**

Prof. Bernard GROBETY	Université de Fribourg (Suisse)	Directeur
Dr. Luigi BURLINI	ETH Zürich (Suisse)	Expert
Dr. Andréa TOMMASI	Université de Montpellier (France)	Expert
Prof. Andreas STRASSER	Université de Fribourg (Suisse)	Président du Jury

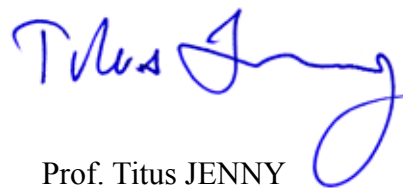
Fribourg, le 13 avril 2007

Le Directeur de thèse



Prof. Bernard GROBETY

Le Doyen



Prof. Titus JENNY

*“How much easier it is to be critical than to be correct”*

Benjamin DISRAELI (1804-1881)



# CONTENTS

ABSTRACT _____	5	2.3 MATHEMATICAL ASPECTS RELATED TO TEXTURE	
RÉSUMÉ _____	7	ANALYSIS _____	22
ACKNOWLEDGMENTS _____	9	2.3.1 Coordinate systems _____	22
<b>1 - FOREWORD</b> _____		2.3.2 Reference sphere, pole figures and inverse pole figures _____	23
1.1 INTRODUCTION _____	11	2.3.3 Orientation _____	24
1.2 GOALS _____	11	2.3.3.1 Orientation matrix representation _____	24
1.3 STRUCTURE _____	12	2.3.3.2 Euler angles representation _____	24
<b>2 - ELECTRON BACKSCATTER DIFFRACTION</b> _____		2.3.4 Misorientation _____	25
2.1 EBSD AND FORMER DIFFRACTION TECHNIQUES _____	13	2.3.5 Orientation Distribution Function (ODF) and texture index (J) _____	25
2.1.1 Macrotecture techniques _____	13	2.3.5.1 Orientation distribution function _____	25
2.1.1.1 X-ray diffraction _____	13	2.3.5.2 Texture index (J) _____	26
2.1.1.2 Neutron diffraction _____	13	2.4 SAMPLE SURFACE PREPARATION _____	26
2.1.2 Microtexture techniques _____	14	2.4.1 Pre-polishing considerations _____	26
2.1.2.1 Kossel X-ray diffraction and selected area electron channeling (SAC) _____	14	2.4.1.1 Peridotite _____	26
2.1.2.2 Electron backscatter diffraction (EBSD) _____	14	2.4.1.2 Ceramics _____	26
2.2 PRINCIPLES OF EBSD _____	14	2.4.2 Polishing _____	27
2.2.1 System set-up _____	14	2.4.2.1 Peridotite _____	27
2.2.2 Electrons-sample interaction and generation of EBSD Kikuchi patterns _____	15	2.4.2.2 Snowball garnets _____	27
2.2.3 EBSD pattern indexing procedure _____	16	2.4.2.3 Ceramics _____	27
2.2.4 Confidence Index (CI), Fit and Image Qua- lity (IQ) _____	18	<b>3 - SEISMIC PROPERTIES OF THE UPPER MANTLE BENEATH LANZAROTE (CANARY ISLANDS): MODEL PREDICTIONS BASED ON TEXTURE MEASUREMENTS BY EBSD</b> _____	
2.2.4.1 Confidence Index (CI) _____	18	ABSTRACT _____	29
2.2.4.2 Fit _____	19	3.1 INTRODUCTION _____	29
2.2.4.3 Image Quality (IQ) _____	19	3.2 GEOLOGICAL BACKGROUND _____	30
2.2.5 Pattern centre calibration _____	19	3.3 SAMPLES _____	31
2.2.6 Orientation mapping _____	19	3.4 METHODOLOGY _____	33
2.2.6.1 Scanning procedure and tricks _____	19	3.4.1 LPO measurement and representation _____	33
2.2.6.2 Orientation of data in stage and beam scan modes _____	22	3.4.2 Calculation of seismic properties _____	36
		3.5 RESULTS _____	36
		3.5.1 Lattice preferred orientation (LPO) _____	36

3.5.2 Seismic properties	40
3.6 DISCUSSION	41
3.6.1 Lattice preferred orientation	41
3.6.2 Anomalous foliation	41
3.6.3 Comparison between measured and calculated velocities	43
3.6.4 Variations of calculated velocities due to P/T estimates	45
3.7 CONCLUSIONS	46

#### 4 - GROWTH MECHANISM OF SNOWBALL GARNETS FROM THE LUKMANIER PASS AREA (CENTRAL ALPS, SWITZERLAND): A COMBINED $\mu$ CT/EPMA/EBSD STUDY

ABSTRACT	47
4.1 INTRODUCTION	47
4.2 GEOLOGICAL SETTING	48
4.3 ANALYTICAL PROCEDURES	49
4.4 3D GEOMETRY	49
4.5 CHEMICAL ZONING	50
4.6 CRYSTALLOGRAPHIC ORIENTATION	51
4.7 DISCUSSION AND CONCLUSIONS	52

#### 5 - CSL GRAIN BOUNDARY DISTRIBUTION IN ALUMINA AND ZIRCONIA CERAMICS

ABSTRACT	53
5.1 INTRODUCTION	53
5.2 EXPERIMENTAL METHODS	54
5.2.1 Ceramic processing and sample preparation	54
5.2.2 Electron backscatter diffraction (EBSD)	54
5.2.3 Simulation of random spatial models	58
5.3 RESULTS AND DISCUSSION	58
5.3.1 Microstructures and textures	58
5.3.2 Grain misorientation distributions	61
5.3.3 CSL grain boundary distributions	61
5.3.3.1 Validity of the simulated spatial models	61
5.3.3.2 CSL grain boundary distributions in measurements and simulated models	63
5.3.3.3 Triple junction character and prominence factors in zirconia	65
5.4 CONCLUSIONS	66

#### 6 - PERSPECTIVES

6.1 CASE STUDY 1	69
6.2 CASE STUDY 2	69
6.3 CASE STUDY 3	70

#### I - APPENDIX OF CASE STUDY 1

I.1 CHEMISTRY AND CRYSTAL STRUCTURE OF PERIDOTITE MINERALS	71
I.1.1 Olivine	71
I.1.2 Ortho- and clinopyroxene	72
I.2 EBSD DATA	73
I.2.1 Crystallographic files used for indexing	73
I.2.2 List of EBSD runs	73
I.2.3 Maps and texture plots	74
I.3 DENSITY AND ELASTIC CONSTANTS	74

#### II - APPENDIX OF CASE STUDY 2

II.1 CHEMISTRY AND CRYSTAL STRUCTURE OF GARNET	81
II.2 EBSD DATA	82
II.2.1 Crystallographic file used for indexing	82
II.2.2 List of EBSD runs and maps	82

#### III - APPENDIX OF CASE STUDY 3

III.1 CHEMISTRY AND CRYSTAL STRUCTURE OF ALUMINA AND ZIRCONIA	83
III.1.1 Alumina	83
III.1.2 Zirconia	84
III.2 PROCESSING OF CERAMIC SAMPLES	84
III.2.1 General considerations	84
III.2.1.1 Procedure	84
III.2.1.2 Sample property requirements	85
III.2.2 Starting material	85
III.2.3 Ceramic powder suspension	86
III.2.3.1 General considerations	86
III.2.3.2 Suspension stability	86
III.2.3.3 Effects of organic surfactants	88
III.2.4 Ball milling	89
III.2.4.1 Principle	89
III.2.4.2 Binder	89
III.2.5 Spray drying	89
III.2.5.1 Drying and granulation processes	89
III.2.5.2 Practical aspects of spray drying	90
III.2.6 Ceramic shaping	90
III.2.6.1 Die pressing	90
III.2.6.2 Wet bag isostatic pressing	90
III.2.7 Sintering	90
III.2.7.1 Principle	90
III.2.7.2 Sintering profiles	91
III.2.8 Density measurements	91
III.2.8.1 Bulk density	91
III.2.8.2 Bulk vs theoretical density	92
III.3 COINCIDENCE SITE LATTICE (CSL)	92

III.3.1 Principle _____	92	III.4.1 Crystallographic files used for indexing ___	97
III.3.2 Deviation from exact CSL _____	93	III.4.2 List of EBSD runs _____	97
III.3.3 Constrained CSL _____	93	III.4.3 Maps and texture plots _____	97
III.3.4 Fractions of CSL grain boundaries _____	93		
III.3.5 Triple junction character _____	93	REFERENCES _____	105
III.4 EBSD DATA _____	97	CURRICULUM VITAE _____	113

\*\*\*\*\*



## ABSTRACT

---

Since the beginning of the nineties, the automation of electron backscatter diffraction (EBSD) has completely revolutionized texture analysis carried out on rocks and man-made materials. Among the most striking advances, not only does EBSD allow a relatively rapid and straightforward bulk texture analysis, but it also allows the grain-by-grain determination of crystallographic orientations. The interest for the technique is obvious for academic purposes but also for the industry, as most of the physical properties of materials depend on the lattice preferred orientation (LPO) of the constituting grains. Since EBSD is the main investigation method applied in each of the three investigated case studies, it is clearly the keystone of the present work.

In the first Case Study, a petrophysical analysis of twelve upper mantle peridotite xenoliths collected in the Quaternary basalt fields of Lanzarote (Canary Islands) is presented. The goal of this project is to determine the deformation mechanisms responsible for the formation of observed textures and to calculate the propagation velocities of seismic waves through the samples. Seismic velocities are of particular interest as two contradictory interpretations resulting from the same campaign of field geophysical measurements are reported in the literature. The present EBSD analysis is aimed at providing new data on the seismic properties of the upper mantle in this region, in order to aid the geological interpretation of geophysical measurements. For each sample, the LPO of olivine, orthopyroxene and clinopyroxene was measured. Two deformation mechanisms, probably dominated by simple shear under low strain rate and relatively high temperature, are put forward. The velocities of P-waves calculated from the LPO and the elastic constants of the minerals for upper mantle pressure and temperature conditions confirm the most recent geo-

physical interpretation. In addition, this project also highlights remarkable examples of anomalous foliation, characterized by an orientation of the foliation plane at right angle with respect to the olivine [100] pole maximum. Based on microstructural, crystallographic and geochemical arguments, the anomalous foliation is interpreted as a result of strong recovery processes.

The second Case Study is devoted to the formation of snowball garnets from the Liassic Stgir series (Lukmanier Pass, Switzerland). For more than two decades, the mechanisms responsible for the formation of snowball garnets have been in the center of an intense debate. Based on a multi-analytical approach involving micro-computed X-ray tomography, electron microprobe and EBSD analyses, two successive growth mechanisms are suggested for the formation of the analyzed garnets: whereas several pieces of evidence seem to indicate that the first stages of growth are initiated in a rotational context, the final stages of growth occur in a post-kinematic regime. This assumption is based on (1) the occurrence and distribution of secondary Mn maxima inside the spiral, (2) the constant crystallographic orientation of the bridges connecting the core and the arms of the spiral and (3) the post-kinematic growth of garnet by replacement of deformed mica-rich levels. In addition, EBSD brings into light the fact that snowball garnets from the Lukmanier Pass are not made of a unique grain with a single crystallographic orientation but of several grains with different, distinct orientations.

In the third Case Study, the distributions of coincidence site lattice (CSL) grain boundaries in alumina and zirconia ceramics are investigated through EBSD. The main interest of this project lies in the fact that most physical properties involved in the processing

and behavior of ceramics depend on the nature and distribution of grain boundaries. 2D spatial models consisting of 50000 randomly oriented grains have been simulated to serve as references for random distributions. Comparison between the simulated and measured distributions has shown higher CSL grain boundary fractions in the latter. This trend is particularly obvious for the samples sintered at high temperature. In alumina, change in individual CSL grain boundary fractions with temperature is crystallographically controlled and directly dependent on the orientation of the misorientation axis with respect to

the [0001] axis. Finally, based on the data of zirconia, this study has also allowed the definition of a so-called general prominence factor likely to be used as a simple criterion to determine the randomness of the CSL grain boundary distribution in FCC-type materials.

This PhD thesis has attempted to show the central role played by EBSD in earth and materials sciences. The various types of materials analyzed as well as the multidisciplinary character of the different case studies give evidence for the polyvalence of the method.

\*\*\*\*\*

## RÉSUMÉ

---

L'automatisation au début des années '90 de la technique de diffraction par électrons rétro-diffusés ou *electron backscatter diffraction* (EBSD) a complètement révolutionné les analyses de textures menées tant sur les roches que sur les matériaux industriels. Parmi plusieurs avancées majeures, cette méthode permet une détermination relativement rapide et simple de l'orientation cristallographique des grains contenus dans les solides polycristallins. L'intérêt est de taille non seulement dans le milieu purement académique mais également dans l'industrie puisque la plupart des propriétés physiques des matériaux dépend de l'orientation cristallographique préférentielle ou *lattice preferred orientation* (LPO) des grains qui les constituent. En tant que méthode d'analyse à la base de chacune des trois études de cas abordées, l'EBSD occupe clairement la position centrale de ce travail.

La première étude de cas présente une analyse pétrophysique de douze xénolithes mantelliques de péridotites échantillonnés dans les laves basaltiques quaternaires de l'île de Lanzarote (archipel des Canaries). Le but de ce projet est tout d'abord de déterminer les mécanismes de déformation à l'origine des textures observées, puis dans un deuxième temps d'utiliser les résultats de LPO obtenus pour calculer les vitesses de propagation des ondes sismiques dans ces échantillons. Cet aspect revêt un intérêt particulier dans la mesure où deux interprétations contradictoires émanant d'une même campagne de sismique-réfraction ont été rapportées dans la littérature. Ce projet a donc pour objectif de fournir de nouveaux éléments sur les propriétés sismiques du manteau supérieur à cet endroit du globe, pour permettre par la suite de confirmer ou d'infirmer les interprétations tirées des mesures de terrain. Pour chaque échantillon, la LPO de l'olivine, de l'orthopyroxène et du clinopyroxène a été déterminée par EBSD. Sur la base des résultats obtenus,

deux mécanismes de déformation, vraisemblablement dominés par une composante de cisaillement simple sous faible taux de contrainte et à température relativement élevée, sont avancés. Les vitesses de propagation des ondes, calculées à partir de la LPO et des constantes élastiques des phases dérivées aux conditions de pression et de température du manteau supérieur, confirment l'interprétation géophysique la plus récente au détriment de la plus ancienne. Dans un autre registre, ce projet a permis également de mettre en évidence de superbes exemples de foliation dite anormale, caractérisée par une orientation du plan de foliation à 90° par rapport aux pôles [100] de l'olivine. Sur la base d'arguments microstructuraux, cristallographiques et géochimiques, ce cas de figure est interprété comme le résultat de processus de recuit très avancés.

La deuxième étude de cas est consacrée à la problématique de la formation des grenats spiralés de la série liasique de Stgir (col du Lukmanier, Suisse). Cette étude s'inscrit dans le débat animé qui sévit dans la communauté scientifique depuis plus de vingt ans au sujet des mécanismes responsables de la formation de ce type de grenats. Sur la base d'une approche multi-analytique impliquant des mesures de micro-tomographie à rayons X, de microsonde électronique et d'EBSD, deux mécanismes de croissance successifs sont avancés pour la formation des grenats analysés: alors que dans un premier temps la géométrie spiralée des grenats semble avoir été initiée par une rotation, plusieurs indices tendent à démontrer qu'une fraction significative de leur croissance s'est produite de manière post-cinématique. Ces indices s'appuient sur (1) la répartition dans la spirale de pics secondaires de haute concentration de manganèse, (2) l'orientation cristallographique constante des ponts entre les différents niveaux de la spirale et (3) la croissance tardive de grenats le long de niveaux déformés riches en

micas. L'EBSD a permis en outre de démontrer que les grenats spiralés du Lukmanier ne sont pas formés d'un seul grain muni d'une orientation cristallographique unique mais de plusieurs grains orientés de manière différente.

Dans la troisième étude de cas, la distribution des joints de grains satisfaisant le formalisme dit de *coincidence site lattice* (CSL) est analysée pour des échantillons de céramique haute performance d'oxyde d'aluminium et de zirconium. L'intérêt principal de ce projet réside dans le fait que la majeure partie des propriétés physiques intervenant dans la synthèse des céramiques et régissant leur comportement dépend directement de la nature et de la répartition des joints de grains. Les résultats obtenus sont comparés avec des distributions simulées générées à partir de modèles spatiaux aléatoires. Que se soit pour l'oxyde d'aluminium ou de zirconium, la fraction de joints de grains CSL se révèle sensiblement plus élevée dans les mesures que dans les simulations. Cette tendance est particulièrement évidente pour les échantillons frittés à haute

température, avec des différences de fréquences pour les joints de grains CSL individuels dépassant régulièrement 100%. Dans le cas de l'oxyde d'aluminium, l'augmentation, respectivement la diminution de la fraction de joints de grains CSL avec la température est contrôlée par la cristallographie : une dépendance directe entre l'orientation de l'axe de misorientation et l'axe [0001] a pu être soulignée. D'autre part, sur la base des résultats obtenus dans l'oxyde de zirconium, cette étude a permis de définir pour la première fois un facteur général de proéminence ou *general prominence factor*, qui pourrait être utilisé à l'avenir comme un critère simple permettant de vérifier la distribution aléatoire de joints de grains CSL dans les matériaux de structure FCC.

Ce travail souligne le rôle central joué par l'EBSD tant en sciences de la Terre qu'en sciences des matériaux. La variabilité des matériaux analysés ainsi que le caractère multidisciplinaire des sujets abordés sont autant d'éléments témoignant de la polyvalence de la méthode.

\*\*\*\*\*

## ACKNOWLEDGMENTS

---

The following thesis, while an individual piece of work, benefited from the insights and collaboration of several people.

First of all, I would like to thank Prof. Bernard Grob ty, who accepted me as one of his PhD students in April 2003. During these four years he has shown a remarkable enthusiasm for my work, even in situations I would have qualified as desperate. I really appreciated to be at liberty to explore the world of EBSD and texture analysis, knowing I would be called back at the right track when I got lost. He always provided timely and instructive comments and evaluation at every stage of the thesis process, allowing me to complete this project. Many thanks for the constant interest in my work and for giving me the opportunity to widen my scientific background. I particularly appreciated the open-door policy of his office, giving evidence of his outstanding availability and generosity in all kinds of situations, even when a tight schedule constrained him to work literally in front of three computers at the same time !

I further want to thank the scientists who collaborated actively on this project. I am very grateful to Karsten Kunze and Luigi Burlini (ETH Z rich) who introduced me to the world of EBSD and texture analysis. Special thanks are addressed to Andr a Tommasi (University of Montpellier) for the enthusiastic welcome in her lab and the perspicacious comments on the peridotite microstructures, as well as to David Mainprice (University of Montpellier) for the free disposal of the Unicef Careware software package. I am also very grateful to Else-Ragnhild Neumann (University of Oslo) for providing seven fresh xenoliths from Lanzarote. Last but not least, I would like to thank the Timanfaya National Park administration for authorizing field work and especially Luz Mej as

for the guided field trips and spontaneous Spanish lessons.

Next I wish to thank Martin Robyr (University of Texas) and Lukas Baumgartner (University of Lausanne), with whom it was a pleasure to collaborate on a common project by exchanging mutual knowledge and analytical expertise. Many thanks also to Jean-Luc Epard and Jean-Claude Vannay (University of Lausanne) for helping out in the Lukmanier field area and to Hansklaus Rummeler and Marie-Christine Maistre (University of Fribourg) for the development of mathematical algorithms, which will be required for the research to come.

I am also indebted to the people of the Labor f r Hochleistungskeramik of the Eidgen ssische Materialpr fungs- und Forschungs-Anstalt (EMPA) in D bendorf for their collaboration on the “ceramic” part of this PhD thesis. Special thanks are addressed to Hans-J rgen Schindler who spent two weeks introducing me to the world of advanced ceramic processing. Many thanks also to Thomas Graule and Andreas Herzog for their useful recommendations to improve the microstructure of ceramic samples.

The technical staff of the Department of Geosciences deserves my deep gratitude as well, especially Christoph Neururer for his competence and insatiable scientific interest, Nicole Bruegger for her administrative work, Daniel Cuennet and Patrick Dietsche for their spontaneous help, and Jean-Paul Bourqui for his excellence in all the culinary aspects of science and ...his unfailing good mood. I also would like to thank the “external” technical staff, Georges Deschenaux, Joseph Gummy and Ren  Vonlanthen, who lent an extremely valuable support by machining custom-made sample holders for EBSD analyses.

I also wish to thank Fiona Gore and Jeff Nottage, who did not let themselves be overawed by the hermetic nature of the texts they were kindly asked to correct. Many thanks again for reviewing and improving the linguistic aspects of the manuscripts.

In Fribourg I had the opportunity to work in ideal conditions, not only because of the overall infrastructure and free access to analytical facilities, but above all due to the great working atmosphere created by the scientific staff and PhD students: André, Andrea, Anne-Christine, Barbara, Cécile, Cédric, Christian, Christophe, Claire, Claudius, Corinne, Giacomo, Damien, Daniel, Daniel, Elias, Giordana,

Gisela, Hajnalka, Jeanne, Jean-Pierre, Jessica, Jon, Jonas, Jürgen, Katja, Kuno, Laureline, Luc, Maëlle, Marino, Martin, Martine, Michèle, Mikaël, Mustafa, Niels, Noémie, Peter, Pia, Raymond, Richard, Sabina, Sébastien, Srđan, Silvia, Simon, Sophie, Stephan, Stéphanie, Thibault and Vincent. To all of them, thanks again.

In this kind of enterprise, moral support plays a crucial role. I address very special thanks to my parents and to my girlfriend Sophie, who lent me ongoing moral support during the most frustrating and discouraging times of my thesis. Their invaluable and irreplaceable contribution makes this thesis also theirs.

\*\*\*\*\*

# 1 - FOREWORD

---

## 1.1 INTRODUCTION

Most solid materials, including rocks, have a polycrystalline structure in that they are composed of a large number of individual grains. Among the microstructural features displayed by polycrystals, the crystallographic orientations of grains have a determining influence on the properties of the materials. Elastic, thermal, plastic, electric, magnetic and diffusion properties are all dependent on crystallographic orientations, making this a challenging field of research for materials scientists. In addition, the distribution of crystallographic orientations is a key feature in earth sciences as well, as it is frequently used to reconstruct the deformation mechanism of rocks. In this PhD thesis, the crystallographic orientations in both man-made polycrystalline materials and natural rocks were investigated using a powerful and increasingly popular analytical technique called electron backscatter diffraction (EBSD).

Before getting to the heart of the matter, however, a point of definition must be clarified. In the literature, the distribution of crystallographic orientations in a polycrystal is called in turn *lattice preferred orientation* (LPO), *crystallographic preferred orientation* (CPO), *crystallographic texture* or simply *texture*. The latter acceptance should not be mistaken with the meaning of texture in general geological literature, where the term describes the overall appearance of a rock and encloses the whole set of microstructural parameters, such as grain size and shape, degree of crystallinity, and arrangement. In this volume, the term *texture* is used as a synonym of LPO, following the nomenclature adopted in materials science and structural geology.

## 1.2 GOALS

The goal of this PhD thesis is to investigate texture and texture-related features in polycrystalline rocks and materials through three different case studies, using electron backscatter diffraction (EBSD) as the main investigation method. EBSD is thus clearly the keystone of the present work. Moreover, since the EBSD system was installed only recently in our department, this PhD thesis also served as an incentive to bring the EBSD lab into service and to explore through a multidisciplinary approach the potential applications of this technique. The underlying goal of this work is therefore to acquire strong expertise in the EBSD technique by investigating different types of materials and rocks under various conditions and acquisition modes.

As each of the three case studies has its own specific objectives, it has not been possible to draw up a list of goals shared by the very different and independent topics of research. Consequently, the subjects of each case study have been briefly outlined below:

- In Case Study 1, the seismic properties of upper mantle xenoliths from Lanzarote (Canary Islands) were investigated using texture measurements through EBSD. Peridotite minerals and particularly olivine have a strong tendency to develop LPO in response to deformation (Hess 1964). Since the elastic behavior of waves in minerals is anisotropic, the seismic properties of rocks are directly dependent on LPO. In this study, the seismic velocities were calculated from the LPO and the elastic constants of the minerals. The results were then used to infer the velocities of seismic waves in depth and confronted with the field geophysical

measurements reported in the literature (BANDA et al. 1981, DAÑOBEITIA & CANALES 2000). EBSD allowed us to characterize the deformation of the upper mantle in this region and to confirm the most recent field geophysical interpretation.

- Case Study 2 dealt with the growth mechanisms of snowball garnets from the Lukmanier Pass area (Switzerland). Snowball garnets define well-developed spiral-shaped garnets characterized by curved inclusion trails rotated over more than 90°. They are typically found in pelitic schists, which underwent non-coaxial deformation in a context of regional metamorphism. For more than two decades, the processes responsible for the formation of snowball garnets have been at the center of an intense debate. Two schools of thought have confronted each other about the rotational (e.g. SCHONEVELD 1977, PASSCHIER et al. 1992) or non-rotational (e.g. BELL et al. 1992) character of their development. In this study, EBSD was performed on snowball garnets from the Lukmanier Pass in order to identify possible changes in crystallographic orientation within the garnet spirals. Results collected from electron probe microanalyses (EPMA), micro X-ray tomography ( $\mu$ CT) and EBSD suggest that the final stages of growth of the investigated garnets occur in a post-kinematic regime by replacement of mica, whereas the first stages are best explained by a rotational regime.

- In Case Study 3, the distributions of coincidence site lattice (CSL) (BOLLMANN 1970, WARRINGTON & BUFALINI 1971) grain boundaries in alumina and zirconia ceramics sintered at two different temperatures

were investigated and compared with the distributions obtained from simulated random 2D spatial models. Coincidence grain boundaries are often considered as indicators of low interfacial energy from which special physical and chemical properties may arise. The distribution of such grain boundaries is thus a prerequisite to understand the properties of ceramics.

### 1.3 STRUCTURE

Whereas Chapter 1 aims at introducing the reader to the main issues tackled in this project, Chapter 2 is devoted to the more technical aspects of EBSD. The aim is not to provide a substitute for the very complete books available on the subject. It is rather to give, as the first EBSD user at the University of Fribourg, a comprehensive summary of the technique, as well as valuable tricks for parameter settings resulting from many sessions of experimenting. Chapter 2 is thus essentially aimed at facilitating the task of the next users of our lab by avoiding time-consuming sessions of unfruitful testing. Three publications, corresponding to the case studies briefly summarized in Section 1.2, were accepted in peer-reviewed journals. They form the core of the thesis and are presented in Chapter 3, 4 and 5 respectively. Some perspectives for further investigations are found in Chapter 6. Finally, Appendices I, II and III contain all EBSD data as well as the useful basics related to the corresponding case studies. In Appendix III, the technical and theoretical aspects for the processing of alumina and zirconia ceramics are discussed in detail.

\*\*\*\*\*

## 2 - ELECTRON BACKSCATTER DIFFRACTION

### 2.1 EBSD AND FORMER DIFFRACTION TECHNIQUES

The goal of this section is to highlight the early methods, some of which are still used nowadays, as well as the precursory techniques that led to the advent of electron backscatter diffraction (EBSD). For a complete history of texture analysis, the reader is referred to DINGLEY (2000) and RANDLE & ENGLER (2000).

In the historical overview that follows, a distinction is made between macrotexture and microtexture techniques. The former only allow average bulk texture measurements (i.e. without reference to the local crystallographic information), while the latter enable the determination of local high resolution orientation data. Macrotexture techniques were already in use in the first half in the 20<sup>th</sup> century, whereas microtexture methods appeared only in the late sixties because they require high performance electron microscopes.

#### 2.1.1 Macrotexture techniques

##### 2.1.1.1 X-ray diffraction

X-ray diffraction, first used by WEVER (1924) to investigate preferred orientations in metals, is still the most widespread technique to investigate macrotexture. Practically, the sample is inserted into a 3-circle texture goniometer and systematically rotated about well-defined angles (typically in 2.5° or 5° steps) in order to bring, for given lattice planes (hkl), the grains in the sample in reflection conditions. For each sample orientation, the reflected intensity, which

is proportional to the volume fraction of grains in reflecting condition, is recorded. The intensities are then projected in a pole figure, as a function of the sample orientation provided by the goniometer radial and azimuthal angles. The intensity distribution in the pole figure is a measure of the average texture of the sample. The main advantage of X-ray diffraction over other macrotexture techniques such as neutron diffraction consists in its ability to record the average texture of a sample rapidly and without any highly sophisticated equipment.

##### 2.1.1.2 Neutron diffraction

Macrotexture analyses through neutron diffraction were first carried out by BROCKHOUSE (1953). The basic principles of the technique are very similar to those of X-ray based texture measurements, with the difference that X-rays are replaced by neutrons. As the absorption of neutrons by matter is almost negligible compared to X-rays, neutron diffraction allows investigations in transmission geometry. Voluminous specimens can be analyzed with very little sample preparation and with much better grain statistics than those obtainable by X-ray diffraction. The low absorption of neutrons by matter also facilitates in situ investigations involving heating, cooling or straining of the samples during measurements. Nevertheless, neutron diffraction requires a supply of fast neutrons which can only be generated in atomic reactors through nuclear fission processes, therefore making the method less straightforward than X-ray diffraction. Moreover, the relatively low intensity of the neutron signal significantly increases the acquisition time by a factor of 10 to 100. Neutron diffraction is thus mainly used for more specific purposes that make up for the higher initial constraints inherent to the technique.

## 2.1.2 Microtexture techniques

### 2.1.2.1 Kossel X-ray diffraction and selected area electron channeling (SAC)

Two techniques, available since the late sixties, can be considered as forerunners of electron backscatter diffraction (EBSD): the Kossel X-ray diffraction (DINGLEY & STEEDS 1974) and the selected area electron channeling or SAC (COATES 1967). Both methods were early scanning electron microscope (SEM)-based diffraction techniques, which provided information about local determination of crystallographic orientations and other microstructural parameters.

The Kossel technique is based on the diffraction of X-rays generated through the interaction of the incident electron beam with the core electrons of the sample atoms. Diffraction of these characteristic X-rays by the crystal lattice planes produces a strip pattern, called Kossel pattern, which is recorded on a sensitive film. The indexing of the Kossel pattern allows the determination of the crystallographic orientation. The SAC technique is based on the diffraction of the incident electron beam by the crystal lattice. The electron beam is focused on the sample site to be analyzed and tilted incrementally without jutting out of the selected sample location. Each time the orientation of the electron beam fulfils Bragg's conditions for a certain lattice plane (hkl), reflection occurs and a band is produced in the so-called electron channeling pattern (ECP). Indexing of the ECP pattern is performed to obtain the crystallographic orientation. The main drawback of both Kossel diffraction and SAC consists in a relatively bad spatial resolution of about 10  $\mu\text{m}$ , making these methods inapplicable to many polycrystalline materials. This severe limitation sounded the knell for both techniques at the expense of EBSD, which appeared very promising in the world of texture analysis.

### 2.1.2.2 Electron backscatter diffraction (EBSD)

First described by VENABLES & HARLAND (1973), EBSD has become the most suitable and popular technique to measure the texture of artificial and natural polycrystalline materials. Compared with existing microtexture techniques, the Kossel diffraction and SAC, and U-stage measurements, EBSD's major advantage lies in its highly improved spatial resolution of less than 0.5  $\mu\text{m}$ . Moreover, as add-on package to an SEM, EBSD also enables rapid microtexture

measurements of large polycrystalline samples, and can be coupled with other continually improved capabilities of SEM's, for example in the field of imaging or chemical analyses through energy dispersive X-ray spectrometry (EDS). The combinations of these techniques and progress in the theory has led to new analysis methods such as orientation imaging microscopy (OIM) and grain boundary distribution. EBSD is thus highly suitable for most texture-related applications, except in cases where a very high spatial resolution is necessary and transmission electron microscopy (TEM)-based techniques are preferable.

## 2.2 PRINCIPLES OF EBSD

The fundamentals of EBSD have been widely discussed in the literature already. A concise review on the subject is available in PRIOR et al. (1999). For a complete description of the world of texture analysis, including EBSD, the following books are available: *Texture and Anisotropy* (KOCKS et al. 1998), *Electron Backscatter Diffraction in Materials Science* (SCHWARTZ et al. 2000) and *Introduction to Texture Analysis* (RANDLE & ENGLER 2000). The sections below only give an overview of the basic principles, including some useful advice about the system available in our department.

### 2.2.1 System set-up

EBSD analyses are based on diffraction patterns generated by backscatter electrons (s. Section 2.2.2), i.e. primary elastically scattered electrons which escape from the sample through the same surface they entered. In order to maximize the proportion of backscatter electrons and increase the number of possible diffraction events in the solid, the sample is tilted within the SEM chamber at 70° from the horizontal (SCHWARZER & WEILAND 1988).

EBSD diffraction patterns are collected on a fluorescent phosphor screen, in which incoming backscatter electrons are converted into light. This signal is then transferred through fiber optics into a retractable charge coupled device (CCD) video camera (DINGLEY & RANDLE 1992) which has the advantage of good signal to noise ratio. The video signal is then transferred to a computer where the patterns can be processed and indexed (s. Section 2.2.3). A sketch of the whole system set-up is shown in Fig. 2.1.

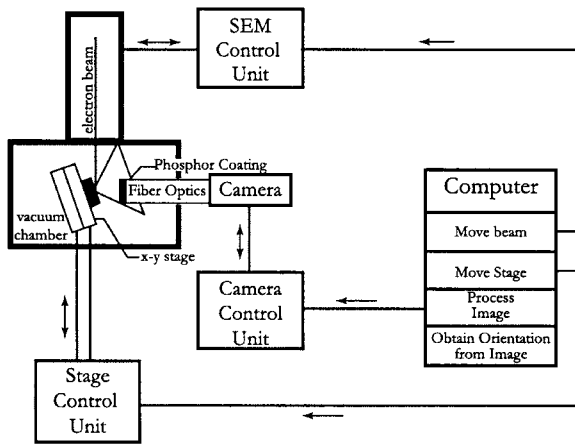


Fig. 2.1 Schematic representation of the EBSD system and the computer interface (after WRIGHT 1993).

The University of Fribourg's EBSD system is mounted on a Philips® FEI XL30 SFEG Sirion SEM, equipped with a 2-sector solid state forescattered electron (FSE) detector. The diffraction patterns collected on the phosphor screen are recorded with a DigiView® CCD camera. The video frames are fed on-line into the processing software EDAX® (TSL) OIM Data Collection 3.5 on a computer. Typical operating conditions to collect EBSD patterns included an acceleration voltage of between 20 and 30 kV for a probe current of 20 nA (in spot 5). A working distance of 15 mm was used in beam scan mode, whereas 20 mm was necessary in stage scan mode to avoid contact with the final lens of the electron gun. The tilting of the sample was achieved without a pre-tilted sample holder through a whole stage rotation of 70°. Because of the large size of the peridotite specimens, a special sample holder was built.

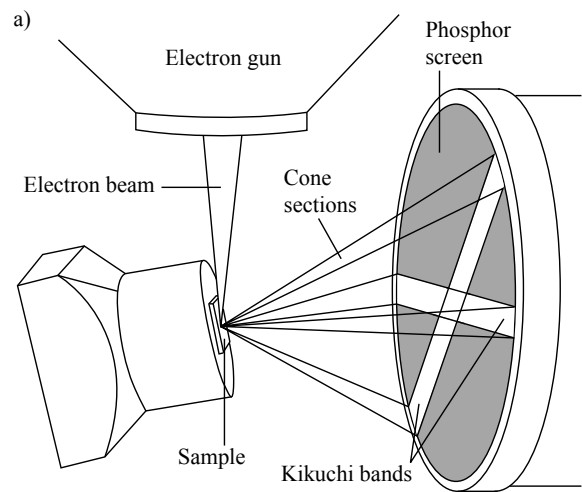
### 2.2.2 Electrons-sample interaction and generation of EBSD Kikuchi patterns

A wide variety of interactions occur between an incident electron beam and the atoms of the sample (GOLDSTEIN et al. 1992). Both elastic and inelastic interactions cause the incident electrons to deviate from the original trajectory, thus leading it to become diffuse in the solid even though it was well-defined initially. The omni-directional population of elastically scattered electrons acts as the source for the EBSD signal. Once they are scattered in all directions the electrons may further interact elastically with the atoms in the crystalline material. For a given wavelength and lattice plane spacing, certain incidence angles satisfy Bragg's

law and lead to constructive interference:

$$2d \sin \theta = n\lambda \quad (\text{Eq. 2.1})$$

where  $\theta$  is the angle between the electron trajectory and the lattice plane,  $n$  an integer (order of diffraction),  $\lambda$  the wavelength of the electron beam energy (depending on the acceleration voltage) and  $d$  the lattice spacing. Because of the omni-directional character of the electron propagation, the trajectories of electrons which satisfy the Bragg conditions do not define one single direction (as in X-ray diffraction analysis) but two cones for every lattice plane population. Since



b)

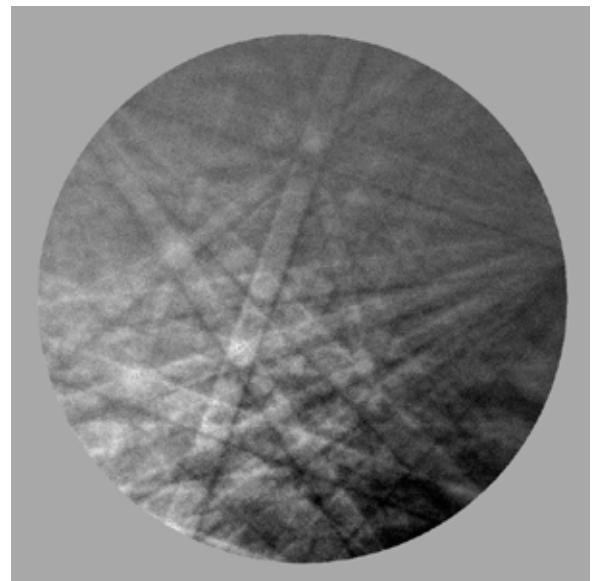


Fig. 2.2 (a) Schematic representation illustrating the generation of an EBSD Kikuchi pattern in the SEM chamber; only two bands are shown for clarity (after HJELÉN et al. 1993). (b) Example of a Kikuchi pattern for olivine (sample PV01). Acceleration voltage: 20 kV; probe current 20 nA.

the Bragg angle for the diffraction of electrons accelerated through a few tens of keV is very small (typically about  $0.5^\circ$  due to the short  $\lambda$  of the electron beam), the opening angles of the diffraction cones are close to  $180^\circ$ . Consequently, the two diffraction cones approximate planes which intersect the phosphor screen of the EBSD apparatus along straight, parallel lines (Fig. 2.2a).

Each pair of parallel lines, known as a Kikuchi band (KIKUCHI 1928), represents a particular lattice plane in the crystal structure. The width of Kikuchi bands is a function of the geometry of the system and the SEM acceleration voltage, which determines the wavelength  $\lambda$  of the electron beam and consequently also the diffraction angle  $\theta$ . A set of several bands defines a so-called EBSD Kikuchi pattern, or simply Kikuchi pattern (Fig. 2.2b), which is the basic raw data for all EBSD analyses. The intersection of bands corresponds to a zone axis or pole, and major zone axes are recognized by the intersection of a large number of bands. As the angular relationship between bands in the pattern reflects the angular relationship between planes in the crystal, the EBSD pattern makes an implicit statement about the crystal symmetry. These angular relationships are used to index the Kikuchi bands and to identify the poles. The Kikuchi pattern thus represents a partial projection of the crystal lattice, which allows researchers to determine the crystallographic orientation of the source point.

### 2.2.3 EBSD pattern indexing procedure

To determine the crystallographic orientation of the source point, the EBSD Kikuchi pattern must be processed through a procedure called indexing. This now fully automated operation is divided into two successive steps: (1) the detection of the diffraction bands and (2) the identification of the diffracting planes associated with the detected bands.

During step (1), the diffraction bands of EBSD Kikuchi patterns are detected using a mathematical algorithm called the Hough Transform (ILLINGWORTH & KITTLER 1988, KRIEGER LASSEN et al. 1992, KUNZE et al. 1993). The equation governing the Hough Transform is:

$$\rho = x \cos \theta + y \sin \theta \quad (\text{Eq. 2.2})$$

where  $(x, y)$  describe a set of pixel coordinates in the EBSD pattern image. During the Hough transformation, each point  $(x, y)$  of the pattern is converted into a sinusoidal curve in the Hough space, where the X- and Y-axes correspond to  $\theta$  and  $\rho$  respectively (Fig. 2.3). The sinusoidal curves of all points belonging to a line in  $(x, y)$  space will intersect in a single point in the Hough space. The  $\rho$  value of this point corresponds to the shortest distance between the line and the origin of the EBSD pattern image in the  $(x, y)$  space, whereas the  $\theta$  value is the angle between  $\rho$  and the horizontal.

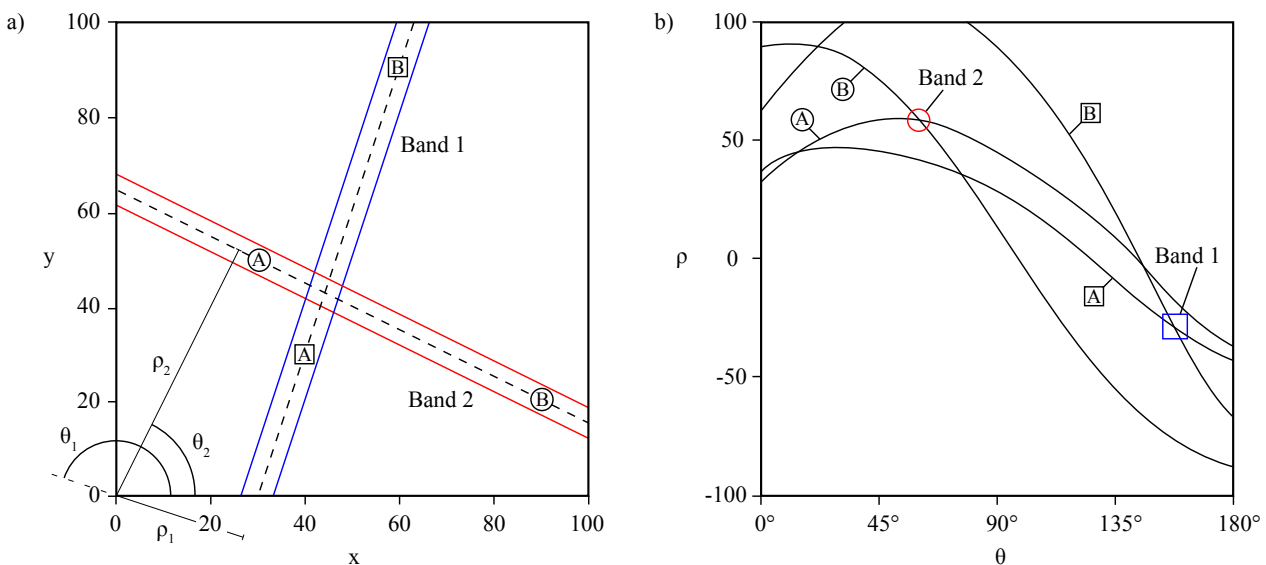


**Fig. 2.3** Schematic illustration of the Hough Transform. Each point of a Kikuchi band (e.g. points A and B of band 1 respectively 2) in the EBSD pattern (a) is represented by a sinusoidal curve in the Hough space (b). (after RANDLE & ENGLER 2000).

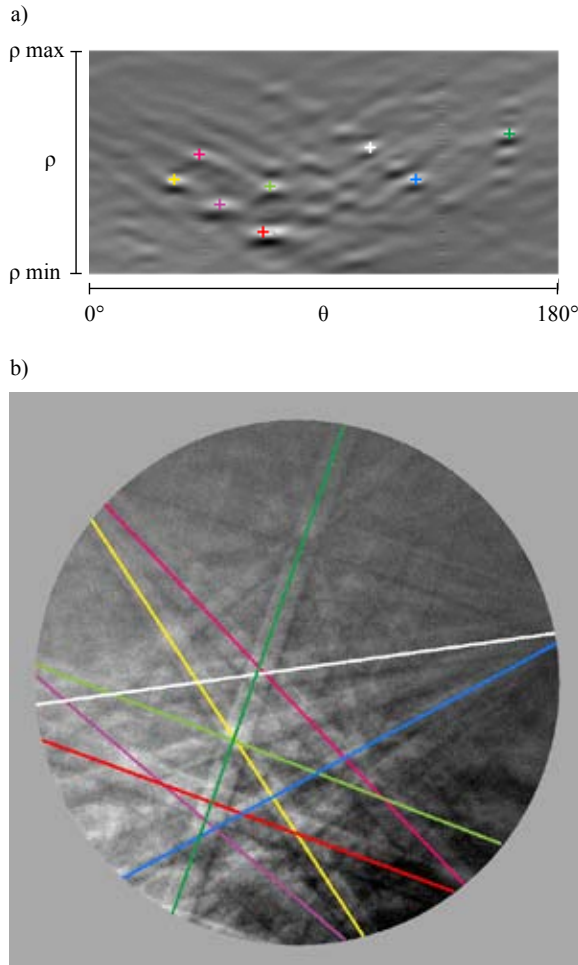


**Fig. 2.4** (a) Hough space after transformation of the olivine pattern shown in Fig. 2.2b. The detected peaks (colored crosses in the Hough space = intersection of sinusoidal curves) correspond to the lines shown in (b).

All  $\rho$  and  $\theta$  pairs for which there is no intersection of sinusoidal curves in the Hough space have no geometrical significance in the EBSD pattern image.

As the Hough transformation is performed considering the gray-tone intensity of points in the original image, the cross points representing bright Kikuchi lines will also be bright. Thus, identifying a band in the diffraction pattern amounts to detecting a peak of high intensity in the Hough space (Fig. 2.4).

During step (2), the reflecting planes associated with the detected bands must be identified. To achieve this, the interplanar angles between the bands are compared to interplanar angles calculated from a theoretical crystallographic data set of the material, commonly called *material file*. A wide choice of material files is available in most EBSD software databases. However, if the needed file does not exist (which might be the

case for some minerals), it has to be created before the indexing procedure can begin. To create such a file, some knowledge of the crystal structure is required, including (1) the point-group symmetry, (2) the unit cell parameters (3) the positions of atoms in the crystal structure and (4) the intensity of major reflections. Whereas (1), (2) and (3) are available for virtually all minerals, (4) must be usually calculated. The reason for this is that not all crystallographic planes satisfying the Bragg conditions give rise to Kikuchi bands. Theory actually shows that interference effects reduce some diffracted intensities to zero and render other reflections not of equal intensity. In other words, scattering from one atom in the unit cell can interfere with scattering from another atom to reduce or increase the intensity of diffraction. For single crystal diffraction, the diffracted intensity  $I_{hkl}$  of a specific reflection (hkl) is proportional to the absolute square of the so-called *structure factor*  $F_{hkl}$ :

$$I_{hkl} \propto |F_{hkl}|^2 \quad (\text{Eq. 2.3})$$

The structure factor is defined as the sum of scattering from all atoms of the unit cell, or:

$$F_{hkl} = \sum_{j=1}^N f_{e,j}(\theta) \exp[2\pi i(hx_j + ky_j + lz_j)] \quad (\text{Eq. 2.4})$$

where  $j$  represents the  $j^{\text{th}}$  atom in the unit cell and  $f_{e,j}(\theta)$  is the corresponding atomic scattering factor for a given diffraction angle  $\theta$ . The exponential function describes the phase shift of waves diffracted by the atom  $j$ , for which the position in the unit cell is defined by the coordinates  $x_j, y_j, z_j$ . The electron scattering factor can be derived for a particular element from the X-ray atomic scattering factor  $f_{x,j}(\theta)$  using the Mott formula:

$$f_{e,j}(\theta) = \frac{4\pi m_0 e^2 \lambda^2}{h^2 \epsilon_0 \sin^2(\theta/2)} (Z - f_{x,j}(\theta)) \quad (\text{Eq. 2.5})$$

with the electron rest mass  $m_0$ , the electron charge  $e$ , the wavelength  $\lambda$ , Planck's constant  $h$ , the permittivity of vacuum  $\epsilon_0$  and the atomic number  $Z$ .

It must be noted that, since electrons interact much stronger with matter than X-rays, multiple (dynamic) diffraction occurs. As the structure factor is proportional to the diffracted intensity only under kinematic conditions, it might, therefore, not be well suited to

estimate the intensity of the Kikuchi bands. Resolution tests, however, have shown that the main part of the EBSD signal originates in a volume much smaller than the calculated interaction volume (HUMPHREYS et al. 1999) and consists of electrons, which have suffered only one diffraction event. For most minerals, the ranking in the electronic structure factor lists thus needs only minor adjustments. There are a few exceptions such as albite, for which the kinematic model is not precise enough (PRIOR & WHEELER 1999). In the future, dynamic diffraction models may give better results in the simulation of EBSD patterns.

The reflecting planes with the largest structure factors are incorporated in the material file, in order to allow the software to identify the detected bands. Once the pattern has been indexed, the orientation of the source point is known. An example of a fully indexed pattern is shown in Fig. 2.5.

In this thesis, the reflectors included in the material files have been generated using the Electron Microscopy Image Simulation software package developed by STADELMANN (1987). The software creates a list of numerous reflectors with the corresponding structure factors (indicated as  $vhkl+i$ ). To obtain the reflectors that give rise to the highest diffracted intensity (without considering multiple scattering), the operator selects only those with the highest absolute square of  $vhkl+i$ . The number of reflectors necessary

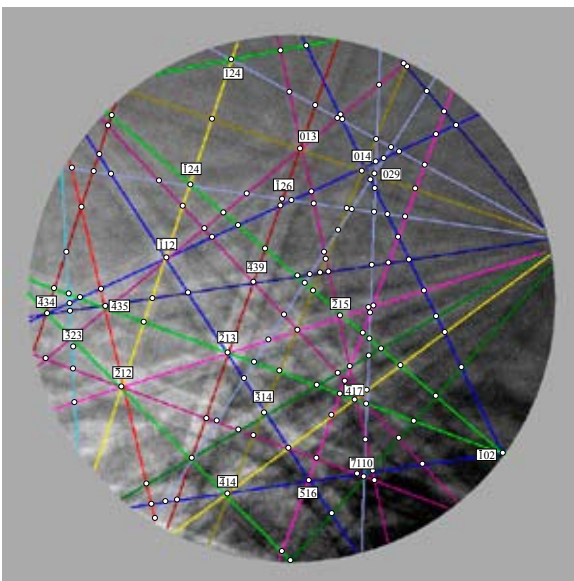


**Fig. 2.5** EBSD Kikuchi pattern of Fig. 2.2b after indexing. Each band corresponds to a distinct set of planes in the crystal; intersections of bands represent zone axes. Only the major zone axes have been labeled for clarity.

for successful indexing increases with the decreasing symmetry. Typically four or five reflectors may be sufficient for cubic crystals, whereas more than 40 may be needed for triclinic ones.

Two material files were created or refined during this PhD thesis to index trigonal alumina and cubic yttrium-stabilized zirconia patterns (s. Table III.7 in the Appendix). Material files for olivine, orthopyroxene, clinopyroxene and garnet were put at our disposal by Karsten Kunze (ETH Zürich, Switzerland).

## 2.2.4 Confidence Index (CI), Fit and Image Quality (IQ)

The EDAX<sup>®</sup> (TSL) OIM Data Collection software proposes three parameters to assess the reliability of indexing: the *Confidence Index (CI)*, the *Fit* and the *Image Quality (IQ)*.

### 2.2.4.1 Confidence Index (CI)

During the automated indexing routine each EBSD pattern is indexed using combinations of three bands known as triplets. They are generated from a selection of bands identified by the Hough Transform. For each given triplet several possible solutions may be found, thereby corresponding to different crystallographic orientations and satisfying the angular relationship of the Kikuchi bands. After processing all the triplets, the software ranks these potential solutions by summing all the votes corresponding to a given orientation (WRIGHT & ADAMS 1992). The CI parameter is then calculated according to the equation:

$$CI = \frac{(V_1 - V_2)}{V_{IDEAL}} \quad (Eq. 2.6)$$

where  $V_1$  and  $V_2$  are the number of votes for the first and second solution and  $V_{IDEAL}$  is the total possible number of votes, which corresponds to the number of different triplets used in the indexing procedure. In EDAX<sup>®</sup> (TSL) OIM the user controls  $V_{IDEAL}$  by limiting the number of bands available to generate triplets.

The confidence index may range from 0 to 1. In order to discriminate between reliable and unreliable indexing, a threshold value for CI must be set. This is particularly important when calculating pole figures or orientation distribution functions from an orientation map, where wrong indexed points with low CI

values may completely distort the results. According to MAULER (2000), a threshold of  $CI \geq 0.2$  is appropriate for peridotite samples. The same value has been used in this PhD thesis.

#### 2.2.4.2 Fit

The fit parameter indicates the average angular deviation between the observed position of the bands and a recalculated position of the bands based on the orientation obtained from the voting procedure. A small angular deviation (e.g.  $0.5^\circ$ ) means a good fit between detected and recalculated data.

#### 2.2.4.3 Image Quality (IQ)

The IQ parameter reflects the intensity and sharpness of the observed bands in the EBSD patterns. It is calculated by summing up the detected peaks in the Hough Transform and it expresses the quality of the original image. Most factors affecting the quality of Kikuchi patterns depend on the quality of the crystal lattice in the diffracting volume. Any natural distortions of the crystal lattice, low crystallinity due to bad polishing, charging effect, too thick coating, grain boundaries or dirty marks lead to more diffuse patterns of a lower quality and IQ. Commonly, patterns with a very low IQ value will also have a poor CI.

The IQ parameter is not an absolute value because it also depends on the width of diffraction bands, which in turn is dependent on the crystal structure and the geometry of the EBSD system. Therefore, IQ values for patterns obtained for different materials or with different equipments cannot be compared to each other.

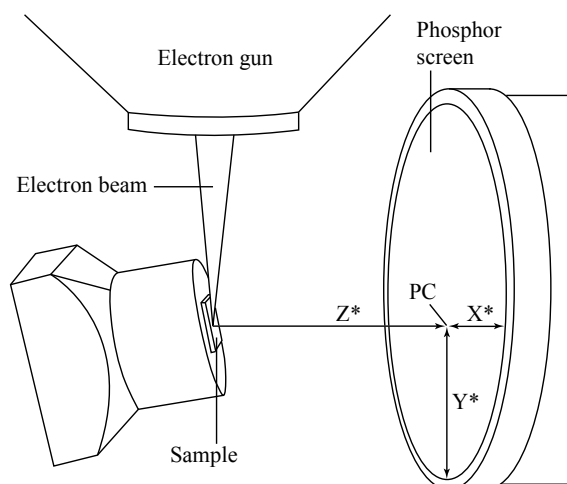


Fig. 2.6 Schematic view of the pattern centre (PC).

## 2.2.5 Pattern centre calibration

To accurately index patterns, it is necessary to perform a calibration that takes into account the geometry of the system. A successful calibration requires an accurate identification of the specimen-to-screen distance and of the pattern centre (PC), defined as the point of intersection on the phosphor screen of a ray perpendicular to a plane containing the electron beam and the horizontal direction of the sample (Fig. 2.6).

A raw PC calibration using very high quality patterns of nickel was performed each time new materials were analyzed. The *Auto Pattern* and *Tuning* methods, described in the EDAX<sup>®</sup> (TSL) OIM Data Collection user manual, were applied in this case. The raw calibration values  $X^*$ ,  $Y^*$  and  $Z^*$  were then used as a standard basis and refined manually for each sample when necessary.

## 2.2.6 Orientation mapping

Computerized indexing of Kikuchi patterns (s. Section 2.2.3) coupled with the SEM's ability to control beam or stage movements have led to fully automated EBSD orientation mapping capabilities (JUUL JENSEN & SCHMIDT 1990, KRIEGER LASSEN et al. 1992, WRIGHT & ADAMS 1992, ADAMS et al. 1993, WRIGHT et al. 1993). During orientation mapping, data are collected spot by spot on a grid defined by the operator. The image is then reconstructed by coloring pixels on the basis of a look-up table (Fig. 2.7). In this thesis, orientation mapping was performed using the softwares EDAX<sup>®</sup> (TSL) OIM Data Collection 3.5 and EDAX<sup>®</sup> (TSL) OIM Analysis 3.08.

As long as the area of interest is small ( $< 1 \text{ mm}^2$ ) a beam-controlled scan is performed. The position of the stage is held fixed while the electron beam scans the selected area. On larger areas, however, the beam scan mode is no longer possible and has to be replaced by a stage-controlled scan mode. Grain statistics dictate the choice of the acquisition mode: whereas the number of grains contained in  $1 \text{ mm}^2$  of high-tech ceramics is generally sufficient to obtain a reliable texture, the same area is meaningless for coarse-grained rocks.

### 2.2.6.1 Scanning procedure and tricks

Because it does not involve automatic movements of the stage, beam scanning is more straightforward and less hazardous than stage scanning. In beam scan

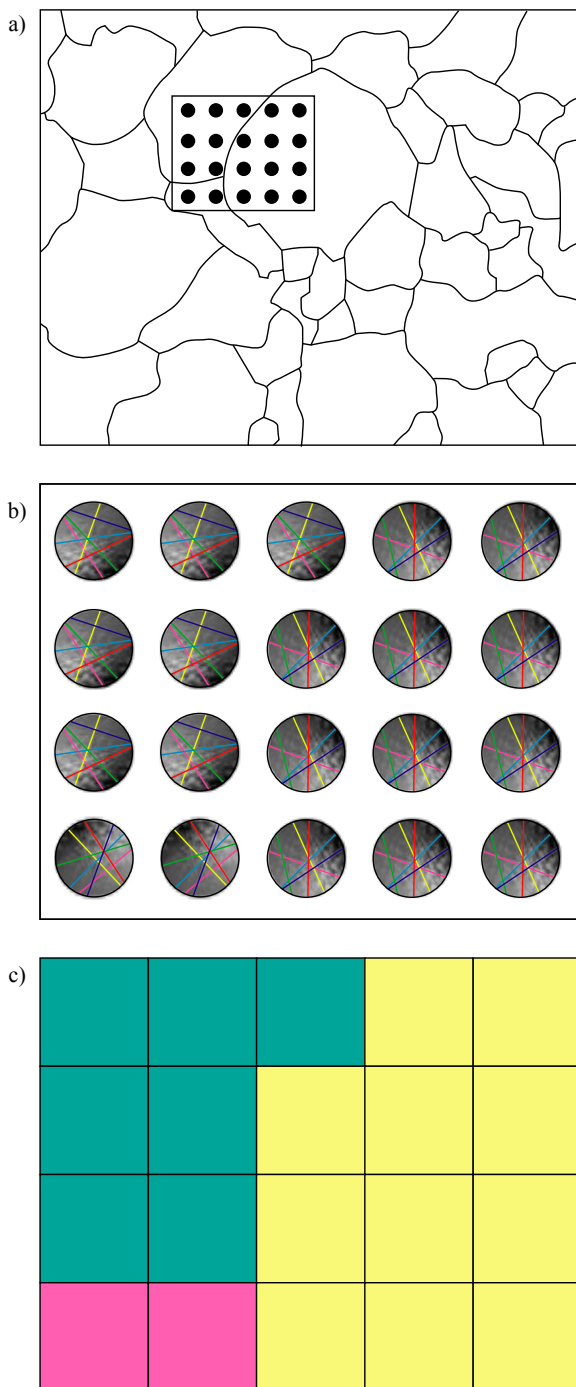


**Fig. 2.7** Schematic illustration of orientation imaging in a polycrystalline material: for each analysis point (a), an EBSD Kikuchi pattern is collected and indexed automatically (b). The image is reconstructed by coloring pixels on the basis of orientation data (c).

mode, the area to be scanned is directly selected by dragging the cursor onto the image preview in EDAX<sup>®</sup> (TSL) OIM Data Collection, without going through a time-consuming determination of manual coordinates. On the contrary, stage scanning involves movements

of the stage inside the SEM chamber. As a collision of the mobile parts with the detectors or the final lens of the electron gun may seriously damage the system, a precise procedure must be followed scrupulously. With our system configuration, the following points should be taken into account:

(a) During the first step the SEM chamber must remain open. The stage file called *NORMAL* is set into the *VENT/PUMP* position and the special sample holder for stage scans is inserted into the SEM chamber according to the corresponding mark on the stage. The stage file *NORMAL* is then replaced by the *OIM* stage file set in position *INITIAL*. Changing this position to *EBSD 70* moves the stage to its tilted position. At this point the SEM chamber can be closed and the air pumped out.

(b) The sample is then moved manually to a 20 mm working distance (WD). A smaller WD would make the sample collide with the final lens during stage scan.

(c) Once the WD is set, the sample is moved to the position corresponding to the first point of the scan. The selected scanning directions are from the back of the chamber towards the door and from top to bottom (s. *Stage Setting* in (g)). However, because it is the stage which is moved and not the beam, the stage motions are actually in the opposite direction. The starting position, which corresponds to the bottom right corner of the area when displayed on the computer screen (scan rotation option set to 0), is chosen accordingly. Finally, the coordinates  $x_0$  and  $y_0$  of the origin point are recorded by the user (e.g.  $x_0 = 9000 \mu\text{m}$  and  $y_0 = -18000 \mu\text{m}$ ).

(d) The sample is then moved manually to the last point of the scan and its coordinates  $x_e$  and  $y_e$  are recorded (e.g.  $x_e = -11000 \mu\text{m}$  and  $y_e = -5000 \mu\text{m}$ ).

(e) The dimensions of the scan are calculated according to the coordinates of the origin ( $x_0, y_0$ ) and the final point ( $x_e, y_e$ ) of the scan (for the example above: the size in  $x = |x_e - x_0| = 20000 \mu\text{m}$ , the size in  $y = |y_e - y_0| = 13000 \mu\text{m}$ ).

(f) The parameters of the camera needed for the EBSD pattern acquisition, i.e. the binning, gain, black level and exposure, are set according to the usual procedure.

(g) Before running the stage scan, the following

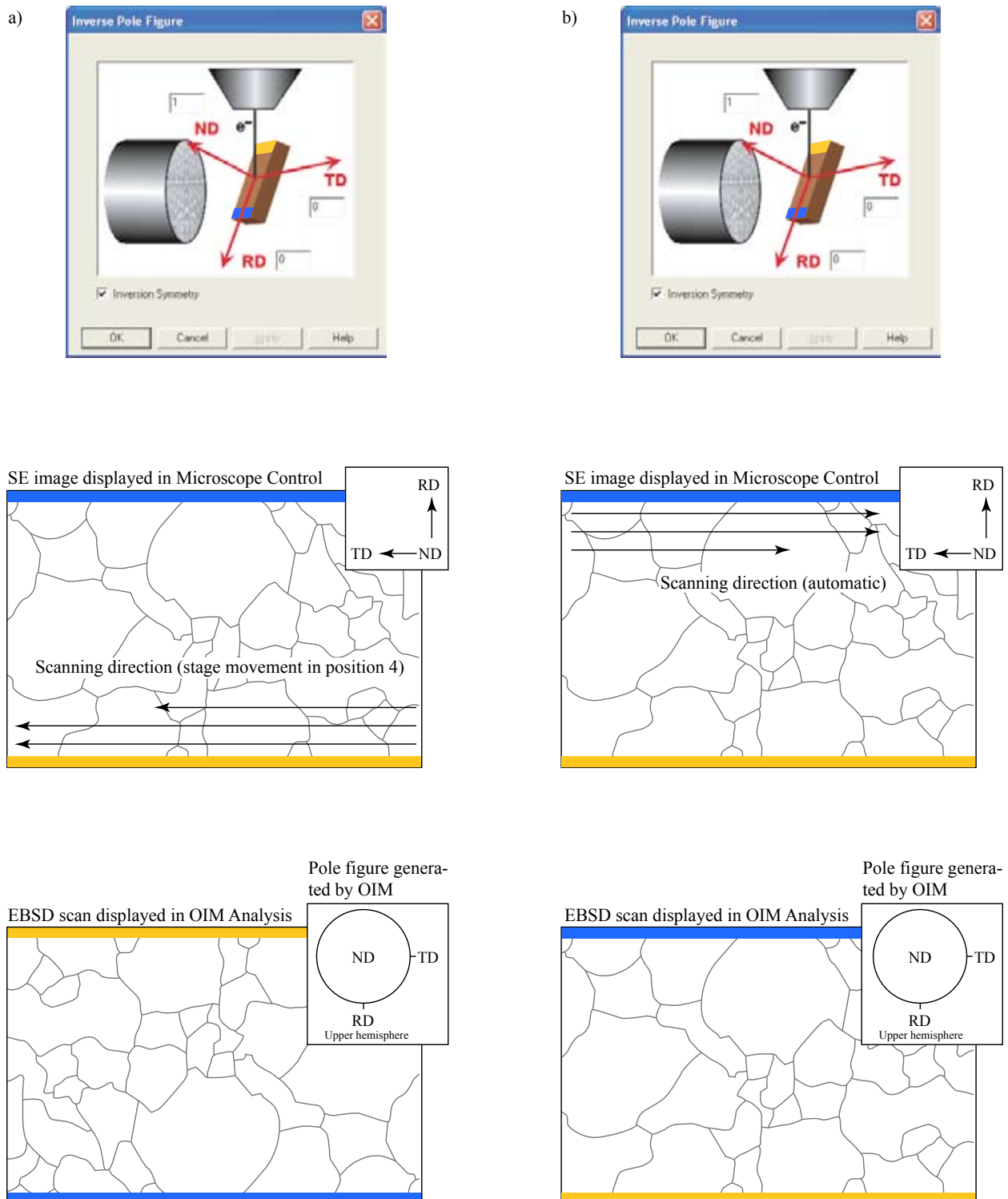


**Fig. 2.8** Orientation mapping as performed in our lab in (a) stage scan mode and (b) beam scan mode. Because of the configuration of the SEM chamber with respect to the EBSD system, the upslope rim of the sample (yellow bar) appears at the bottom of the image when displayed in the Microscope Control program, whereas the downslope rim (blue bar) is at the top. In this configuration, the RD direction points upwards and TD to the left of the image. In stage scan mode, the scanning direction (determined by the movement of the stage) is chosen in such a way that the reconstructed EBSD scan in EDAX<sup>®</sup> (TSL) OIM Analysis is oriented in the same way as the pole figure generated by the program (TD right and RD bottom). In beam scan mode, however, the scanning direction is exactly reversed: the EBSD scan obtained (bottom right) has to be rotated by 180° before being compared with the corresponding pole figure.

parameters must be checked in EDAX® (TSL) OIM Data Collection:

*Environment Setting:*

- Specimen Tilt = 70
- Scan Tilt = Y
- Library link for stage control: StageEDAX.dll

*Beam Control Setting:*

- Tilt correct = yes
- Wait for reply = yes

*Stage Setting:*

- Using a pre-tilted or pre-rotated sample holder = no
- Stage movement directions in position 4 : Y points up et X left
- Log stage command to a text file = yes

*Stage Scan properties:*

- Square grid
- Magnification = 100 (default)
- Start x : value  $x_o$  (for the example above:  $x_o = 9000 \mu\text{m}$ )
- Start y : value  $y_o$  (for the example above:  $y_o = -18000 \mu\text{m}$ )
- Size: physical size of the scan calculated from  $x_o$ ,  $x_e$ ,  $y_o$  et  $y_e$  (for the example above: size in x = 20000  $\mu\text{m}$ ; size in y = 13000  $\mu\text{m}$ ).

(h) In the ClmShell32 application, verify that the stage orientation option is set to position 4.

(i) The *Active Scan* pop-up menu in EDAX® (TSL) OIM Data Collection must be free of data entered during earlier sessions, in order to prevent the software from performing the same scan again.

- (j) Run the stage scan.

### 2.2.6.2 Orientation of data in stage and beam scan modes

Once the data have been collected attention must be paid to the orientation of the EBSD scan with respect to the pole figure generated by EDAX® (TSL) OIM Analysis. In stage scan mode, the stage movement is chosen so that the scanning direction corresponds to TD and the direction of line skip to RD (s.

Section 2.3.1 for abbreviations). With this configuration, the resulting EBSD scan has the same orientation as the pole figure generated by EDAX® (TSL) OIM Analysis, in which the positions of TD, RD and ND are set. In beam scan mode, however, the situation is exactly the reverse. The scanning direction and line skip in the Philips® FEI XL30 SFEG Sirion SEM point towards the opposite directions of TD and RD respectively, which leads to a 180° relationship between the scan and the pole figure generated by the software. This problematic is illustrated graphically in Fig 2.8.

It must be noted, however, that the newest version of EDAX® (TSL) OIM Analysis 4 (not available in our lab) is more flexible than the 3.08 version on that score. The TD, RD and ND positions of the pole figures can be adjusted by the user in accordance with the scanning direction, thus avoiding post-acquisition rotation of the scan.

## 2.3 MATHEMATICAL ASPECTS RELATED TO TEXTURE ANALYSIS

This section gives a concise overview of the mathematical background used in texture analysis. For more details the reader is referred to BUNGE (1982), RANDLE (1993 & 2000) and KOCKS (1998). Please note that the term *direction* used below always refers to the position of a single linear feature (vector, axis) with respect to a coordinate system, whereas *orientation* describes the relation between two complete coordinate frames.

### 2.3.1 Coordinate systems

In order to specify the orientation of a single crystal relative to the polycrystalline sample it belongs to, two sets of orthogonal reference axes, known as *coordinate systems*, must be defined (BOLLMANN 1970, MCKIE & MCKIE 1974). One is assigned to the crystal and written  $C_c \{x_c, y_c, z_c\}$  while the other is attributed to the sample and noted  $C_s \{x_s, y_s, z_s\}$ . By convention both frames are Cartesian and right-handed.

The crystal coordinate system  $C_c \{x_c, y_c, z_c\}$  is specified by directions in the crystal. For convenience, directions are chosen in order to match the crystal symmetry. For orthogonal systems (cubic, tetragonal, orthorhombic) the axes [100], [010] and [001] already form an orthogonal frame and are used for  $x_c$ ,  $y_c$  and

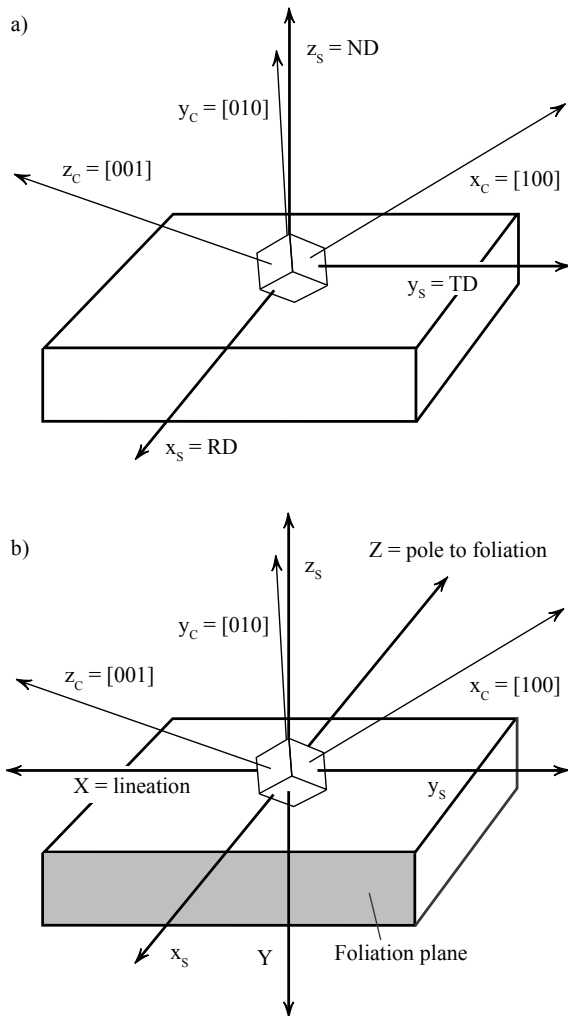


**Fig. 2.9** Sample and crystal coordinate systems  $C_s \{x_s, y_s, z_s\}$  and  $C_c \{x_c, y_c, z_c\}$  as commonly chosen in materials science (a). An example of common configuration in earth sciences for orthogonal crystals is shown in (b). (after RANDLE 2000).

$z_c$ , respectively. For non-orthogonal systems (hexagonal, trigonal, monoclinic, triclinic), an orthogonal frame needs to be associated with the crystal axes. In the hexagonal and trigonal systems, the axis [0001] is associated with  $z_c$ , whereas  $x_c$ , and  $y_c$  are attributed either to [-10-10] and [-12-10], or to [2-1-10] and [0-1-10]. The latter option is the one used in EDAX<sup>®</sup> (TSL) OIM softwares.

The sample coordinate system  $C_s \{x_s, y_s, z_s\}$  is chosen according to important surfaces or directions, often associated with the shape or microscopic fabric of the specimen. As a general rule,  $z_s$  is attributed to the normal to the surface to analyze.

In materials science, there are obvious choices determined by the processing geometry. For example a

fabricated piece of metal will have the rolling direction RD assigned to  $x_s$ , the transverse direction (TD) to  $y_s$  and the through-thickness direction, i.e. the direction normal to the rolling plane (ND) to  $z_s$  (Fig. 2.9). In earth sciences macroscopic features like the orientations of platy and elongated crystals (the rock foliation and lineation) determine the choice of the sample coordinates. The directions  $y_s$  and  $z_s$  are generally placed in the foliation plane, whereby the  $y_s$  direction is orientated parallel to any existing lineation. This notation may be confusing because standard geological representations of LPO are often shown according to the tectonic directions X, Y and Z, with XY defining the foliation plane and X the lineation. There is no general convention for the assignments of tectonic axes to the directions  $x_s$ ,  $y_s$  and  $z_s$ , and different schemes are found in the literature. One of the most widespread choices is to assign X to  $-y_s$ , Y to  $-z_s$  and Z to  $-x_s$ . In this case, the system is left-handed with respect to X, Y and Z directions, although right-handed with respect to  $x_s$ ,  $y_s$  and  $z_s$ . Another frequently used option is to attribute X to  $y_s$ , the other axes being the same, so that the system becomes right-handed with respect to X, Y and Z as well.

Whichever option is selected, the most important point is to know exactly to which directions in the sample coordinate system the structural directions were attributed. Hence the foliation and the lineation must be identified at an early stage in the sample preparation in order to avoid troublesome and somewhat haphazard post-processing rotation of the data. This latter procedure must be followed, however, when the hand specimen lacks any visible fabric or is too small to be sawed in the desired direction.

### 2.3.2 Reference sphere, pole figures and inverse pole figures

Directions or orientations are often given in polar coordinates, which can be graphically represented with the help of a reference unit sphere. The direction is represented by the point of intersection between the direction line D going through the center and the surface of the unit sphere. The position of the point is given by two angles:  $\Psi$  representing the azimuth of the pole and  $\Omega$  the angle between the direction D and the polar axis (Fig. 2.10).

However, this three dimensional representation is not practical and often replaced by a well-known stereographic or equal area projection of the unit sphere.

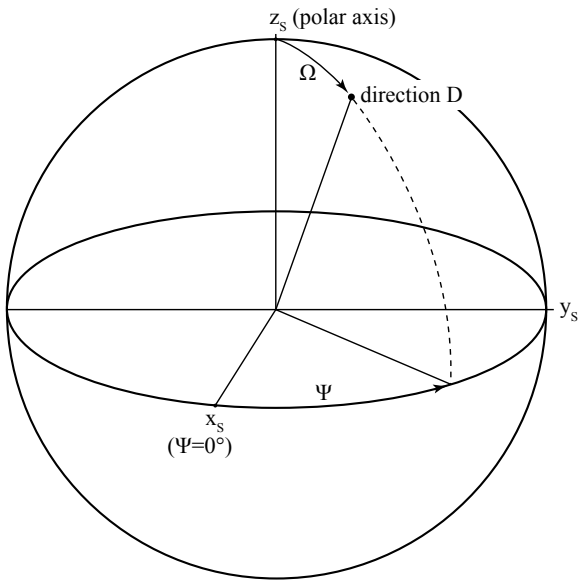


Fig. 2.10 Illustration of the reference sphere (after MATTHIES et al. 1990).

Common two-dimensional representations include pole and inverse pole figures. In pole figures, the reference directions coincide with the sample coordinate system  $C_s \{x_s, y_s, z_s\}$  and single crystal directions (e.g.  $z_c = [001]$ ) are projected into that frame. In an inverse pole figure, the reference is given by the crystal coordinates  $C_c \{x_c, y_c, z_c\}$  and one of the sample directions (e.g.  $z_c = ND$ ) is projected. Materials scientists commonly use projections of the upper hemisphere whereas earth scientists often pick the lower hemisphere. In this study, the Unicef Careware software package (MAINPRICE 1990 & 1999) was used to generate pole figures for the peridotite minerals, whereas EDAX® (TSL) OIM Analysis 3.08 was used for the pole figures of the ceramic project.

### 2.3.3 Orientation

The orientation of a single crystal relative to the sample is given by the rotation required to make the crystal coordinates  $C_c$  coincide with the sample coordinates  $C_s$ . Commonly rotation operations are expressed either by an *orientation matrix* or by *Euler angles*.

#### 2.3.3.1 Orientation matrix representation

In the orientation matrix representation, the orientation  $g$  of the crystal coordinate system  $C_c$  relative to the sample coordinate system  $C_s$ , is given by the relation:

$$C_c = g \cdot C_s \quad (\text{Eq. 2.7})$$

in which  $g$  is expressed by a 3x3 square orientation matrix defined as follows:

$$g = \begin{pmatrix} \cos\alpha_1 & \cos\beta_1 & \cos\gamma_1 \\ \cos\alpha_2 & \cos\beta_2 & \cos\gamma_2 \\ \cos\alpha_3 & \cos\beta_3 & \cos\gamma_3 \end{pmatrix} \quad (\text{Eq. 2.8})$$

where  $\alpha_n$  (with  $n=1,2,3$ ) represent the angles between the unit cell edges (e.g. the crystallographic directions  $[100]$ ,  $[010]$ ,  $[001]$ ) and  $x_s$  respectively,  $\beta_n$  the angles between  $[100]$ ,  $[010]$ ,  $[001]$  and  $y_s$ ,  $\gamma_n$  the angles between  $[100]$ ,  $[010]$ ,  $[001]$  and  $z_s$  (Fig. 2.11). The matrix representation is mostly used when mathematical manipulations are necessary. Of the nine components of the matrix, only three are independent.

#### 2.3.3.2 Euler angles representation

To indicate an orientation, the so-called Euler angles  $\phi_1$ ,  $\Phi$  and  $\phi_2$  (BUNGE 1965 & 1982) are used as a standard method. They represent a set of three rotations that are needed to make the principal axes of the sample coincide with the principal axes of the crystal lattice. Several other equivalent conventions describe this sequence of rotations (i.e. ROE 1965, KOCKS 1988).

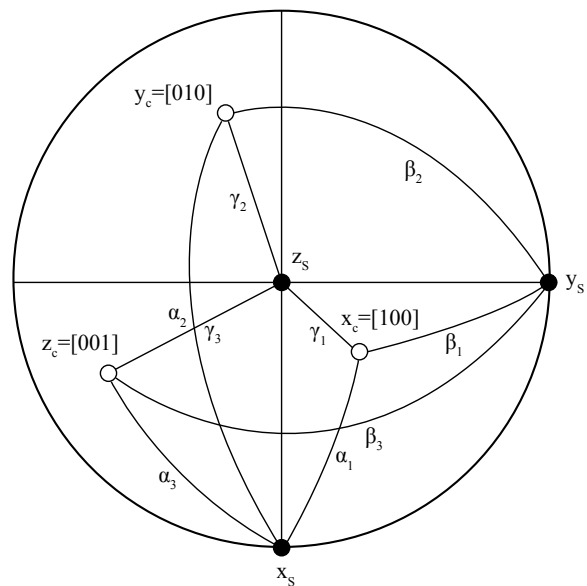
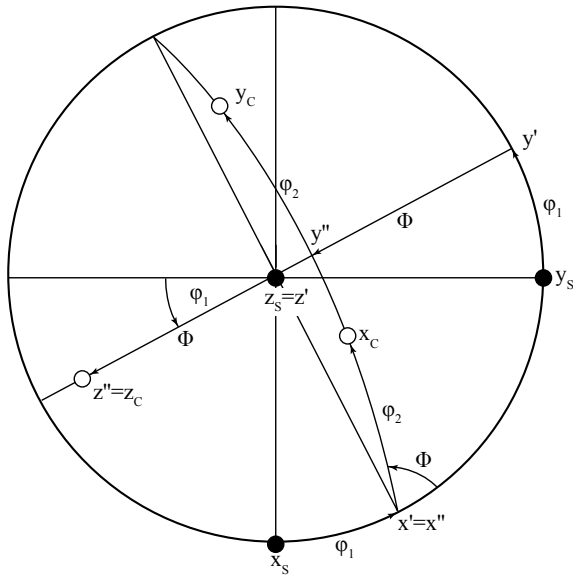
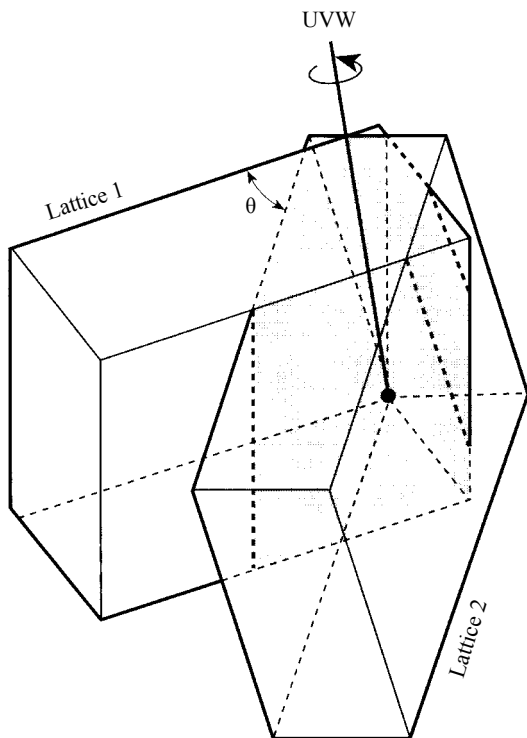


Fig. 2.11 Stereographic projection (upper hemisphere) showing the angles used in the matrix representation. ( $C_c \{x_c, y_c, z_c\}$  = crystal coordinates system;  $C_s \{x_s, y_s, z_s\}$  = sample coordinates system).



**Fig. 2.12** Stereographic projection (upper hemisphere) showing the sequence of rotations ( $\varphi_1$ ,  $\Phi$  and  $\varphi_2$ ) required to make the sample coordinate system  $C_s$  coincide with the crystal coordinate system  $C_c$  (after BUNGE 1982).  $C'$   $\{x', y', z'\}$  and  $C''$   $\{x'', y'', z''\}$  are the sample coordinates after the first and second rotation respectively. The angle  $\varphi_1$  is defined by the rotation of  $C_s$  into  $C'$  around  $z_s$ ,  $\Phi$  is defined by the rotation of  $C'$  into  $C''$  around  $x'$  and  $\varphi_2$  is defined by the rotation of  $C''$  into  $C_c$  around  $z''$ .



**Fig. 2.13** Misorientation between two crystals described by the angle/axis pair ( $\theta / UVW$ ) representation (after FISCHMEISTER 1985).

Bunge's convention, which was used here, is described in Fig. 2.12.

### 2.3.4 Misorientation

Misorientation is defined as the difference in orientation between two neighboring grains. In other words it is the rotation, defined by the rotation matrix  $\Delta g_{12}$ , which is required to make the crystal lattice of grain 1 coincide with the crystal lattice of grain 2. Given two grains with orientations defined by  $g_1$  and  $g_2$ , the rotation matrix  $\Delta g_{12}$  can be expressed by the equation:

$$\Delta g_{12} = g_2 \cdot g_1^{-1} \quad (\text{Eq. 2.9})$$

As with orientations, the misorientation  $\Delta g$  can be represented by three Euler angles. However, misorientations are commonly described in terms of a single rotation axis UVW and an angle  $\theta$  (IBE & LÜCKE 1972, POSPIECH 1972, HANSEN et al. 1978). This is known as the angle/axis representation. The axis UVW is a crystallographic direction common to both crystal lattices, whereas  $\theta$  depicts the rotation around UVW required to make the two crystal lattices coincide (Fig. 2.13).

Other representations of misorientation include the Rodrigues vector and quaternion descriptions. For more information see KOCKS (1998).

### 2.3.5 Orientation Distribution Function (ODF) and texture index (J)

#### 2.3.5.1 Orientation distribution function

The *orientation distribution function (ODF)*  $f(g)$  expresses the volume fraction of orientations in the interval between  $g$  and  $g+dg$  in a space containing all possible orientations (BUNGE 1982):

$$\Delta V / V = \int f(g) dg \quad (\text{Eq. 2.10})$$

$$dg = \frac{1}{8\pi^2} \sin \Phi d\varphi_1 d\Phi d\varphi_2 \quad (\text{Eq. 2.11})$$

where  $\Delta V/V$  is the volume fraction of crystals with orientation  $g$ ,  $f(g)$  is the texture function and  $dg$  is the volume of the region of integration in orientation space. Practically, the ODF can be calculated in two ways: the so-called *direct* methods and the *series*

expansion methods.

In the direct methods the ODF is directly calculated from the pole figure. A regular grid with a spacing of a few degrees (typically 2.5 or 5°) is applied to the pole figure and the individual poles are counted for each cell. The values obtained are then normalized to the cell size and the total number of poles. From these discrete values the continuous distribution function (ODF) is derived by interpolation.

The series expansion methods are based on the assumption that pole figure data can be fitted by a series of spherical harmonic functions. The series expansion  $f(g)$  is given by (BUNGE 1982):

$$f(g) = \sum_{l=0}^{l_{\max}} \sum_{m=-l}^l \sum_{n=-l}^l C_l^{mn} T_l^{mn}(g) \quad (\text{Eq. 2.12})$$

where  $T_l^{mn}(g)$  are the spherical harmonic functions calculated for each orientation ( $g$ ) and  $C_l^{mn}$  are the series expansion coefficients. The expansion index  $l_{\max}$ , called Series Rank ( $L$ ) in the EDAX® (TSL) OIM Analysis software, is used to truncate the series expansion. An  $l_{\max}$  value of 22 is generally considered to yield sufficiently accurate results with a reasonable computation time.

The truncation of the series expansion leads to both positive and negative values. However, since the ODF is a probability density function, it has to be positive everywhere. To overcome this negativity problem, the  $C_l^{mn}$  coefficients are adjusted by a Gaussian spread function  $K$ :

$$K = \frac{\exp\left[-\frac{l^2\omega^2}{4} - \exp\left(-\frac{(l+1)^2\omega^2}{4}\right)\right]}{1 - \exp\left(-\frac{\omega^2}{4}\right)} \quad (\text{Eq. 2.13})$$

The Gaussian half-width parameter  $\omega$ , which has to be set by the user in the EDAX® (TSL) OIM Analysis software, has a marked influence on the peak geometry. A small  $\omega$  value will sharpen the peaks (without making data more accurate), whereas a large value will have a smoothing effect. Even if the choice of  $\omega$  is somewhat arbitrary, a small  $\omega$  should be avoided when the number of measured orientations is small. This invariably leads to the creation of artifacts, individual points becoming sharp peaks in the ODF repre-

sentation. In the Unicef Careware software package (MAINPRICE 1990 & 1999), the user does not intervene in the choice of the Gaussian half-width, which is set to a fixed value of 8.5°.

### 2.3.5.2 Texture index ( $J$ )

The texture index  $J$  indicates how strongly a sample is textured. It is defined as the mean square value of the ODF  $f(g)$  (BUNGE 1982):

$$J = \int f(g)^2 dg \quad (\text{Eq. 2.14})$$

The  $J$  index has a value of 1 for a random distribution and a value of infinity for a single crystal, provided the expansion index  $l_{\max}$  is an infinite number.

## 2.4 SAMPLE SURFACE PREPARATION

### 2.4.1 Pre-polishing considerations

#### 2.4.1.1 Peridotite

For statistical reasons, LPO analyses of polycrystalline samples require that the orientation of a sufficient number of grains be measured. According to BEN ISMAIL & MAINPRICE (1998), at least 100 to 150 grains should be analyzed in order to obtain a representative texture. All peridotite xenoliths investigated in this study are coarse-grained with individual crystals of several millimeters in size. Scanning of large areas was therefore imperative. Rectangular blocks of peridotite with analyzable surfaces ranging from 2 to 6 cm<sup>2</sup> were prepared, allowing the measurement of more than 300 grains for each sample.

The peridotite xenoliths are very brittle with weak cohesion between grains. In order to avoid sample break up during grinding, all blocks were impregnated with an epoxy Araldit® D glue before surface preparation.

#### 2.4.1.2 Ceramics

The density of a green body shaped by cylindrical die pressing is not homogeneous throughout the whole sample (s. Section III.2.6.1). Indeed, the top and

bottom surfaces of the cylindrical green body show a relatively large density variation normal to the pressing axis while the density in the middle of the sample is more constant. Such density heterogeneities are often translated into the sintered body. In order to analyze the most homogenous surface possible in terms of density, each sample was sawed transversally half way between its upper and lower bases. One of the two new surfaces was then prepared for EBSD analyses.

## 2.4.2 Polishing

### 2.4.2.1 *Peridotite*

EBSD measurements require that a pristine crystalline lattice extend to within a few nanometers of the specimen surface. A deteriorated surface would seriously affect the Kikuchi pattern quality and make reliable EBSD data acquisition impossible. To minimize the mechanical damage of the surface to be analyzed, the peridotite sample blocks were first grinded on Struers® diamond-bearing discs. The next polishing steps were achieved on a synthetic Teflon® plate using successive diamond-bearing pastes starting with a grain size of 15 µm and ending with 0.25 µm. At last, chemical-mechanical lapping (FYNN & POWELL 1979, LLOYD 1987) with a basic colloidal silica solution (particle size 0.025 µm) was performed. After 10 h of lapping, the samples were

rinsed in water.

To reduce the charging effects under the SEM electron beam, silver painting was applied on the ridges of the sample blocks. Finally, each specimen was coated with a 2 nm carbon layer using a BalTec® MED 020 high vacuum coating system equipped with a quartz film thickness monitor. The minute carbon thickness applied was sufficient to avoid charging and did not deteriorate the EBSD patterns.

### 2.4.2.2 *Snowball garnets*

The polishing procedure for the snowball garnet samples was exactly the same as the one followed for the peridotite samples. Nevertheless, the analyzed specimens consisted of thin sections instead of blocks. Because of the physical limitations of the sample holder, however, the thin sections were mounted on rectangular blocks. This configuration also turned out to be more practical when applying silver painting on the samples.

### 2.4.2.3 *Ceramics*

The surface preparation for alumina and zirconia ceramics was very similar to the procedure followed for rocks. Because of the smallest size of the ceramic bodies, however, the duration of the chemical-mechanical lapping with the colloidal solution was limited to 6 h instead of 10.

\*\*\*\*\*



### 3 - SEISMIC PROPERTIES OF THE UPPER MANTLE BENEATH LANZAROTE (CANARY ISLANDS): MODEL PREDICTIONS BASED ON TEXTURE MEASUREMENTS BY EBSD

VONLANTHEN P., KUNZE K., BURLINI L. & GROBÉTY B.

published in *Tectonophysics* 428, 65-85 (2006)

#### ABSTRACT

We present a petrophysical analysis of upper mantle xenoliths, collected in the Quaternary alkali basalt fields (Series III and IV) from the island of Lanzarote. The samples consist of eight harzburgite and four dunite nodules, 5 to 15 cm in size, and exhibit a typical protogranular to porphyroclastic texture. An anomalous foliation resulting from strong recovery processes is observed in half of the specimens. The lattice preferred orientations (LPO) of olivine, orthopyroxene and clinopyroxene were measured using electron backscatter diffraction (EBSD). In most samples, olivine exhibits LPO's intermediate between the typical single crystal texture and the [100] fiber texture. Occasionally, the [010] fiber texture was also observed. Simultaneous occurrence of both types of fiber textures suggests the existence of more than one deformation regime, probably dominated by a simple shear component under low strain rate and moderate to high temperature. Orthopyroxene and clinopyroxene display a weaker but significant texture. The LPO data were used to calculate the seismic properties of the xenoliths at PT conditions obtained from geothermobarometry, and were compared to field geophysical data reported from the literature. The velocity of P-waves (7.9 km/s) obtained for a direction corresponding to the existing seismic transect is in good agreement with the most recent geophysical interpretation. Our results are consistent with a roughly W-E oriented fastest P-wave propagation direction in the uppermost mantle beneath the Canary Islands, and with the lithosphere structure proposed by previous authors involving a crust-mantle boundary at around 18 km in depth, overlaid by intermediate material between 11 and 18 km.

#### 3.1 INTRODUCTION

Anisotropy of petrophysical properties and structure is a well established feature of the upper mantle, documented by numerous field observations (e.g. RAIFF et al. 1969, FORSYTH 1975, NATAF et al. 1984, TANIMOTO & ANDERSON 1985, SHEARER & ORCUTT 1986, MONTAGNER & TANIMOTO 1990, SILVER & CHAN 1991) and laboratory experiments (e.g. CARTER & AVÉ LALLEMANT 1970, NICOLAS et al. 1973, KUNZE & AVÉ LALLEMANT 1981, ZEUCH & GREEN 1984, CHOPRA & PATERSON 1981, ZHANG & KARATO 1995, TOMMASI et al. 1999, ZHANG et al. 2000, BYSTRICKY et al. 2000).

During sea-floor spreading, plastic deformation of the lithosphere and the upper part of the asthenosphere generates a lattice preferred orientation (LPO) of upper mantle minerals. Since olivine is elastically anisotropic (VERMA 1960, KUMAZAWA & ANDERSON 1969) and constitutes the volumetrically dominant phase, LPO of olivine is considered the main source for seismic anisotropy in the upper mantle (HESS 1964).

Ultramafic xenoliths represent a unique opportunity to investigate the geochemical and geophysical nature of upper mantle material. Calculations of seismic properties from xenolith LPO's help to evaluate

the magnitude of seismic velocities in the upper mantle (e.g. MAINPRICE & SILVER 1993, BARRUOL & KERN 1996, KERN et al. 1996, BEN ISMAIL & MAINPRICE 1998, MAINPRICE et al. 1998, SOEDJATMIKO & CHRISTENSEN 2000, SARUWATARI et al. 2001, PERA et al. 2003) and can be used to better constrain the interpretations inferred from field geophysical measurements. In the last few decades, the upper mantle xenoliths of Lanzarote have been investigated by numerous petrological and geochemical studies (SIENA et al. 1991, NEUMANN et al. 1995, THOMAS et al. 1999, NEUMANN et al. 2004). However, our knowledge on the petrophysical properties of the upper mantle beneath this island remains controversial. Using the seismic refraction method, BANDA et al. (1981) calculated a very low mantle velocity of 7.4 km/s for Pn-waves in the NNE-SSW direction. However, this interpretation was questioned recently by DAÑOBEITIA & CANALES (2000), who proposed an upper mantle velocity of 7.6-7.8 km/s in the same direction. In this paper, we present an electron backscatter diffraction (EBSD) study carried out on twelve ultramafic xenoliths sampled on the island of Lanzarote. The objective is to measure LPO's of olivine, orthopyroxene and clinopyroxene and to infer the seismic properties of the upper mantle in depth. These results are used to better constrain the deformation regimes and the geodynamic setting of the upper mantle and are compared to the interpretations deduced from field geophysical measurements.

### 3.2 GEOLOGICAL BACKGROUND

The geodynamic setting of the Canary Archipelago continues to be a debated issue among earth scientists. Historically, four concepts were proposed to explain the magmatic activity of the Canary Islands: (1) the hot spot model (MORGAN 1971, BURKE & WILSON 1972, SCHMINCKE 1973, VOGT 1974, KHAN 1974, MORGAN 1983), (2) the propagating fracture hypothesis, possibly related to the tectonics of the Moroccan Atlas (DASH & BOSSHARD 1969, MACFARLANE & RIDLEY 1969, BOSSHARD & MACFARLANE 1970, LE PICHON & FOX 1971, GRUNAU et al. 1975, ANGUIA & HERNÁN 1975), (3) the uplift tectonic concept (ARAÑA & ORTIZ 1986) and (4) the local extensional ridge theory (FÜSTER 1975). Among these, the hot spot model has clearly gained in popularity in the last two decades (e.g. SCHMINCKE 1982, HOLIK et al. 1991, WATTS 1994, HOERNLE et al. 1995, NEUMANN et al. 1995, CARRACEDO et al. 1998, DAÑOBEITIA & CANALES 2000, RHODES & DAVIES 2001). However, numerous inconsisten-

cies between the evolution of the Canary Islands and the classical hot spot scheme have been reported by HOERNLE & SCHMINCKE (1993). To explain these differences, these authors suggested that the Canary Islands plume corresponds to a "blob type" (ALLÈGRE et al. 1984) hot spot, whereas others (ANGUITA & HERNÁN 2000) proposed a unifying model partly reconciling three of the historically cited hypotheses, thus giving more weight to the regional tectonics. Whatever the scenario, it seems now widely accepted that volcanism in the Canary Islands cannot be attributed to a classical hotspot alone and is not completely independent of the regional tectonics. The question whether the importance of tectonics is major or minor has not been elucidated yet.

Lanzarote is the easternmost island of the Canary Archipelago, located about 140 km off the African continent in the Atlantic Ocean. Together with the island of Fuerteventura, Lanzarote represents the emergent part of the East Canary Ridge (Fig. 3.1), a NNE-SSW linear volcanic structure about of 400 km in length and 65 km in width (MARINONI & PASQUARÉ 1994). Subaerial volcanic activity in Lanzarote dates back to the mid-Miocene (ABDEL MONEM et al. 1971, COELLO et al. 1992). It can be divided into (1) a shield-building stage, mainly Miocene in age (14.5 - 8.7 Ma), followed

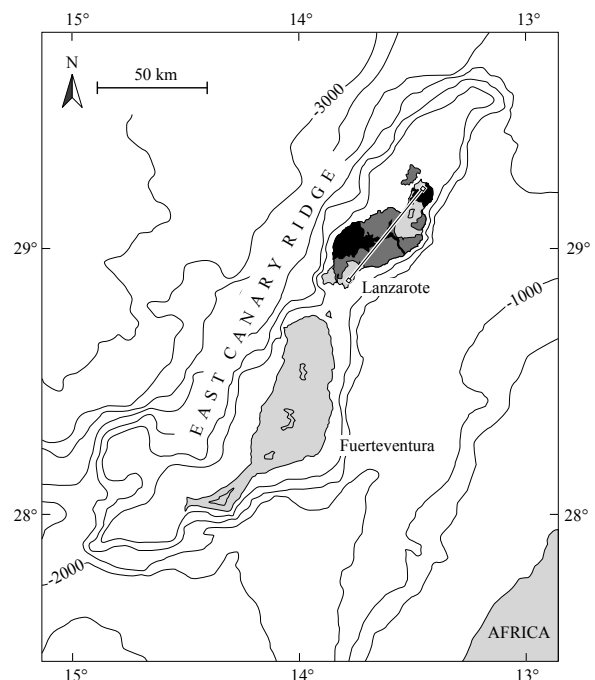


**Fig. 3.1** Map of the East Canary Ridge with altitude contours at 500 m intervals. Areas above sea level are light shaded. Quaternary lava fields for Series III and IV in Lanzarote are shown in dark gray and black, respectively; the straight line represents the seismic transect of BANDA et al. (1981).

by sporadic volcanic activity interrupted by long-lasting erosive periods up to the early Pliocene (3.8 Ma), and (2) a post-shield or post-erosion stage, Plio-Quaternary in age (2.7 Ma – Recent), characterized by the formation of small NE-NNE aligned volcanoes with associated lava fields. The volcanic products of the shield-building stage are known as Series I, whereas the post-shield stage volcanics comprise the Series II, III and IV, the latter referring to the Historical volcanic products (FÚSTER et al. 1968). Recent eruptions on Lanzarote occurred between 1730 and 1736 and in 1824. Like the other islands of the Canaries, Lanzarote is built on a pre-Miocene basal complex (FÚSTER & AGUILAR 1965, STILLMAN et al. 1975, ROBERTSON & STILLMAN 1979, ROBERTSON & BERNOUILLI 1982, LE BAS et al. 1986), consisting of Cretaceous turbidites overlain by interbedded Albian-Oligocene sediments and submarine volcanics. However, the basal complex does not crop out in Lanzarote.

The crustal and upper mantle structure beneath Lanzarote was investigated by gravimetric (MACFARLANE & RIDLEY 1969, CAMACHO & VIEIRA 1991), seismic (BANDA et al. 1981) and magnetotelluric (ORTIZ et al. 1986) studies. On the basis of seismic refraction data, BANDA et al. (1981) divided the crust into an upper layer, about 5 km in thickness, formed by pelagic and volcanoclastic sediments overlain by Tertiary and Quaternary volcanics, and a lower layer, about 6 km in thickness, containing the base of the ophiolitic sequence. In this interpretation, the Moho lies at a depth of 11 km and overlies anomalously hot upper mantle material characterized by a very low Pn-wave velocity of 7.4 km/s. However, after re-interpreting the data of BANDA et al. (1981), DAÑOBEITIA & CANALES (2000) located the Moho at 18 km, considering the material between 11 and 18 km as resulting from underplating. These authors hence suggested a higher Pn-wave velocity for the upper mantle (7.6 – 7.8 km/s).

### 3.3 SAMPLES

In this study, twelve peridotite xenoliths collected in the Quaternary lava fields (Series III and IV) of Lanzarote were examined. From these, seven samples (labeled LA) were already investigated from a geochemical point of view in a former study by NEUMANN et al. (1995) and were kindly put at our disposal. The other five samples (labeled PV) are part of the ETH Zürich collection.

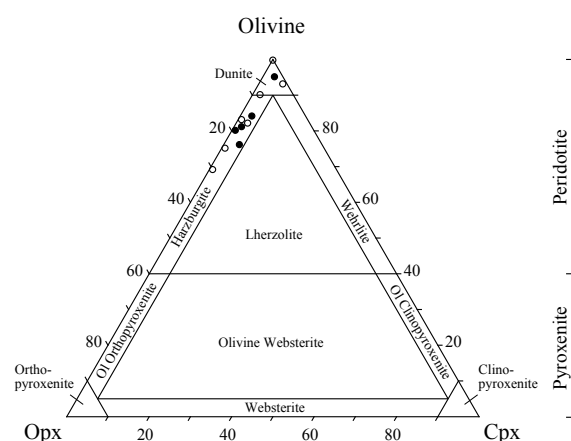


**Fig. 3.2** Modal compositions (based on EBSD scans) for the twelve spinel-peridotites from Lanzarote. The samples analyzed in the geochemical study of NEUMANN et al. (1995) are represented by open circles.

The xenoliths of Lanzarote form rounded nodules, typically 5-15 centimeters in size, embedded in alkali basalts. Eight samples are spinel-harzburgites (PV01, PV05, PV06, PV08, LA2-4, LA6-1, LA6-35, LA8-4) and four are spinel-dunites (PV04, LA6-16, LA6-19, LA8-7) (Fig. 3.2). According to the nomenclature of MERCIER & NICOLAS (1975), the fabric of the samples can be classified either as protogranular or porphyroclastic, except for sample LA8-7, which is extensively recrystallized and tends to adopt an equigranular fabric (Fig. 3.3). A correlation exists between fabric and composition, the protogranular samples being mainly spinel-harzburgites, whereas all spinel-dunites (except PV04) are either porphyroclastic or equigranular.

The protogranular fabric (PV01, PV04, PV05, PV06, PV08, LA2-4, LA8-4) is characterized by very coarse strain-free to moderately strained olivine and orthopyroxene grains up to 15 mm in size. Most protogranular samples show a strong recovery texture, generally indicative of high temperature conditions typically in the order of 1200°C (NICOLAS & POIRIER 1976). If present, the subgrain boundaries are straight and widely spaced. The grain boundaries are either slightly curved, indicating migration, or straightened by grain boundary area reduction. Small rounded olivine grains showing a possible pathway of a percolating magma were also observed (Fig. 3.4a). Orthopyroxene often displays corroded grain shapes with embayments filled by olivine or an aggregate of secondary olivine, clinopyroxene and spinel. Clinopyroxene is generally scarce and interstitial, but may form larger subhedral grains up to 5 mm in size.

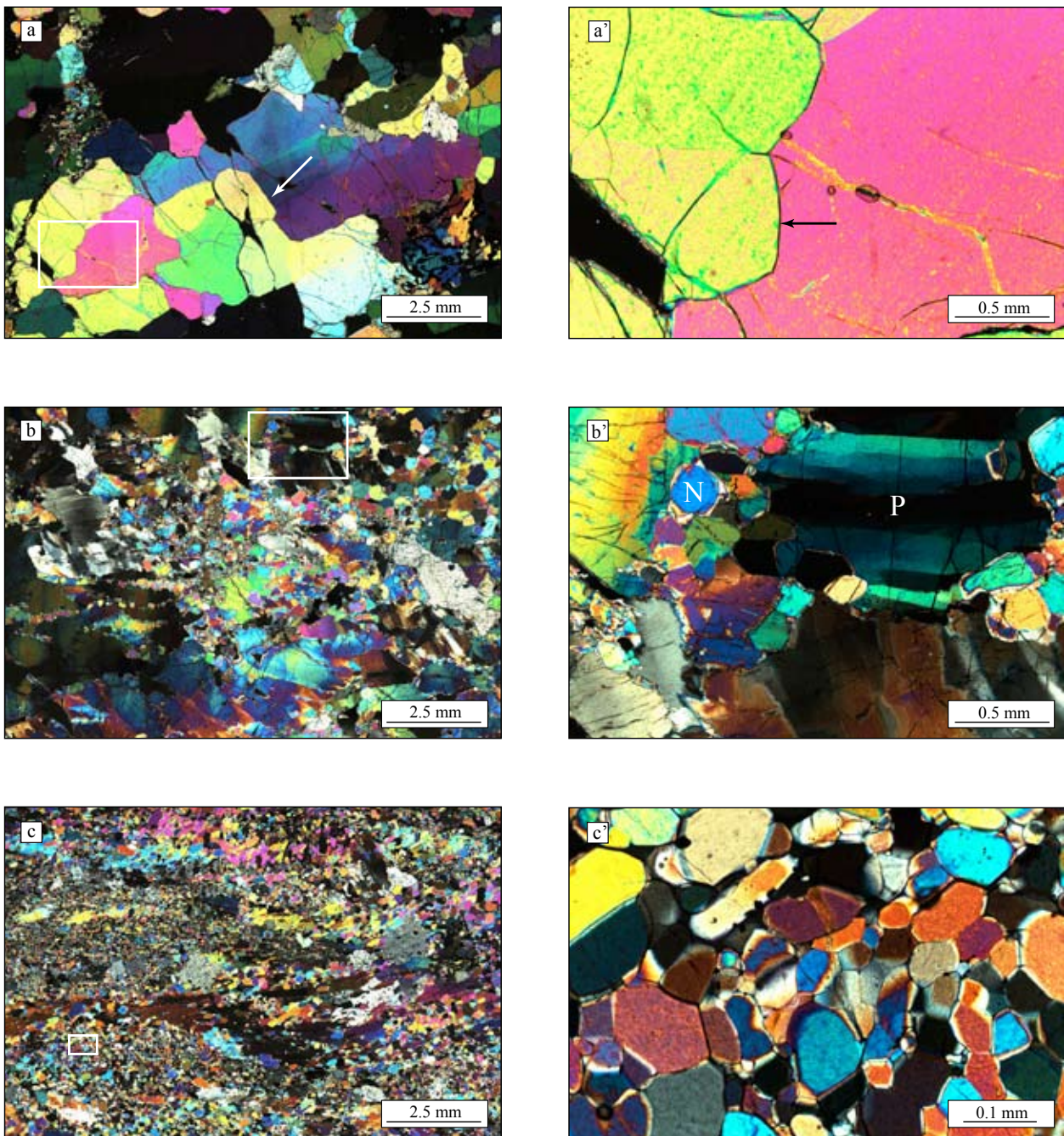


**Fig. 3.3** Typical microstructures of Lanzarote peridotites. For each fabric type, a close-up view of the framed area in the left image is presented on the right. (a-a') Coarse-grained protogranular sample (PV06) showing clear signs of recovery: large and optically strain-free grains, widely spaced subgrain boundaries, stepwise straight grain boundaries due to area reduction (white arrow) and smoothly curved grain boundaries indicating grain boundary migration (black arrow). (b-b') Partly recrystallized porphyroclastic harzburgite (LA6-35) showing well developed and closely spaced subgrain boundaries in remnant porphyroclasts (P). Neoblasts (N) are optically strain-free. (c-c') Pervasively recrystallized dunite (LA8-7) equilibrated at high temperature (annealing) with a mosaic equigranular fabric. Foliation horizontal; crossed polarizers.

The porphyroclastic samples (LA6-1, LA6-16, LA6-19, LA6-35) show clear signs of plastic deformation by dislocation creep, as evidenced by undulose extinction and narrowly spaced subgrain boundaries in the coarse (up to 10 mm) olivine porphyroclasts.

Recrystallization into small (typically 0.1 to 1 mm in size) subhedral and strain-free neoblasts is strong to moderate. The porphyroclast grain boundaries are often serrated or imbricated. Little signs of recovery processes were observed in these samples. This

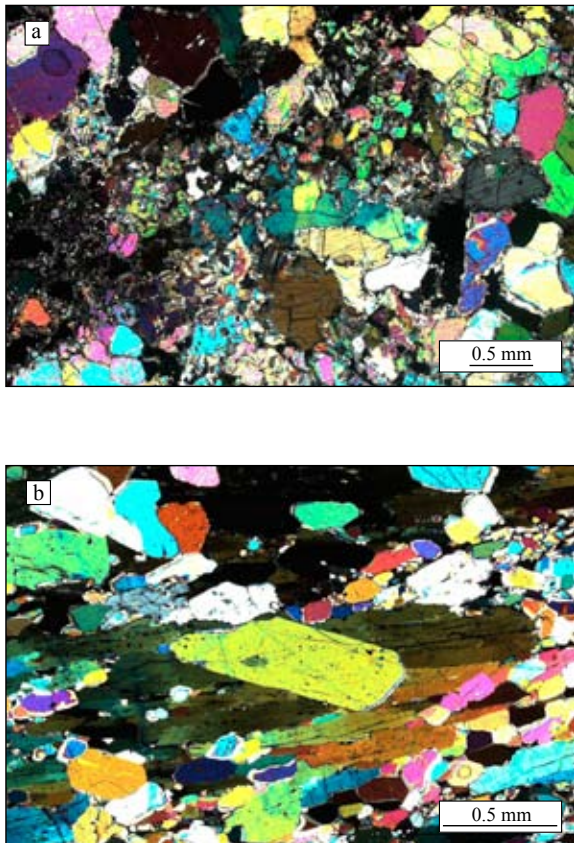


**Fig. 3.4** (a) Recrystallization of rounded olivine grains indicating a possible pathway of percolating magma in sample PV04 (protogranular). (b) Subautomorphic olivine grain truncating a former porphyroclast in sample LA8-7 (equigranular). Crossed polarizers.

porphyroclastic fabric is generally interpreted as the result of a deformation under moderately high temperature (typically 1000-1100°C), partly confirmed by the thermometric analyses of NEUMANN et al. (1995). In their description, the coarse, strained porphyroclasts are identified as generation I as opposed to the neoblasts of generation II. Orthopyroxene also displays large (up to 10 mm) porphyroclasts of generation I, frequently with narrow exsolution lamellae of clinopyroxene and spinel. Rare kink bands are observed in orthopyroxene of sample LA6-35. Partial or complete recrystallization of orthopyroxene in aggregates of minute olivine, orthopyroxene, clinopyroxene and spinel is commonly observed. In most samples, clinopyroxene occurs either as neoblasts, usually smaller than 0.1 mm, or as exsolution lamellae in orthopyroxene.

At increasing strain, the porphyroclastic fabric evolves towards a dynamically recrystallized and equigranular microstructure (LA8-7). The neoblasts form

a groundmass of equi-dimensional, optically strain-free olivine grains, occasionally embedding relicts of earlier porphyroclasts. Recrystallization by sub-grain rotation is predominant, as evidenced by bands or patchy areas containing newly formed neoblasts with similar crystallographic orientations. However, tabular shaped “subautomorphic” olivine (BOULLIER & NICOLAS 1975, MERCIER 1979) truncating the residual porphyroclasts (Fig. 3.4b) clearly indicates a later growth from recrystallized nuclei.

In both protogranular and porphyroclastic fabrics, the shape preferred orientation of the large olivine grains marks a weak foliation, which is barely visible in hand specimen, but obvious in thin section and EBSD maps. Most protogranular samples, however, show an anomalous grain shape foliation relative to olivine LPO, which is oriented normal to the olivine [100] pole maximum. This feature, already mentioned by COISY (1977) in peridotites from the French Massif Central, is discussed in detail in Section 3.6.2.

Geothermometry (NEUMANN et al. 1995) performed on the porphyroclast and neoblast assemblages revealed an extremely wide spectrum of equilibration temperatures, ranging from 750 to 1290°C. Geobarometric analyses based on microthermometric measurements on the densest CO<sub>2</sub>-fluid inclusions indicated a pressure of 0.6-0.8 GPa (20-26 km depth) for the xenoliths, suggesting a very high geothermal gradient beneath Lanzarote, with a temperature of about 1100°C at 26 km depth (NEUMANN et al. 1995). Trace elements and isotope analysis of ultramafic xenoliths revealed that the upper mantle beneath the Canary Islands became strongly depleted during the opening of the Atlantic Ocean, after about 25-30 % partial melting. Metasomatic processes related to the intrusion of carbonate-rich melts, attributed to Cenozoic intraplate volcanism, were also put forward by NEUMANN et al. (2004).

## 3.4 METHODOLOGY

### 3.4.1 LPO measurement and representation

The lattice preferred orientations (LPO's) of olivine, orthopyroxene and clinopyroxene were measured by electron backscatter diffraction (EBSD). The EBSD

Sample	Rock type	Fabric	Measurements	Measurements with CI>0.2	Average CI	Total number of grains	Area [cm <sup>2</sup> ]	Phase [vol.%]		
								OI	Opx	Cpx
PV01	harzburgite	protogranular	25696	12245 (48%)	0.23	335	2.54	76	20	4
PV04	dunite	protogranular	27336	19590 (72%)	0.34	350	2.70	95	2	3
PV05	harzburgite	protogranular	56776	41737 (74%)	0.36	450	5.62	84	13	3
PV06	harzburgite	protogranular	58256	38975 (67%)	0.33	397	5.76	81	17	2
PV08	harzburgite	protogranular	55266	41691 (75%)	0.37	396	5.48	80	19	1
LA2-4	harzburgite	protogranular	62586	43020 (69%)	0.33	638	6.21	69	30	1
LA6-1	harzburgite	porphyroclastic	50406	34147 (68%)	0.34	2964	5.00	83	16	1
LA6-16	dunite	porphyroclastic	30261	19384 (64%)	0.31	358	2.99	93	1	6
LA6-19	dunite	porphyroclastic	57316	43759 (76%)	0.40	1160	5.68	100	0	0
LA6-35	harzburgite	porphyroclastic	41396	29856 (72%)	0.36	3000	4.09	75	24	1
LA8-4	harzburgite	protogranular	53856	35881 (67%)	0.32	715	5.33	82	15	3
LA8-7	dunite	equigranular	48546	35099 (72%)	0.37	4932	4.18	90	8	2

**Table 3.1** Characteristics from EBSD scans for the twelve Lanzarote xenoliths. Only grains with a minimum of 2-3 (equigranular) respectively 7-10 (protogranular) successful measurements were retained for the grain count statistics, in order to avoid artificial overestimations of the number of grains.

technique (e.g. VENABLES & HARLAND 1973, ADAMS et al. 1993, PRIOR et al. 1999) is based on automatic analysis of Kikuchi-type diffraction patterns generated by backscattered electrons. For each point of analysis, the crystallographic orientation, commonly expressed by Euler angles ( $\phi_1$ ,  $\Phi$ ,  $\phi_2$ ; BUNGE 1982), is determined after indexing of the corresponding diffraction pattern. All EBSD data were collected at the University of Fribourg using a Philips® FEI XL30 SFEG Sirion scanning electron microscope (SEM). The best results were obtained with an acceleration voltage of 20 or 25 kV for a probe current of 20 nA. Recording and processing of the EBSD patterns were performed with the EDAX® (TSL) OIM 3.5 software package.

EBSD measurements were carried out on massive sample blocks, approximately  $4 \times 2 \times 1$  cm in size. Because Lanzarote xenoliths are often brittle and prone to break up when manipulated, each block was impregnated with epoxy glue before surface polishing. Usual grinding and polishing with diamond paste was followed by lapping for 10 h using a colloidal silica suspension (grain size 25 nm). To avoid specimen charging, the sample surface was coated with a 2 nm carbon layer and connected with silver paint to the sample holder.

For statistical reasons, LPO analysis of a polycrystalline sample requires that the orientation of a sufficient number of grains is measured. According to BEN ISMAIL & MAINPRICE (1998), at least 100 to 150 grains should be analyzed in order to obtain a representative LPO of a rock. Due to the coarse grain size distribution of most Lanzarote xenoliths, data were collected on grids with 100  $\mu$ m steps using a computer-control-

led SEM stage. This allowed the measurement and mapping of several hundreds of grains per sample on areas ranging from  $14.5 \times 17.5$  mm<sup>2</sup> for the smallest specimen and up to  $17.0 \times 36.5$  mm<sup>2</sup> for the largest. For each point of analysis, a Confidence Index (CI) expresses the reliability of indexing. CI values are always comprised between 0 and 1 and experience has shown that a pattern with a CI>0.2 is almost certainly indexed correctly. In our samples, the average Confidence Index (CI) was between 0.31 (LA6-16) and 0.40 (LA6-19) except for sample PV01 (0.23). The points of the scans with a CI<0.2 were not considered for further texture analysis. The consistently high CI values of our EBSD data make indexing errors due to pseudo-symmetry of olivine very unlikely. Wrong indexing is generally accompanied by a very low CI, due to the fact that more than one solution with similar likelihood is proposed during the indexing procedure. As a consequence, the quality of EBSD maps would markedly deteriorate, since large grains will typically contain speckled points indexed by any of the pseudo-symmetric orientations. Such features are never observed in this study. The scanning parameters, average CI values and modal composition for the twelve Lanzarote xenoliths are presented in Table 3.1.

In order to obtain data compatible with the format of most of the already published EBSD analyses on upper mantle material (e.g. MAINPRICE & SILVER 1993, BEN ISMAIL & MAINPRICE 1998, MAINPRICE et al. 2000, VAUCHEZ & GARRIDO 2001, PERA et al. 2003), the Unicef Careware software package (MAINPRICE 1999) was chosen to generate orientation distribution functions (ODF) and to calculate seismic properties. The ODF  $f(g)$ , defined by BUNGE (1982) as the volume

a)	Olivine ( $\rho_0 = 3.355$ [g/cm <sup>3</sup> ])						Orthopyroxene ( $\rho_0 = 3.370$ [g/cm <sup>3</sup> ])						Clinopyroxene ( $\rho_0 = 3.327$ [g/cm <sup>3</sup> ])					
$C_{ij}(P_0, T_0)$	320.5	68.1	71.6	0.0	0.0	0.0	236.9	79.9	63.2	0.0	0.0	0.0	237.8	83.5	80.0	0.0	9.0	0.0
	68.1	196.5	76.8	0.0	0.0	0.0	79.9	180.5	56.8	0.0	0.0	0.0	83.5	183.6	59.9	0.0	9.5	0.0
	71.6	76.8	233.5	0.0	0.0	0.0	63.2	56.8	230.4	0.0	0.0	0.0	80.0	59.9	229.5	0.0	48.1	0.0
	0.0	0.0	0.0	64.0	0.0	0.0	0.0	0.0	0.0	84.3	0.0	0.0	0.0	0.0	0.0	76.5	0.0	8.4
	0.0	0.0	0.0	0.0	77.0	0.0	0.0	0.0	0.0	0.0	79.4	0.0	9.0	9.5	48.1	0.0	73.0	0.0
	0.0	0.0	0.0	0.0	0.0	78.7	0.0	0.0	0.0	0.0	0.0	80.1	0.0	0.0	0.0	8.4	0.0	81.6
b)	Olivine ( $\rho(P, T) = 3.248$ [g/cm <sup>3</sup> ])						Orthopyroxene ( $\rho(P, T) = 3.276$ [g/cm <sup>3</sup> ])						Clinopyroxene ( $\rho(P, T) = 3.214$ [g/cm <sup>3</sup> ])					
$C_{ij}(P, T)$	289.6	60.2	64.9	0.0	0.0	0.0	209.8	63.6	36.8	0.0	0.0	0.0	207.0	67.0	52.2	0.0	8.3	0.0
	60.2	173.4	73.0	0.0	0.0	0.0	63.6	154.7	51.4	0.0	0.0	0.0	67.0	156.9	52.3	0.0	8.4	0.0
	64.9	73.0	209.2	0.0	0.0	0.0	36.8	51.4	187.8	0.0	0.0	0.0	52.2	52.3	182.5	0.0	47.6	0.0
	0.0	0.0	0.0	51.7	0.0	0.0	0.0	0.0	0.0	72.4	0.0	0.0	0.0	0.0	0.0	65.5	0.0	9.1
	0.0	0.0	0.0	0.0	63.9	0.0	0.0	0.0	0.0	0.0	66.5	0.0	8.3	8.4	47.6	0.0	60.5	0.0
	0.0	0.0	0.0	0.0	0.0	64.0	0.0	0.0	0.0	0.0	0.0	67.9	0.0	0.0	0.0	9.1	0.0	69.1

$$\rho(P, T) = \rho_0 \{ [1 + (K'/K)(P - P_0)]^{1/K'} [1 - \alpha_{av}(T - T_0)] \} \quad (\text{Eq. 3.4})$$

$$C_{ij}(P, T) = C_{ij}(P_0, T_0) + (dC_{ij}/dP)(P - P_0) + 1/2(d^2C_{ij}/dP^2)(P - P_0)^2 + (dC_{ij}/dT)(T - T_0) \quad (\text{Eq. 3.5})$$

with:

$\rho(P, T)$  = density derived for P/T conditions of 0.7 [GPa] and 1000 [°C]

$\rho_0$  = density at room pressure ( $P_0$ ) and temperature ( $T_0$ )

K = bulk modulus in [GPa]: ol = 126.3 (ABRAMSON et al. 1997); opx = 115.5 (CHAI et al. 1997); cpx = 113.0 (LEVIEN et al. 1979)

K' = bulk modulus pressure derivatives: ol = 4.28; opx = 7.82; cpx = 4.80; same authors

$\alpha_{av}$  = volume thermal expansion coefficient\* in [°C<sup>-1</sup>]: ol =  $3.81 \cdot 10^{-5}$  (HAZEN 1976); opx =  $3.45 \cdot 10^{-5}$  (JACKSON et al. 2003); cpx =  $4.10 \cdot 10^{-5}$  (FINGER & OHASHI 1976)

$C_{ij}(P, T)$  = elastic constants in [GPa] derived for P/T conditions of 0.7 [GPa] and 1000 [°C]

$C_{ij}(P_0, T_0)$  = elastic constants in [GPa] at room pressure and temperature for ol (ABRAMSON et al. 1997), opx (CHAI et al. 1997) and cpx (COLLINS & BROWN 1998)

$dC_{ij}/dP$  = first order pressure derivatives (nondimensional) for ol (ABRAMSON et al. 1997), opx (FRISILLO & BARSCH 1972\*\*) and cpx (MATSUI & BUSING 1984\*\*\*)

$d^2C_{ij}/dP^2$  = second order pressure derivatives in [GPa<sup>-1</sup>] for ol and opx; same authors

$dC_{ij}/dT$  = temperature derivatives in [GPa/°C] for ol (ISAAK 1992), opx (CHAI et al. 1997) and cpx (FRISILLO & BARSCH 1972\*\*\*\*)

\* average values considered constant over the temperature range of interest

\*\* extrapolated to 1000 [°C], as suggested by MAINPRICE et al. (2000)

\*\*\* theoretical values

\*\*\*\* opx values were taken instead of the missing data for cpx, as recommended by ESTEY & DOUGLAS (1986)

**Table 3.2** Density and elastic constants of olivine, orthopyroxene and clinopyroxene (a) for room conditions and (b) derived for upper mantle P/T conditions of 0.7 GPa and 1000°C. Density and elastic constant variations as a function of pressure and temperature were calculated using the Eq. 3.4 and 3.5, respectively.

fraction of orientations in the interval between  $g$  and  $g+dg$  in a space containing all possible orientations, is given by:

$$\Delta V / V = \int f(g) dg \quad (\text{Eq. 3.1})$$

$$dg = \frac{1}{8\pi^2} \sin \Phi d\phi_1 d\Phi d\phi_2 \quad (\text{Eq. 3.2})$$

where  $\Delta V/V$  is the volume fraction of crystals with orientation  $g$ ,  $f(g)$  is the texture function and  $dg$  is the volume of the region of integration in orientation space. Spherical harmonics truncated at an expansion degree of  $l_{\max} = 22$  with a default Gaussian half-width of  $8.5^\circ$  were used.

The strength of the texture was expressed by the texture index  $J$  calculated as the mean square value of the ODF (BUNGE 1982):

$$J = \int f(g)^2 dg \quad (\text{Eq. 3.3})$$

A purely random LPO gives a  $J$  of 1, whereas for a single crystal, the texture index tends towards infinity (in reality to about 270 due to the truncation in spherical harmonic calculations and the Gaussian used).

LPO's are plotted on lower hemisphere equal area nets displaying multiple of uniform distribution contouring. As Lanzarote xenoliths are often small in size (typically only a few cm) and lack a clear macroscopic fabric, the geometric elements commonly used for the

structural reference frame (foliation and lineation) were often not visible at the scale of hand specimen. This, added to the need for large areas of analysis, led us to choose the sample's orientation based on the shape of the hand specimen rather than on the textural parameters. All orientation data acquired on non-oriented samples were rotated after EBSD acquisition. Depending on the possibility or impossibility to determine the foliation plane in three dimensions (from grain shape in EBSD orientation maps and observation on perpendicular cuts of the sample block), two different rotation procedures were applied. (1) If the foliation could be identified, orientation data were rotated in order to place the foliation either horizontally, for the samples with a normal foliation ( $Z$  = pole of the normal foliation), or vertically for those with an anomalous foliation ( $X$  = pole of the anomalous foliation). This setting is considered the most appropriate because it assumes that the original foliation, which should have developed contemporaneously with the LPO, was in horizontal position. This option also makes texture comparisons between samples with both normal and anomalous foliations possible. In texture and seismic plots, the visible foliation is indicated by continuous line, whereas the original foliation is approximated by a dashed line. As lineation was never observed in these samples, the orientation data were then rotated within the foliation plane assuming olivine [100] (for the samples with a normal foliation) or [010] (for those with anomalous foliation) pole maxima (eigenvectors) as lineation indicators placed in the projection plane towards  $X$  or  $Z$ , respectively. (2) Orientation data of the samples, for which neither foliation nor lineation could be determined, were rotated so that olivine [100] and [010] pole maxima (eigenvectors) correspond to the  $X$  and  $Z$  structural directions, respectively. Previous authors (e.g. BEN ISMAÏL & MAINPRICE 1998, MAINPRICE et al. 2000) had also identified those directions with  $X$  and  $Z$  in oceanic upper mantle peridotites.

From the twelve Lanzarote xenoliths, an average sample LPO (e.g. MAINPRICE & HUMBERT 1994, BEN ISMAÏL & MAINPRICE 1998, PERA et al. 2003) was calculated for olivine, orthopyroxene and clinopyroxene after rotation in the common reference frame. Averages were obtained by merging all the orientations of a given phase, each measurement having the same weight independently of the size of the scan. Pole figures for ortho- and clinopyroxene were calculated only for the total data set but not for the individual samples, as the number of grains per scan was too small to generate any representative texture.

### 3.4.2 Calculation of seismic properties

The density and elastic constants used for the determination of the seismic velocities from LPO's were extrapolated to a pressure of 0.7 GPa and a temperature of 1000°C for the whole sample population (Table 3.2). These P/T estimates were taken from the thermobarometric analyses of NEUMANN et al. (1995). As olivine showed little chemical variability from one sample to another ( $Fo_{89.7-92.1}$  on the samples analyzed by NEUMANN et al. 1995), the variation of density and elastic constants with iron content was not taken into account and a fixed composition of  $Fo_{90}$  was assumed for calculations.

The effective elastic constants of the samples were calculated using the Voigt average over all reliable crystal orientation measurements. For any propagation direction, the velocity of compressional ( $V_p$ ) and shear waves ( $V_{s_1}$  and  $V_{s_2}$ ) is calculated. Anisotropy of P-waves ( $AV_p$ ) is defined by the relation  $100\%(V_{p_{max}} - V_{p_{min}})/[\frac{1}{2}(V_{p_{max}} + V_{p_{min}})]$ , where  $V_{p_{max}}$  and  $V_{p_{min}}$  are the maximum and minimum P-wave velocity observed in a given sample, respectively. Calculations of S-wave anisotropy ( $AV_s$ ) are based on the velocities of the fast and slow S-wave members produced by shear wave splitting. For each given direction,  $AV_s$  is determined using the relation  $100\%(V_{s_1} - V_{s_2})/[\frac{1}{2}(V_{s_1} + V_{s_2})]$ , where  $V_{s_1}$  is the faster wave members and  $V_{s_2}$  the slower (MAINPRICE & SILVER 1993). Calculations were performed for each sample from the corresponding LPO, assuming a modal composition of 100% olivine. The seismic behavior of the peridotite average sample was determined based on olivine, orthopyroxene and clinopyroxene average sample LPO's, assuming a composition of 84 vol.% olivine, 14 vol.% orthopyroxene and 2 vol.% clinopyroxene.

## 3.5 RESULTS

### 3.5.1 Lattice preferred orientation (LPO)

LPO's of olivine for each of the twelve xenoliths are presented in Fig. 3.5, whereas Fig. 3.6 shows the average sample LPO's for olivine, orthopyroxene and clinopyroxene.

LPO data of olivine can be divided in two groups. Group I (Fig. 3.5a) is characterized by a strong clus-

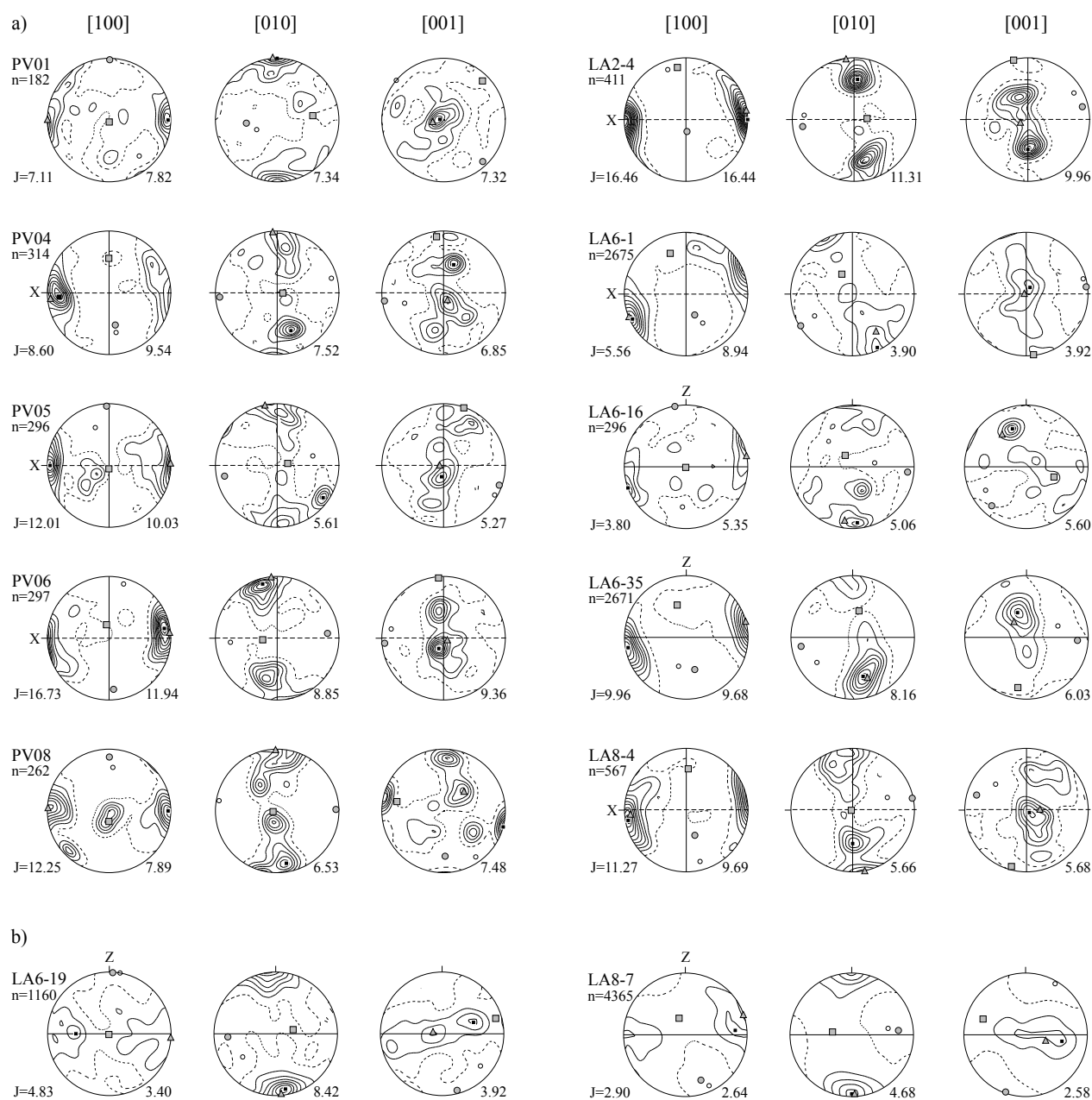


**Fig. 3.5** Olivine pole figures showing the preferred orientations of the [100], [010] and [001] axes for the twelve Lanzarote xenoliths. LPO's of group I are shown in (a), those of group II in (b). Pole figures are represented on lower hemisphere equal area projections. When observed, foliation is represented by a continuous line either horizontally for the samples with a normal foliation ( $Z =$  pole of the normal foliation) or vertically for those with an anomalous foliation ( $X =$  pole of the anomalous foliation). For the latter, the approximate position of the original foliation is indicated by a dashed line. Samples lacking any visible foliation are oriented with the maximum alignment (eigenvectors) of olivine [100] and [010] to the left and to the top, respectively. In case of an asymmetric distribution of [100] axes relative to the pole maximum, the data were rotated so that the tails are counterclockwise from their maxima (assuming a dextral shear). Contours are multiples of uniform distribution (1 m.u.d. intervals) beginning at 0.5 (dashed line); the number on the bottom right of each plot expresses the maximum density (position marked by a small black square on pole figures). Labels on the left side of each plot row indicate sample number, approximate number of grains  $n$  analyzed and texture index  $J$ . The three eigenvectors  $e_1$ ,  $e_2$  and  $e_3$  are plotted as grey triangles, squares and discs, respectively.

tering of the [100] poles parallel to the X structural direction. The distribution of [010] and [001] axes is less straightforward and ranges between two end members. At one end, [010] and [001] have clear but

relatively weak maxima in the Z and Y directions, respectively. This LPO is commonly referred as single crystal texture and corresponds to the type A of BEN ISMAIL & MAINPRICE (1998). At the other end, [010] and

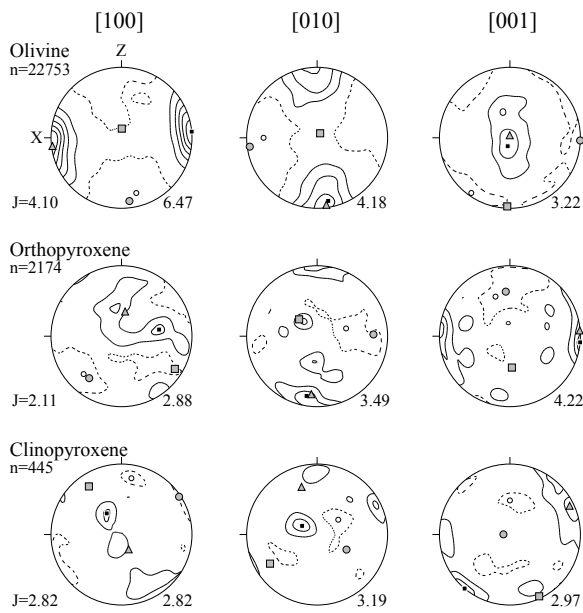


**Fig. 3.6** Average sample LPO's of olivine, orthopyroxene and clinopyroxene plotted on lower hemisphere equal area nets. Symbols, references and calculation methods as in Fig. 3.5.

[001] tend to form diffuse girdles in the YZ structural plane normal to the X structural direction, with [100] acting as an approximate axis of rotational symmetry. Occasionally, secondary peaks appear within these girdles. This LPO was described as [100] fiber texture by BUNGE (1982) and corresponds to the type B of BEN ISMAIL & MAINPRICE (1998). Since most of the samples of group I show an intermediate LPO between both end members, they have been attributed to a common textural entity in our study. The LPO's of group II (Fig. 3.5b) show a clustering of [010] poles parallel to the Z structural direction, with [100] and [001] distributed along girdles in the XY structural plane. This LPO is known as [010] fiber texture and was reported as type D in BEN ISMAIL & MAINPRICE's database. The texture index J for olivine is comprised between 2.90 (LA8-7) and 16.73 (PV06). The olivine average sample is characterized by a texture index J of 4.10. As this average is strongly dominated by the samples of group I, it logically tends to the type A single crystal texture.

In order to analyze olivine pole figure symmetry in a more quantitative way, ternary PGR diagrams defined by point (P), girdle (G) and random (R) apices (WOODCOCK 1977, VOLLMER 1990) were calculated from the three eigenvalues ( $e_1$ ,  $e_2$  and  $e_3$ ) of the [100], [010] and [001] distributions. The definitions of VOLLMER (1990), with  $P = e_1 - e_2$ ,  $G = 2(e_2 - e_3)$ ,  $R = 3e_3$  and  $P+G+R = 1$ , were used for calculation. In the PGR diagrams (Fig. 3.7), the distribution of [100] matches

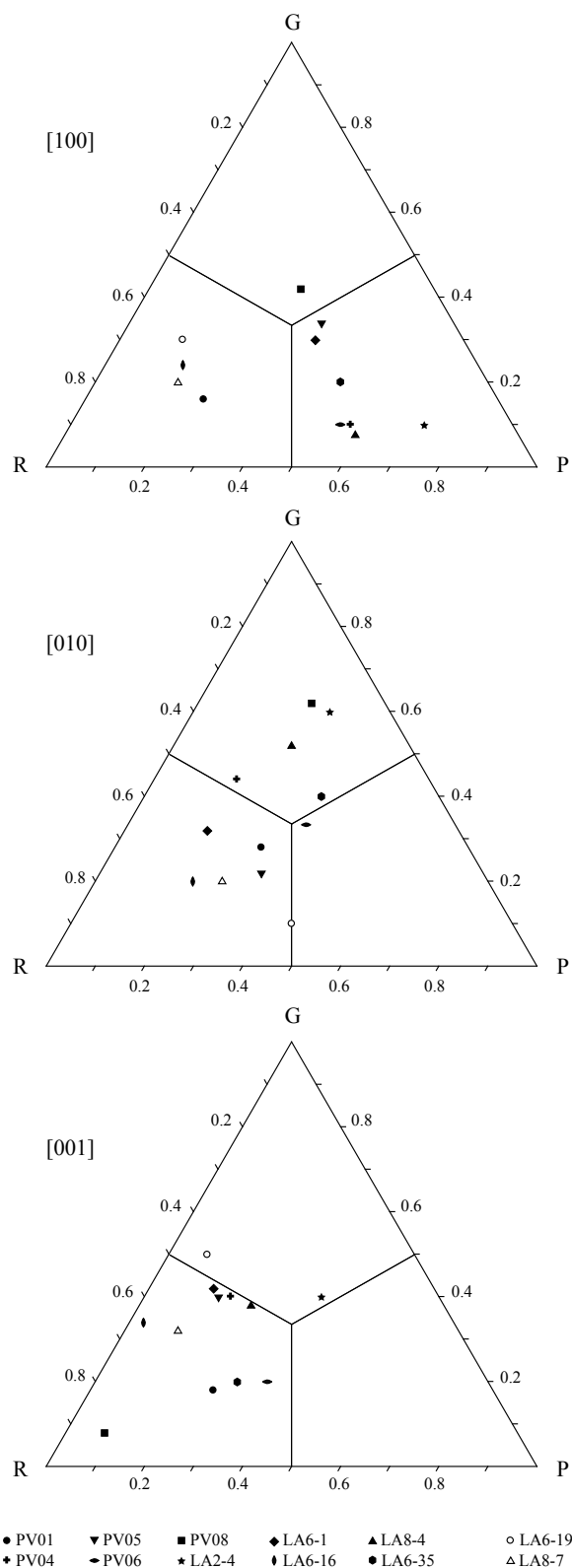


**Fig. 3.7** PGR diagrams of olivine [100], [010] and [001] crystallographic axes calculated from eigenvalues  $e_1$ ,  $e_2$  and  $e_3$  normalized to 1, with  $P = e_1 - e_2$ ,  $G = 2(e_2 - e_3)$ ,  $R = 3e_3$  and  $P+G+R = 1$ . The majority of xenoliths fall in the P domain for [100], in the R or G fields for [010] and in the R domain for [001]. Samples of group I and II are represented by full and open symbols, respectively.

fairly well the subdivisions put forward in the qualitative analysis, the samples of group I being mainly located in the P domain, whereas those of group II are all in the R field. Three samples of group I, however, depart from the rule: PV08, which develops a stronger girdle (G) component due to a secondary maximum in the XY plane, as well as PV01 and LA6-16, which are

maintained in the R field of the diagram due to their weak [100] pole maxima. The distribution of [010] is more dispersed: samples of group I are mainly spread within the R and G fields, whereas both samples of group II, despite a stronger point (P) component, do not cross the R-P field boundary. Finally, nearly all samples plot in the R field for [001], which reflects

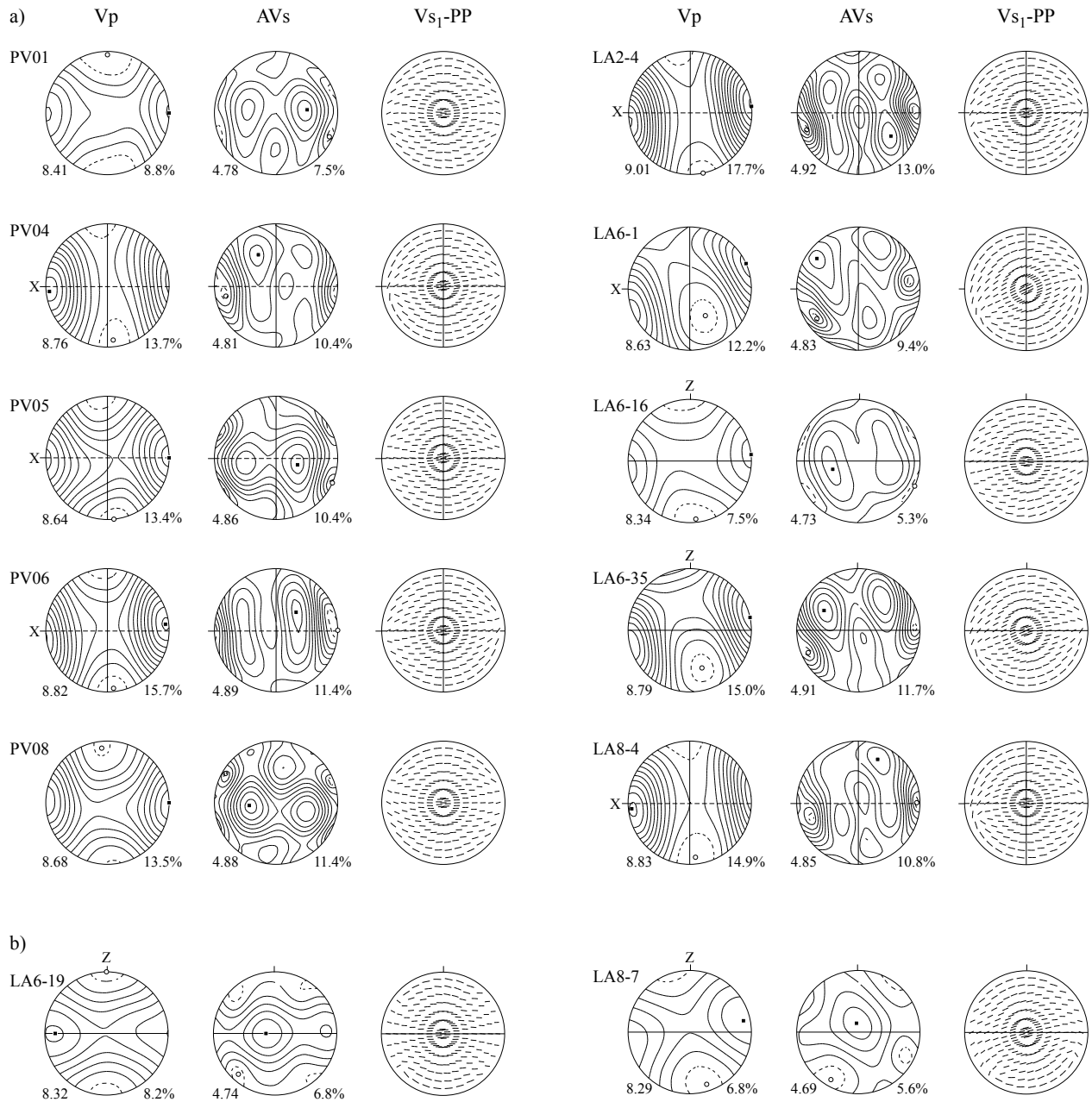


**Fig. 3.8** Calculated seismic properties of the xenoliths using the LPO of Fig. 3.5 projected on lower hemisphere equal area nets. Column 1 ( $V_p$ ) displays the velocity distribution of the P-waves (0.1 km/s intervals); the numbers right and left of the diagram show respectively the P-wave anisotropy ( $AV_p$ ) and the maximum velocity in km/s. Column 2 ( $AV_s$ ) shows the distribution of S-wave anisotropy (1% contour intervals), resulting from shear wave splitting. Maximum anisotropy is presented at the bottom right and maximum  $V_{s_1}$  at the bottom left. For both Column 1 and 2, the dashed line represents the minimum contour, and the directions corresponding to the maximum and minimum value in the plot are marked by solid square and open circle, respectively. Column 3 ( $V_{s_1-PP}$ ) exhibits the polarization plane of the faster S-wave. All calculations were performed using the Voigt average. X, Y and Z as in Fig. 3.5.

the large dispersion of maxima in [001] pole figures. The two samples of group II mark a trend towards the G field.

LPO of the orthopyroxene average sample is characterized by several weakly clustered maxima. The fabric for [001] shows one single maximum very close to the X structural direction, which is the normal feature commonly reported in the literature (e.g. MAINPRICE et al. 2000). Several weak [010] poles are observed in the YZ plane, whereas the maximum of the [100] pole distribution is asymmetric to the X, Y and Z tectonic orientations. The J index for orthopyroxene average sample is 2.11.

The LPO patterns of the clinopyroxene average sample display also a weak texture. The orientation distribution of the [001] axes shows a more pronounced obliquity than orthopyroxene relative to the X structural direction. [010] poles have three maxima, the strongest being close to the Y direction, whereas [100] axes distribution shows several very weak maxima oblique to the YZ plane. The texture index J equals 2.82.

### 3.5.2 Seismic properties

The projections of the calculated seismic properties of the xenoliths (Fig. 3.8), considering only the contribution of olivine grains, display either an orthorhombic symmetry (PV01, PV05, PV06, PV08, LA6-1, LA6-16, LA6-19, LA6-35 and LA8-7) or tend to a transverse isotropic character with a symmetry axis parallel to  $V_{p_{\max}}$  (PV04, LA2-4 and LA8-4).  $V_{p_{\max}}$

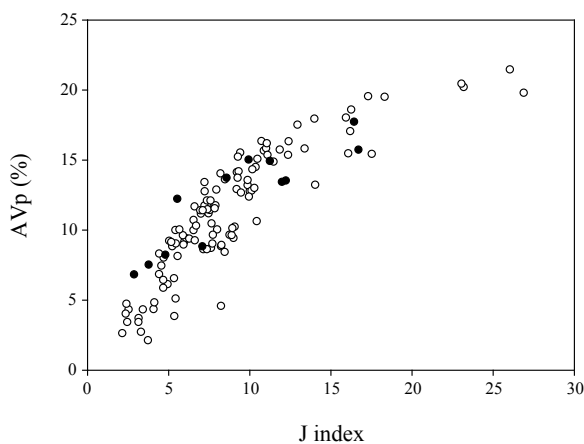


**Fig. 3.9** Plot of fabric strength (*J* index) vs anisotropy of *P*-waves (*AVp*). The results for Lanzarote xenoliths (full circles) are compared with the updated olivine database (open circles) of BEN ISMAIL & MAINPRICE (1998).

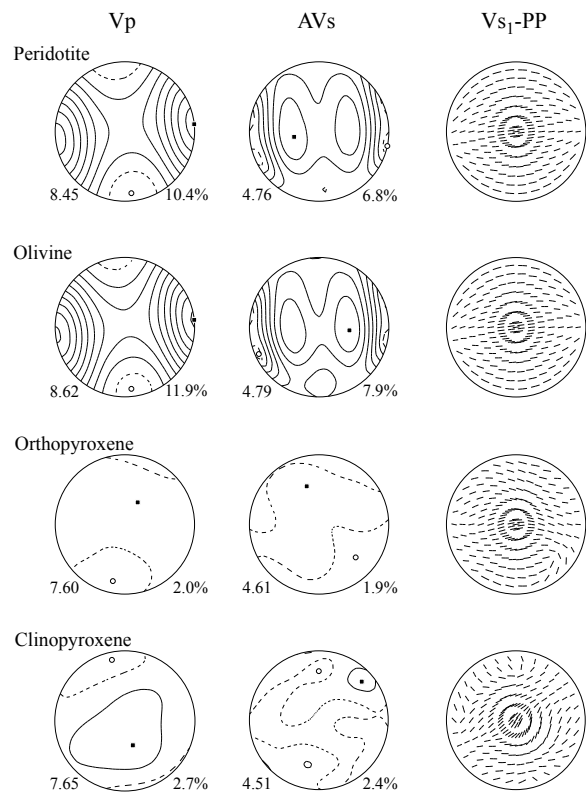


**Fig. 3.10** Calculated seismic properties of the Lanzarote peridotite average sample (top), assuming a modal composition of 84 vol.% olivine, 14 vol.% orthopyroxene and 2 vol.% clinopyroxene. Seismic properties of the olivine, orthopyroxene and clinopyroxene average samples are shown for comparison. Layout and reference frame as in Fig. 3.8.

ranges from 8.29 to 9.01 km/s ( $V_{p_{\text{mean}}} = 8.62$  km/s),  $V_{s_{1\text{max}}}$  from 4.69 to 4.92 km/s ( $V_{s_{1\text{mean}}} = 4.82$  km/s) and  $V_{s_{2\text{max}}}$  from 4.56 to 4.63 km/s ( $V_{s_{2\text{mean}}} = 4.59$  km/s). The seismic anisotropy varies between 6.8 and 17.7 % for  $AV_p$  ( $AV_{p_{\text{mean}}} = 12.3$  %) and 5.3 to 13.0 % for the maxima of  $AV_s$  plots ( $AV_{s_{\text{mean}}} = 9.5$  %). When plotted versus fabric strength (Fig. 3.9),  $AV_p$  is in good agreement with the results derived from the updated olivine database of BEN ISMAIL & MAINPRICE (1998).

The fastest propagation of *P*-waves generally corresponds to the X structural direction ([100] pole maximum), whereas the slowest *P*-waves tends to propagate along the Z structural direction ([010] pole maximum). However, because of the slightly asymmetric character of LPO's and the commonly observed obliquity of the pole maxima with respect to the structural directions, some samples (e.g. LA6-1 and LA6-35) show a slight obliquity of their seismic maximum and minimum relative to X and Z, respectively. The maximum anisotropy of *S*-waves has no clear preferred orientation and points variably to a direction intermediate between X,

Y and Z reference axes. AVs maxima strictly parallel to the Z tectonic axes have never been observed. In most samples, the  $V_{s_1}$  polarization plane is parallel or sub-parallel to the foliation plane perpendicular to Z. For a few samples, however, the  $V_{s_1}$  polarization plane is tilted around the Y direction.

The projections of the seismic velocities of the olivine and the peridotite average samples have a clear orthorhombic symmetry (Fig. 3.10). Seismic velocities and anisotropy of the olivine average sample reach 8.62 km/s ( $V_{p_{max}}$ ), 4.79 km/s ( $V_{s_{1max}}$ ), 4.60 km/s ( $V_{s_{2max}}$ ), 11.9 % (AVp) and 7.9 % (AVs). The peridotite average sample has slightly lower velocities (8.45 km/s for  $V_{p_{max}}$ , 4.76 km/s for  $V_{s_{1max}}$  and 4.59 km/s for  $V_{s_{2max}}$ ), and seismic anisotropies (10.4 % for AVp and 6.8 % for AVs) than the olivine average sample. Orthopyroxene and clinopyroxene show very little anisotropy and lower absolute velocities compared to olivine.

## 3.6 DISCUSSION

### 3.6.1 Lattice preferred orientation

Two groups of olivine LPO were distinguished in the ultramafic xenoliths of Lanzarote. Group I (10 samples) is represented by fabrics intermediate between the single crystal and the [100] fiber textures, whereas group II (2 samples) is approximated by the [010] fiber texture. These LPO's are typical of the upper mantle and have been widely reported in the literature (e.g. BROTHERS & RODGERS 1969, NICOLAS et al. 1973, MERCIER & NICOLAS 1975, CHRISTENSEN & SALISBURY 1979, CHRISTENSEN 1984, MAINPRICE & SILVER 1993, Ji et al. 1994, BEN ISMAIL & MAINPRICE 1998, MAINPRICE et al. 2000). It is currently admitted that simple shear or a combination of simple and pure shear is the dominant deformation regime in the oceanic upper mantle (NICOLAS 1976). Generally, a simple shear component is indicated by a more or less pronounced obliquity of olivine [100] and [010] axes relative to the X and Z structural directions, respectively (ZHANG & KARATO 1995). This characteristic is a common feature of the LPO in Lanzarote xenoliths. If we refer to the experimental deformation experiments of TOMMASI et al. (1999) for polycrystalline olivine samples, the predominance of the single crystal and [100] fiber textures (group I) tends to indicate that low strain rate

simple shear, with a possible tensional component (transtension), is the prevalent deformation regime for the source region of most of the Lanzarote xenoliths. These textures are consistent with the activation of the (010)[100] and (0kl)[100] slip systems at high to moderate operating temperatures (RALEIGH 1968, CARTER & AVÉ LALLEMANT 1970), in good agreement with the geothermometric determinations of NEUMANN et al. (1995). On the other hand, the occurrence of the [010] fiber texture (group II) is less common in the upper mantle. According to TOMMASI et al. (1999), axial [010] LPO patterns with strong clustering of the [010] poles result either from widening-thinning shear (transpression) or axial shortening, the former being more likely in our xenoliths, due to the slight obliquity of the pole maxima. Whatever the scenario, the simultaneous occurrence of [100] and [010] fiber textures indicate that at least two deformation regimes operated at different locations in the upper mantle beneath Lanzarote, suggesting a different source location or depth for the xenoliths of group I and II.

Ortho- and clinopyroxene display weaker LPO's. The larger bulk moduli of pyroxene relative to olivine require a higher stress to activate the dominant slip systems (WENK & BENNET 1991). In addition, as pyroxene represents only a small volume of the bulk composition, most of the strain is accommodated by the more ductile olivine matrix. Despite their weak textures, both ortho- and clinopyroxene show comparable orientations of the [001] maximum, i.e. slightly oblique to the X structural direction in the XZ plane. This preferred orientation is consistent with a deformation regime dominated by simple shear and compatible with the dominant dislocation glide direction in orthopyroxene (COE & KIRBY 1975) and clinopyroxene (VAN ROERMUND & BOLAND 1981). In the samples characterized by an anomalous foliation (YZ plane in texture plots), the orientation of the orthopyroxene [001] pole maximum close to the X direction is an additional argument for our choice of reference frame.

### 3.6.2 Anomalous foliation

Anomalous foliations, with olivine [100] pole maximum oriented normal to the visible foliation plane, were observed in about half of the samples analyzed in this study. On the basis of microstructural (straight and parallel subgrain and grain boundaries) and crystallographic (similar lattice orientation of adjacent grains, orientation of orthopyroxene [001] maximum normal to the foliation) arguments, this feature is

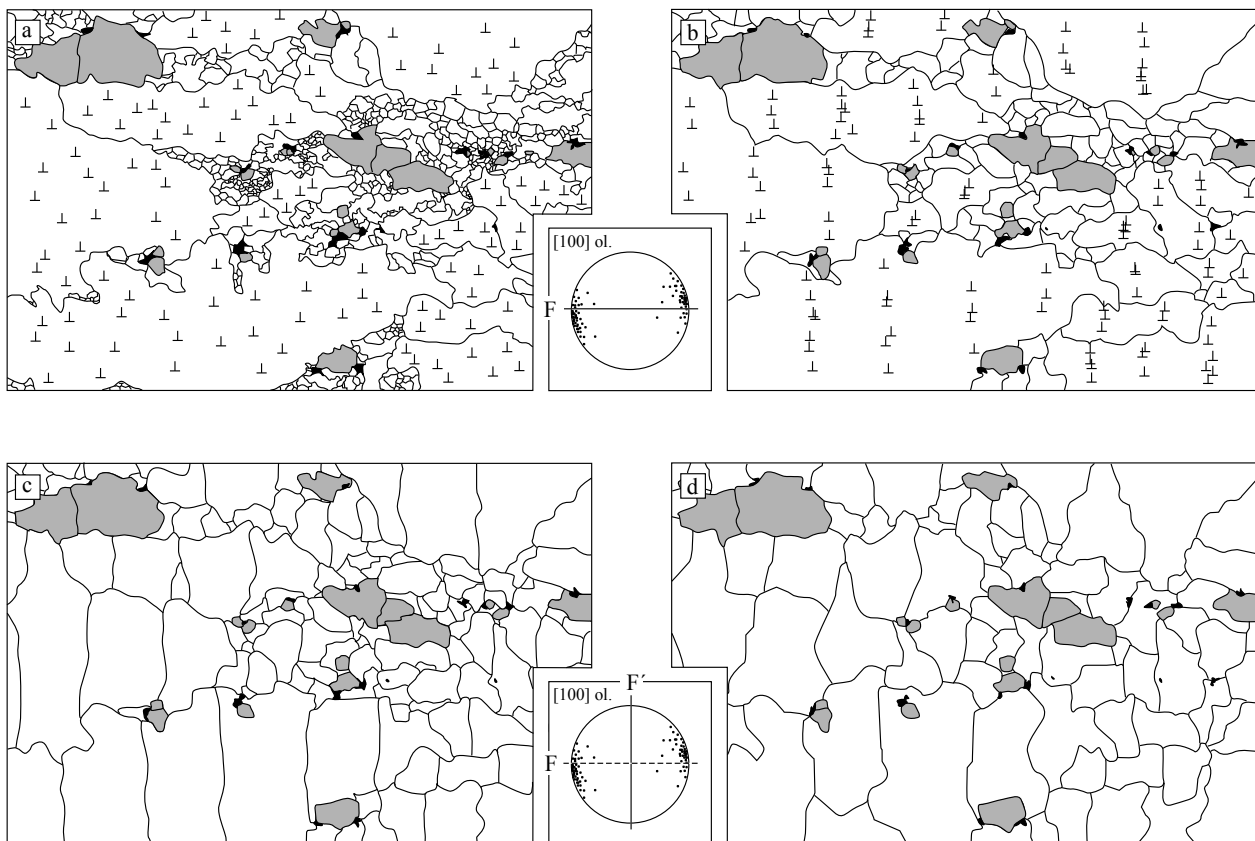


**Fig. 3.11** Sketch illustrating the development of anomalous foliation in peridotite. Olivine grains are shown in white, pyroxene in grey and spinel in black; edge dislocations in large olivine porphyroclasts are indicated by  $\perp$  symbols. (a) In response to stress (shear plane perpendicular; shear direction left-right), olivine has deformed through dislocation creep (mainly on the (010)[100] slip system), leading to a preferred orientation of the [100] axes close to the foliation  $F$  (trace marked by continuous line, top pole figure). (b) Reduction in free energy forces the dislocations to migrate to form well-developed and equally spaced subgrain boundaries. (c) When the difference in orientation across subgrain boundaries parallel to the (100) planes (normal to shear direction) becomes too large to be accommodated by dislocations, they evolve to grain boundaries. Depending on the spacing between the subgrain boundaries, the individual new grains may be elongated perpendicular to the original porphyroclasts. This marks a new foliation  $F'$  (continuous line, bottom pole figure) normal to  $F$  (dashed line). As the overall olivine LPO is unaffected by this process,  $F'$  appears now normal to the [100] axes of olivine. (d) Grain boundary migration and area reduction may further modify the microstructure leading to a possible weakening of the anomalous foliation with time. The presence of the original foliation  $F$  is sometimes suggested by the arrangement and shape of pyroxene and spinel grains, and above all by the completely unusual LPO of olivine at right angle to the visible foliation  $F'$ .

interpreted as a result of intensive recovery. The processes involved migration of edge dislocations on the (010)[100] slip system, development of widely spaced subgrain boundaries after alignment of dislocations, and individualization of new grains with a long axis at right angle to the primary foliation (Fig. 3.11). An example from our sample set is shown in Fig. 3.12.

It must be noted, however, that a right angle relationship between the foliation and the olivine [100] pole maxima is not necessarily the result of recovery processes. JUNG & KARATO (2001) showed experimentally that, in a water saturated system under high temperature and moderate stress, olivine [100] maxima can be orientated normal to the shear plane. The

development of such patterns requires the activation of the (100)[001] slip system, enabled by the fixation of hydroxyl groups in the olivine structure. Yet, this hypothesis seems very unlikely in our case for several reasons: (1) the source region of Lanzarote peridotites was described by NEUMANN et al. (2004) as a very depleted and only weakly metasomatized mantle, as evidenced by the absence of water bearing phases like phlogopite or amphibole. The patterns observed by JUNG & KARATO (2001), however, were from samples deformed under high water fugacity, comparable to the conditions found in mantle wedges above subduction zones. (2) In our samples, the orientations of subgrain boundaries perpendicular to the [100] axis clearly suggest a dislocation glide on the (010)[100] slip system

(assuming edge dislocation). If plastic deformation had occurred according to the (100)[001] slip system, the subgrain boundaries would have been parallel to the [100] axis. (3) Finally, the patterns of JUNG & KARATO (2001) were extracted from fine grained experimental samples characterized by a very high degree of recrystallization. The samples from Lanzarote with a foliation normal to the olivine [100] maxima, however, display a completely different microstructure and grain size distribution, making a similar deformation path rather unlikely. Added to the initial observations, these arguments make recovery the most convincing explanation accounting for the occurrence of anomalous foliation in Lanzarote peridotites.

Maxima of olivine [100] perpendicular to the foliation were also reported in high pressure metaperidotites from Alpe Arami and Cima di Gagnone, Switzerland

(MÖCKEL 1969, FRESE et al. 2003). These peridotites, however, are considered to be from subduction zone upper mantle, where water fugacity and stress are sufficiently high to activate the (100)[001] slip system. The hypothesis of JUNG & KARATO (2001) is thus convenient in those cases.

### 3.6.3 Comparison between measured and calculated velocities

In a previous study, BANDA et al. (1981) investigated the deep structure of Lanzarote using the seismic refraction method. Based on data collected on a NNE-SSW seismic transect, these authors suggested a depth of 11 km for the Moho and calculated a velocity of 7.4 km/s for Pn-waves in the upper mantle. At the time, this very low mantle velocity was interpreted as a con-

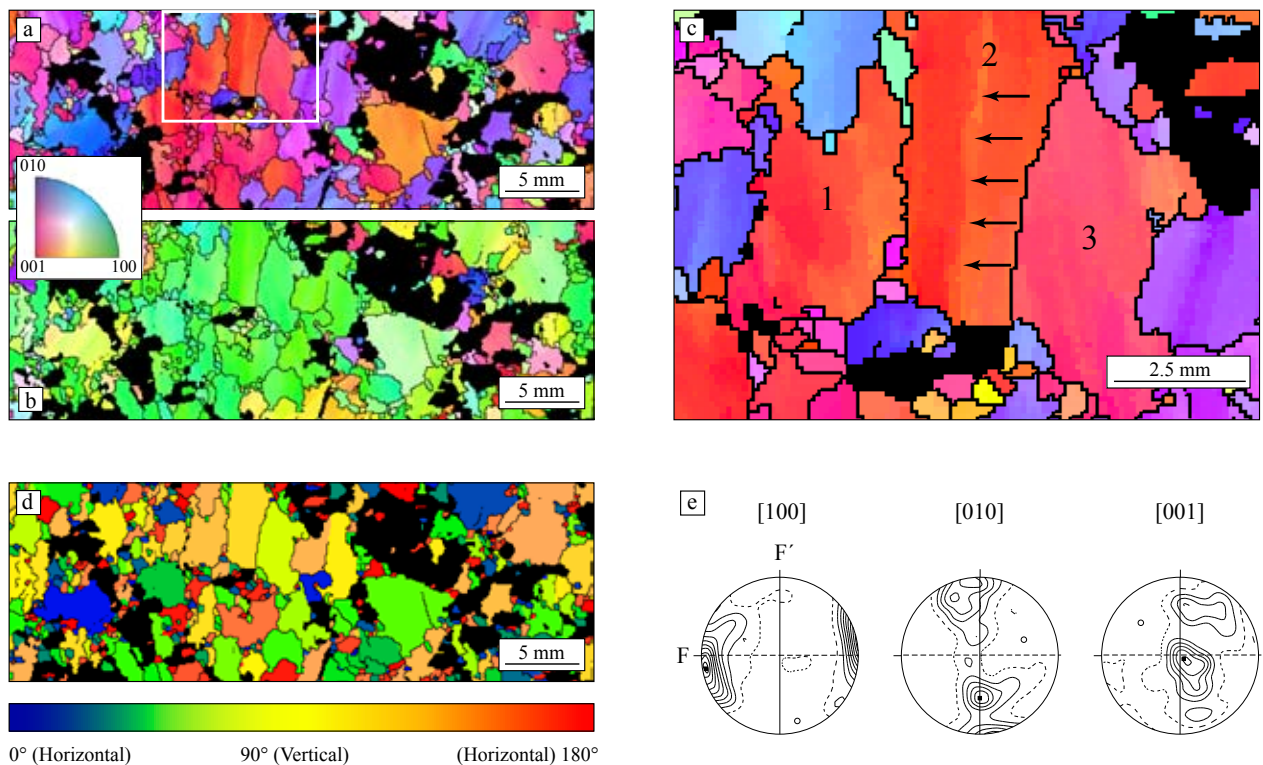


**Fig. 3.12** Sample LA8-4 as an example with the anomalous foliation. Olivine inverse pole figure maps showing the crystallographic axes falling (a) parallel to the page normal (ND) and (b) parallel to the horizontal (TD). The recurrent greenish colors in (b) indicate that the [100] axis is preferentially oriented in horizontal position. Black are other minerals (opx, cpx and spinel). (c) Close-up view of the framed area in (a) showing three adjacent olivine grains with similar crystallographic orientation. These grains are separated by nearly straight grain boundaries, suggesting that they originally formed one single crystal with a long axis oriented horizontally. The vertical boundary separating two areas with different shades of red in grain 2 (arrows) suggests the development of a subgrain boundary. (d) Grain shape orientation map showing a weak preferred orientation of the larger olivine grains indicating a vertical alignment of their long axis (colors mainly range from pale green, yellow to salmon pink). (e) Olivine texture plot of the same sample with the visible foliation  $F'$  (continuous line) and the approximate position of the original foliation  $F$  (dashed line). The location of [100] pole maximum relative to the actual foliation  $F'$  coupled with the observations put forward in (a), (b), (c) and (d) strongly suggest that  $F'$  is an anomalous foliation.

sequence of the anomalous character of the mantle close to the passive continental margin. Re-examining the record section of BANDA et al. (1981), DAÑOBEITIA & CANALES (2000) proposed a depth of 18 km for the Moho and velocities of 7.6 - 7.8 km/s for Pn-waves. They interpreted the interval between 11 and 18 km as underplated material. In order to compare the velocities extracted from the seismic survey with the present calculated values, the orientation relationship between the average sample seismic stereoplot and the seismic transect of BANDA et al. (1981) needs to be established. Peridotite xenoliths provide no information on their original position and orientation in the mantle. However, helpful indications for the alignment of the stereoplot in space can be extracted from surface wave seismic investigations and tomography models.

A recent study (GAHERTY 2001), based on anomalous polarization anisotropies of Love-Rayleigh waves in the North Atlantic near Iceland, has suggested a vertical transport direction (lineation) in the first kilometers of the lithosphere. In this model, the olivine [100] maximum is vertical for rocks above 100 km depth, whereas a more classical horizontal position of lineation in the mantle is proposed for greater depths. It is suggested that the development of the vertical orientation was associated with the upwelling flow of the mantle below the Mid-Atlantic ridge, from which the fabric was preserved or “frozen” during the subsequent cooling of the lithosphere. This feature was observed not only in the immediate vicinity of the ridge, but also for progressively older lithospheric mantle (> 40 My), suggesting that no reorientation of the original fabric occurred in response to horizontal flow. It is not known whether such a vertical orientation is a general feature of the uppermost mantle in slow-spreading ridge systems, and whether it can be preserved unchanged at farther distance from the ridge, e.g. until beneath Lanzarote (150 My). A vertical fabric preserved from the upwelling flow below the Mid-Atlantic ridge would tend to show a XY structural plane parallel to the ridge, favoring a fast wave propagation direction in the NNE-SSW direction when projected on the Earth surface.

However, if we refer to the anisotropy maps inferred from seismic tomography, the fastest propagation direction of Rayleigh waves (and thus also of P-waves) in the upper mantle beneath the Canary region is observed at a strike of about 118° (SILVEIRA et al. 1998), i.e. at about 90° from the direction suggested by the model of GAHERTY (2001). This result was obtained from measurements based on a 50 s

wave period, which corresponds to an approximate depth of 75-100 km. Because of the shallower origin of our samples (20-26 km), this fastest wave propagation direction does not provide an irrefutable argument allowing our seismic stereoplot to be orientated in space. Nevertheless, it is inconsistent with a vertical fabric orientation of the upper mantle immediately above 100 km depth. The fastest propagation directions of Rayleigh waves inferred from other tomography models (e.g. TANIMOTO & ANDERSON 1985, NATAF et al. 1986, MONTAGNER & TANIMOTO 1991) are consistent with the direction given by SILVEIRA et al. (1998), but as they were deduced from waves in the 100-250 s period range (about 150-400 km), they are less relevant for our purpose.

Further indications on the seismic properties of the uppermost mantle in the region were given by CONTRUCCI et al (2004), based on seismic reflection investigations carried out off the Moroccan coast. In their model, the Pn-wave velocity in the lithospheric mantle reaches 8.0 to 8.3 km/s for a seismic transect oriented at a strike of 129°. Even if this record section is located about 500 km North-East of Lanzarote, the lithospheric crust in both places have the same age (HINZ et al. 1982, ROESER 1982, ROEST et al. 1992), thus making a comparison of mantle properties between both locations reasonable. The velocity obtained by CONTRUCCI et al. (2004) for a strike of 129° is in good agreement with the fastest P-wave propagation direction of SILVEIRA et al. (1998), pointing at a strike of 118°. This is a strong argument for the non-preservation of the potentially vertical fabric of the mantle (GAHERTY 2001) and its reorientation in response to horizontal flow (BLACKMAN et al., 1996). Furthermore, it suggests a preservation of the fastest wave propagation direction from the asthenosphere to very shallow depth in the mantle.

On the basis of the above discussion, the seismic stereoplot of the peridotite average sample was orientated assuming a horizontal flow of the upper mantle and a fastest wave propagation direction corresponding to the strike mentioned by SILVEIRA et al. (1998). As structural axes are orthogonal (with Z vertical), Y has a strike of 28° (118° - 90°). The original seismic transect of BANDA et al. (1981) had a strike of approximately 38°, that is, at about 10° from the Y axis in the XY plane. When projected in the seismic stereoplot of our peridotite average sample, the direction of the seismic transect of BANDA et al. (1981) corresponds to a velocity slightly smaller than 7.9 km/s (Fig. 3.13). This

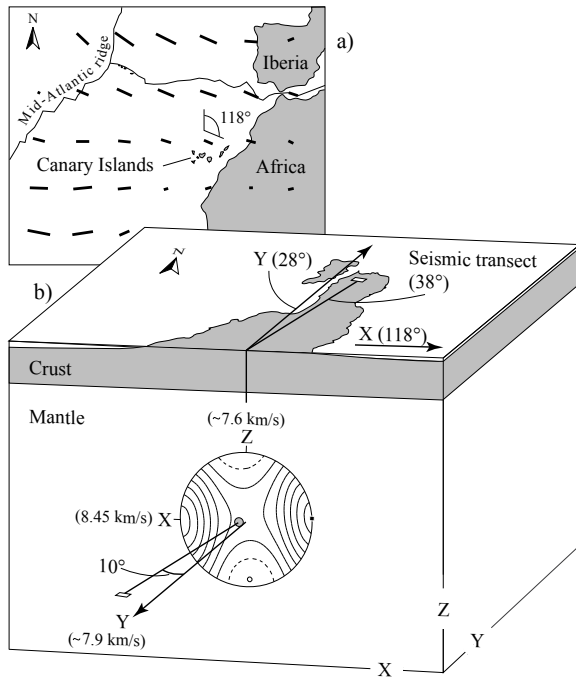


**Fig. 3.13** (a) Sketch map showing the fastest wave propagation direction in the upper mantle below the Canary Islands according to SILVEIRA *et al.* (1998). (b) Block diagram showing the orientation in space of the P-wave velocity plot of the peridotite average sample. The strike values for X, Y and the seismic transect of BANDA *et al.* (1981) are put in brackets. The calculated velocity of P-waves remains slightly below 7.9 km/s for a strike of 38°, which is the direction of the seismic transect. As the direction of interest is close to the Y direction, the velocity is only weakly influenced by any potential obliquity of the original texture.

value is in good agreement with the interpretation of DAÑOBEITIA & CANALES (2000), but much higher than the value of 7.4 km/s put forward by BANDA *et al.* (1981). Our results suggest that the velocity obtained by these latter authors is too low to be characteristic of the upper mantle, giving an additional argument for the presence of material different from the typical mantle rocks between 11 and 18 km in depth. Whether or not this material results from underplating (DAÑOBEITIA & CANALES, 2000) cannot be inferred from our study. The gabbroic xenoliths collected in Lanzarote by SCHMINCKE *et al.* (1998) and NEUMANN *et al.* (2000), however, might give some indications on the nature of this zone. Finally, it must be noted that, whichever the orientation of the seismic stereoplot, our calculated velocities will always give higher values than the one suggested by BANDA *et al.* (1981). This basically means that our conclusions relative to both field interpretations are independent on the correctness of the stereoplot orientation in space.

### 3.6.4 Variations of calculated velocities due to P/T estimates

To check the validity of our argumentation relative to the wide range of pressure and temperature put forward by NEUMANN *et al.* (1995), the seismic velocity of the peridotite average sample was calculated for low T / high P and high T / low P end members, i.e. 800°C / 0.8 GPa and 1200°C / 0.6 GPa, which corresponds to the highest and slowest seismic velocities. Even if these extreme intervals in P/T conditions might have little geological significance with respect to the geothermal gradient, they give an idea of the possible error spread of calculated P-wave velocity. For 800°C and 0.8 GPa, the seismic properties of P-waves are the following:  $V_{p_{\min}} = 7.73$  km/s,  $V_{p_{\max}} = 8.56$  km/s,  $AV_p = 10.2\%$ , whereas for 1200°C and 0.6 GPa, the calculations led to:  $V_{p_{\min}} = 7.50$  km/s,  $V_{p_{\max}} = 8.34$  km/s,  $AV_p = 10.6\%$ . Even if considering the latter interpretation as the true prevailing P/T conditions in the lithospheric uppermost mantle beneath Lanzarote, the calculated seismic velocity in the transect direction of BANDA *et al.* (1981), i.e. near Y, gives a value on the order of 7.75 km/s, i.e. far bigger than the velocity suggested from the original interpretation of those authors.

For a mantle lying at 11 km depth (0.4 GPa), calculations show that a velocity of 7.4 km/s in the direction of interest would require a tremendously high temperature without any geological significance. This makes the occurrence of other material type, e.g. mafic rocks, more convincing than mantle rocks in this depth range. The absence of mantle material between 11 and 18 km might also be suggested by the mineralogy of the samples with respect to the stability fields of peridotites. If mantle material would occur at such shallow depth, one would certainly expect to find a non-negligible amount of plagioclase-bearing peridotites in the xenolith population. On the contrary, plagioclase is absent in our sample set and occur only twice in minor amount in the whole sample population investigated by NEUMANN *et al.* (1995), thus giving an additional argument for a Moho lying at greater depth. In addition, serpentinization, which is often referred to as a possible explanation for the slowing down of seismic velocity in the upper mantle (e.g. CONTRUCCI *et al.*, 2004), was never observed in our samples and thus cannot account for the slow velocity of BANDA *et al.* (1981). Lastly, in order to discard the possible influence of nonrepresentative sampling with respect to the true mantle fabric distribution, an average velocity for both porphyroclastic and protogranular samples was calculated separately for 800°C / 0.8 GPa and 1200°C

/ 0.6 GPa end members. A similar approach was performed considering successively samples of group I and II, and finally assuming the same LPO types but for a single orientation (J of 270). Even so, the calculated P-wave velocity was in all cases higher than 7.7 km/s in the direction of interest, strongly suggesting that the observations put forward above are not due to bad sampling.

Finally, it must be noted that the slight velocity difference observed between the interpretation of DAÑOBEITIA & CANALES (2000) and our calculated values might be due to several factors, some of them being inherent to the approach adopted here. This includes (1) the limitations to obtain a set of fully representative samples from the anisotropic uppermost mantle, (2) the presence of large olivine porphyroclasts, e.g. in sample LA2-4, which tend to strengthen the average LPO and related seismic anisotropy, (3) the use of the Voigt average for calculation of seismic properties, which gives for olivine values of about 2% higher than the Reuss averaging method and (4) the inaccurate knowledge of the P/T conditions for the xenoliths source region, necessary to calculate the elastic constants at elevated pressure and temperature. In addition, melt occurrence in the upper mantle leads to a slight decrease of the measured velocity, thus increasing the gap between velocities obtained from seismic transects and values calculated from texture data (e.g. HESS 1964, KERN et al. 1996).

### 3.7 CONCLUSIONS

In this paper, a petrophysical analysis of the ultramafic xenoliths of Lanzarote was presented. From the measured LPO's, the seismic velocities in their anisotropic distribution were calculated and compared

to the existing geophysical interpretations. The main points of interest are summarized below.

(1) Lanzarote xenoliths exhibit two types of olivine preferred orientation. The first texture group showed a clustering of the [100] axis around the X direction, with fabrics intermediate between the single crystal and [100] fiber textures, whereas the second displayed a [010] fiber texture, with strong clustering of the [010] axes around the Z direction. The simultaneous occurrence of both textural groups suggests the coexistence of two different deformation regimes, probably dominated by a simple shear component under low strain rate and moderate to high temperature.

(2) Strong recovery processes led to the development of an anomalous foliation, with the olivine [100] maximum oriented perpendicular to the visible foliation. The possibility that this feature resulted from deformation in a water-rich environment was ruled out on the basis of microstructural, crystallographic and geochemical evidence.

(3) Velocities of P-waves calculated from the peridotite average sample range from 7.62 km/s to 8.45 km/s. The value slightly smaller than 7.9 km/s, obtained in the direction of the seismic transect of BANDA et al. (1981), is in good agreement with the latest interpretation of DAÑOBEITIA & CANALES (2000). Our results are consistent with a roughly W-E oriented fastest wave propagation direction and an original foliation in horizontal position.

(4) Average sample calculations performed separately for varied P/T conditions, as well as for each fabric types, suggest that our interpretations are robust, even if errors in P/T estimates and truly representative sampling are considered.

\*\*\*\*\*

# 4 - GROWTH MECHANISM OF SNOWBALL GARNETS FROM THE LUKMANIER PASS AREA (CENTRAL ALPS, SWITZERLAND): A COMBINED $\mu$ CT/EPMA/EBSD STUDY

ROBYR M., VONLANTHEN P., BAUMGARTNER L. & GROBÉTY B.

accepted in *Terra Nova* (17.11.06)

---

## ABSTRACT

For two decades considerable efforts have been made to explain the formation of snowball garnets by either the rotational or non-rotational models. On the basis of morphological, chemical and crystallographic evidence, this paper presents new data on snowball garnets showing that the formation of these microstructures can be explained by the combination of the two previously proposed mechanisms operating consecutively during garnet growth. The crystallization sequence of garnet revealed by Mn contouring and the distribution of crystallographic orientations within the spiral indicate that the final stages of garnet growth are controlled by post-kinematic crystallization. However, some microstructural arguments plead for a rotational contribution during the first stages of growth. In this view the overall spiral geometry is thought to overestimate the true amount of rotation experienced by the garnets. Results also reveal the existence of complex snowball garnets consisting of several grains formed from distinct nucleation sites.

## 4.1 INTRODUCTION

Snowball garnets, also referred to as spiral-shaped garnets, are characterized by the presence of sigmoidal inclusion trails with a relative rotation angle exceeding  $90^\circ$  (WILLIAMS & JIANG 1999). The formation of snowball garnets is explained by two controversial models: one argues for porphyroblast rotation with respect to the foliation in a single tectonic phase of non-coaxial flow (e.g. SCHONEVELD 1977, PASSCHIER et al. 1992), whereas the other argues for porphyroblast growth without rotation, involving overgrowth of successive generations of near orthogonal foliations (e.g. BELL et al. 1992). So far, most efforts to assess these two models have focused on geometrical proofs. However, this approach has failed to resolve the issue completely since most geometries observed in snowball garnets can be explained by both the rotational and the

non-rotational models (e.g. JOHNSON 1993, STALLARD 2003).

An alternative way of deciphering the development of snowball garnet porphyroblasts consists of combining chemical zoning and crystallographic orientation analysis with geometrical arguments. In a recent paper, IKEDA et al. (2002) used a combined approach to account for the formation of snowball garnets. Based on the chemical zoning and the monocrystalline nature of the investigated garnets, they concluded that growth and rotation occur simultaneously during a single metamorphic event. In light of new evidence provided by micro-computed X-ray tomography ( $\mu$ CT), electron probe microanalysis (EPMA) and electron backscattered diffraction (EBSD) techniques, we present an alternative model to account for the growth of snowball garnets.

## 4.2 GEOLOGICAL SETTING

The samples were collected in the Lukmanier Pass area, Central Alps, Switzerland (Fig. 4.1). This region comprises two major tectonic units: the Gotthard Massif to the north, partly overlain by a Mesozoic sedimentary cover, and the Lukmanier Massif to the south. Previous investigations (e.g. CHADWICK 1968) show that the Lukmanier area has a complex tectonic history involving three main phases of deformation. All of them are related to southwards and upwards tectonic movements resulting from the Tertiary continent-continent collision between the Eurasian and Apulian plates.

The two initial phases of deformation ( $D_1$  and  $D_2$ ) correspond to a crustal thickening event related to top-to-the-N directed movements which most probably reflect the southward underthrusting of the Mesozoic sedimentary cover beneath the frontal part of the Apulian plate. Whereas the first deformation ( $D_1$ ) was responsible for isoclinal folding and imbricate-stacking of basement and sedimentary cover units, the  $D_2$  phase generated the axial planar surface of the large isoclinal folds observed in the Lukmanier Pass area. Intensive SE-directed backfolding and backthrusting ( $D_3$ ) subsequently caused the upwards movements of crustal material and the exhumation of the Lukmanier metamorphic rocks.

The occurrence of snowball garnets is restricted to specific levels of the Liassic Stgir series (cover of the Gotthard Massif) (CHADWICK 1968, FOX 1975), which are characterized by thin alternations of quartz and

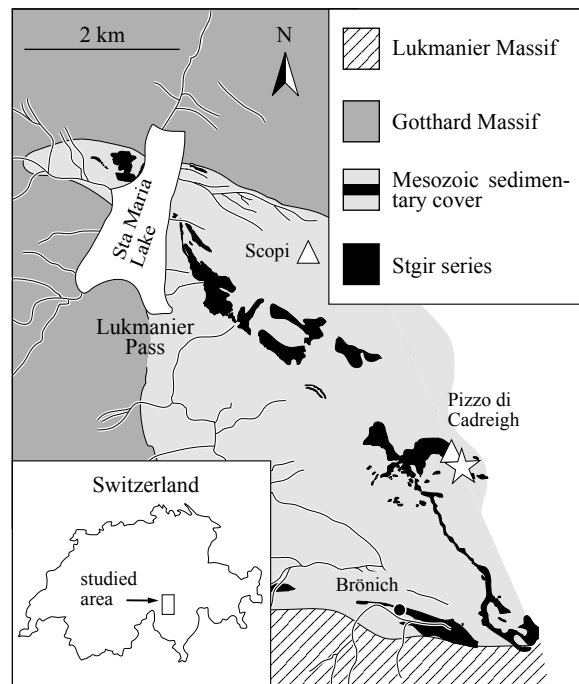


**Fig. 4.1** Simplified geological map of the Lukmanier Pass area. The sampling location (708.163 / 156.045, Swiss national grid coordinates) is indicated by a star.

mica-rich layers. The main structural element in those garnet-bearing levels consists of a N-dipping penetrative crenulation cleavage ( $S_2$ ) (Fig. 4.2a), associated with a monotonous N-S mineral lineation. Shear indicators clearly show a top-to-the-N directed sense of shear for  $S_2$ . The relationship between crystallization and deformation indicates that the main stage of garnet growth occurred contemporaneously with the  $S_2$  for-

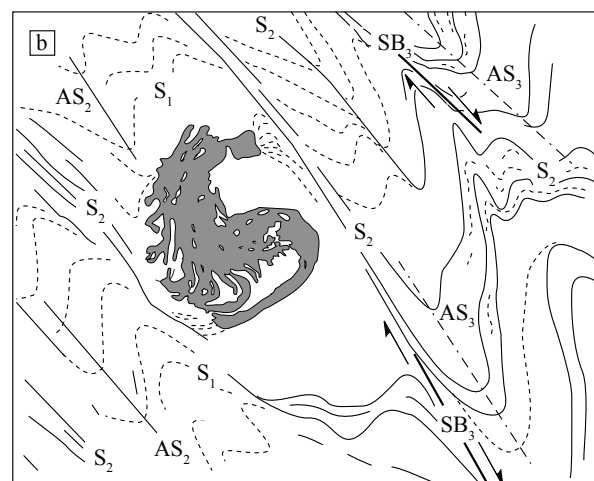
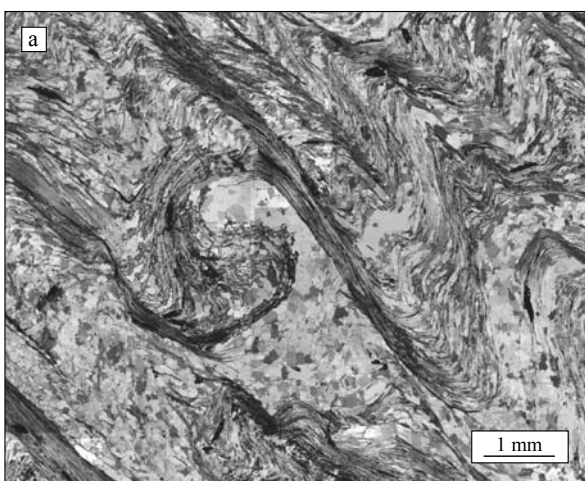


**Fig. 4.2** Photomicrograph (a) and sketch (b) of the same area illustrating the relationship between the snowball garnets and the foliations  $S_1$ ,  $S_2$  and  $S_3$ , AS = axial surface; SB = shear bands.

mation, i.e. during the  $D_2$  phase. The overprinting of  $S_2$  over the earlier schistosity ( $S_1$ ) resulted in the formation of closely-spaced microlithons displaying a subhorizontal E-W crenulation lineation parallel to the rotation axis of the snowball garnets. Both  $S_1$  and  $S_2$  foliations were subsequently folded to form asymmetric, centimeter to kilometer-scale folds ( $F_3$ ) verging to the SW. A slightly NE-dipping crenulation cleavage ( $S_3$ ) is locally visible in the hinges of the  $F_3$  folds but no penetrative schistosity is reported. Occasionally,  $D_3$  produced shear bands ( $SB_3$ ) with top-to-the-S directed movements (Fig. 4.2b).

The studied samples contain the mineral assemblage garnet + muscovite + biotite + quartz + plagioclase with minor epidote, chlorite and ilmenite. Although the garnet-forming reaction has not yet been fully established, the systematic occurrence of garnet crystals along mica-rich layers strongly suggests mica as reactant. Regional mapping of the mineral distribution throughout the Lukmanier Pass indicates a metamorphic field gradient characterized by peak conditions increasing gradually from the chloritoid zone to the north of the Santa Maria Lake, to the staurolite-kyanite zone in the Brönich area to the south (FOX 1975). Thermobarometric analysis of metapelites indicate peak conditions evolving from 410°C for the chloritoid zone (RAHN et al. 2002) to 550°C / 5.5 kbar for the staurolite-kyanite zone (ENGI et al. 1995).

### 4.3 ANALYTICAL PROCEDURES

3D imaging was obtained by  $\mu$ CT using a high resolution Skyscan-1072 system with a conical 100 kV X-ray source. A Cameca SX 50 electron microprobe (beam current of 150 nA at 25kV) was used for the mapping of chemical elements through wavelength dispersive X-ray spectroscopy (WDS). Crystallographic orientations were collected by EBSD using a Philips FEI XL30 SFEG Sirion scanning electron microscope (probe current of 20 nA for an acceleration voltage of 30 kV).

### 4.4 3D GEOMETRY

$\mu$ CT images reveal that the geometry of most garnets is characterized by a core region, around which two spiral arms are wound over more than 300°. Because of their very elongated shape parallel to the apparent

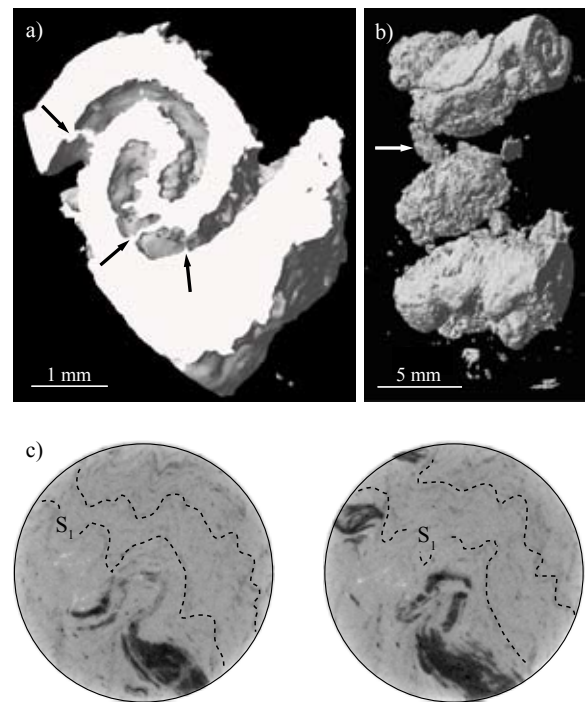


**Fig. 4.3** (a)  $\mu$ CT image of sample Luk\_02\_5 illustrating the typical spiral morphology of snowball garnets. The core region of the spiral is connected to the arms by thin curved bridges (black arrows). (b)  $\mu$ CT view of three vertically aligned garnets. The two porphyroblasts on top are connected to each other by a thick garnet appendage (white arrow). (c) Selected 2D sections (normal to the cylinder axis) based on  $\mu$ CT data showing trails of garnet grains (in black) mimicking the foliation  $S_1$  (dashed line) of the host rock.

rotation axis, the studied garnets look more like rolled cylinders than snowballs. The core region and the base of the spirals are commonly connected with the adjacent arms by short, curved garnet bridges (Fig. 4.3a). According to SCHONEVELD (1977), bridges are created by thin mica-rich layers progressively captured from the surrounding matrix and dragged towards the center as the spiral forms. Replacement of mica by garnet is commonly believed to freeze the bridge geometry.

Neighboring spiral garnets are occasionally linked to each other by appendages (Fig. 4.3b), consisting of small aligned garnet grains. Selected 2D sections of tomographic images reveal that the trails left by these grains mimic the  $S_1$  foliation (Fig. 4.3c). Optical microscopy observations indicate that most of these grains occur within mica-rich layers. The correspondence in geometry between the tortuous and crenulated external foliation ( $S_1$ ) and the alignment of garnet grains replacing mica suggests that the nucleation and growth of garnet continued after  $D_2$  had stopped.

## 4.5 CHEMICAL ZONING

Compositional zoning is a recurrent characteristic of garnet porphyroblasts, commonly interpreted as a primary growth feature (e.g. SPEAR 1993). Because of its very limited partitioning with the other phases present in pelitic schists, Mn is generally considered as the element best reflecting the successive steps of garnet growth. Assuming a local chemical equilibrium along the garnet-matrix boundary and no post-growth intracrystalline diffusion, the gradual decrease in Mn concentration from core to rim is frequently used as a proxy of time reflecting garnet growth history (e.g.

KRETZ 1973, CARLSON 1989 & 1991, SPEAR & DANIEL 1998).

X-ray compositional maps show a broadly concentric zoning of most major elements, characterized by a gradual decrease of Mn (Fig. 4.4a and 4.4c) and Ca from core to rim, counterbalanced by a simultaneous increase of Fe and Mg. The strong correlation in the zoning of Mn, Ca, Fe and Mg suggests that these elements achieved local equilibrium during garnet growth, thus justifying the use of Mn as a time marker. Although the variation in Mn concentration shows a roughly concentric pattern, secondary Mn maxima do

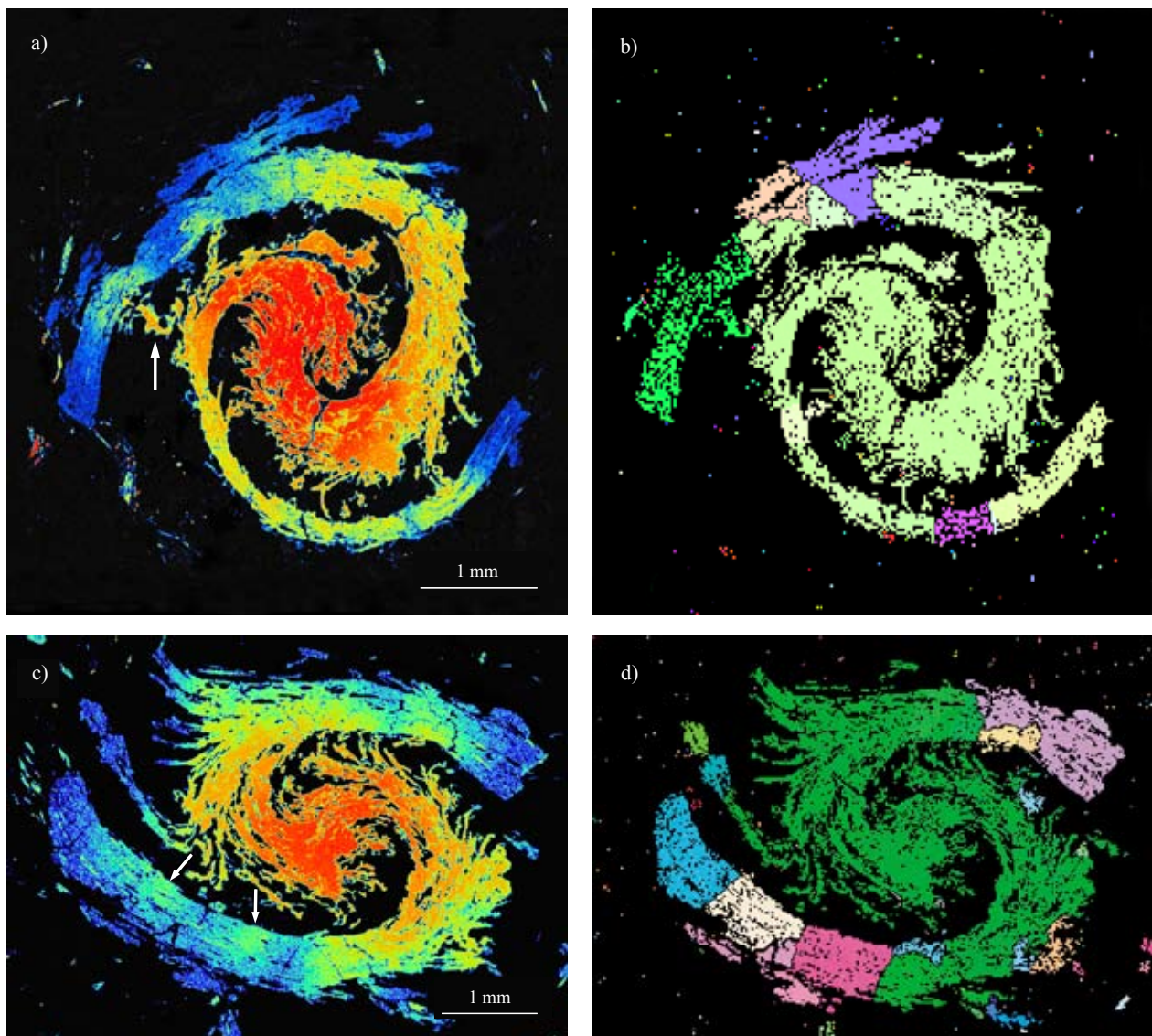


**Fig. 4.4** WDS X-ray maps of Mn (left, concentration decreasing from red to blue) and EBSD crystallographic orientation maps (right) for samples Luk\_02\_1 (a and b) and Luk\_02\_7 (c and d). Secondary Mn maxima (arrows) are centered in grains with crystallographic orientations different from the one of the core region. In sample Luk\_02\_1, the primary core orientation is maintained in two segments of the spiral arms connected to the center by garnet bridges (b, light green), along which a smooth decrease in Mn concentration is observed (a).

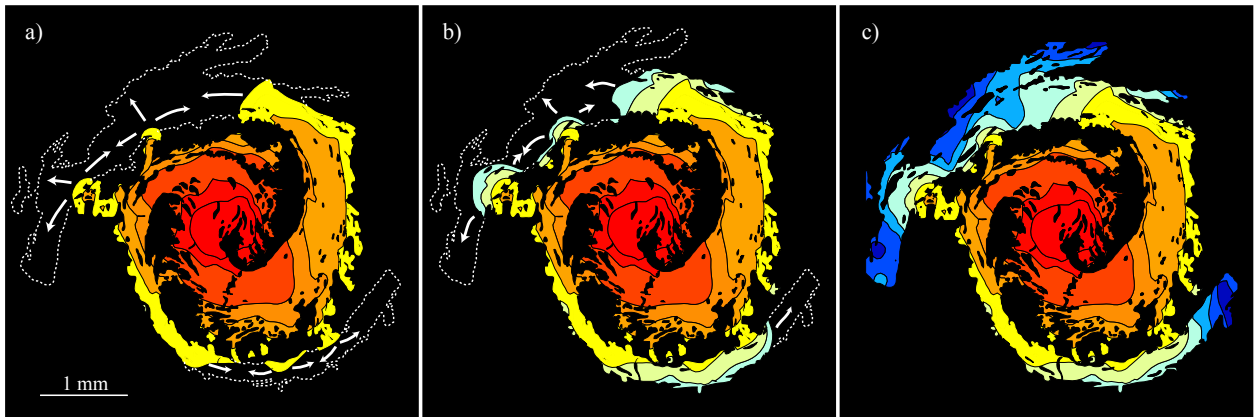


Fig. 4.5 Contoured Mn maps retracing the growth history of sample Luk\_02\_1. Arrows indicate the direction of growth.

exist, e.g. in the left spiral end in sample Luk\_02\_1 (Fig. 4.4a), as well as, to some extent, in the upwards-oriented spiral termination in sample Luk\_02\_7 (Fig. 4.4c).

The gradients on contoured Mn maps of sample Luk\_02\_1 (Fig. 4.5) indicate not only a decrease in Mn concentration from core to rim in the center and along the spiral curvature, but also across two bridges connecting the core to the arms. The patterns observed after considering Mn concentration levels as time lines suggest that the areas of the arms located in the continuation of the bridges crystallized early in the microstructure development, before being reached by the crystallization front advancing along the spiral curvature. In this growth scheme the bridges served as short cuts, making the crystallization path from the core to the arms significantly faster. Subsequent growth, either from the bridges or the secondary nucleation sites, led to the formation of the final garnet microstructure.

## 4.6 CRYSTALLOGRAPHIC ORIENTATION

EBSD is used to identify possible changes in crystallographic orientation within the garnet spirals. By assuming a continuous incorporation of atoms onto the preexisting garnet structure, a single crystallographic orientation would be expected for the whole spiral, as was observed by IKEDA et al. (2002) in their X-ray based texture analysis of snowball garnets of different origins. Our EBSD maps, however, reveal that the snowball garnets from the Lukmanier Pass are composed of several grains with different, distinct crystallographic orientations. The core region and the base of the spiral arms are generally formed by one

single, large grain, whereas the arm terminations are made of smaller and often box-shaped crystals separated by straight grain boundaries (Fig. 4.4b and 4.4d). The angular misorientation between those grains is typically a few tens of degrees, indicating that they are not subgrains formed by deformation of the arms. Some of the box-shaped grains contain secondary Mn-maxima. Both the difference in crystallographic orientation and the occurrence of additional Mn maxima point to growth from new nucleation sites. Among the end grains, however, some of them do not show any anomalous zoning. This may be explained by the fact that the thin sections used for chemical mapping cross-cut these grains at some distance from their nucleation center.

Garnet grains with different lattice orientations totally fill the spiral terminations in sample Luk\_02\_7 (Fig. 4.4d). In sample Luk\_02\_1 (Fig. 4.4b), however, the primary core orientation is maintained in an interstitial segment of the upper arm and in the final segment of the lower arm. Both portions are connected to the core by a thin, curved garnet bridge. As previously discussed, based on chemical Mn zoning patterns, these bridges were interpreted as preferential

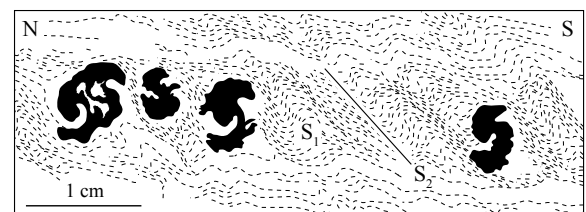


Fig. 4.6 Sketch cross-section perpendicular to the crenulation axis showing the distribution of snowball garnets relative to  $S_1$  and  $S_2$ . Garnet grains are located preferentially on the overturned limbs of microlithons.

crystallization paths between the core and the arms, suggesting an earlier crystallization of garnet across the bridges. The correspondence in crystallographic orientation between two regions of the spiral separated by grains with different lattice orientations further supports the role of crystallization short cuts played by mica bridges. For such a crystallization path to occur the position and final curvature of the spiral arms had to be already acquired before garnet crystallized. Therefore, we suggest that significant parts of the overall geometry were completed relatively early in the microstructure development and that the replacement of mica by garnet in the last portions of the spiral arms was mostly post-deformational.

## 4.7 DISCUSSION AND CONCLUSIONS

Combined chemical and crystallographic analyses provide several pieces of evidence showing that the spiral-shaped overall geometry was already achieved prior to the last stages of garnet crystallization. This strongly supports a final post-kinematic growth of garnet, mainly by replacement of mica.

The mechanism responsible for the first stages of snowball garnet formation is more difficult to assess; however, assumptions can be made on the basis of microstructural observations. During the crustal thickening event ( $D_2$ ), garnets grew on the overturned limbs of microlithons (Fig. 4.6) and are aligned in a direction corresponding to the crenulation lineation. This indicates that the first step of garnet crystallization post-dated the beginning of the microlithon formation and occurred when the  $D_2$  deformation was still in progress. The growth of snowball garnets on the overturned limb of microlithons during a single deformation phase is best explained through a single and continuous rotation of garnet grains rather than through an incremental superimposition of foliations resulting from numerous

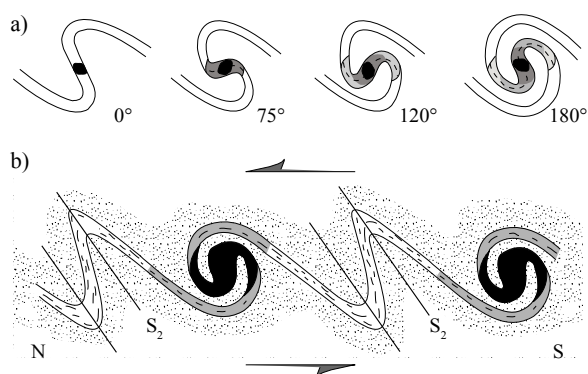


**Fig. 4.7** (a) Growth model proposed for the studied snowball garnets. Starting from a nucleus on the overturned limb of the microlithon, a  $180^\circ$  rotation is sufficient to account for an apparent rotation of about  $300^\circ$ . (b) Idealized sketch showing the alignment of garnet grains in a crenulated rock. Syn-rotational growth is shown in black, post-deformation growth in gray.

changes in the stress field. Our model suggests that a rotation of  $180^\circ$  may be sufficient to produce a spiral-shaped geometry mimicking an amount of rotation of approximately  $300^\circ$  (Fig. 4.7). This implies that the final geometry of snowball garnets greatly overestimates the actual extent of rotation. This assumption does not dispute the shear sense in the foliation plane since it is determined by the sense of rotation of the garnet during its initial growth stage.

Our data supports the idea that the growth of the snowball garnets from the Lukmanier area cannot be explained by either of the two classical models considered separately. In contrast, this study illustrates that snowball garnets may undergo a complex growth history in which both end-member mechanisms can operate consecutively. Additional chemical, structural, and crystallographic analyses on a larger sample population are required to better understand the mechanism of snowball garnet formation, and to determine if our observations are valid on a larger scale.

\*\*\*\*\*

## 5 - CSL GRAIN BOUNDARY DISTRIBUTION IN ALUMINA AND ZIRCONIA CERAMICS

VONLANTHEN P. & GROBÉTY B.

accepted in *Ceramics International* (15.03.07)

### ABSTRACT

The distributions of general and coincidence site lattice (CSL) grain boundaries (GB's) in texture-free alumina and zirconia ceramics sintered at two different temperatures were investigated based on electron backscatter diffraction (EBSD) measurements. Results were compared with the distributions obtained from random 2D spatial models and with calculated random distributions reported in the literature. All alumina samples independent on sintering temperature show the same characteristic deviations of the measured general GB distributions from the random model. No such features can be seen in zirconia. The total fractions of CSL GB's in alumina and zirconia samples are clearly larger, for both sintering temperatures, than those observed in the random simulations. A general GB prominence factor, similar to the twin prominence factor for FCC metals, was defined to simplify the representation of the CSL GB content in zirconia. The observed deviations from the random model show no dependence on sintering temperature nor on lattice geometry. In alumina, however, the change in the CSL GB character distribution with sintering temperature seems to be crystallographically controlled, i.e. directly dependent on the orientation of the CSL misorientation axis.

### 5.1 INTRODUCTION

Grain boundaries (GB's) have a significant influence on important sintering processes such as densification (BERNACHE-ASSOLANT 1993), grain growth (RODEL & GLAESER 1990), creep (CANNON et al. 1980, CARRY & MOCELLIN 1987, PRIESTER & LARTIGUE 1991), segregation (SWIATNICKI et al. 1995, CHO et al. 2002), diffusion (MISTLER & COBLE 1974), as well as on electrical (MORRIS 1976), mechanical (ZDANIEWSKI & KIRCHNER 1987), superconducting (DIMOS et al. 1988, KING et al. 1993, LAVAL & SWIATNICKI 1994) and optical (WYNER 1979) properties. The importance of GB's on the overall properties of ceramics depends on several factors, including the density of GB's in the material, the chemical composition of the interface and the crystallographic texture, i.e. the GB plane orientations and

grain misorientation. A special role is played by the coincidence site lattice (CSL) GB's (BOLLMANN 1970, WARRINGTON & BUFALINI 1971). CSL GB's are characterized by the multiplicity index  $\Sigma$ , which is defined as the ratio between the crystal lattice site density of the two grains meeting at the GB and the density of sites that coincide when superimposing both crystal lattices. For simple structures, it is generally admitted that GB's with low  $\Sigma$  values have a tendency for low interfacial energy and special properties. Thus, the study of the proportion of special GB's and of the distribution of grain misorientation inferred from the CSL model can be considered as a prerequisite to understand the relationship between microstructure and the properties of ceramics, from which further detailed investigations are carried out (e.g. PRIESTER & LARTIGUE 1991, SWIATNICKI et al. 1995).

In recent years, a scanning electron microscope (SEM)-based technique known as electron backscatter diffraction (EBSD) has been used in a few specific studies dealing with GB's in ceramic materials, e.g. to investigate the relationship between grain misorientation and crack propagation (GLASS et al. 1998), abnormal grain growth (KIM et al. 2002), and doping (CHO et al. 1998, CHO et al. 2002) in alumina, or to determine the lattice preferred orientation (LPO) in zirconia (FARYNA et al. 2000) and zirconia-based ceramic composites (FARYNA et al. 2002). The distribution of grain misorientation and CSL GB's in similar materials were investigated by other authors (e.g. PRIESTER & LARTIGUE 1991) through time consuming and fastidious TEM analyses of individual GB's. In general, the authors compared CSL distributions of samples with different compositions or process histories, but not with modeled distributions. In this paper, the grain misorientation and CSL GB distributions for texture-free alumina and zirconia ceramics sintered at two different temperatures are presented based on large GB sampling, and the results are compared with the values obtained from simulated random 2D spatial models.

## 5.2 EXPERIMENTAL METHODS

### 5.2.1 Ceramic processing and sample preparation

Two ceramic suspensions, containing respectively 80% Mg-doped alumina (Alcoa CT3000 SG<sup>®</sup>) and 80% zirconia (Tosoh TZ-8YS<sup>®</sup>, 8 mol.% yttrium-stabilized) (Fig. 5.1) in distilled water were ball milled for 24 hours in polyethylene jars. An organic surfactant and a molecular binder were added to the suspensions to prevent coagulation and to ensure compact strength after shaping. The powders were dried and granulated using a Büchi<sup>®</sup> B-190 mini spray dryer and subsequently pressed uniaxially into disks, 15 mm in diameter and approximately 10 mm thick, at 75 to 200 MPa. Isostatic pressing at 200 MPa was then performed to remove the internal residual strain induced by die pressing. Four alumina and four zirconia compacts were prepared. Two of each kind were sintered at 1550°C for 4 hours at a basic heating rate of 300°C/h. A lower rate of 100°C/h was chosen below 300°C to induce a complete burnout of the binder, as well as between 800°C and 1150°C to improve the densification of the compacts. The remaining two alumina

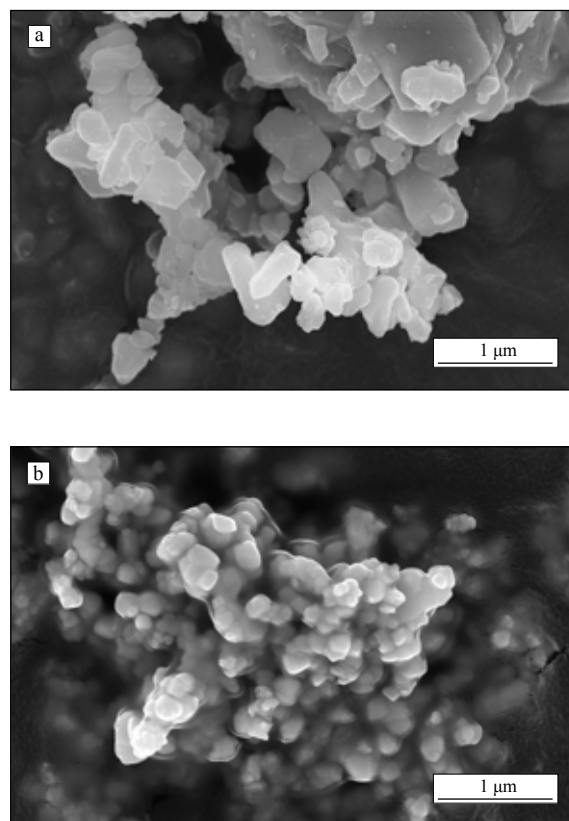


**Fig. 5.1** SEM secondary electron images of the as-received powders. The particles are platelet-shaped in alumina (a) and more regular in zirconia (b).

and two zirconia green bodies were fired at 1700°C following the same heating profile. Bulk density measurements were performed using Archimedes' principle. They revealed values ranging from 97.0 to 98.2% of their respective theoretical density (Table 5.1).

For each sample, one of the two flat surfaces of the disk was prepared for EBSD, first through grinding and polishing with diamond paste, then through lapping for 6 hours using a colloidal silica suspension (grain size 25 nm). To avoid specimen charging, the sample surface was coated with a 4 nm carbon layer and connected with silver paint to the sample holder.

### 5.2.2 Electron backscatter diffraction (EBSD)

The EBSD technique is based on automatic analysis of Kikuchi-type diffraction patterns generated by backscattered electrons (s. PRIOR et al. (1999) for a complete review). For each point of analysis, the crystallographic orientation is determined after indexing of the corresponding diffraction pattern. The Electron

Sample	Firing temperature [°C]	Bulk/Theoretical density * [%]	Scan	Step size [μm]	Area [μm <sup>2</sup> ]	Measurements with CI ≥ 0.2 [%]	Average CI**	Number of grains	Average grain diameter*** [μm]
A1	1550	98.0	1	5	500x500	44.6	0.25 (0.48)	5195	2.1
			2	0.4	50x50	65.1	0.37 (0.53)	556	
			3	0.4	50x50	67.3	0.38 (0.53)	549	
			4	0.4	50x50	74.5	0.43 (0.56)	730	
A2	1550	98.0	1	5	500x500	44.9	0.25 (0.48)	5233	2.1
			2	0.4	50x50	75.1	0.44 (0.56)	639	
			3	0.4	50x50	65.0	0.36 (0.52)	613	
			4	0.4	50x50	65.3	0.37 (0.52)	575	
A3	1700	98.2	1	15	1500x1500	55.7	0.31 (0.50)	6495	6.2
			2	0.8	100x100	82.7	0.48 (0.57)	281	
			3	0.8	100x100	82.7	0.49 (0.57)	260	
			4	0.8	100x100	81.5	0.49 (0.58)	284	
A4	1700	98.2	1	15	1500x1500	52.9	0.29 (0.49)	6164	6.4
			2	0.8	100x100	79.0	0.45 (0.55)	264	
			3	0.8	100x100	82.0	0.48 (0.57)	265	
			4	0.8	100x100	80.8	0.48 (0.57)	250	
Z1	1550	97.5	1	5	500x500	72.7	0.43 (0.57)	8475	3.5
			2	0.4	50x50	94.3	0.59 (0.62)	251	
			3	0.4	50x50	94.9	0.59 (0.62)	210	
			4	0.4	50x50	94.6	0.59 (0.62)	194	
Z2	1550	97.2	1	15	1500x1500	63.5	0.37 (0.53)	7408	5.8
			2	0.8	100x100	92.8	0.57 (0.60)	344	
			3	0.8	100x100	92.3	0.57 (0.61)	336	
			4	0.8	100x100	90.5	0.55 (0.60)	332	
Z3	1700	97.7	1	15	1500x1500	61.6	0.36 (0.53)	7187	7.8
			2	0.8	100x100	92.6	0.56 (0.60)	157	
			3	0.8	100x100	92.5	0.56 (0.60)	181	
			4	0.8	100x100	92.8	0.55 (0.59)	181	
Z4	1700	97.5	1	15	1500x1500	73.0	0.43 (0.56)	8507	8.3
			2	0.8	100x100	95.4	0.58 (0.60)	160	
			3	0.8	100x100	95.5	0.60 (0.62)	158	
			4	0.8	100x100	95.7	0.61 (0.63)	172	

\* measured according to Archimedes' principle and assuming a theoretical density of 3.98 and 6.08 [g/cm<sup>3</sup>] for alumina and zirconia, respectively

\*\* in brackets the average CI considering only the values ≥ 0.2

\*\*\* calculated from EBSD scans 2, 3 and 4 using the equivalent disc diameter method

**Table 5.1** Bulk properties and EBSD data for the eight ceramic samples.

Microscopy Image Simulation (EMS) software developed by STADELMANN (1987) was used to generate the reflectors included in the crystallographic material files needed for indexing. All EBSD data were collected with a Philips® FEI XL30 SFEG Sirion SEM equipped with the EDAX® (TSL) OIM 3.5 software package. The best results were obtained with an acceleration voltage of 20 or 25 kV for a probe current of 20 nA.

For each sample, four scans were performed in beam scan mode. The data of the first scans (numbered 1 in Table 5.1) were used to generate the pole figures of the samples. To avoid redundant point measurements from the same grains and improve grain

statistics, large step sizes were selected, i.e. 5 μm/step for an area of 500 μm x 500 μm and 15 μm/step for an area of 1500 μm x 1500 μm were chosen for the fine (1550°C) and coarse (1700°C) grained samples, respectively. The data of the three other scans (2, 3 and 4) were used to map the microstructure and highlight the GB's (Fig. 5.2). In order to improve the pixel resolution of the maps, small step size / areas of 0.4 μm / 50 μm x 50 μm and 0.8 μm / 100 μm x 100 μm were preferred for the fine and coarse grained samples, respectively.

To estimate the strength of the LPO, the texture index J was calculated as the mean square value of the orientation distribution function (BUNGE 1982). A

purely random LPO gives a  $J$  of 1, whereas for a single crystal, the texture index tends to infinity (in reality to about 24 due to the truncation to 22 in spherical harmonics calculations and the Gaussian half-width of  $15^\circ$  used).

The GB's satisfying the CSL model for  $\Sigma$  values up to 49 were automatically detected for the cubic material (zirconia), using the list integrated in the software (s. also PUMPHREY & BOWKETT 1971). For alumina, the Constrained CSL model (SINGH et al. 1990) adapted for hexagonal lattices by GRIMMER (1989) was used, considering  $\Sigma$  values up to 28 (Table 5.2). In this latter case coincidence is defined for specific  $c/a$  ratios; only CSL's with misorientation axes parallel to  $[0001]$  are independent of the lattice parameters. Following the recommendations of GRIMMER (1989), all common (unspecific) and specific coincidence

misorientations for  $c/a$  ratios ranging from 2.699 and 2.763 were included, assuming that small deviations from the exact  $c/a$  value for the studied alumina (2.726 in the present samples, calculated using the Rietveld refinement method) could be accommodated by dislocations. For both alumina and zirconia, the Brandon criterion (BRANDON 1966) was used to account for the allowed deviation  $\Delta\theta$  of experimental values from the theoretical values:

$$\Delta\theta = 15\Sigma^{-0.5} \quad (\text{Eq. 5.1})$$

Special GB's corresponding to given  $\Sigma$  values were counted and expressed as a fraction of the total GB's. To improve GB statistics, averaging between data collected from the different scans within the same samples and from different samples of the same material sintered at the same temperature was performed.

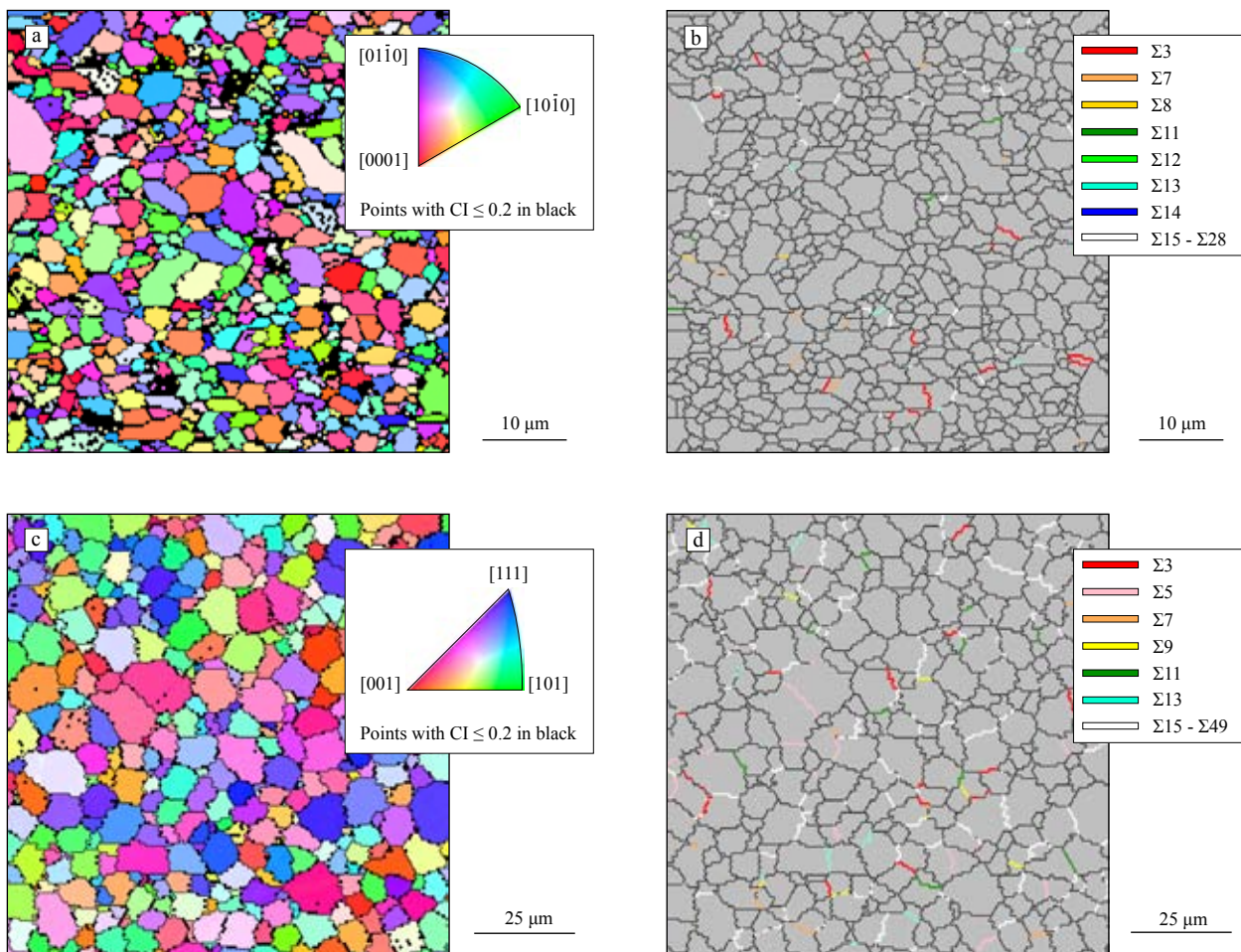


**Fig. 5.2** Inverse pole figure maps showing the crystallographic orientation of the normal to the sample surface ( $ND$ ) for alumina ( $a$ ; sample A2 scan 2) and zirconia ( $c$ ; sample Z2 scan 3), and CSL GB maps ( $b$ ,  $d$ ) of the corresponding areas. CSL misorientations with high  $\Sigma$  values were grouped for clarity. Since the EDAX<sup>®</sup> (TSL) OIM software only highlights GB's between contiguous points, a smooth cleaning up according to the grain dilation method was performed before generating the CSL GB maps.

$\Sigma$	Alumina					Zirconia							
	c/a	Miller indices [uv.w]				$\theta$ [°]	$\Delta\theta$ [°]	$\Sigma$	Miller indices [uvw]			$\theta$ [°]	$\Delta\theta$ [°]
3	all	0	0	0	1	60.00	8.67	3	1	1	1	60.00	8.66
7 <sub>1</sub>	all	0	0	0	1	38.21	5.67	5	1	0	0	36.87	6.71
7 <sub>2</sub>	2.739	2	4	-6	1	85.90	5.67	7	1	1	1	38.21	5.67
7 <sub>3</sub>	2.739	4	2	-6	1	85.90	5.67	9	1	1	0	38.94	5.00
8	2.699	2	4	-6	1	86.42	5.30	11	1	1	0	50.48	4.52
11 <sub>1</sub>	2.739	2	1	-3	1	68.68	4.52	13 <sub>1</sub>	1	0	0	22.62	4.16
11 <sub>2</sub>	2.739	1	2	-3	1	68.68	4.52	13 <sub>2</sub>	1	1	1	27.80	4.16
11 <sub>3</sub>	2.739	1	2	-3	0	95.22	4.52	15	2	1	0	48.19	3.87
12	2.763	28	56	-84	11	94.78	4.33	17 <sub>1</sub>	1	0	0	28.07	3.64
13 <sub>1</sub>	all	0	0	0	1	27.80	4.16	17 <sub>2</sub>	2	2	1	61.93	3.64
13 <sub>2</sub>	2.739	3	6	-9	0	57.42	4.16	19 <sub>1</sub>	1	1	0	26.53	3.64
13 <sub>3</sub>	2.739	5	10	-15	2	94.41	4.16	19 <sub>2</sub>	1	1	1	46.83	3.64
13 <sub>4</sub>	2.739	10	5	-15	2	94.41	4.16	21 <sub>1</sub>	1	1	1	21.79	3.27
13 <sub>5</sub>	2.763	2	4	-6	1	85.59	4.16	21 <sub>2</sub>	2	1	1	44.40	3.27
14 <sub>1</sub>	2.711	7	14	-21	5	75.52	4.01	23	3	1	1	40.45	3.13
14 <sub>2</sub>	2.717	32	64	-96	13	94.10	4.01	25 <sub>1</sub>	1	0	0	16.25	3.00
15 <sub>1</sub>	2.699	17	34	-51	7	93.82	3.87	25 <sub>2</sub>	3	3	1	51.68	3.00
15 <sub>2</sub>	2.717	2	4	-6	1	86.18	3.87	27 <sub>1</sub>	1	1	0	31.58	2.89
17 <sub>1</sub>	2.739	2	2	-4	1	71.12	3.64	27 <sub>2</sub>	2	1	0	35.42	2.89
17 <sub>2</sub>	2.739	5	4	-9	1	96.76	3.64	29 <sub>1</sub>	1	0	0	43.61	2.79
17 <sub>3</sub>	2.739	4	5	-9	1	96.76	3.64	29 <sub>2</sub>	2	2	1	46.39	2.79
17 <sub>4</sub>	2.763	28	14	-42	11	72.90	3.64	31 <sub>1</sub>	1	1	1	17.90	2.69
18	2.711	2	1	-3	1	68.83	3.53	31 <sub>2</sub>	2	1	1	52.19	2.69
19 <sub>1</sub>	all	0	0	0	1	46.83	3.44	33 <sub>1</sub>	1	1	0	20.05	2.61
19 <sub>2</sub>	2.739	5	10	-15	1	65.10	3.44	33 <sub>2</sub>	3	1	1	33.55	2.61
19 <sub>3</sub>	2.739	10	5	-15	1	65.10	3.44	33 <sub>3</sub>	1	1	0	58.98	2.61
19 <sub>4</sub>	2.739	1	1	-2	0	86.98	3.44	35 <sub>1</sub>	2	1	1	34.04	2.54
20 <sub>1</sub>	2.717	32	16	-48	13	72.45	3.35	35 <sub>2</sub>	3	3	1	43.23	2.54
20 <sub>2</sub>	2.755	2	4	-6	1	85.70	3.35	37 <sub>1</sub>	1	0	0	18.92	2.47
21 <sub>1</sub>	all	0	0	0	1	21.79	3.27	37 <sub>2</sub>	3	1	0	43.13	2.47
21 <sub>2</sub>	2.711	28	14	-42	5	99.59	3.27	37 <sub>3</sub>	1	1	1	50.57	2.47
21 <sub>3</sub>	2.739	3	3	-6	0	64.62	3.27	39 <sub>1</sub>	1	1	1	32.21	2.40
22 <sub>1</sub>	2.699	68	34	-102	7	64.42	3.20	39 <sub>2</sub>	3	2	1	50.13	2.40
22 <sub>2</sub>	2.724	2	4	-6	1	86.09	3.20	41 <sub>1</sub>	1	0	0	12.68	2.34
23 <sub>1</sub>	2.711	2	4	-6	1	86.26	3.13	41 <sub>2</sub>	2	1	0	40.88	2.34
23 <sub>2</sub>	2.739	1	1	-2	0	55.58	3.13	41 <sub>3</sub>	1	1	0	55.88	2.34
23 <sub>3</sub>	2.739	5	10	-15	1	87.51	3.13	43 <sub>1</sub>	1	1	1	15.18	2.29
23 <sub>4</sub>	2.739	10	5	-15	1	87.51	3.13	43 <sub>2</sub>	2	1	0	27.91	2.29
23 <sub>5</sub>	2.739	4	4	-8	1	91.25	3.13	43 <sub>3</sub>	3	3	2	60.77	2.29
24	2.699	1	1	-2	0	65.38	3.06	45 <sub>1</sub>	3	1	1	28.62	2.24
25 <sub>1</sub>	2.699	2	1	-3	1	68.90	3.00	45 <sub>2</sub>	2	2	1	36.87	2.24
25 <sub>2</sub>	2.704	3	6	-9	1	102.71	3.00	45 <sub>3</sub>	2	2	1	53.13	2.24
25 <sub>3</sub>	2.750	58	116	-174	23	94.59	3.00	47 <sub>1</sub>	3	3	1	37.07	2.19
26	2.758	2	1	-3	1	68.57	2.94	47 <sub>2</sub>	3	2	0	43.66	2.19
27 <sub>1</sub>	2.728	62	124	-186	25	94.25	2.89	49 <sub>1</sub>	1	1	1	43.58	2.14
27 <sub>2</sub>	2.750	2	4	-6	1	85.75	2.89	49 <sub>2</sub>	5	1	1	43.58	2.14
27 <sub>3</sub>	2.763	16	8	-24	11	64.79	2.89	49 <sub>3</sub>	3	2	2	49.22	2.14
28 <sub>1</sub>	2.711	14	7	-21	1	82.82	2.83						
28 <sub>2</sub>	2.711	5	4	-9	1	97.18	2.83						

**Table 5.2** Coincidence rotations used to determine CSL GB's in rhomboedral alumina (GRIMMER, 1989) and cubic zirconia (e.g. PUMPHREY & BOWKETT, 1971). Subscripts are used to differentiate angle/axis pairs characterized by the same multiplicity index  $\Sigma$ .

In the EDAX<sup>®</sup> (TSL) OIM software, the reliability of indexing is expressed by a confidence index (CI) comprised between 0 and 1. It is generally admitted that patterns with a CI value  $\geq 0.2$  are almost certainly

indexed correctly. In this study, the consistently high CI values (s. Table 5.1) of our EBSD data exclude indexing errors due to pseudo-symmetry, which might occur e.g. in alumina. Wrong indexing is generally

accompanied by a very low CI, due to the fact that more than one solution with similar likelihood is proposed during the indexing procedure. As a consequence, the quality of EBSD maps would markedly deteriorate, since large grains will typically contain speckled points indexed by any of the pseudo-symmetric orientations (K. KUNZE, personal communication). Such features were never observed.

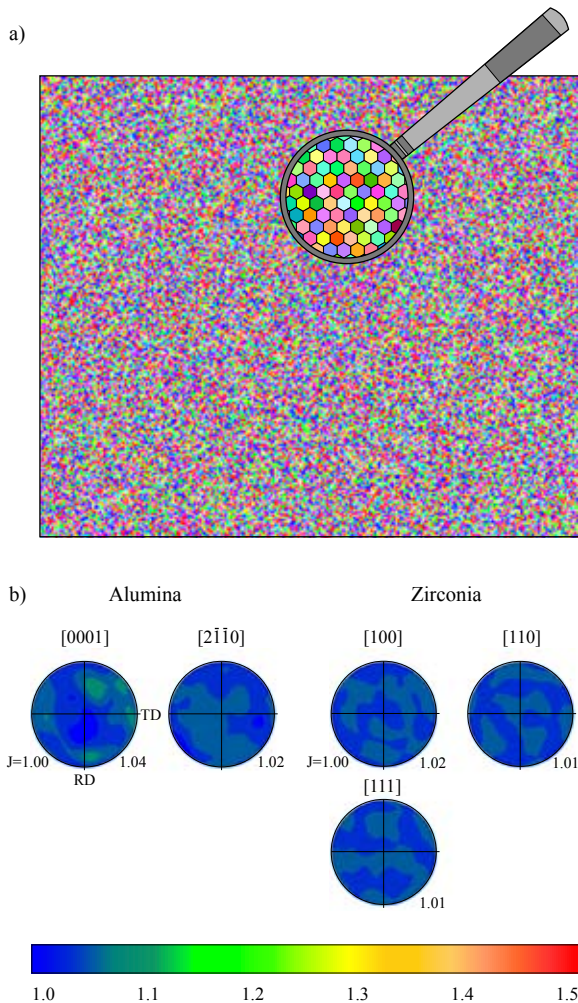


**Fig. 5.3** (a) Map of the simulated spatial model containing 50000 hexagonal-shaped and randomly orientated grains. (b) Pole figures for the simulated textures with crystallographic properties corresponding to alumina and zirconia. Pole figures are represented on upper hemisphere equal area projections. The number on the bottom right of each plot is the maximum density expressed in multiples of uniform distribution (s. scale bar). For each sample, the texture index  $J$ , calculated for an expansion index of 22 and a Gaussian half-width of  $15^\circ$  is shown on the bottom left. TD, RD and ND (page normal) are indicated for the first plot only. Texture indexes  $J$  of 1.00 for both alumina and zirconia indicates that the simulated spatial models are texture-free.

### 5.2.3 Simulation of random spatial models

In order to compare the distributions of grain misorientation and CSL GB's obtained from the measured samples with the distributions expected for purely random textures, 2D models containing 50000 randomly orientated grains (Fig. 5.3) were simulated for alumina and zirconia. Hexagonal-shaped grains were chosen to approximate the well equilibrated microstructure observed in the samples. The grid of the models consists thus of a regular honeycomb-type arrangement of grains, each having six neighbors and  $120^\circ$  triple junctions. The microstructure corresponds to a cut through a 3D arrangement of Kelvin-polyhedra normal to the two-folded axes. This latter model was used previously by GARBACZ & GRABSKI (1993) in 3D simulations of GB character distribution.

A random number calculator was used to generate the Euler angles  $\varphi_1$ ,  $\Phi$  and  $\varphi_2$  necessary to define the orientation of the grains, following the equations first defined by BUNGE (1982) and used for similar purposes by PAN & ADAMS (1994):

$$\varphi_1 = 2r_1\pi; \Phi = \cos^{-1}(1 - 2r_2); \varphi_2 = 2r_3\pi \quad (Eq. 5.2)$$

where  $r_1$ ,  $r_2$  and  $r_3$  are randomly generated numbers comprised between 0 and 1. Each of the 50000 Euler triplets was attributed to a grain of the honeycomb microstructure and the grain orientation data were loaded into the EDAX® (TSL) OIM Analysis software to generate the grain misorientation and CSL distributions.

## 5.3 RESULTS AND DISCUSSION

### 5.3.1 Microstructures and textures

Typical microstructures for alumina and zirconia ceramics sintered at  $1550^\circ\text{C}$  and  $1700^\circ\text{C}$  are presented in Fig. 5.4. The average grain diameter increased by approximately 100% for zirconia and 200% for alumina in the samples fired at  $1700^\circ\text{C}$  (s. Table 5.1). Zirconia specimens are characterized by a well equilibrated equi-dimensional microstructure with a large number of six-sided grains. The remaining pores are located almost exclusively in the interior of the grains. The alumina samples have a wider grain size and

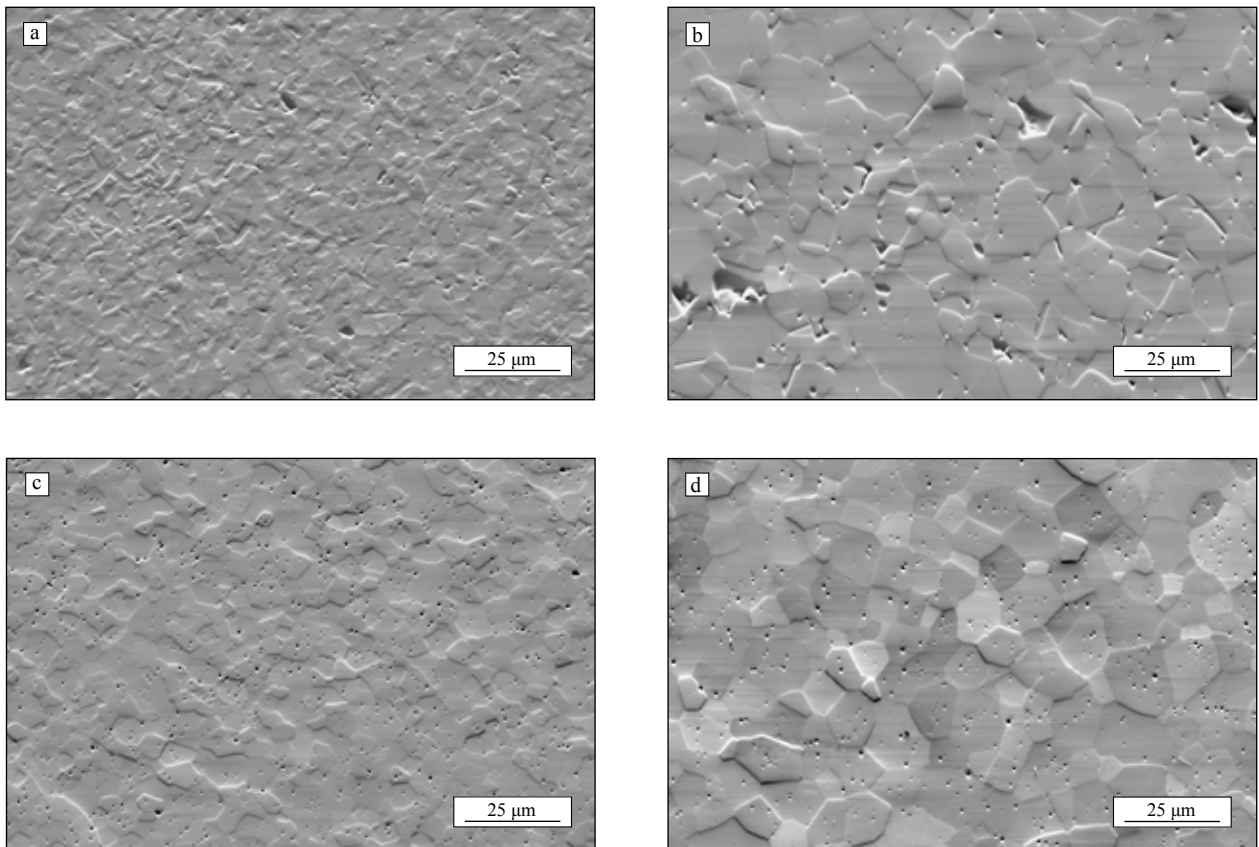


**Fig. 5.4** SEM forescattered electron images showing typical microstructures of alumina (a, b) and zirconia (c, d) samples. Contrast and topography from one grain to the next express changes in crystallographic orientations. The samples displayed in (a) and (c) were sintered at 1550°C and those in (b) and (d) at 1700°C.

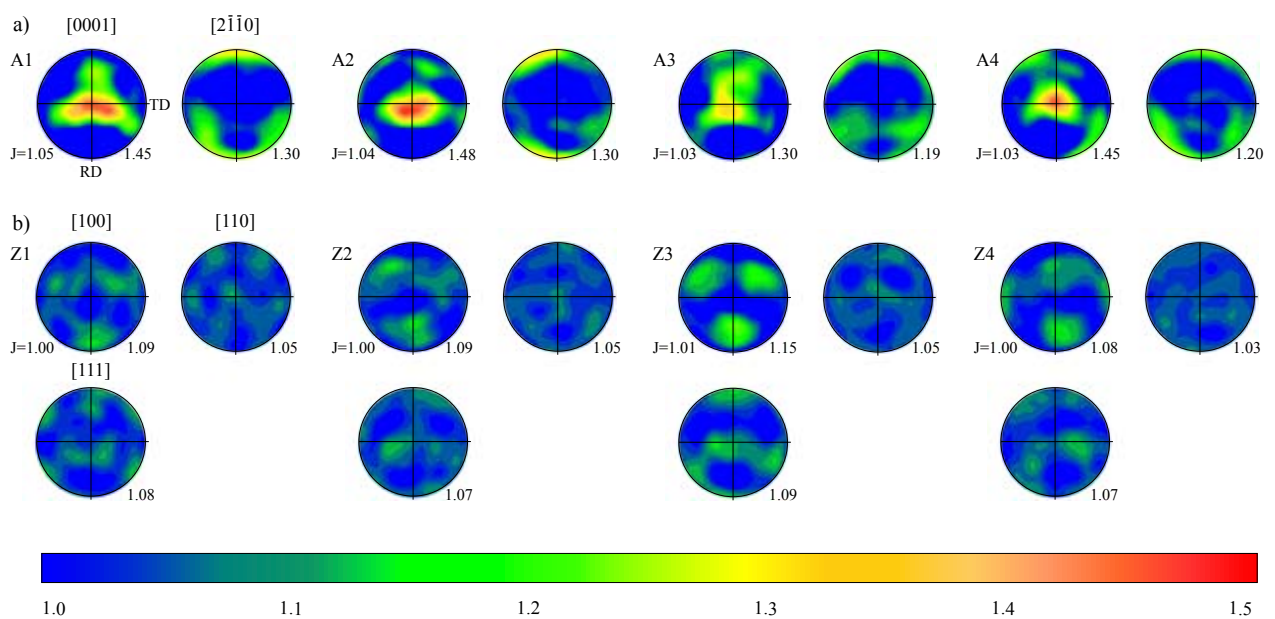


**Fig. 5.5** (a) Alumina pole figures showing the preferred orientations of the  $[0001]$  and  $[2-1-10]$  axes. A very weak but obvious texture is observed with the  $[0001]$  pole maximum orientated parallel to ND (direction of uniaxial pressing). (b) Zirconia pole figures displaying the preferred orientations of the  $[100]$ ,  $[110]$  and  $[111]$  axes. The constantly small J index values indicate absence of significant texture. Pole figures are represented on upper hemisphere equal area projections and were calculated from the data of the scans labeled 1 in Table 5.1. Symbols and reference axes as in Fig. 5.3.

shape distribution. Abnormal grain growth, however, was never observed. The porosity is concentrated at GB's and triple junctions. Occasionally, large pores resulting from insufficient powder compaction during the shaping process are encountered.

The LPO for the 8 samples (Fig. 5.5) were calculated from EBSD scans (numbered 1 in Table 5.1) containing several thousands of grains each. From the texture indexes  $J$ , which vary between 1.00 and 1.05, the samples can be considered as texture-free.

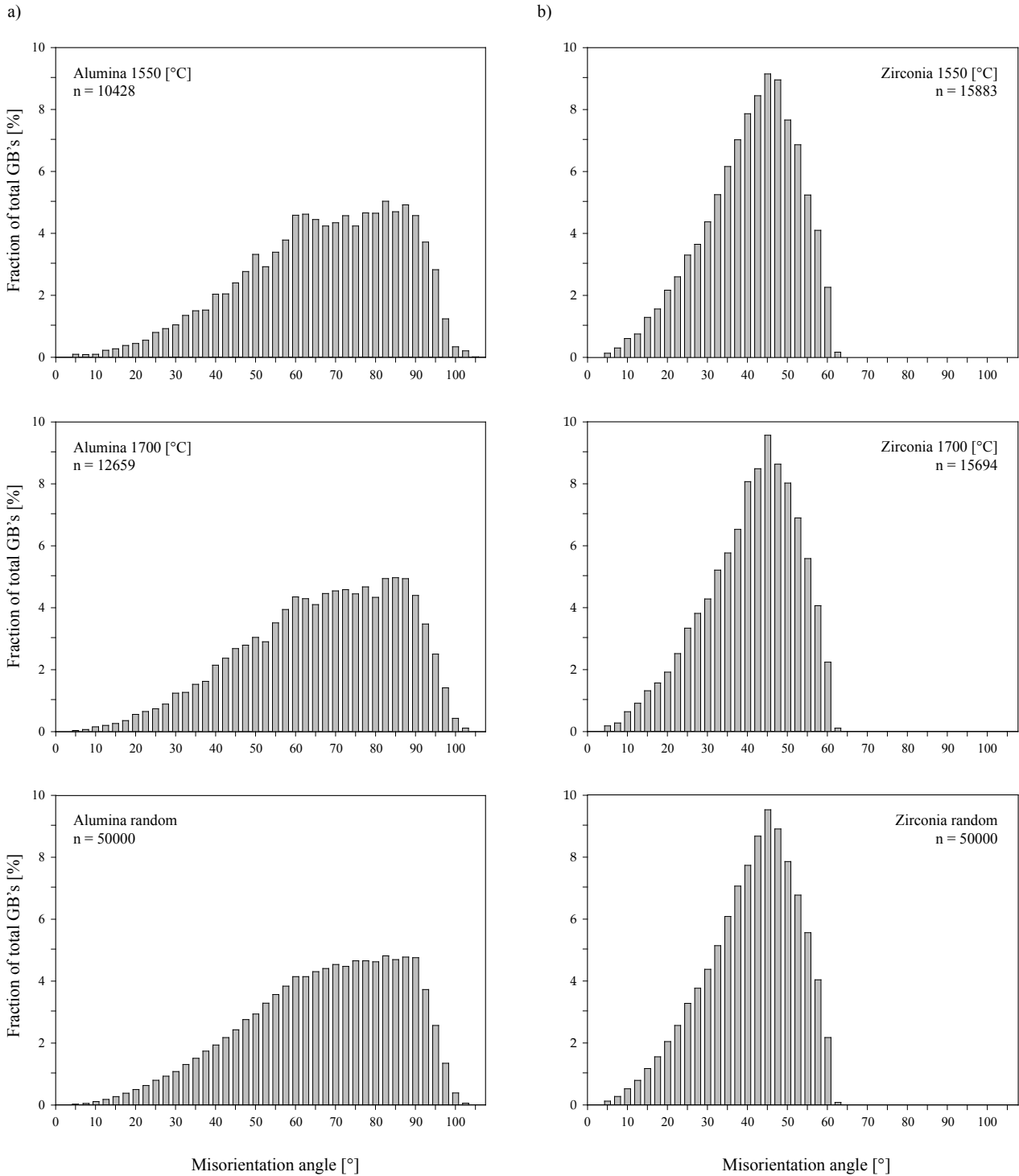


**Fig. 5.6** Histograms of misorientation angles for (a) alumina and (b) zirconia ceramics sintered at 1550°C and 1700°C;  $n$  = number of grains. The distribution for the spatial models simulated for 50000 randomly orientated grains is indicated for comparison.

Nevertheless, small peaks are present in some of the pole figures. In alumina a very weak but obvious LPO was observed, the [0001] pole maximum being orientated parallel to the normal direction (ND). This is probably due to the reorientation of the platelet-shaped crystallites present in the initial powder (s. Fig. 5.1a.) in response to the uniaxial pressing of the green bodies. The LPO of zirconia is purely random, except for sample Z3, for which a very weak [111] pole maximum is orientated parallel to ND.

### 5.3.2 Grain misorientation distributions

The grain misorientation distributions were calculated up to  $107.5^\circ$  for alumina and  $62.8^\circ$  for zirconia, i.e. the limits imposed by symmetry. The histograms of the measured misorientation angles for both alumina and zirconia were compared with the model random distributions using the Kolmogorov-Smirnov test (WHEELER et al. 2001). Using all misorientations, i.e. without prior classification, the measured distributions cannot be distinguished from the random distribution even as far down as the  $\alpha=0.2$  level. The same holds for histograms of the same data with a restricted number of classes (Fig. 5.6).

Visual inspection of the histograms for the measured alumina grain misorientation distributions shows, however, that the positions of the relative maxima and minima are not completely random. There are relative maxima in both distributions at around  $50^\circ$ ,  $60^\circ$ , and between  $82.5^\circ$  and  $92.5^\circ$ . Relative maxima for similar misorientation angles are also found in other misorientation distributions for alumina published so far (e.g. CHO et al. 1998, CHO et al. 2002). All samples had, similar to the present ones, a weak texture, which may be the reason for these characteristic maxima (s. Section 5.3.3). The increase in temperature and the associated increase in grain size have no effect in the distribution observed in the present samples, i.e. the details of the distributions (relative maxima) remain the same. This is consistent with the distributions extracted from Monte Carlo grain growth simulations of HASSOLD et al. (2003), which showed that the fraction of CSL GB's does not change with time, i.e. with increasing grain size, except for low angle GB's ( $\Sigma 1$ ).

The misorientation distributions of the zirconia average samples show no relative maxima and the differences between the distributions are as small as the differences between measured and random distributions.

## 5.3.3 CSL grain boundary distributions

### 5.3.3.1 Validity of the simulated spatial models

Two methods are described in the literature to obtain random CSL GB distributions for microstructures consisting of cubic phases. Model distributions are either calculated from randomly generated pairs of grain orientations or they are extracted from a plane or space filling arrangement of randomly orientated grains, as was done in the present study. It has been shown that the two methods are not equivalent (GARBACZ & GRABSKI 1993) and that the values obtained from random spatial models built with Kelvin polyhedra-shaped grains fit better with measured random grain misorientation and CSL GB distributions. The 3D model, however, does also not reflect truly the geometry of the EBSD measurements, which are obtained from a 2D cut through the 3D microstructure. Therefore, we decided to extract the random CSL GB distribution from a 2D honeycomb microstructure. The CSL GB frequencies obtained for zirconia are close to the values obtained by GARBACZ & GRABSKI (1993). For  $\Sigma$  values up to 37, the differences are less than 10 rel%.

With regards to alumina, there are no data given in the literature for the theoretical CSL distribution in a random texture with trigonal symmetry. However, the analytical expression given by MORAWIEC et al. (1993) to calculate the number fraction of individual CSL GB's, although based on randomly distributed orientation matrices and not on a physical random microstructure, can be used as a rough guideline to test the validity of our simulated 2D model. According to these authors, the calculated number fraction of CSL GB's with given  $\Sigma$ ,  $f_{c\Sigma}$ , is given by:

$$f_{c\Sigma} = \frac{\lambda N^2}{\pi N(g)} (\Delta\theta - \sin \Delta\theta) \quad (\text{Eq. 5.3})$$

$\Sigma$	$\lambda$	N	$f_{c\Sigma}$	$f_{s\Sigma}$
3	1	6	0.110	0.087
$7_1$	1	3	0.061	0.049
$13_1$	1	3	0.024	0.016
$19_1$	1	3	0.014	0.013
$21_1$	1	3	0.012	0.011

**Table 5.3** Fractions  $f_{c\Sigma}$  (%) of CSL GB's calculated according to Eq. 5.3 for the common (unspecific) coincidence misorientations in alumina. Fractions obtained from the simulated random 2D spatial model ( $f_{s\Sigma}$ ) are shown for comparison.

$N$  is the order of the subgroup of the crystallographic point symmetry containing only rotations (6

for trigonal point groups),  $\lambda$  and  $N(g)$  are parameters taking into account the orientation of the CSL misori-

$\Sigma$	Alumina							$\Sigma$	Zirconia						
	$f_{M\Sigma_{A1}}$	$f_{M\Sigma_{A2}}$	$f_{M\Sigma_{1550}}$	$f_{M\Sigma_{A3}}$	$f_{M\Sigma_{A4}}$	$f_{M\Sigma_{1700}}$	$f_{S\Sigma}$		$f_{M\Sigma_{Z1}}$	$f_{M\Sigma_{Z2}}$	$f_{M\Sigma_{1550}}$	$f_{M\Sigma_{Z3}}$	$f_{M\Sigma_{Z4}}$	$f_{M\Sigma_{1700}}$	$f_{S\Sigma}$
3	0.49	0.79	0.64	0.65	0.69	0.67	0.09	3	1.89	2.00	1.97	1.74	1.91	1.82	1.54
7 <sub>1</sub>	0.06	0.04	0.05	0.05	0.16	0.10	0.05	5	1.49	1.59	1.56	1.03	1.75	1.38	1.08
7 <sub>2</sub>	0.04	0.07	0.05	0.05	0.11	0.08	0.06	7	0.86	0.83	0.84	1.11	0.58	0.85	0.85
7 <sub>3</sub>	0.41	0.31	0.36	0.70	0.58	0.64	0.31	9	1.10	1.10	1.10	0.79	1.08	0.93	0.87
8	0.13	0.22	0.17	0.35	0.05	0.20	0.12	11	1.41	1.02	1.15	1.27	1.50	1.38	0.67
11 <sub>1</sub>	0.15	0.07	0.11	0.00	0.11	0.05	0.10	13 <sub>1</sub>	0.31	0.30	0.31	0.40	1.00	0.69	0.25
11 <sub>2</sub>	0.17	0.22	0.20	0.15	0.32	0.23	0.15	13 <sub>2</sub>	0.71	0.30	0.43	0.40	0.25	0.32	0.32
11 <sub>3</sub>	0.13	0.26	0.20	0.10	0.16	0.13	0.15	15	1.18	1.13	1.15	1.03	0.17	0.61	0.79
12	0.00	0.02	0.01	0.00	0.00	0.00	0.02	17 <sub>1</sub>	0.39	0.26	0.31	0.08	0.33	0.20	0.13
13 <sub>1</sub>	0.06	0.07	0.07	0.00	0.00	0.00	0.02	17 <sub>2</sub>	0.79	0.64	0.69	0.40	0.42	0.41	0.34
13 <sub>2</sub>	0.15	0.18	0.16	0.10	0.11	0.10	0.12	19 <sub>1</sub>	0.39	0.26	0.31	0.16	0.50	0.32	0.26
13 <sub>3</sub>	0.06	0.02	0.04	0.05	0.05	0.05	0.01	19 <sub>2</sub>	0.24	0.23	0.23	0.16	0.25	0.20	0.18
13 <sub>4</sub>	0.13	0.15	0.14	0.25	0.11	0.18	0.12	21 <sub>1</sub>	0.16	0.26	0.23	0.08	0.33	0.20	0.15
13 <sub>5</sub>	0.04	0.00	0.02	0.05	0.05	0.05	0.02	21 <sub>2</sub>	0.24	0.34	0.31	0.71	0.50	0.61	0.49
14 <sub>1</sub>	0.11	0.11	0.11	0.25	0.26	0.26	0.11	23	0.24	0.53	0.43	0.79	0.67	0.73	0.41
14 <sub>2</sub>	0.00	0.00	0.00	0.00	0.05	0.03	0.01	25 <sub>1</sub>	0.16	0.19	0.18	0.16	0.17	0.16	0.09
15 <sub>1</sub>	0.11	0.09	0.10	0.05	0.21	0.13	0.05	25 <sub>2</sub>	0.16	0.61	0.46	0.24	0.42	0.32	0.37
15 <sub>2</sub>	0.00	0.04	0.02	0.00	0.05	0.03	0.05	27 <sub>1</sub>	0.31	0.19	0.23	0.32	0.25	0.28	0.15
17 <sub>1</sub>	0.17	0.07	0.12	0.10	0.05	0.08	0.08	27 <sub>2</sub>	0.47	0.53	0.51	0.47	0.33	0.41	0.33
17 <sub>2</sub>	0.04	0.09	0.07	0.05	0.05	0.05	0.04	29 <sub>1</sub>	0.16	0.11	0.13	0.16	0.08	0.12	0.04
17 <sub>3</sub>	0.11	0.09	0.10	0.10	0.21	0.16	0.07	29 <sub>2</sub>	0.00	0.42	0.28	0.47	0.33	0.41	0.29
17 <sub>4</sub>	0.00	0.02	0.01	0.00	0.00	0.00	0.02	31 <sub>1</sub>	0.16	0.23	0.20	0.16	0.08	0.12	0.07
18	0.00	0.02	0.01	0.05	0.00	0.03	0.03	31 <sub>2</sub>	0.55	0.42	0.46	0.47	0.17	0.32	0.28
19 <sub>1</sub>	0.00	0.00	0.00	0.05	0.00	0.03	0.01	33 <sub>1</sub>	0.08	0.11	0.10	0.24	0.75	0.49	0.14
19 <sub>2</sub>	0.11	0.13	0.12	0.10	0.05	0.08	0.06	33 <sub>2</sub>	0.39	0.30	0.33	0.40	0.33	0.36	0.25
19 <sub>3</sub>	0.00	0.04	0.02	0.15	0.05	0.10	0.02	33 <sub>3</sub>	0.39	0.08	0.18	0.08	0.17	0.12	0.12
19 <sub>4</sub>	0.06	0.02	0.04	0.05	0.05	0.05	0.03	35 <sub>1</sub>	0.31	0.30	0.31	0.32	0.25	0.28	0.23
20 <sub>1</sub>	0.11	0.18	0.14	0.05	0.11	0.08	0.07	35 <sub>2</sub>	0.31	0.38	0.36	0.08	0.25	0.16	0.24
20 <sub>2</sub>	0.00	0.02	0.01	0.00	0.00	0.00	0.01	37 <sub>1</sub>	0.16	0.08	0.10	0.08	0.08	0.08	0.01
21 <sub>1</sub>	0.04	0.00	0.02	0.05	0.05	0.05	0.01	37 <sub>2</sub>	0.31	0.11	0.18	0.16	0.25	0.20	0.21
21 <sub>2</sub>	0.13	0.02	0.08	0.10	0.05	0.08	0.06	37 <sub>3</sub>	0.39	0.19	0.26	0.08	0.25	0.16	0.03
21 <sub>3</sub>	0.00	0.02	0.01	0.00	0.00	0.00	0.01	39 <sub>1</sub>	0.08	0.15	0.13	0.16	0.08	0.12	0.02
22 <sub>1</sub>	0.06	0.07	0.07	0.30	0.05	0.18	0.06	39 <sub>2</sub>	0.31	0.49	0.43	0.40	0.25	0.32	0.39
22 <sub>2</sub>	0.00	0.00	0.00	0.00	0.00	0.00	0.00	41 <sub>1</sub>	0.08	0.04	0.05	0.08	0.17	0.12	0.04
23 <sub>1</sub>	0.02	0.00	0.01	0.00	0.05	0.03	0.01	41 <sub>2</sub>	0.31	0.19	0.23	0.32	0.08	0.20	0.17
23 <sub>2</sub>	0.04	0.07	0.05	0.05	0.00	0.03	0.02	41 <sub>3</sub>	0.00	0.04	0.03	0.00	0.25	0.12	0.05
23 <sub>3</sub>	0.02	0.04	0.03	0.05	0.05	0.05	0.06	43 <sub>1</sub>	0.00	0.08	0.05	0.00	0.00	0.00	0.03
23 <sub>4</sub>	0.09	0.09	0.09	0.05	0.16	0.10	0.04	43 <sub>2</sub>	0.24	0.23	0.23	0.08	0.17	0.12	0.17
23 <sub>5</sub>	0.09	0.04	0.06	0.00	0.11	0.05	0.06	43 <sub>3</sub>	0.08	0.11	0.10	0.16	0.25	0.20	0.09
24	0.06	0.00	0.03	0.00	0.00	0.00	0.03	45 <sub>1</sub>	0.00	0.19	0.13	0.16	0.08	0.12	0.18
25 <sub>1</sub>	0.04	0.00	0.02	0.00	0.00	0.00	0.01	45 <sub>2</sub>	0.31	0.23	0.26	0.24	0.08	0.16	0.16
25 <sub>2</sub>	0.09	0.13	0.11	0.05	0.11	0.08	0.05	45 <sub>3</sub>	0.16	0.11	0.13	0.24	0.42	0.32	0.17
25 <sub>3</sub>	0.02	0.02	0.02	0.00	0.05	0.03	0.01	47 <sub>1</sub>	0.08	0.11	0.10	0.08	0.25	0.16	0.16
26	0.00	0.07	0.03	0.00	0.05	0.03	0.05	47 <sub>2</sub>	0.08	0.15	0.13	0.00	0.00	0.00	0.14
27 <sub>1</sub>	0.00	0.09	0.04	0.05	0.00	0.03	0.05	49 <sub>1</sub>	0.08	0.08	0.08	0.00	0.00	0.00	0.00
27 <sub>2</sub>	0.00	0.07	0.03	0.10	0.00	0.05	0.04	49 <sub>2</sub>	0.08	0.26	0.20	0.24	0.08	0.16	0.13
27 <sub>3</sub>	0.06	0.00	0.03	0.00	0.16	0.08	0.04	49 <sub>3</sub>	0.16	0.34	0.28	0.00	0.25	0.12	0.13
28 <sub>1</sub>	0.06	0.09	0.08	0.00	0.00	0.00	0.04								
28 <sub>2</sub>	0.06	0.04	0.05	0.00	0.00	0.00	0.04								
Total	3.75	4.21	3.98	4.33	4.55	4.44	2.67		17.75	17.85	17.82	16.14	17.79	16.94	13.23

**Table 5.4**  $\Sigma$  number fractions (%) of the total GB's for the individual and average samples, as well as for the simulated random models. For each individual sample, the values are obtained by averaging the fractions of CSL GB's over three EBSD scans (scans 2, 3 and 4). The values of the average samples are calculated by summing all CSL GB's occurring in the same material for a given sintering temperature.

entation axis relative to the crystal rotation axis and  $\Delta\theta$  is the angle given by the Brandon criterion. The calculation of  $f_{\Sigma}^c$  is complicated by the  $c/a$  dependence of the CSL. Therefore, only the calculated frequencies of the common (unspecific) CSL misorientations are presented (Table 5.3). They are all larger than the fractions  $f_{\Sigma}^s$  obtained from the present 2D random model, an observation already made for the cubic system (GARBAZ & GRABSKI 1993). The details and the full set of results will be presented in a forthcoming paper.

The good correspondence between the calculated and simulated values for both alumina and zirconia is an indication that our simulated random CSL GB distributions are reliable.

### 5.3.3.2 CSL grain boundary distributions in measurements and simulated models

#### Alumina

In alumina the total number fraction of CSL GB's is  $3.98 \pm 0.2\%$  for the average sample sintered at  $1550^\circ\text{C}$  and  $4.44 \pm 0.1\%$  for the one sintered at  $1700^\circ\text{C}$  (Table 5.4). These values are significantly higher than the number fraction of CSL GB's for the simulated random model, i.e. 2.67%. The GB character distribution (Fig. 5.7a) shows a predominance of  $\Sigma 3$  GB's in the measured samples. The other CSL GB's, however, also contribute to the differences between the measurements and the spatial model, as shown by the relative difference parameter  $\eta$ :

$$\eta = \frac{f_{\Sigma}^m - f_{\Sigma}^s}{f_{\Sigma}^s} \cdot 100 \quad (\text{Eq. 5.4})$$

where  $f_{\Sigma}^m$  and  $f_{\Sigma}^s$  are the  $\Sigma$  number fractions relative to the total number of GB's for the measured average samples and simulated random models, respectively. To avoid bias due to insufficient GB sampling, calculations according to Eq. 5.4 was limited to CSL GB's for which  $f_{\Sigma}^m > 0.1\%$ .

For the alumina samples sintered at  $1550^\circ\text{C}$ , all except one of the  $f_{\Sigma}^m$ 's are larger than the  $f_{\Sigma}^s$ 's (relative difference  $\eta > 0$ ) (Fig. 5.8a). However,  $\eta$  is, for most GB's less than the  $1-\sigma$  error calculated from counting statistics. The largest difference is for the  $\Sigma 3$  GB fraction. In the literature, high  $\Sigma 3$  number fractions are also reported for REE-doped alumina samples characterized by very weak textures (LARTIGUE & PRIESTER 1988, CHO et al. 2002) and for alumina produced by

gel-casting (WEI et al. 2005). In this latter study, the idiomorphic and platelet morphology (normal to the [0001] axis) of the initial particles, which were deposited in an oriented manner onto a substrate, was interpreted to be responsible for the increased concentration of  $\Sigma 3$  GB's, for which the [0001] axis is the misorientation axis. The starting powder used in the present investigation also consists of platelet-shaped crystallites (s. Fig. 5.1a) and the pressure applied during the manufacturing of the green bodies might, therefore, explain the increase in  $\Sigma 3$  GB's.

For the alumina samples sintered at  $1700^\circ\text{C}$ , more than 80% of the  $f_{\Sigma}^m$ 's are larger than the  $f_{\Sigma}^s$ 's. Two thirds of them show a relative difference  $\eta > 100\%$ , with again a high  $\Sigma 3$  number fraction. The deviation relative to the random model is, therefore, statistically significant.

About 65% of the CSL misorientations for which  $f_{\Sigma}^m$  is  $> 0.1\%$  in one or two of the samples show an increase relative to the samples sintered at the lower temperature, i.e. the relative difference  $\xi$ , defined as follows, is larger than 0:

$$\xi = \frac{f_{\Sigma}^m_{1700} - f_{\Sigma}^m_{1550}}{f_{\Sigma}^m_{1550}} \cdot 100 \quad (\text{Eq. 5.5})$$

where  $f_{\Sigma}^m_{1550}$  and  $f_{\Sigma}^m_{1700}$  are the measured  $\Sigma$  number fractions relative to the total number of GB's for the average samples sintered at  $1550^\circ\text{C}$  and  $1700^\circ\text{C}$ , respectively. Increase or decrease of the amount of CSL GB's with sintering temperature seems to be crystallographically controlled. The fractions of CSL misorientations with rotation axes parallel or slightly inclined with respect to the basal plane, i.e. normal to the [0001] axis, decrease with temperature, whereas the misorientations with rotation axes normal to the basal plane, i.e. parallel to the [0001] axis, increase (Fig. 5.9). This may be explained by the anisotropy of physical parameters that influence grain growth, such as GB mobility. Prism faces (parallel to the [0001] axis) tend to move faster (along the [2-1-10] axis) than the basal planes (along the [0001] axis) (SCOTT et al. 2002). Therefore, the surface ratio  $S_{\text{prism}}/S_{\text{basal}}$  decreases with increasing grain size, whereas the number fraction ratio  $f_{\text{prism}}/f_{\text{basal}}$  increases. As GB planes for grain misorientations with the CSL misorientation axes parallel to the [0001] axis are likely to be also parallel to the [0001] axis, the  $\Sigma$  number fraction of such GB's is expected to increase, as observed.

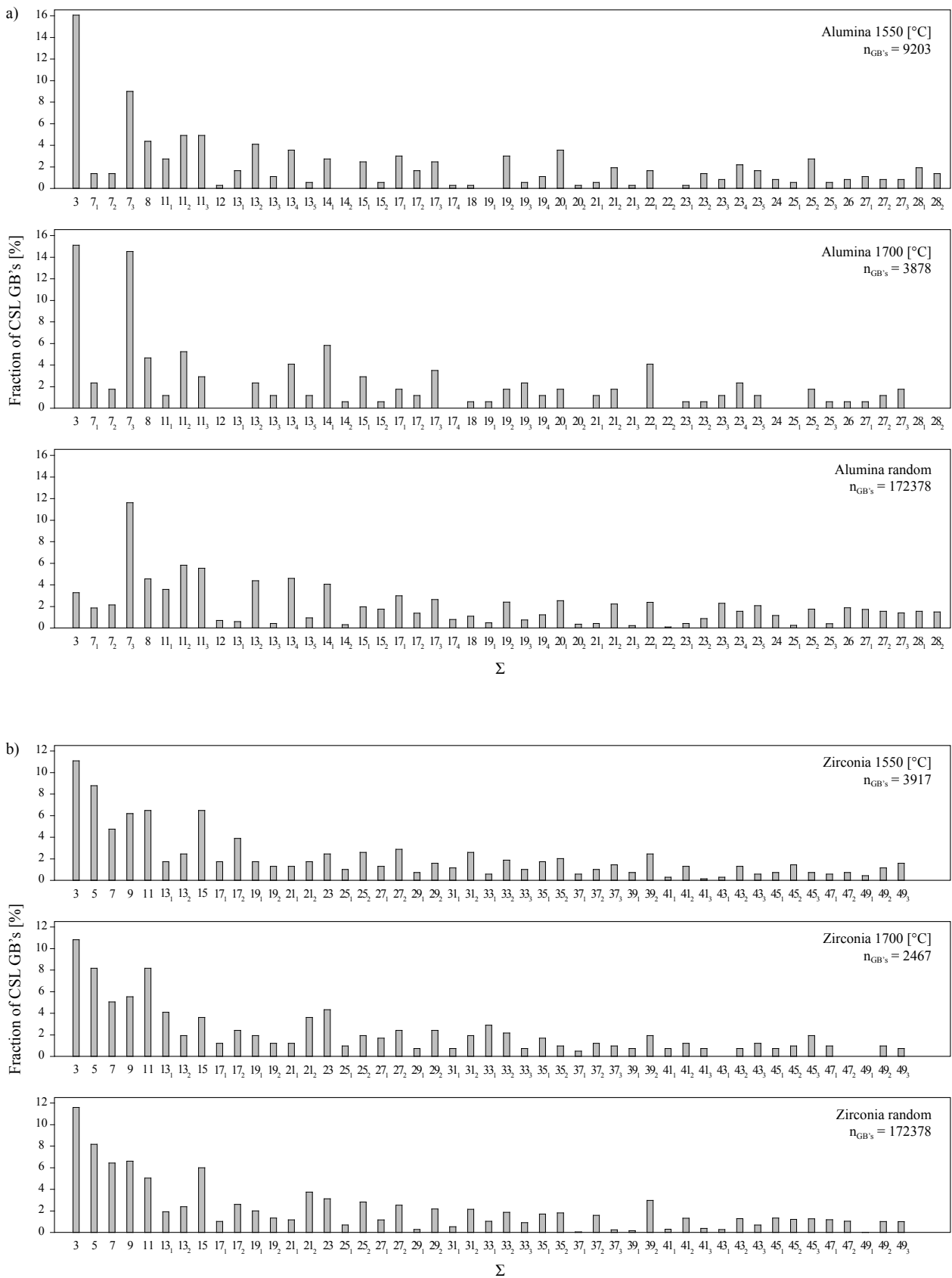


**Fig. 5.7** GB character distribution in (a) alumina ( $\Sigma 3$ - $\Sigma 28$ ) and (b) zirconia ( $\Sigma 3$ - $\Sigma 49$ ) for the two different sintering temperatures, as well as for the random spatial models;  $n_{GB's}$  = total number of GB's (CSL and non-CSL).

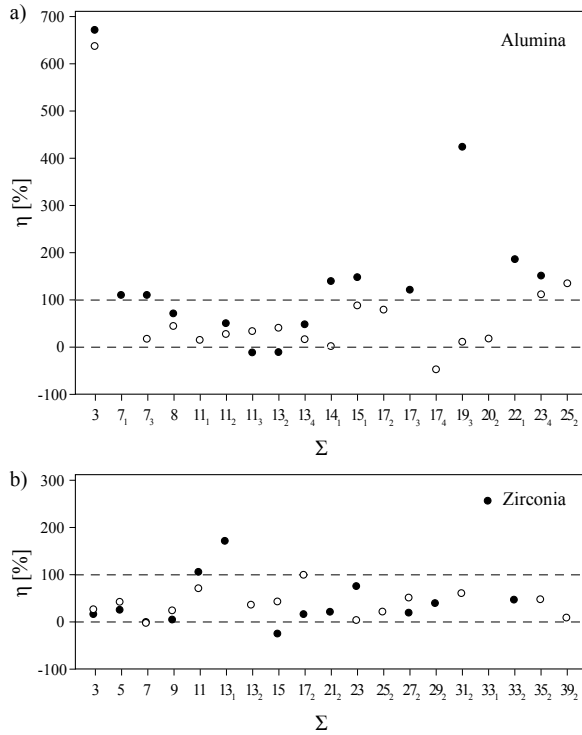


**Fig. 5.8** Relative difference  $\eta$  for CSL GB's in (a) alumina and (b) zirconia sintered at 1550°C (open circles) and 1700°C (full circles). Only the  $\Sigma$  values for which  $f_M \Sigma > 0.1\%$  are presented.  $\eta = 0$  indicates that the proportions of CSL GB's in the measured samples and in the models are equal.  $\Sigma$  values with  $\eta > 100\%$  are mainly observed for high sintering temperature.

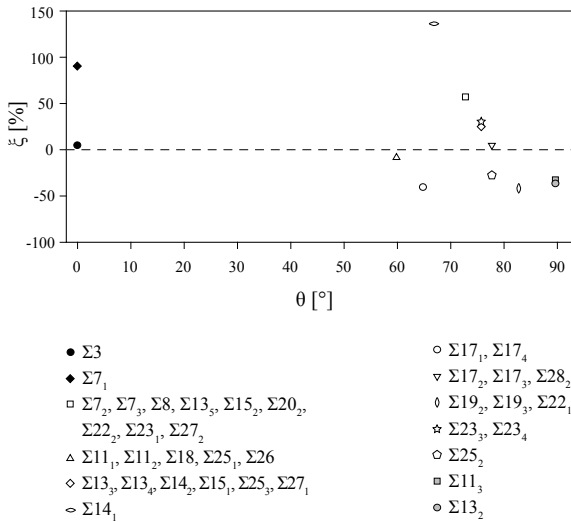


**Fig. 5.9** Plot of the relative difference  $\xi$  vs the angle  $\theta$  between [0001] and the CSL misorientation axis in alumina. Only data for which  $f_M \Sigma_{1550}$  and/or  $f_M \Sigma_{1700} > 0.1\%$  are considered. For the values with the misorientation axis parallel to [0001] ( $\theta = 0^\circ$ ),  $f_M \Sigma_{1700}$  is larger than  $f_M \Sigma_{1550}$  ( $\xi$  positive), whereas  $f_M \Sigma_{1700}$  is smaller than  $f_M \Sigma_{1550}$  ( $\xi$  negative) for all values with the misorientation axis normal or slightly inclined with respect to [0001] ( $\theta = 90^\circ$ ).  $\Sigma$  values for different c/a with the same misorientation axis and angle plus symmetrically equivalent  $\Sigma$  values were added together.

## Zirconia

Zirconia globally shows higher  $f_M \Sigma$ 's compared to alumina, as expected for a phase with cubic symmetry. The GB character distribution shows that the number fraction of CSL GB's decreases exponentially with increasing  $\Sigma$ , as predicted by the random 2D model (Fig. 5.7b). The total fractions of CSL GB's are very similar for both average samples, i.e.  $17.82\% \pm 0.1\%$  for the average sample sintered at 1550°C and  $16.94\% \pm 0.8\%$  for the one sintered at 1700°C (Table 5.4). These values are 4.59% and 3.71% higher than the total fraction of CSL GB's predicted from the random 2D model, even though the Kolmogorov-Smirnov test indicates that the measured distributions cannot be distinguished from the latter.

The relative difference  $\eta$  of three fourths of the CSL GB's (considering only  $f_M \Sigma > 0.1\%$ ) in zirconia (Fig. 5.8b) decreases with higher sintering temperature. None of the CSL GB's in the 1550°C average sample and only three in the 1700°C average sample ( $\Sigma 11$ ,  $\Sigma 13_1$  and  $\Sigma 33_1$ ) have number fractions that differ by more than 100% from the random model.

About 65% of the CSL misorientations for which  $f_M \Sigma$ 's is larger than 0.1% in one or two of the samples show a decrease relative to the samples sintered at the lower temperature ( $\xi$  negative, not presented), but only two show differences larger than 50%.

### 5.3.3.3 Triple junction character and prominence factors in zirconia

The number of CSL GB's in zirconia is a sizeable amount of the total number of GB's present in the samples, which increases the probability that two or three CSL GB's meet at a triple junction. In both average zirconia samples, the triple junction character, i.e. the fractions  $J_n$  of junctions with  $n$  CSL GB's ( $n = 0, 1, 2, 3$ ), fit relatively well with simulated triple junction distribution curves reported in the literature (MINICH et al. 2002). GB's meeting at a triple junction follow the misorientation conservation law, which states that the total misorientation around each triple junction has to be zero. In terms of the CSL theory, the general misorientation law becomes the sigma combination rule:

$$\Sigma a \cdot \Sigma b = m^2 \Sigma c \quad (\text{Eq. 5.6})$$

where the  $\Sigma$ -terms represent numerical  $\Sigma$ -values and  $m$  can be any common divisor of  $a$  and  $b$ .

SCHUH et al. (2005) have presented a generalized description of the GB character distribution for FCC metals based on these conservation laws. The microstructure of FCC metals with low to medium stacking fault energies is dominated by  $\Sigma 3$  GB's, which are the result of annealing twinning. The larger the number of  $\Sigma 3$  GB's in a microstructure the higher is the likelihood that two of them meet at a triple junction. The third GB is determined by the sigma combination rule and must be a  $\Sigma 9$  ( $m=1$ ) or a  $\Sigma 1$  ( $m=3$ ) GB. A  $\Sigma 3$  and  $\Sigma 9$  meeting at a triple junction fix the third GB to be a  $\Sigma 3$  ( $m=3$ ) or a  $\Sigma 27$  ( $m=1$ ). The number fractions of these GB's are thus related. The prominence of  $\Sigma 3$ ,  $\Sigma 9$  and  $\Sigma 27$  GB's may be expressed by so called *twin* prominence factors  $A_3$  and  $A_9$  (SCHUH et al. 2005):

$$A_3 = \frac{f\Sigma 3}{f\Sigma 3 + f\Sigma 9 + f\Sigma 27} \quad (\text{Eq. 5.7})$$

$$A_9 = \frac{f\Sigma 9}{f\Sigma 9 + f\Sigma 27} \quad (\text{Eq. 5.8})$$

with  $f\Sigma i$  representing the number fraction for  $\Sigma$  GB's of type  $i$ . As expected, these factors have similar values and for the samples analyzed by SCHUH et al. (2005) they are between 0.5 and 0.9, with a maximum at 0.75. Furthermore, in most samples  $A_3 \approx A_9$ , so that one parameter is sufficient to describe a large part of the CSL GB population.

Zirconia has also an FCC structure, but with high stacking fault energy, which explains its rather low CSL GB fraction (17.5%). This value is at the lower end of the range investigated by SCHUH et al. (2005). The prominence factors calculated both for the zirconia average samples ( $A_{3,1550} = 0.52$ ,  $A_{3,1700} = 0.53$ ,  $A_{9,1550} = 0.60$ ,  $A_{9,1700} = 0.57$ ) and for the simulated random model ( $A_{3,s} = 0.53$ ,  $A_{9,s} = 0.64$ ) fall in the range given for FCC metals. Therefore, the limit of 0.5 given by SCHUH et al. (2005) might be a too small lower bound for the twin prominence factors in FCC metals and the range given by GERTSMAN & TANGRI (1995) and PALUMBO et al. (1992) are probably more appropriate to describe microstructures dominated by annealing twinning.

Parameters similar to the twin prominence factors may be used to visualize differences between the measured and a random CSL GB distribution. For CSL GB triplets related by the function

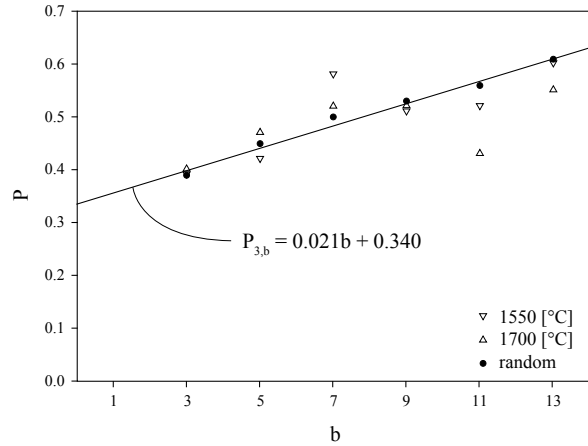


Fig. 5.10 Linear dependence of the general prominence factor  $P$  as a function of parameter  $b$  in zirconia.

$$\Sigma 3 \cdot \Sigma b = \Sigma c \quad (\text{Eq. 5.9})$$

the following *general* prominence factor  $P$  is linearly dependent on  $b$  for values up to  $b=13$ :

$$P_{3,b} = \frac{f\Sigma 3}{f\Sigma 3 + f\Sigma b + f\Sigma c} \quad (\text{Eq. 5.10})$$

$$P_{3,b} = 0.021b + 0.340 \quad (\text{Eq. 5.11})$$

The linear dependence resulting from Eq. 5.11 is a consequence of the symmetry relationships between such triplets. This equation describes over 70% of the CSL GB's up to  $\Sigma 39$ . The values of  $P_{3,b}$  for both average samples are very close to the theoretical values except  $P_{3,7}$  for the samples sintered at 1550°C and  $P_{3,11}$  for the samples sintered at 1700°C (Fig. 5.10). A more in depth presentation will be given in a forthcoming paper.

## 5.4 CONCLUSIONS

In this paper the grain misorientation and CSL GB distributions in texture-free alumina and zirconia ceramics sintered at two different temperatures were presented and compared with simulated random 2D models. The main points are the following:

- (1) The grain misorientation distribution for alumina show relative maxima at 50°, 60°, and between 82.5° and 92.5° for both sintering temperatures,

whereas no relative maxima are observed for zirconia. The maxima and minima in the misorientation distribution are present in all alumina samples independent on the sintering temperature and are most likely due to properties of the starting powders and green body manufacturing processes. This has to be considered when comparing GB character dependencies.

(2) 2D models for random CSL GB distributions were calculated for microstructures consisting of cubic and trigonal phases. They may serve as reference for the interpretation of EBSD results.

(3) The total number fractions of CSL GB's for both alumina and zirconia are significantly higher in the measurements than in the simulated models. In alumina, this feature is particularly obvious for  $\Sigma 3$ , even though most CSL GB's contribute to the trend. Relative difference over 100% is predominant in the samples sintered at the high temperature. It has been

shown that the increase or decrease of the amount of CSL GB's with sintering temperature is crystallographically controlled and dependent on the orientation of the CSL misorientation axis with respect to the [0001] axis.

(4) The twin prominence factors  $A_3$  and  $A_9$  both for the zirconia average samples and the simulated random model are within the lower and upper bounds defined by SCHUH et al. (2005) for FCC metals, i.e. 0.5 and 0.9. This suggests that the lower limit of 0.5 might be too small to characterize the twin prominence factors in FCC metals.

(5) A general (non-twin dependent) prominence factor has been proposed for FCC-materials. This parameter shows, for the random case, a linear relationship with  $\Sigma$ , which could be used as a very simple criterion to determine the randomness of CSL GB distribution in FCC-type materials.

\*\*\*\*\*



## 6 - PERSPECTIVES

---

Because of the very diverse nature of the topics treated in the three case studies, extracting a general conclusion valid for all these investigation fields is unrealistic. Instead of harking back to the conclusive remarks presented at the end of each chapter, the text below rather focuses on some possible perspectives for further research.

### 6.1 CASE STUDY 1

The orientation of anisotropy in the uppermost mantle lithosphere of slow-spreading ridge environments is a debated and often oversimplified issue. Up to now, it is not clear whether the vertical fabric inherited from the ridge may be preserved at very large distances, nor how fast this original fabric might be reoriented, e.g. in response to plastic flow in reheated mantle environments or due to regional tectonics. In a novel seismic refraction survey in the western Atlantic, GAHERTY et al. (2004) put forward that the maximum P-wave velocity in the upper 10 km of mantle lithosphere formed at slow spreading ridges is parallel to the spreading direction, a conclusion which corroborates our orientation choice. In order to better constrain the orientation of anisotropy in the first kilometers of the uppermost mantle, investigations on orientated samples are necessary. Unfortunately, no oceanic upper mantle terrane crops out above the Atlantic Ocean. The upper mantle section of the islets of São Pedro e Paulo, far off the Brazilian coast is interpreted as a relict of sub-continental mantle (BONATTI 1990) and thus, it is of little interest for our purpose. Tens of oceanic upper mantle peridotites, however, have been sampled during the Ocean Drilling Program (ODP), either from oceanic core complexes directly bordering the Mid-Atlantic ridge or from uplifted mantle ter-

ranes located at farther distance from the ridge. Some of these samples have been used already for general structural investigations (e.g. SCHROEDER & JOHN 2004, BLACKMAN et al. 2006); to our knowledge, however, no EBSD studies have been carried out based on the oceanic upper mantle peridotites from the ODP. Even though most of the samples are strongly serpentinized, they represent a unique opportunity to study orientated oceanic upper mantle peridotites generated at slow spreading ridges and to better constrain the dynamic of the lithosphere.

### 6.2 CASE STUDY 2

The snowball garnets from the Lukmanier Pass area have provided very promising results giving new pieces of evidence which may help to solve the controversies around snowball garnet growth. EBSD maps have shown unexpected results indicating the polycrystalline nature of the spirals. Little has been said, however, about the crystallographic relationship between the different segment-shaped grains of the spirals and between those grains and the core region. Preliminary observation seems to indicate that at least some of the grains forming the spiral are related through rotations around a unique axis. Further research on a larger sample population is necessary to determine if this trend is confirmed and, if yes, to understand the mechanisms involved. Mathematical algorithms have been developed with this in view by our collaborators from the Department of Mathematics. They should allow us to calculate the common rotation axis from the crystallographic orientation of the individual grains.

One could easily imagine that the garnet grains which have grown at the ends of the spiral arms have

conserved a preferred crystallographic orientation inherited from the parent mica lattice. TEM analyses are planned to compare the crystallographic orientations of mica and garnet and to deduce possible topotaxial relationships. Finally, in order to better understand the growth mechanism of the garnets, visualization of the grain distribution in 3D is necessary. Serial sectioning of spiral garnets and further EBSD analysis are envisaged.

### 6.3 CASE STUDY 3

The analysis of grain misorientation and CSL GB distributions has led to a very extensive characterization of our alumina and zirconia ceramics. Further research could take advantage of these well characterized samples to investigate the influence of individual GB's on ceramic properties. Among the wealth of possible investigation fields, GB diffusion and particularly the GB diffusion of metals through the ceramic bodies is of particular interest. Ceramic parts coated with a thin metallic layer of a few nm are used in applications such as, for example, the central monolith pieces of catalytic converters, which consist of honeycomb alumina or cordierite ceramics coated by platinum, rhodium and palladium. These metals are used as catalysts to favour the redox reactions necessary to trans-

form toxic molecules in less harmful ones. One of the undesirable aspects of this kind of materials, though, is the diffusion (mainly along GB's) of metal through the ceramics. This process may arise either during the processing of the product, or it is simply the consequence of ageing when the material is used at relatively high temperature. In this latter case, a progressive loss of the ceramic properties may be observed (e.g. SERIER et al. 1993). Consequently, avoiding or at least slowing down the diffusion of metals through the material is clearly of economic interest for the ceramic industry, besides being an environmental issue as well. This may be achieved by GB engineering, i.e. by producing microstructure with a high fraction of GB with small diffusion coefficients.

The structure and type of GB's (in terms of CSL) have a significant influence on the rate of GB diffusion (e.g. KAUR et al. 1995). However, data available in the literature for ceramics are often restricted to average values. Further research would involve diffusion experiments and analyses based on two main techniques: (1) glow discharge optical electron spectroscopy (GD-OES; DELFOSSE & AEBERHARD 1997) to measure the diffusion profiles inside the ceramics and (2) analytical electron microscopy (AEM; KOHLSTEDT 1990) to investigate the distribution of metal in individual GB's. Significant advances may be expected with possible applications in GB engineering.

\*\*\*\*\*

# I - APPENDIX OF CASE STUDY 1

## I.1 CHEMISTRY AND CRYSTAL STRUCTURE OF PERIDOTITE MINERALS

The chemistry and crystallography of the upper mantle minerals olivine, ortho- and clinopyroxene are summarized below. Most concepts and figures are based on the reference book *An Introduction to the Rock-forming Minerals* (DEER et al. 1992).

### I.1.1 Olivine

Olivine is the dominating mineral in the uppermost part of the mantle and designates the continuous solid solution between the end-members forsterite ( $\text{Mg}_2\text{SiO}_4$ ) and fayalite ( $\text{Fe}_2\text{SiO}_4$ ). Only Mg-rich members (typically  $\text{Fo}_{87-96}$ ) are present in peridotite rocks. A limited substitution of Mg/Fe cations by Mn or Ca is commonly observed in natural olivine. However, the corresponding pure end-members tephroite ( $\text{Mn}_2\text{SiO}_4$ ), monticellite ( $\text{CaMgSiO}_4$ ) and kirschsteinite ( $\text{CaFeSiO}_4$ ) are very rare in nature.

Olivine belongs to the nesosilicate group and crystallizes with the orthorhombic space group symmetry Pbnm. The structure consists of individual  $\text{SiO}_4$  tetrahedra which cross-link chains of octahedrally coordinated M-cations (Mg, Fe) (Fig. I.1). Half of them, known as  $M_1$ , are located at centers of symmetry, whereas the other half, called  $M_2$ , are located on reflection planes. Alternatively, the olivine structure can be described as a slightly distorted hexagonal closed-packing of oxygen atoms in which one-eighth of the tetrahedral and half of the octahedral interstices are filled.

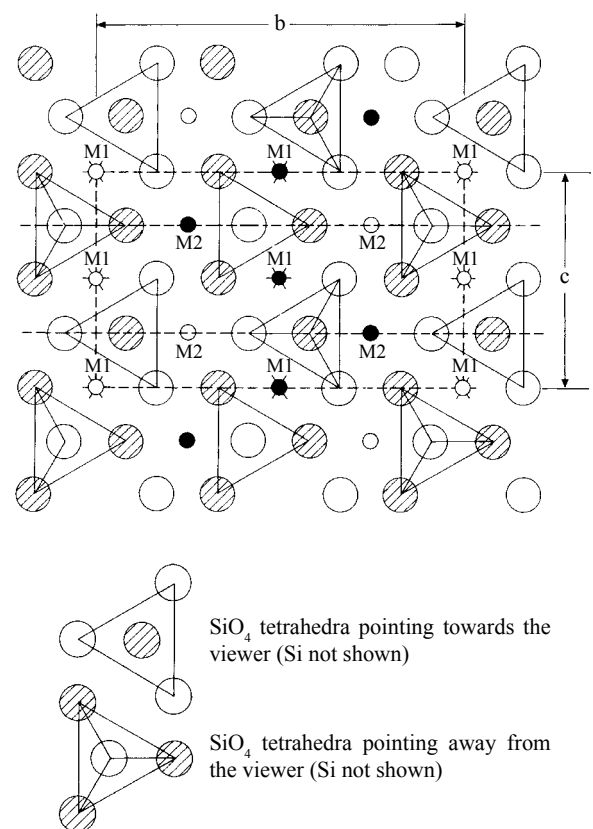


**Fig. I.1** [100] axis projection of an idealized olivine structure. Small open circles are M atoms at  $x = 0$ ; small solid circles are M atoms at  $x = 1/2$ ;  $M_1$  at centers of symmetry,  $M_2$  on reflection planes (after BRAGG & BROWN 1926).

The unit cell parameters of olivine increase almost linearly with the Fe content. Upper mantle olivine with a composition  $\text{Fo}_{90}$  has the following unit cell parameters of  $a = 4.76 \text{ \AA}$ ,  $b = 10.22 \text{ \AA}$  and  $c = 5.99 \text{ \AA}$  (Fig. I.2).

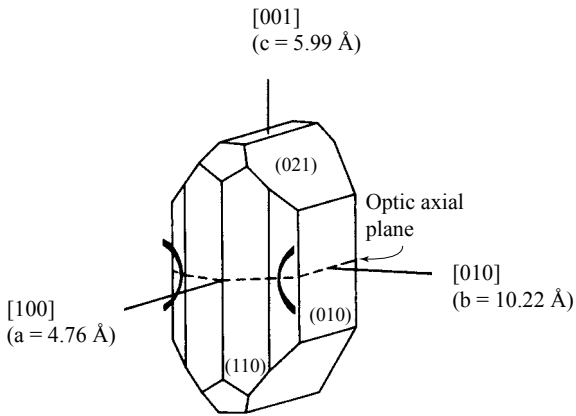


**Fig. I.2** Schematic illustration of a forsterite single crystal with the cell parameter values *a*, *b* and *c* in the [100], [010] and [001] directions, respectively (after DEER et al. 1992).

**I.1.2 Ortho- and clinopyroxene**

Ortho- and clinopyroxenes are the second most important constituents of peridotite rocks. Orthopyroxenes are members of the solid solution between the end-members enstatite ( $Mg_2Si_2O_6$ ) and ferrosilite ( $Fe_2Si_2O_6$ ), the Mg-rich members being the dominant pyroxene minerals in peridotite. Clinopyroxenes have a more variable chemistry. Most of them, however, can be considered as members

of the continuous solid-solution between diopside ( $CaMgSi_2O_6$ ) and hedenbergite ( $CaFeSi_2O_6$ ), with limited substitution of Ca by Mg and Fe, respectively Mg and Fe by Al (Fig. I.3). Of these, diopside, easily identified in hand specimen due to its bright green color, is relatively frequent in upper mantle rocks.

Both ortho- and clinopyroxenes are inosilicates, characterized by single chains of  $SiO_4$  tetrahedra parallel to the [001] axis (Fig. I.4). The chains are linked to each other by octahedral layers containing 6- or 8-coordinated cations (Fe, Mg, Ca, Na...), which occupy two different sites:  $M_1$ , lying between the apices of the  $SiO_4$  tetrahedra and  $M_2$ , lying between their bases. Whereas the large cations (Na, Ca, Li) always occupy the  $M_2$  sites, the smaller ones (Fe, Mg...) can be located on both the  $M_1$  and  $M_2$  sites.

Pyroxene is stiffer than olivine under common upper mantle P/T conditions. Because of the arrangement of tetrahedra in chains parallel to the [001] axis, dislocations glide in pyroxene is almost restricted to the (100)[001] system, even though minor slip in the [100] and [010] glide directions has also been observed (MERCIER 1985). The high bulk moduli of pyroxene minerals explain why deformation in peridotite rocks is preferentially accommodated by olivine rather than pyroxene.

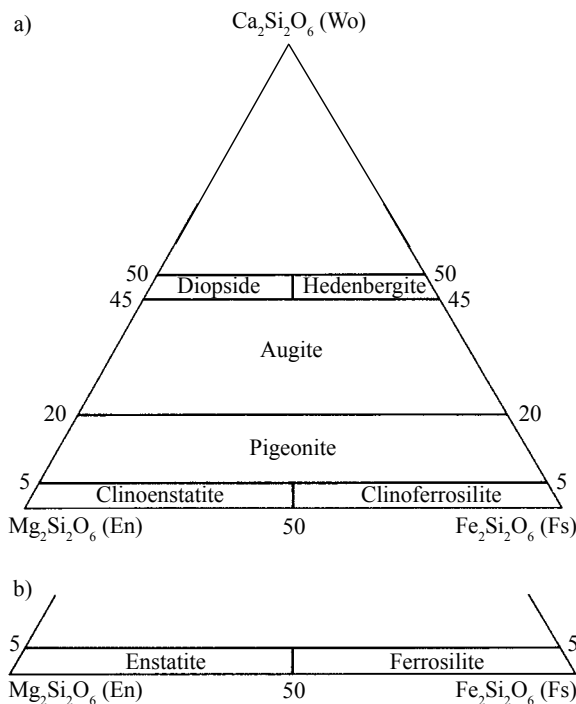


**Fig. I.3** Composition range and nomenclature of (a) the Ca-Mg-Fe clinopyroxenes, and (b) orthopyroxenes (after MORIMOTO 1988).

The cell parameters for enstatite (space group: Pbc<sub>a</sub>) range between *a* = 18.22-18.43 Å, *b* = 8.81-9.08 Å and *c* = 5.17-5.24 Å and for diopside (space group: C2/c) between *a* = 9.75-9.85 Å, *b* = 8.90-9.00 Å, *c* = ~5.3 Å and  $\beta$  = ~105° (Fig. I.5).

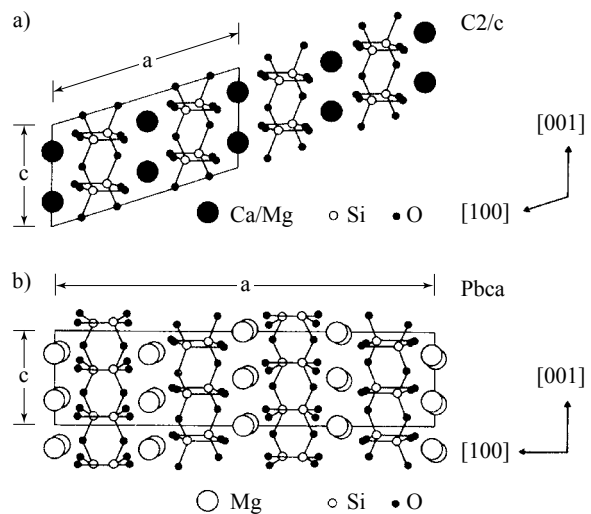


**Fig. I.4** Projection of the diopside (a) and enstatite (b) structures down the [010] axis (after ZUSSMAN 1968).

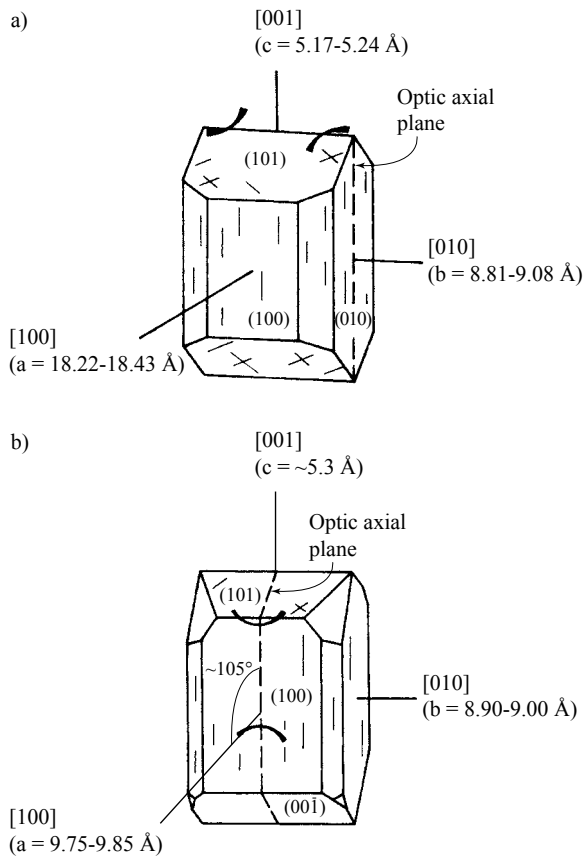


**Fig. 1.5** Schematic view of enstatite (a) and diopside (b) single crystals (after DEER et al. 1992).

## I.2 EBSD DATA

### I.2.1 Crystallographic files used for indexing

The crystallographic files used for the indexing of peridotite minerals are those developed by Karsten Kunze's group at the ETH Zürich (Switzerland). The lattice constants and reflections for olivine, orthopyroxene and clinopyroxene are shown in Table I.1.

It must be noted that the crystallographic parameters used to index clinopyroxene are the ones optimized by MAULER et al. (1998) for omphacite. However, they proved to be completely adequate to index diopside patterns as well, despite the slight crystallographic differences between both minerals. In this respect, the EBSD technique appears not to be very sensitive (s. also the comments of MAULER (2000)).

### I.2.2 List of EBSD runs

The list of EBSD runs for the twelve peridotite samples is shown in Table I.2.

	Olivine	Orthopyroxene	Clinopyroxene*
Space group	Pbnm	Pbca	C2/c
Lattice constants			
a [nm]	4.762	18.241	9.585
b [nm]	10.225	8.83	8.776
c [nm]	5.994	5.185	5.26
$\alpha$ [°]	90.0	90.0	90.0
$\beta$ [°]	90.0	90.0	106.85
$\gamma$ [°]	90.0	90.0	90.0
Reflectors (hkl)	0 1 1	4 2 0	1 1 0
	0 2 1	2 2 1	2 0 0
	1 0 1	3 2 1	1 1 -1
	1 1 1	6 1 0	0 2 0
	1 2 0	1 3 1	0 2 1
	0 0 2	2 0 2	-2 2 1
	0 3 1	5 2 1	3 1 0
	1 3 0	5 0 2	3 1 -1
	1 3 1	5 1 2	2 0 -2
	1 1 2	6 3 1	-1 3 1
	0 4 1	10 1 0	0 0 2
	2 1 0	2 5 0	2 2 1
	1 2 2	0 2 3	3 1 1
	1 4 0	12 0 0	1 1 2
	2 1 1	1 3 3	0 0 2
	2 4 1	0 6 0	-3 3 1
	0 6 1	11 0 2	4 2 -1
	1 3 3	11 3 1	0 4 1
	0 4 3	0 4 3	-4 0 2
	1 7 0	12 1 2	2 0 2
	3 2 2	1 0 4	1 3 -2
	3 4 0	14 5 0	2 4 -1
	4 0 0		4 2 -2
	1 9 2		5 1 0
			1 5 0
			-3 1 3
			2 2 -3
			-5 3 1
			-6 0 2
			-1 3 3
			4 0 2
			4 2 2
			-3 5 2
			5 3 1
			-7 1 2
			-3 1 4
			0 6 2
			3 5 2
			-6 0 4
			7 5 0

\* optimized for omphacite (MAULER et al. 1998)

**Table I.1** Lattice constants and reflectors used for the indexing of peridotite minerals.

Sample	Scan mode	Step size [ $\mu\text{m}$ ]	Area [ $\text{cm}^2$ ]	Measurements	Measurements with CI $\geq 0.2$	Average CI*	Phase [vol.%]			Approximate number of grains				LPO (J index**)
							Ol	Opx	Cpx	Ol	Opx	Cpx	Total	
PV01	stage scan	100	2.54	25696	12245 (47.7%)	0.23 (0.40)	76	20	4	182	116	37	335	7.11
PV04	stage scan	100	2.70	27336	19590 (71.7%)	0.34 (0.45)	95	2	3	314	12	24	350	8.60
PV05	stage scan	100	5.62	56776	41737 (73.5%)	0.36 (0.46)	84	13	3	296	94	60	450	12.01
PV06	stage scan	100	5.76	58256	38975 (66.9%)	0.33 (0.45)	81	17	2	297	70	30	397	16.73
PV08	stage scan	100	5.48	55266	41691 (75.4%)	0.37 (0.47)	81	19	1	262	119	15	396	12.25
LA2-4	stage scan	100	6.21	62586	43020 (68.7%)	0.33 (0.45)	69	30	1	411	203	24	638	16.46
LA6-1	stage scan	100	5.00	50406	34147 (67.7%)	0.34 (0.47)	83	16	1	2675	227	62	2964	5.56
LA6-16	stage scan	100	2.99	30261	19384 (64.1%)	0.31 (0.44)	93	1	6	296	3	59	358	3.80
LA6-19	stage scan	100	5.68	57316	43759 (76.3%)	0.40 (0.51)	100	0	0	1160	0	0	1160	4.83
LA6-35	stage scan	100	4.09	41396	29856 (72.1%)	0.36 (0.47)	75	24	1	2671	270	59	3000	9.96
LA8-4	stage scan	100	5.33	53856	35881 (66.6%)	0.32 (0.44)	82	15	3	567	132	16	715	11.27
LA8-7	stage scan	100	4.18	48546	35099 (72.3%)	0.37 (0.48)	90	8	2	4365	536	28	4932	2.90

\* in brackets the average CI considering only the values  $\geq 0.2$

\*\* calculated for olivine using the Unicef Careware software package of MAINPRICE (1990 & 1999) for an expansion coefficient of 22 and a Gaussian half width of 8.5°

**Table I.2** EBSD data for the twelve peridotite scans.

### I.2.3 Maps and texture plots

For each of the twelve peridotite xenoliths, phase and crystallographic orientation maps, as well as texture plots for olivine [100], [010] and [001] axes are presented. Following the common practice in earth sciences, the texture plots represent *lower* hemisphere equal area projections. However, as EDAX® (TSL) OIM Analysis 3.08 automatically creates upper hemisphere projections and does not allow to introduce lower hemisphere ones, the texture plots were obtained indirectly by flipping twice (180° horizontally and vertically) the raster images of the plots generated by the software. Contours are multiples of uniform distribution, assuming 0.5 intervals. In order to ensure an exact correspondence with the results of Chapter 3, the maximum densities of the LPO were calculated using the Unicef Careware software package of MAINPRICE (1990 & 1999). Spherical harmonics truncated at an expansion of 22 with a Gaussian half width of 8.5

were used for ODF calculations.

The legend and the layout of the peridotite maps and texture plots (Fig. I.7) are shown in Fig. I.6. All texture data are non-rotated with respect to external reference frames.

### I.3 DENSITY AND ELASTIC CONSTANTS

To calculate the seismic properties of rocks starting from the LPO, the density and elastic constants of rock-forming minerals have to be known for the pressure and temperature conditions prevailing in the xenolith source region. The density (Table I.3) was calculated according to Eq. 3.4, whereas the elastic constant calculation (Table I.4) is based on Eq. 3.5 (s. Section 3.4.2). A complete review of the method can be found also in MAINPRICE et al. (2000).

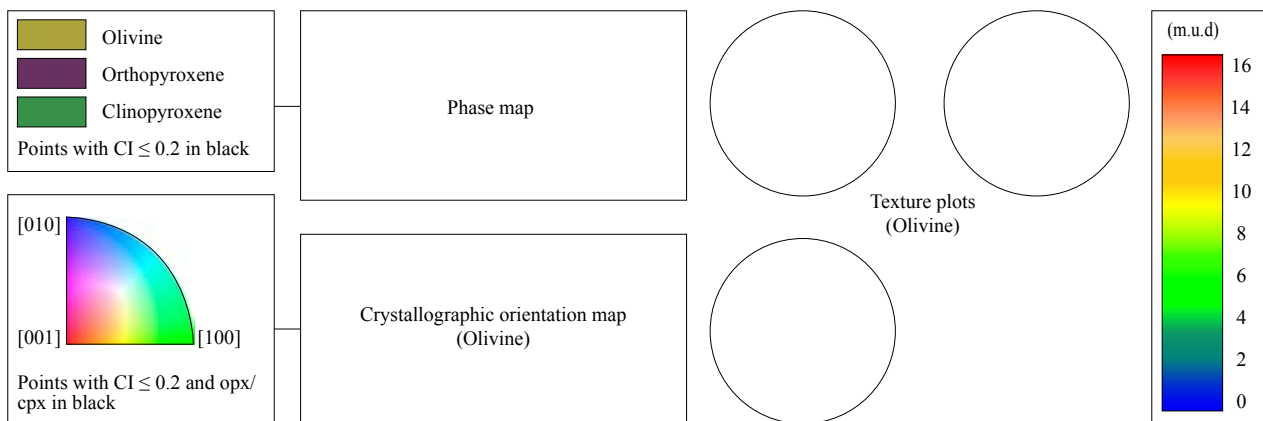


**Fig. I.6** Legend and layout for the peridotite maps and plots displayed in Fig. I.7.

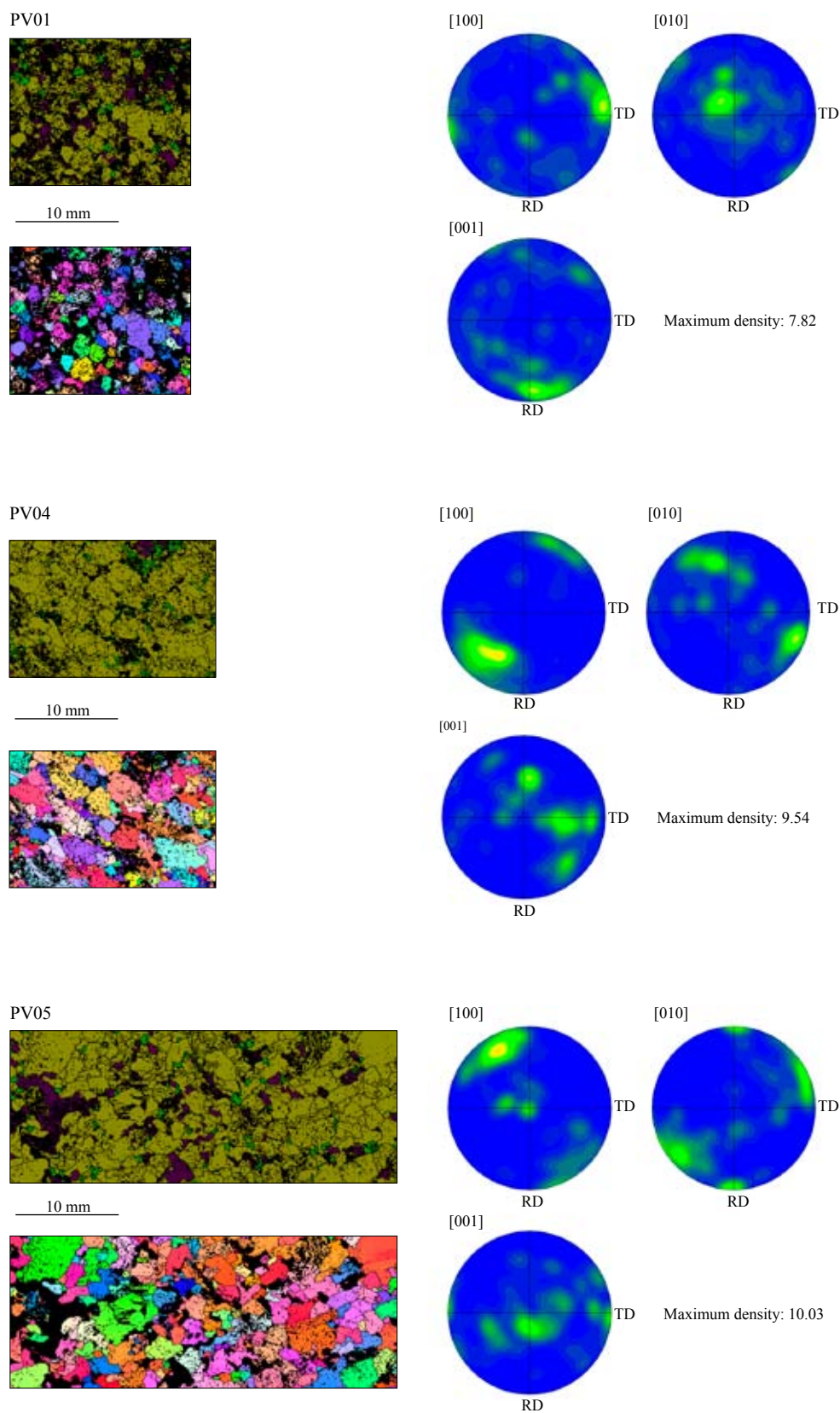
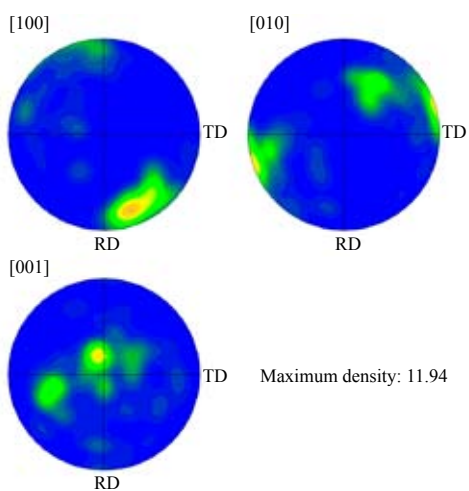
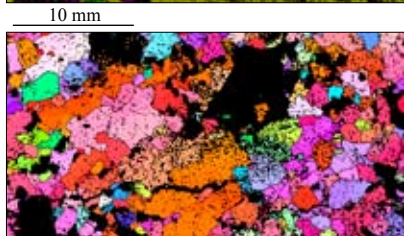
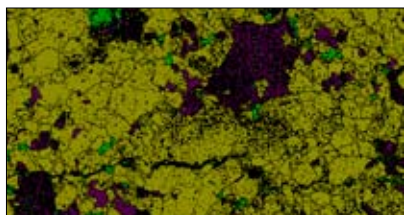
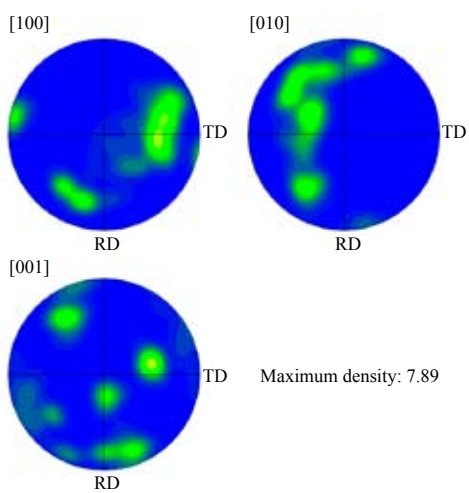
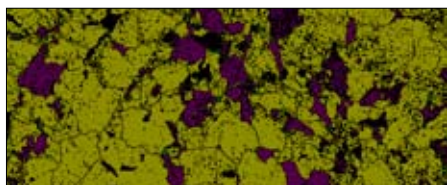


**Fig. I.7** Phase maps, crystallographic orientation maps and texture plots for olivine [100], [010] and [001] axes for the twelve Lanzo xenoliths (s. also next pages).

PV06



PV08



LA2-4

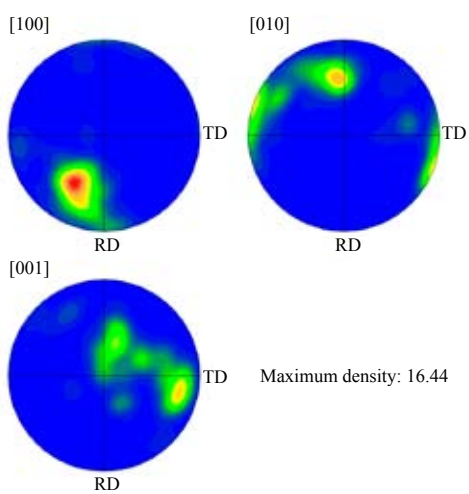
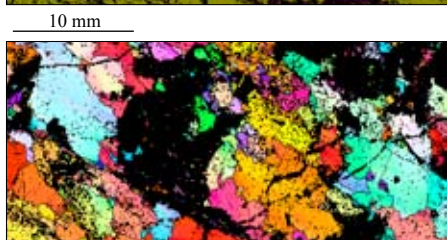
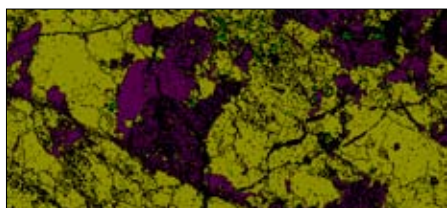
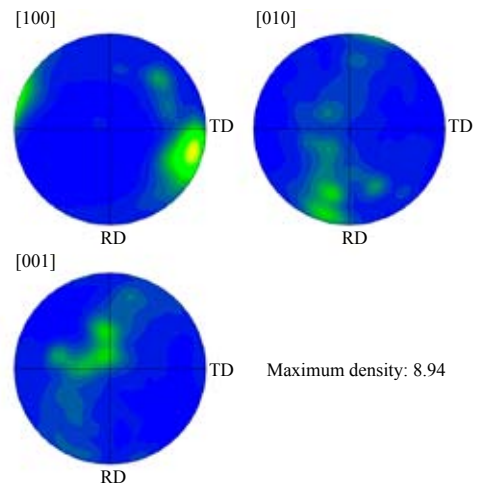
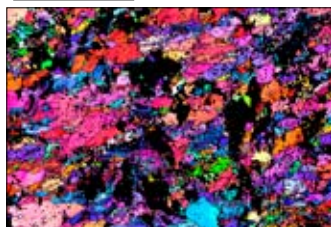
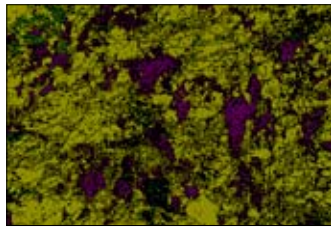
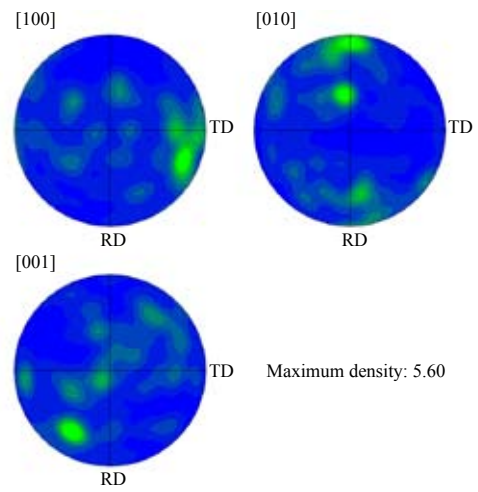
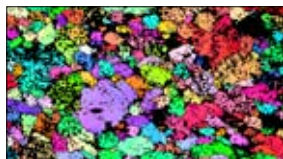
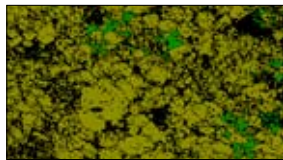


Fig. I.7 (continued).

LA6-1



LA6-16



LA6-19

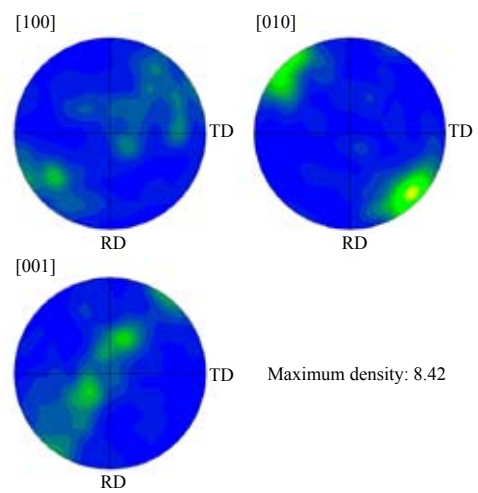
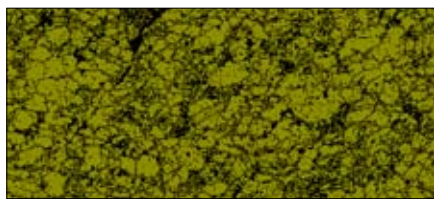
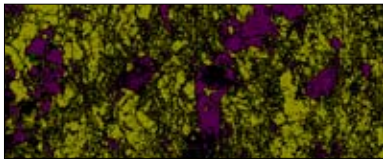
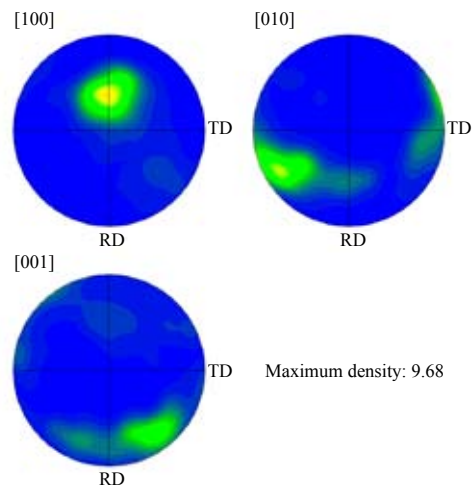
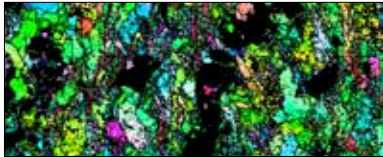


Fig. I.7 (continued).

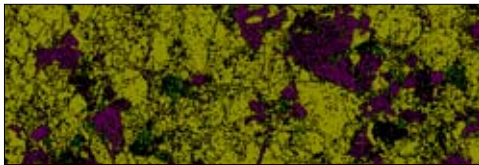
LA6-35



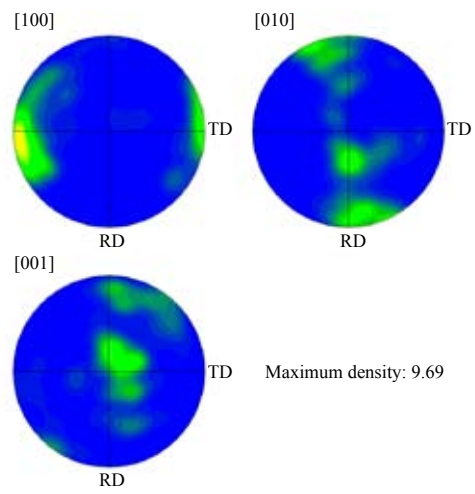
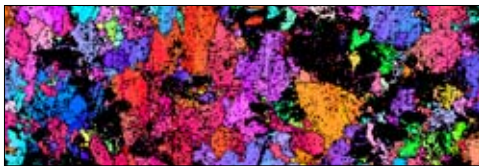
10 mm



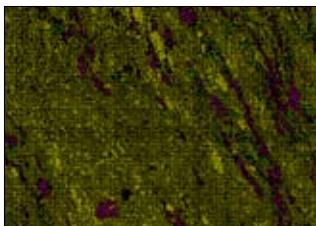
LA8-4



10 mm



LA8-7



10 mm

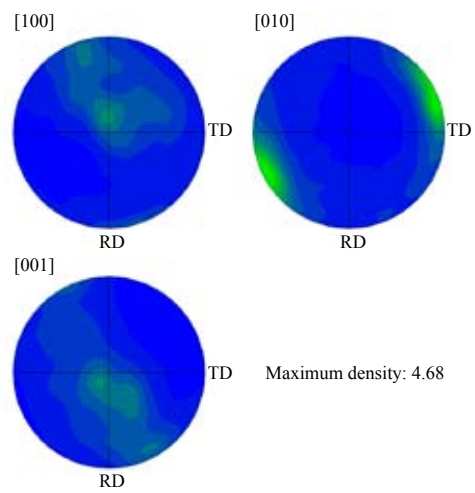
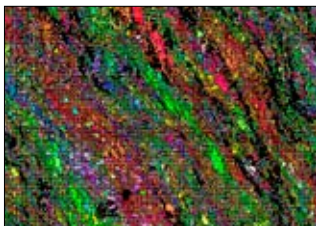


Fig. I.7 (continued).

	$\rho_0$ [g/cm <sup>3</sup> ]	K'	K [GPa]	$\alpha_{av}$ [°C <sup>-1</sup> ]	$\rho$ (PT) [g/cm <sup>3</sup> ]	$\rho$ (PT) [g/cm <sup>3</sup> ]	$\rho$ (PT) [g/cm <sup>3</sup> ]
					P=0.8 [GPa], T=800 [°C]	P=0.7 [GPa], T=1000 [°C]	P=0.6 [GPa], T=1200 [°C]
Olivine	3.355	4.28	126.3	0.0000381	3.276	3.248	3.220
Orthopyroxene	3.370	7.82	115.5	0.0000345	3.302	3.276	3.250
Clinopyroxene	3.327	4.80	113.0	0.0000410	3.244	3.214	3.183

**Table I.3** Density for olivine, orthopyroxene and clinopyroxene at 800°C and 0.8 GPa, 1000°C and 0.7 GPa, 1200°C and 0.6 GPa.  $\rho_0$  = density at room temperature ( $T_0=25^\circ\text{C}$ ) and pressure ( $P_0=0.0001$  GPa);  $K$  = bulk modulus;  $K'$  = bulk modulus pressure derivatives;  $\alpha_{av}$  = volume thermal expansion coefficient (average values considered constant within the temperature range of interest).

	$C_{ij}(P_0, T_0)$ [GPa]	$(dC_{ij}/dP)$	$d^2C_{ij}/dP^2$ [GPa <sup>-1</sup> ]	$dC_{ij}/dT$ [GPa/°C]	$C_{ij}(PT)$ [GPa]	$C_{ij}(PT)$ [GPa]	$C_{ij}(PT)$ [GPa]	
					P=0.8 [GPa], T=800 [°C]	P=0.7 [GPa], T=1000 [°C]	P=0.6 [GPa], T=1200 [°C]	
Olivine	$c_{11}$	320.5	6.54	0	-0.0364	297.5	289.6	281.7
	$c_{12}$	68.1	3.86	0	-0.0109	62.7	60.2	57.6
	$c_{13}$	71.6	3.57	0	-0.0094	67.2	64.9	62.7
	$c_{22}$	196.5	5.38	0	-0.0276	179.4	173.4	167.3
	$c_{23}$	76.8	3.37	0	-0.0063	74.6	73.0	71.4
	$c_{33}$	233.5	5.51	0	-0.0289	215.5	209.2	202.8
	$c_{44}$	64.0	1.67	0	-0.0138	54.6	51.7	48.8
	$c_{55}$	77.0	1.81	-0.000007	-0.0147	67.1	63.9	60.8
Orthopyroxene	$c_{66}$	78.7	1.93	0	-0.0165	67.5	64.0	60.5
	$c_{11}$	236.9	10.27	-0.000047	-0.0352	217.8	209.8	201.7
	$c_{12}$	79.9	6.22	-0.000033	-0.0212	68.4	63.6	58.7
	$c_{13}$	63.2	6.63	-0.000026	-0.0318	43.9	36.8	29.8
	$c_{22}$	180.5	8.87	-0.000038	-0.0328	162.2	154.7	147.3
	$c_{23}$	56.8	7.26	-0.000031	-0.0107	54.3	51.4	48.6
	$c_{33}$	230.4	11.07	-0.000053	-0.0516	199.3	187.8	176.4
	$c_{44}$	84.3	1.23	0	-0.0131	75.1	72.4	69.6
Clinopyroxene	$c_{55}$	79.4	0.75	0	-0.0138	69.3	66.5	63.6
	$c_{66}$	80.1	2.78	0	-0.0145	71.1	67.9	64.7
	$c_{11}$	237.8	5.00	0	-0.0352	214.5	207.0	199.4
	$c_{12}$	83.5	5.90	0	-0.0212	71.8	67.0	62.1
	$c_{13}$	80.0	4.60	0	-0.0318	59.0	52.2	45.4
	$c_{15}$	9.0	-1.00	0	0	8.2	8.3	8.4
	$c_{22}$	183.6	7.50	0	-0.0328	164.2	156.9	149.6
	$c_{23}$	59.9	4.10	0	-0.0107	54.9	52.3	49.8
	$c_{25}$	9.5	-1.60	0	0	8.2	8.4	8.5
	$c_{33}$	229.5	4.70	0	-0.0516	193.3	182.5	171.7
	$c_{35}$	48.1	-0.70	0	0	47.5	47.6	47.7
	$c_{44}$	76.5	2.50	0	-0.0131	68.3	65.5	62.6
$c_{46}$	8.4	1.00	0	0	9.2	9.1	9.0	
$c_{55}$	73.0	1.30	0	-0.0138	63.3	60.5	57.6	
$c_{66}$	81.6	2.40	0	-0.0145	72.3	69.1	66.0	

**Table I.4** Elastic constants for olivine, orthopyroxene and clinopyroxene at 800°C and 0.8 GPa, 1000°C and 0.7 GPa, 1200°C and 0.6 GPa.  $C_{ij}(P_0, T_0)$  = elastic constants at room temperature ( $T_0=25^\circ\text{C}$ ) and pressure ( $P_0=0.0001$  GPa);  $dC_{ij}/dP$  = first order pressure derivatives;  $d^2C_{ij}/dP^2$  = second order pressure derivatives;  $dC_{ij}/dT$  = temperature derivatives.

\*\*\*\*\*



## II - APPENDIX OF CASE STUDY 2

### II.1 CHEMISTRY AND CRYSTAL STRUCTURE OF GARNET

Garnet forms a widespread mineral group, frequently encountered in metamorphic rocks, as well as in some igneous rocks (e.g. peridotites, kimberlites, granites and pegmatites), and as detrital grains in sediments. Garnet minerals belong to the nesosilicate group and comply with the general formula  $X_3Y_2Si_3O_{12}$ . Depending on the presence or absence of 8-coordinated Ca in the X-site, garnet minerals can be divided in two groups: (1) the so-called ugrandite series, including uvarovite ( $Ca_3Cr_2Si_3O_{12}$ ), grossular ( $Ca_3Al_2Si_3O_{12}$ ) and andradite ( $Ca_3Fe_2Si_3O_{12}$ ) and (2) the pyrospite series, which comprises pyrope ( $Mg_3Al_2Si_3O_{12}$ ), almandine

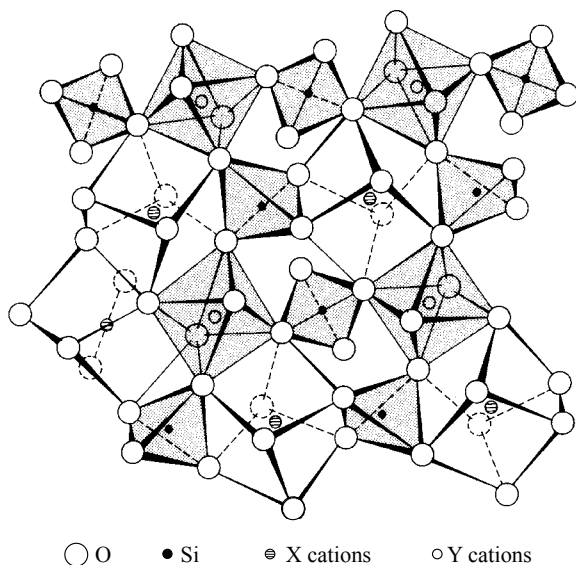


**Fig. II.1** Portion of the garnet structure projected down the [001] axis, showing the framework of alternating tetrahedra, octahedra (shaded) and distorted cubes (after NOVAK & GIBBS 1971).

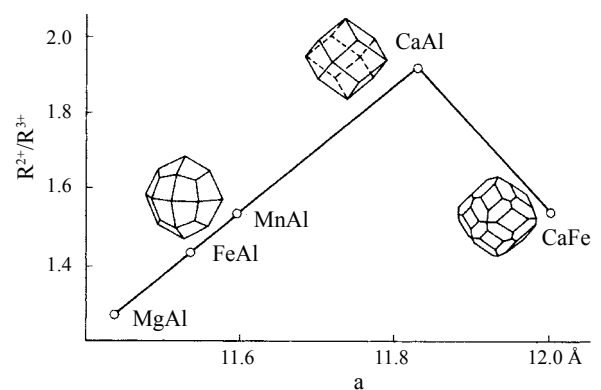


**Fig. II.2** Variation in habit of garnet single crystals with respect to the cation ratio and cubic cell edge (after Kostov 1968).

( $Fe_3Al_2Si_3O_{12}$ ) and spessartine ( $Mn_3Al_2Si_3O_{12}$ ). A continuous variation in composition occurs within these two series, but the miscibility between both groups is limited, due to the large difference in the X-site cation diameter.

Garnet has a cubic structure (space group Ia3d) and consists of individual  $SiO_4$  tetrahedra linked to each other by  $YO_6$  octahedra (Fig. II.1). X atoms occupy cavities coordinated by eight oxygens, the result being a distorted cube. Because of large compositional vari-

	Garnet
Space group	Ia3d
Lattice constant a [nm]	11.455
Reflectors (hkl)	4 0 0
	4 2 0
	4 4 4
	6 4 0
	6 4 2

**Table II.1** Lattice constants and reflectors used for indexing garnet.

ations, cell parameters may range between 11.4 and 12.0 Å. The chemistry and cell edge length strongly influence the habit of single crystals, as shown in Fig. II.2.

## II.2 EBSD DATA

### II.2.1 Crystallographic file used for indexing

The crystallographic file developed by Karsten Kunze's group (ETH Zürich, Switzerland) was used to index garnet patterns. No adjustment was needed to match the lattice parameters of the analyzed garnets and to obtain excellent indexing of the patterns.

Lattice constants and reflection planes are shown in Table II.1.

### II.2.2 List of EBSD runs and maps

The scanning parameters for the two maps shown in Fig. II.3 are presented in Table II.2.

Sample	Scan mode	Step size	Area	Measurements
		[ $\mu\text{m}$ ]	[ $\text{cm}^2$ ]	
Luk_02_1	stage scan	25	0.25	40001
Luk_02_7	stage scan	25	0.33	52461

**Table II.2** EBSD data for the two samples shown in Fig. II.3. No CI values are indicated because a substantial amount of the scanned areas consists of pelitic matrix for which CI=0.

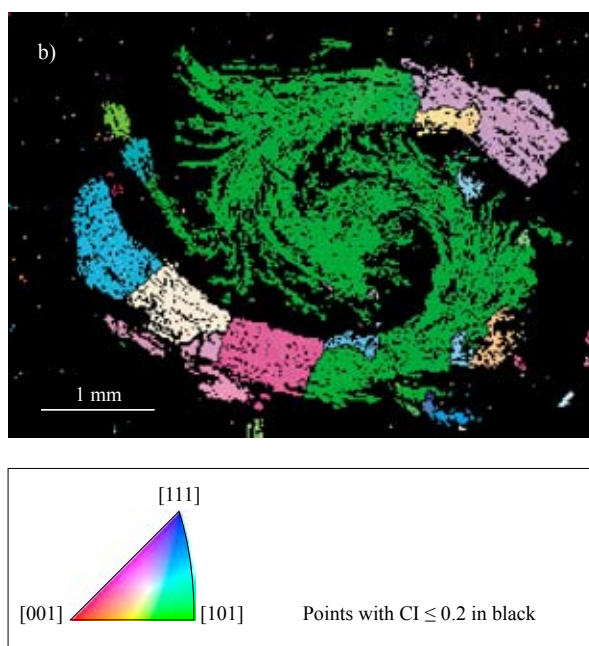
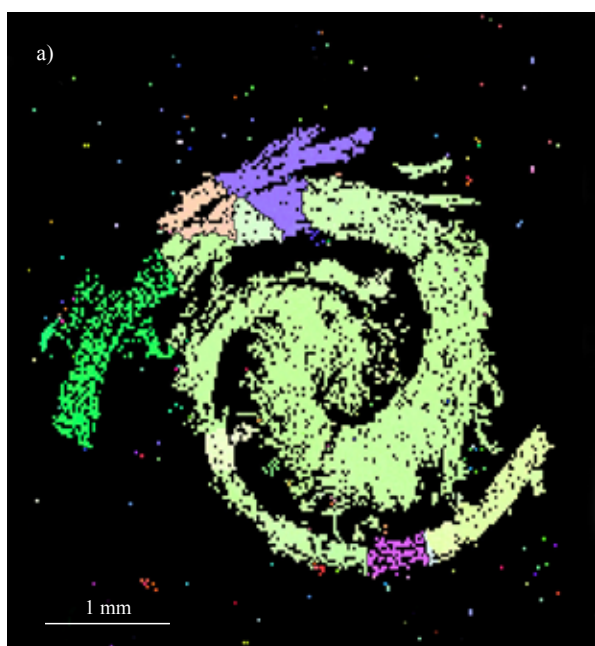


**Fig. II.3** Crystallographic orientation maps of samples Luk\_02\_1 (a) and Luk\_02\_7 (b).

\*\*\*\*\*

## III - APPENDIX OF CASE STUDY 3

### III.1 CHEMISTRY AND CRYSTAL STRUCTURE OF ALUMINA AND ZIRCONIA

Most of the fundamentals reported below about the chemistry and crystal structure of alumina and zirconia are based on the book *Ceramic Microstructures - Property Control by Processing* (LEE & RAINFORTH 1994).

#### III.1.1 Alumina

Alumina, known as corundum in mineral form, has the chemical formula  $\text{Al}_2\text{O}_3$ . Although the substitution of Al by other elements is limited, sapphire and ruby, the natural gems of corundum, owe their respective blue and red color to the replacement of Al by trace amounts of Ti/Fe and Cr, respectively. Industrial alumina is produced from bauxite ores, which contain impure hydroxides such as gibbsite ( $\text{Al}(\text{OH})_3$ ), boehmite and diaspore (both polymorphs of  $\text{AlO}(\text{OH})$ ). The production of alumina is achieved through the so-called Bayer process, a multi-stage refining method involving calcination and dehydroxylation of the bauxite constituents. In the final product, minor amounts of  $\text{Na}_2\text{O}$ ,  $\text{Fe}_2\text{O}_3$ ,  $\text{MgO}$ ,  $\text{SiO}_2$  and  $\text{CaO}$  are always present as impurities.  $\text{Na}_2\text{O}$  has a particularly detrimental effect on the final properties of alumina, as it negatively influences the electrical conductivity, rheology, pH and slip stability of the ceramics. The presence of a small amount of  $\text{MgO}$ , on the other hand, is beneficial to the ceramic processing, as it prevents abnor-

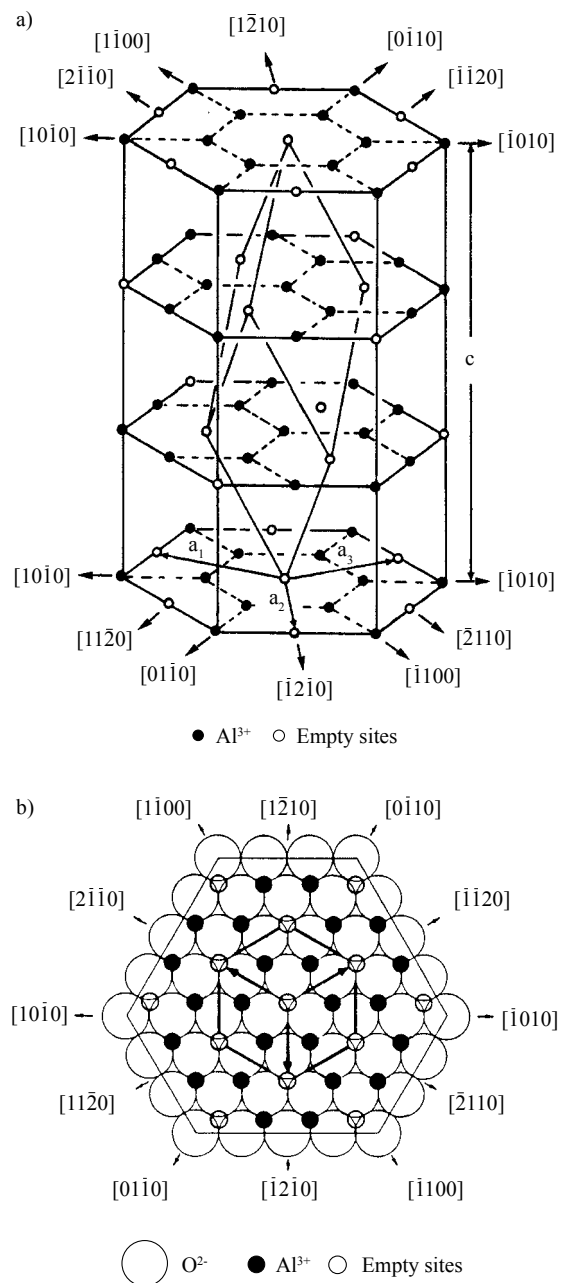


**Fig. III.1** The cation sublattice in  $\alpha$ -alumina (a). The basal plane of  $\alpha$ -alumina (b), showing the hexagonal close packed anion sublattice and the cations occupying two-thirds of the octahedral interstices (after KRONBERG 1957).

mal grain growth by limiting the grain boundary (GB) migration during sintering (e.g. BENNISON & HARMER 1990). In some very specific uses, MgO also reduces the development of porosity when alumina compacts are fired at very high temperature under H atmosphere (COBLE 1961).

Various intermediate metastable alumina phases, denoted as  $\gamma$ ,  $\chi$ ,  $\eta$ ,  $\iota$ ,  $\epsilon$ ,  $\delta$ ,  $\theta$ ,  $\kappa$ , may form successively during the refining process. However, only the final form  $\alpha$  is stable. The structure of  $\alpha$ -alumina is described using a hexagonal unit cell.  $O^{2-}$  anions are in approximately hexagonal close packed arrangement with  $Al^{3+}$  cations occupying two-thirds of the octahedral interstices (Fig. III.1).

### III.1.2 Zirconia

Industrial zirconia ( $ZrO_2$ ) is principally derived from two mineral sources, zircon ( $ZrSiO_4$ ) and baddeleyite (impure monoclinic  $ZrO_2$ ). Because of its relative abundance in secondary deposits, zircon is by far the most commonly exploited. The production of pure zirconia from ores can be achieved through various different refining processes, most of which are based on the property of zircon to dissociate into zirconia and silica above  $1750^\circ C$ .

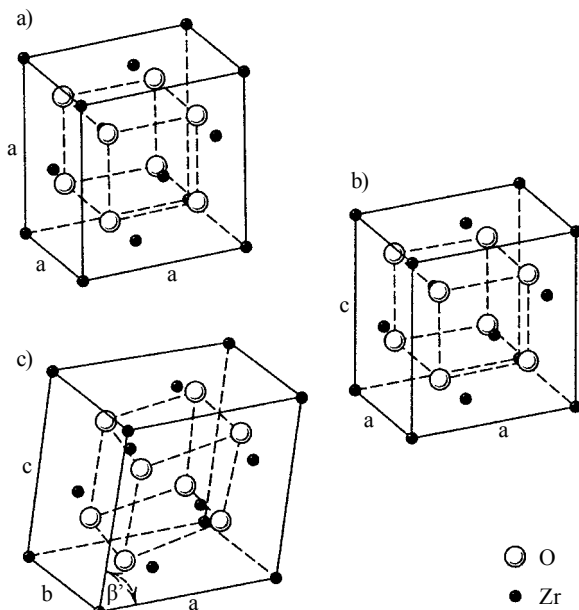


**Fig. III.2** The three polymorphs of zirconia: (a) cubic phase, (b) tetragonal phase, with  $c/a=1.02$ , and (c) monoclinic phase (after HEUER & RÜHLE 1984).

Zirconia occurs in three different polymorphs at room pressure (Fig. III.2): a monoclinic phase (space group  $P2_1/c$ ), a tetragonal phase (space group  $P4_2/nmc$ ) and a cubic phase (space group  $Fm3m$ ). Monoclinic  $ZrO_2$  is thermodynamically stable from room temperature to about  $1170^\circ C$ , at which temperature it changes to the tetragonal phase, which in turn is stable to  $2370^\circ C$ . Above this temperature the cubic phase becomes stable up to the melting point of  $2680^\circ C$ . Cubic zirconia has a fluorite structure, with  $Zr^{4+}$  cations octahedrally coordinated with  $O^{2-}$  anions in tetragonal arrangement. The structure of tetragonal zirconia is very similar to the cubic polymorph, differing only by a 2% elongation of the  $c$  axis. The monoclinic phase results from a displacive shear process, involving a large volume increase. This feature is the basis for the transformation toughening of zirconia.

Zirconia used for engineering applications is generally stabilized in the cubic or tetragonal structure through the addition of a few percent of other oxides, such as  $Y_2O_3$ ,  $CaO$  or  $MgO$ . These stabilizers form a solid solution with zirconia, thus preserving the cubic phase at lower temperatures.

## III.2 PROCESSING OF CERAMIC SAMPLES

### III.2.1 General considerations

#### III.2.1.1 Procedure

While metals and polymers are usually molten, cast and machined into their final shape, the processing of ceramics poses a more greater challenge on account of their refractoriness and brittleness. Because of their high temperature of fusion, very few ceramic materials are processed from the melt. Instead, the starting point in ceramic processing is usually fine powders that have to be put in suspension, milled, spray dried, shaped and subsequently heat-treated to be converted into dense solids. These successive steps are shown in Fig. III.3 and will be discussed in more details throughout this section.

Since the fundamentals of ceramic processing are widely discussed in the literature, only an overview of the basic principles is presented. Special attention is given to ceramic suspension as it is one of the most

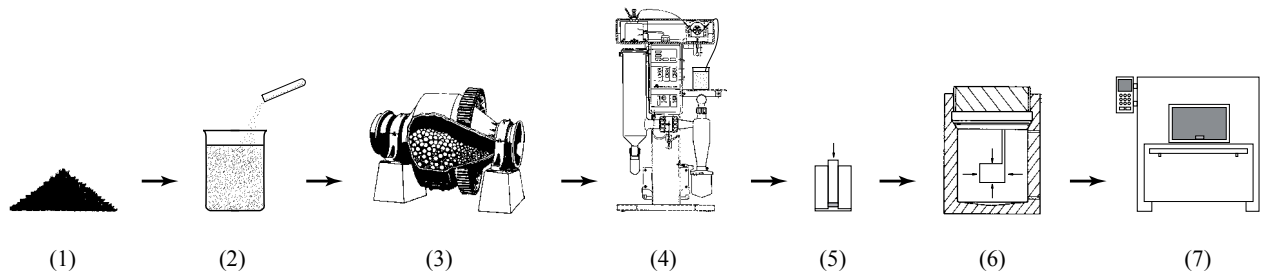


**Fig. III.3** Illustration of the procedure followed for the ceramic sample processing. Beginning with the starting materials (1), the powder is put in suspension (2) and additives like surfactants or binders are added. The suspension is ball milled (3) in order to disperse agglomerated particles and then spray dried (4) to form flowable granules. The granulated powder is then shaped and compacted through uniaxial (5) and isostatic (6) pressing and finally sintered under normal atmospheric conditions (7).

delicate steps in successful ceramic processing. The theoretical background of this section is based on the reference books of REED (1995), RING (1996), BARSOU (1997) and MYERS (1999).

### III.2.1.2 Sample property requirements

The alumina (labeled A) and zirconia (labeled Z) ceramics were processed in such a way that their properties satisfy the analytical requirements of EBSD. Some of our samples may therefore not match all industrial standards, such as the average grain size, which is preferably small in industrial ceramics to maximize the material strength, but is coarse in this study to allow EBSD measurements and GB determination. Generally speaking, the investigated ceramics had to fulfill the following conditions:

- *Small sample size*: For a greater freedom of movement inside the SEM chamber, small samples (typically  $< 1\text{ cm}^3$ ) are preferred.

- *Coarse and equigranular fabric*: A micrometer-sized fabric is needed first because EBSD data acquisition on fine-grained non-conductive materials turns out to be very problematic and secondly because the visualization of GB's on maps requires a few points of analysis per grain. Moreover, abnormal grain growth must be avoided, as it reduces the material strength and reduces the number of analyzable GB's per scan.

- *Random texture*: The stronger the LPO, the worse documented the GB population will be.

### III.2.2 Starting material

The preparation of the samples began with the following raw materials:  $\alpha$ -alumina ( $\text{Al}_2\text{O}_3$ ) powder,

Alumina CT 3000 SG<sup>®</sup> (ALCOA WORLD CHEMICALS 1982), and yttrium-stabilized cubic zirconia ( $\text{ZrO}_2$ ) powder, Zirconia TZ-8YS<sup>®</sup> (TOSOH CORPORATION 1993). Characteristics of both products are shown in Table III.1. These powders were chosen for several reasons. First their rather large initial grain size (compared to other powder types) is suitable for coarse-grained (typically  $\mu\text{m}$ -sized) ceramics processing. Then both powders are known for providing excellent sintering reactivity and are designed for applications requiring high density. In addition, Zirconia TZ-8YS<sup>®</sup> has the advantage of being fully stabilized in the cubic form due to doping with 8 mol.% of  $\text{Y}_2\text{O}_3$  (Fig. III.4). The occurrence of one single polymorph of zirconia simplifies the EBSD pattern indexation procedure and prevents possible indexation errors due to structural similarities between polymorphs. Finally, Alumina CT 3000 SG<sup>®</sup> is doped with MgO, which is known to prevent abnormal grain growth of alumina during sintering (e.g. BENNISON & HARMER 1990).

	Alumina CT 3000 SG	Zirconia TZ-8YS
Particle size $D_{50}$ [ $\mu\text{m}$ ]	0.8	0.6
Granule size $D_{50}$ [ $\mu\text{m}$ ]	20	60
Specific surface area (BET) [ $\text{m}^2/\text{g}$ ]	7.5	7
Bulk powder density [ $\text{g}/\text{cm}^3$ ]	no data	1.2
Composition [wt%]:		
$\text{Al}_2\text{O}_3$	99.80	0.10
$\text{Na}_2\text{O}$	0.08	0.12
$\text{Fe}_2\text{O}_3$	0.02	0.01
MgO	0.07	/
$\text{SiO}_2$	0.03	0.02
CaO	0.02	/
$\text{ZrO}_2$	/	86.45
$\text{Y}_2\text{O}_3$	/	13.30
Binder	/	/
Green density [ $\text{g}/\text{cm}^3$ ]	2.25	2.70

**Table III.1** Characteristics of Alumina CT 3000 SG<sup>®</sup> and Zirconia TZ-8YS<sup>®</sup> (after ALCOA WORLD CHEMICALS 1982 and TOSOH CORPORATION 1993).

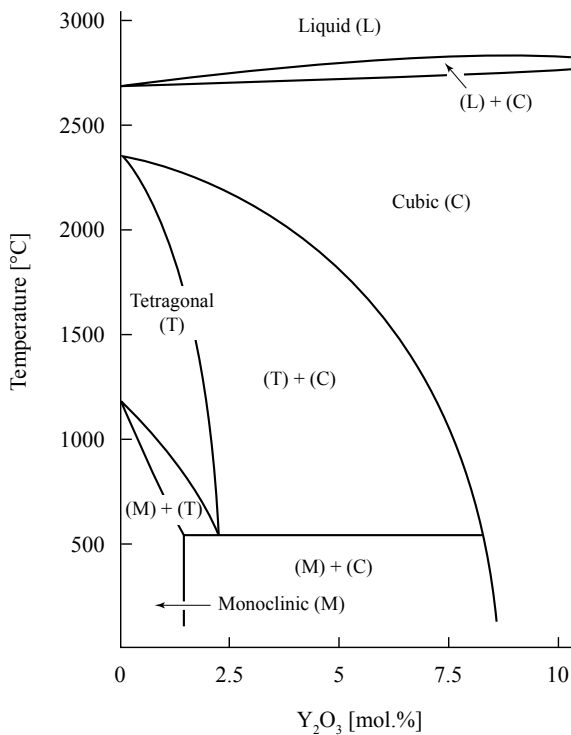


**Fig. III.4** Equilibrium phase diagram of yttrium-stabilized zirconia. Pure cubic ZrO<sub>2</sub> is only stable at temperatures between 2370°C and the melting point at approximately 2680°C. Upon doping with a few percent of Y<sub>2</sub>O<sub>3</sub>, the stability field of the cubic polymorph is greatly extended to lower temperatures (after SCOTT 1975).

### III.2.3 Ceramic powder suspension

#### III.2.3.1 General considerations

Ceramic raw powders consist of agglomerated particles (Fig. III.5) which would result in non-uniform and porous materials if shaped directly. The starting powders therefore have to be deagglomerated first. Deagglomeration, however, cannot be achieved through simple dry crushing or grinding as the fine particles would immediately reaggregate due to excess surface free energy. Instead, powders are put into liquid form in a so-called *ceramic suspension* (also known as *slurry*) and ball milled during several hours. The ceramic suspension also allows the uniform dissolution of various additives, like the organic surfactants and the binders needed for particle dispersion in the liquid and compact strengthening after forming.

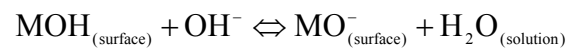
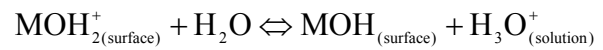
#### III.2.3.2 Suspension stability

When ceramic powder is put into water, it is of critical importance to prevent coagulation, i.e. to maintain

the suspension stable. The behavior of fine particles in water depends on (1) repulsive electrostatic interaction and (2) attractive van der Waals interaction. A suspension will remain stable if the repulsive energy barrier is sufficiently high to prevent attractive forces from getting the upper hand.

#### Repulsive electrostatic interaction

Oxide surfaces in contact with water will either transform to hydroxide or chemisorb water molecules (Fig. III.6). In both cases the surface may be protonated or deprotonated depending on pH, e.g. for a hydroxide surface:



At low pH the surface will thus be positively charged, whereas at high pH the charge is negative. The pH value for which the net surface charge of the

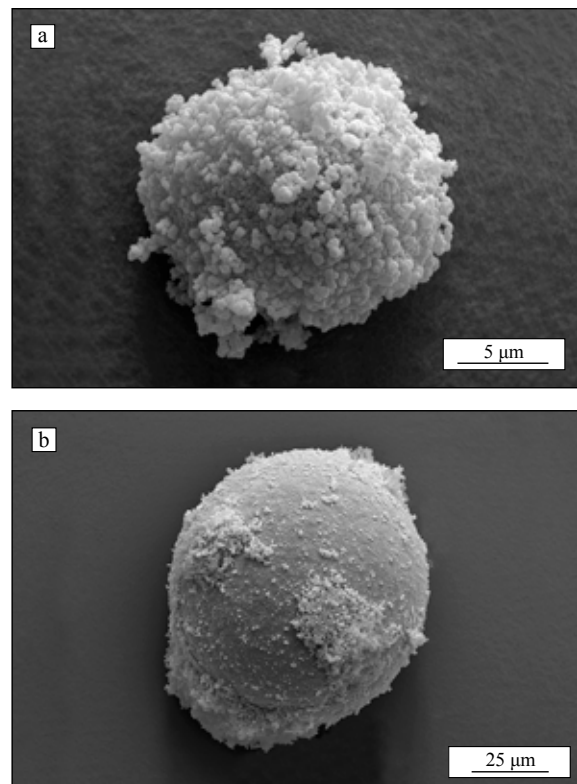


**Fig. III.5** SEM images of the as-received powders of Alumina CT 3000 SG® (a) and Zirconia TZ-8YS® (b) (s. also Fig. 5.1). The individual crystallites are agglomerated into soft granules, which will be destroyed during the first steps of sample processing.

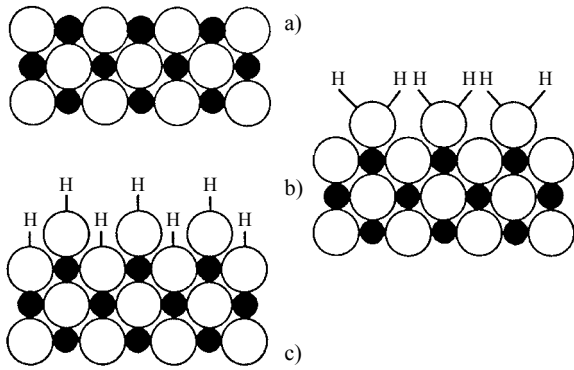


**Fig. III.6** Atomic structure of different states of an oxide surface: (a) a dry surface, (b) surface with physically adsorbed water, and (c) surface with chemically adsorbed water (after MORRISON 1985).

material is zero is called *point of zero charge (PZC)* of the material. When the PZC is less than the pH of the solvent (less than 7 for water), the surface of the particle is deprotonated, i.e. negatively charged. When the PZC is greater than the pH, the surface of the particle is protonated and becomes positively charged. As a result alumina particles (PZC = 9) are positively charged (protonation) when put in water, whereas zirconia (PZC = 4.5) become negatively charged (deprotonation).

Charged (protonated or deprotonated) surfaces influence the behavior of ions and polar molecules in the solution. Coulombic forces repel like-charged

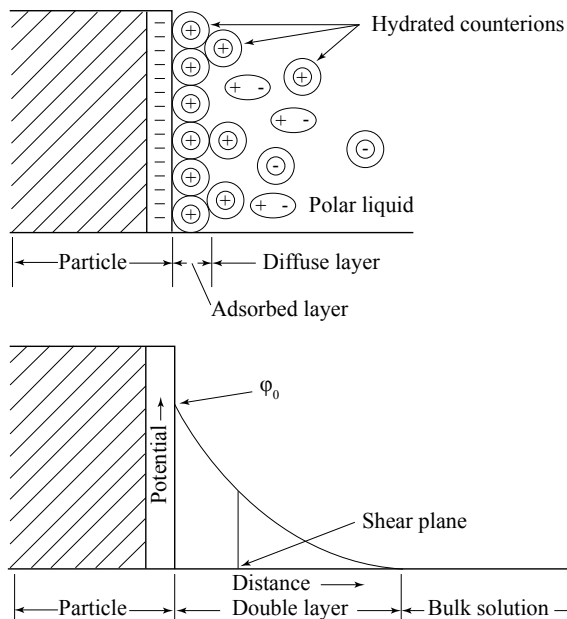


**Fig. III.7** Electrical double layer model for particle charging in a polar liquid and profile of the resulting electrical potential (after REED 1985).

ions but attract polar liquid molecules and oppositely charged ions into a region near the subsurface, increasing their concentration to the level found in the bulk. Thus each particle is surrounded by a relatively static adsorbed layer of counterions, called the Stern layer, itself wrapped in a diffuse layer formed by a concentration gradient of counterions and polar liquid molecules. This configuration is commonly known as the *diffuse electrical double-layer model*. As a result the electrical potential decreases as distance increases (Fig. III.7). Two particles with identically charged double layers will repel each other whereas particles with different charges will attract each other. However, mutually repelling charged double-layers are not always sufficient to prevent agglomeration of the particles. The driving force behind coagulation is the ever-present Van der Waals attractive interaction, which can overcome the repulsive energy barrier between two electrical double layers.

#### *Attractive Van der Waals interaction*

Van der Waals forces comprise three types of interactions: the dipole-dipole interaction, the dipole-induced dipole interaction and the so-called London dispersive force. Of the three, the latter is the most important contributor dictating the attractive potential between two particles at a short distance, regardless of the surface charge. Basically the London dispersive force results from the movement of the outer valence shell electrons of an atom. Asymmetric charge distribution produces an instantaneous dipole in the atom, which generates a short-lived electric field capable of polarizing a neighboring atom (Fig. III.8). The result is a net attraction between the two species.

#### *Total interaction between particles in suspension*

The total potential energy  $U_T$  between two particles in suspension is the algebraic sum of the repulsive potential energy  $U_R$  and the attractive Van der Waals potential energy  $U_A$ , or:

$$U_T = U_R + U_A \quad (\text{Eq. III.1})$$

$$U_T = \frac{\epsilon_w a^2 \phi_0^2}{4(h+a)} \exp\left[-\left(\frac{h}{\kappa^{-1}}\right)\right] + \frac{-Aa}{24h} \quad (\text{Eq. III.2})$$

where  $\epsilon_w$  is the dielectric constant of water,  $a$  the grain diameter,  $\phi_0$  the surface potential,  $h$  the distance between particle surfaces,  $\kappa^{-1}$  the double-layer thick-

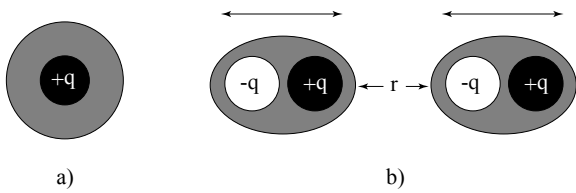


**Fig. III.8** Illustration of the London dispersion forces: (a) the time averaged charge distribution of an isolated atom or molecule is symmetrical and the net dipole moment is zero; (b) Interaction between the atoms may lead to an asymmetric charge distribution with a permanent dipole moment (after MYERS 1999).

ness and  $A$  the so-called Hamaker constant. The dependence of  $U_A$ ,  $U_R$  and  $U_T$  on the separation of particles is illustrated in Fig. III.9a. When particle separations are large, the total interaction energy is 0. Decreasing the particle separation decreases the energy to a secondary minimum. By further decreasing the particle separation, a repulsive maximum is reached. The maximum in the potential curve is of critical importance for the suspension stability because it represents an energy barrier that prevents coagulation. The higher the energy barrier, the more stable the suspension will be. From the Eq. III.2, it can be derived that as particle diameter decreases, the magnitude of the van der Waals interaction energy *and* the electrostatic interaction energy decrease at all separation distance, but in different proportions. As a result the total interaction energy shows a positive maximum which decreases with reduction in particle diameter (Fig. III.9b).

These properties of slurry stability have two main consequences when putting alumina and zirconia powders in suspension: (1) Alumina (PZC = 9) and zirconia (PZC = 4.5) have oppositely charged double layers. (2) The energy barrier preventing coagulation is low due to the small average grain size of the particles. These problems can be overcome through the addition of organic surfactants. Used as dispersing agents, these chemicals are particularly efficient when the surface potential of the particles is small and the double layer thickness thin, i.e. when the electrostatic repulsion is not sufficient to stabilize the colloidal suspension against coagulation.

**III.2.3.3 Effects of organic surfactants**

Surfactants are organic chemicals, whose molecules have hydrophobic and hydrophilic ends. In this PhD thesis, Dolapix CE64<sup>®</sup>, a carboxylic (-COOH) acid preparation belonging to the polar anionic surfactants, was used. When added to a ceramic-water suspension in the range of 0.1 to 1 % of the solid content, Dolapix CE64<sup>®</sup> has a double advantage: (1) a *wetting effect* lowering the surface tension of water and improving the wetting of suspended particles, and (2) a so-called *steric stabilization effect*.

The steric stabilization effect occurs when the hydrophobic parts of surfactant molecules are adsorbed onto the charged surface of the ceramic particles. When

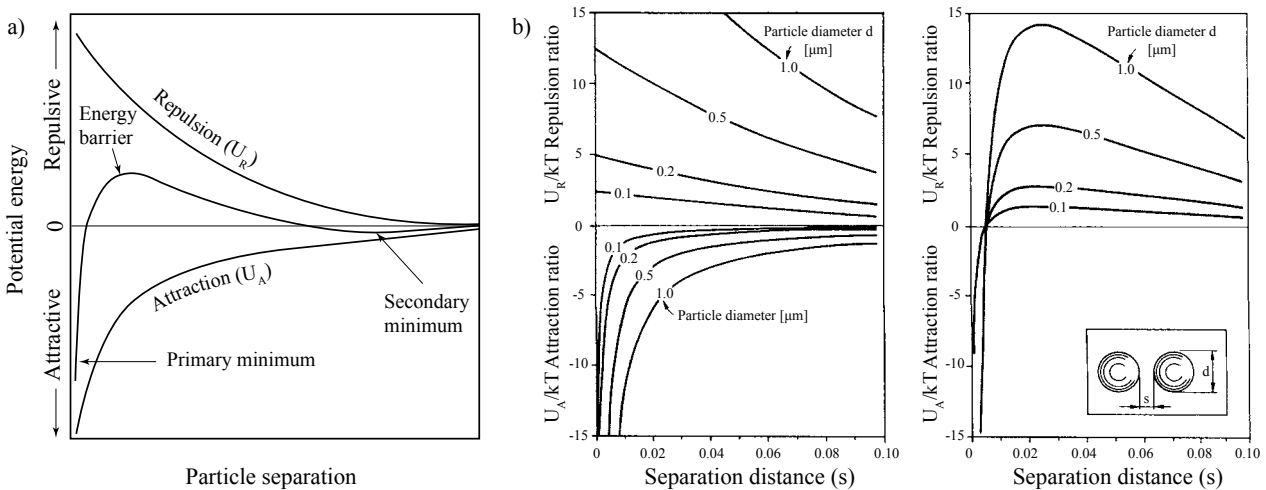


**Fig. III.9** (a) Potential energy of interaction between two particles with electrical double layers. A suspension will only remain stable if the energy barrier of the total interaction curve is sufficiently high to prevent coagulation of the particles (after REED 1995). (b) Plot of the attractive and repulsive potentials (left) and total interaction potential (right) affecting two spherical particles as a function of particle diameter; dielectric constant, surface potential and double layer thickness are kept constant. The smaller the particle diameter, the lower the energy barrier preventing coagulation (after RING 1996).

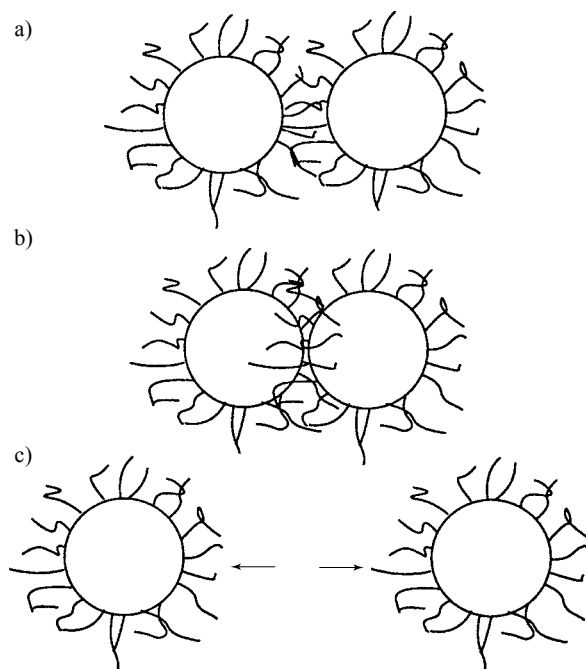


**Fig. III.10** (a) At small distance, the local concentration of hydrophilic chains increases above the normal equilibrium value giving rise to an osmotic pressure effect: water molecules move into the area between the particles and prevent them from coagulation. (b) Interpenetration hinders the free movement of the hydrophilic chains; the entropy decreases and therefore, the Gibbs free energy increases. (c) Energy minimization will force the particles to separate again. (after RING 1996).

two particles approach each other, the hydrophilic ends of surfactant molecules intermingle. This overlap is the base of the steric stabilization. Two distinct phenomena intervene in the steric stabilization (Fig. III.10). (1) An osmotic pressure effect forces water molecules to migrate between the two particles, thus preventing them from coming too close to each other. (2) An entropic effect, due to the reduction of possible conformations of the intermingled hydrophilic chains, leads to a decrease in entropy, i.e. to a corresponding increase of the Gibbs free energy. The only way for the system to lower the Gibbs free energy is to increase the number of possible conformations. Particles with intermingled surfactant chains will therefore tend to separate. The net result of both the osmotic pressure and entropic effects is a significant reinforcement of

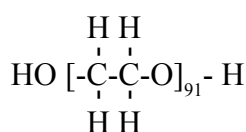


**Fig. III.11** Molecular structure of PEG of molecular weight of 4000 g/mol (after REED 1995).

the energy barrier which prevents the coagulation of particles.

## III.2.4 Ball milling

### III.2.4.1 Principle

Ball milling of a suspension is required to deagglomerate the initial raw powder and to improve the dissolution of the organic surfactant. For this purpose, a mill equipped with self-rotating cylinders was used. It supports simple cylindrical plastic jars filled with the suspension and a wear resistant media consisting of zirconia balls. The constant rotation of the mill coupled with the tumbling of zirconia balls produces a grinding action by impacting and shearing aggregates and particles. In this particular case, the milling time was set to 24 h.

### III.2.4.2 Binder

After ball milling, a molecular binder consisting of polyethylene glycol (PEG) (Fig. III.11) was added to the suspension. The most important function of PEG is to ensure compact strength after shaping. The strengthening effect of PEG is due to the hydrogen bonding attraction between the hydrated and polar groups of the molecular polymer chains. PEG also has a plasticizing and lubricating effect, which greatly facilitates the compaction of the material during die pressing.

## III.2.5 Spray drying

### III.2.5.1 Drying and granulation processes

Once the suspension has been ball milled, it must be dried and transformed into a flowable powder, i.e. a powder that will fill the die uniformly and offer little internal resistance during the shaping process. To achieve this, the solid particles in suspension are granulated into soft spherical agglomerates (granules) in a process called *spray drying*. In this study, a Büchi B-190 mini spray dryer (Fig. III.12) was used. During spray drying, the suspension is pumped under pressure through a pneumatic nozzle into a current of warm air, where atomization occurs. The minute droplets of the atomized spray are rapidly dried and transformed into granules held together by the PEG. Attracted by gravity, the droplets flow through the spray drying cham-

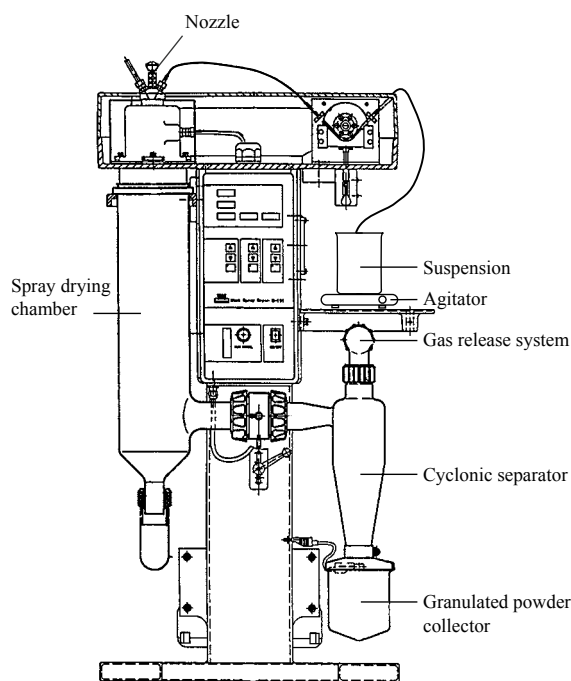


**Fig. III.12** Schematic representation of the Büchi B-190 mini spray dryer; height: ca 1 m. (after BÜCHI LABORTECHNIK AG 2000).

ber until they reach the powder collector. A cyclonic separator is then used to separate the particles from the gas.

### III.2.5.2 Practical aspects of spray drying

When a suspension is spray dried, the following points are crucial: (1) A large amount of the original powder may not be granulated properly, but may instead form flakes onto the inside wall of the cyclonic separator. Since this material is detrimental to the final product, it should not be used or mixed with the granulated powder accumulated in the collector. In some extreme cases, satisfactory granulated powder may represent only one fifth of the original input. (2) The atomizing nozzle can get clogged very rapidly when the suspension is too dense. To overcome this, the suspension may be diluted by adding distilled water before pumping. (3) In order to avoid the gravitational sedimentation of particles, the suspension must be kept in motion by an agitator during the whole process. This also prevents differential settling when the suspension contains several powders with different densities. (4) Granules with a hollow or donut shape might arise when the inlet temperature and the binder content are high and/or when the solid matter in the slurry is low. As hollow granules are detrimental to the

final density of the green body, these parameters must be checked periodically.

## III.2.6 Ceramic shaping

### III.2.6.1 Die pressing

The granulated powders were shaped into disks by uniaxial die pressing. This process is particularly suitable in the manufacturing of fairly dense green bodies having non-complex shapes. The pressure applied was comprised between 75 and 200 MPa in a die of 15 mm in diameter. Because of the strengthening effect of the PEG binder, none of the samples were damaged upon ejection (springback).

During die pressing part of the applied load is transferred to the die wall. The resisting force induced by friction creates undesirable density gradients in the compact (Fig. III.13). To alleviate this problem isostatic pressing is generally performed after die pressing to homogenize the density of green bodies.

### III.2.6.2 Wet bag isostatic pressing

With wet bag isostatic pressing, the pressure is transferred to the compact from all directions uniformly with the help of a liquid medium. The samples are introduced into rubber bags (commonly condoms) placed in a sealed oil reservoir. In this study an isostatic pressure of 200 MPa was applied during 5 minutes.

## III.2.7 Sintering

### III.2.7.1 Principle

Sintering is the process by which a powder compact is transformed into a strong, dense ceramic body upon heating. The driving force operative during sintering is the lowering of the surface free energy of the ceramic particles by grain growth and filling of porosity.

The migration of atoms necessary for grain growth and reduction of porosity can occur along various diffusion paths (Fig. III.14). If GB and volume diffusion from a non-superficial source dominate, densification and shrinkage occur: the pores get smaller and tend to disappear with time. If vapor and surface diffusion from a superficial source dominate, coarsening hap-

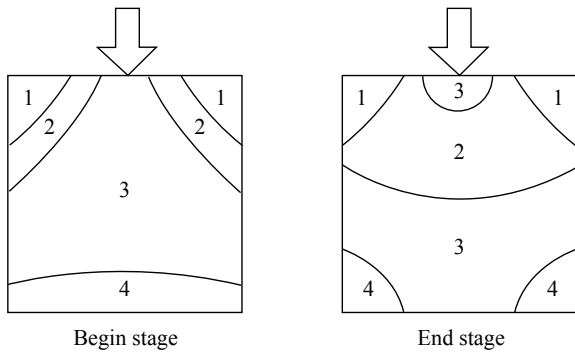


**Fig. III.13** Evolution of the density distribution ( $D_1 > D_2 > D_3 > D_4$ ) in a green body after cylindrical single action die pressing (after REED 1995).

pens: pores and grains get larger with time and no densification occurs.

**III.2.7.2 Sintering profiles**

Two different sintering profiles were used (Fig. III.15). The first set of samples (A1, A2, Z1, Z2) was fired at 1550°C during 4 h (profile 1), whereas the second set (A3, A4, Z3, Z4) was sintered at 1700°C during the same duration (profile 2). The temperature increase was fixed at a basic rate of 300°C/h. However, a smaller rate of 100°C/h was chosen below 300°C to induce a complete burnout of PEG, as well as between 800°C and 1150°C to contribute to the densification of the compacts. The temperature decrease was fixed at a rate of 600°C/h after a small annealing time at 1650°C.

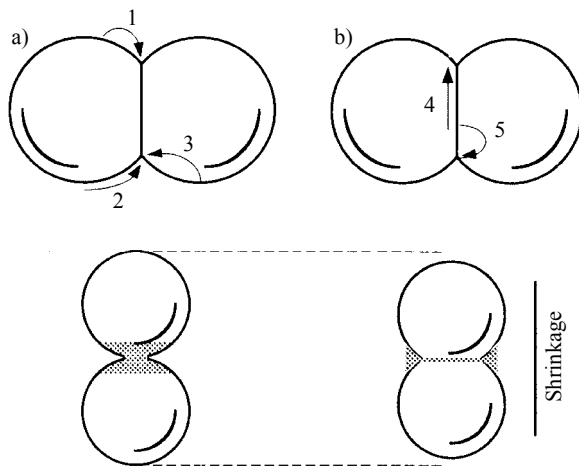


**Fig. III.14** Basic atomic mechanisms leading to (a) coarsening through (1) vapor diffusion, (2) surface diffusion, (3) volume diffusion from a superficial source and (b) densification through (4) GB diffusion and (5) volume diffusion from a non-superficial source (after BARSOUM 1997).

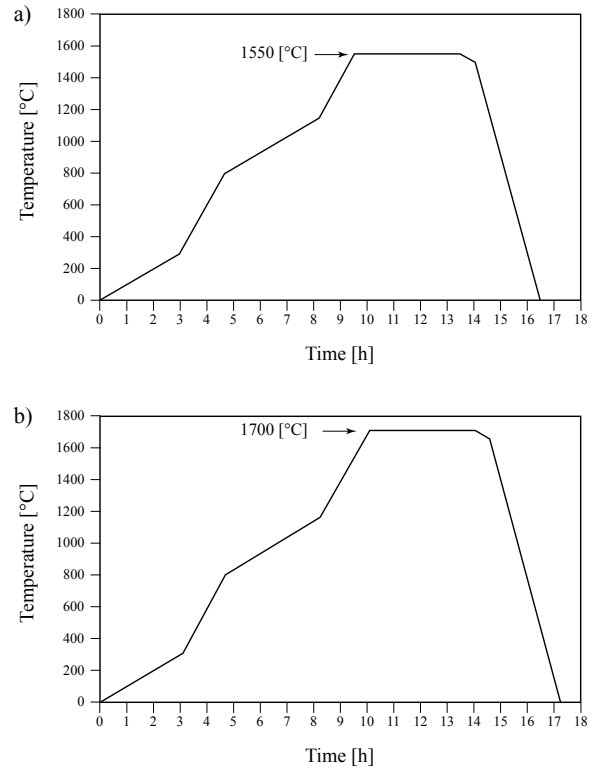


**Fig. III.15** Sintering profiles 1 (a) and 2 (b).

**III.2.8 Density measurements**

**III.2.8.1 Bulk density**

Density measurements were performed to verify that the ceramics had a sufficiently low porosity. The bulk density  $\rho$  is defined as:

$$\rho = \frac{M}{V_s + V_{OP} + V_{CP}} \quad (\text{Eq. III.3})$$

where  $M$  is the mass of the ceramic sample,  $V_s$  the volume of the solid,  $V_{OP}$  and  $V_{CP}$  the volumes of the open and the closed porosity, respectively. The sum  $V_s + V_{OP} + V_{CP}$  is the bulk volume of the sample. Archimedes' principle was used to measure the bulk density  $\rho$  of the ceramics. This method is only suitable, however, when the open porosity is low, i.e. when water cannot penetrate through the pores into the sample. Pycnometric measurements revealed open porosity values lower than 0.25 % for our samples, making the use of Archimedes' principle very appropriate.

Sample	Sintering temperature [°C]	Bulk density* [g/cm <sup>3</sup> ]	Bulk / Theoretical density** [%]
A1	1550	3.90	98.0
A2	1550	3.90	98.0
A3	1700	3.91	98.2
A4	1700	3.91	98.2
Z1	1550	5.93	97.5
Z2	1550	5.91	97.2
Z3	1700	5.94	97.7
Z4	1700	5.93	97.5

\* calculated using Archimedes'principle

\*\* assuming a theoretical density of 3.98 and 6.08 [g/cm<sup>3</sup>] for alumina and zirconia ceramics, respectively

Table III.2 Density of the final ceramics.

III.2.8.2 Bulk vs theoretical density

The theoretical density (also known as ultimate density) is the density calculated from the unit cell of the material. The ratio between bulk and theoretical densities, normalized over 100%, is a value widely used in the literature to compare the density of materials. The investigated samples have bulk/theoretical density ratios ranging from 97.0 to 98.2 % (Table III.2). In alumina, the remaining porosity is concentrated at GB's and triple junctions, whereas in zirconia it is located almost exclusively in the interior of the grains (s. Fig. 5.4 in Chapter 5).

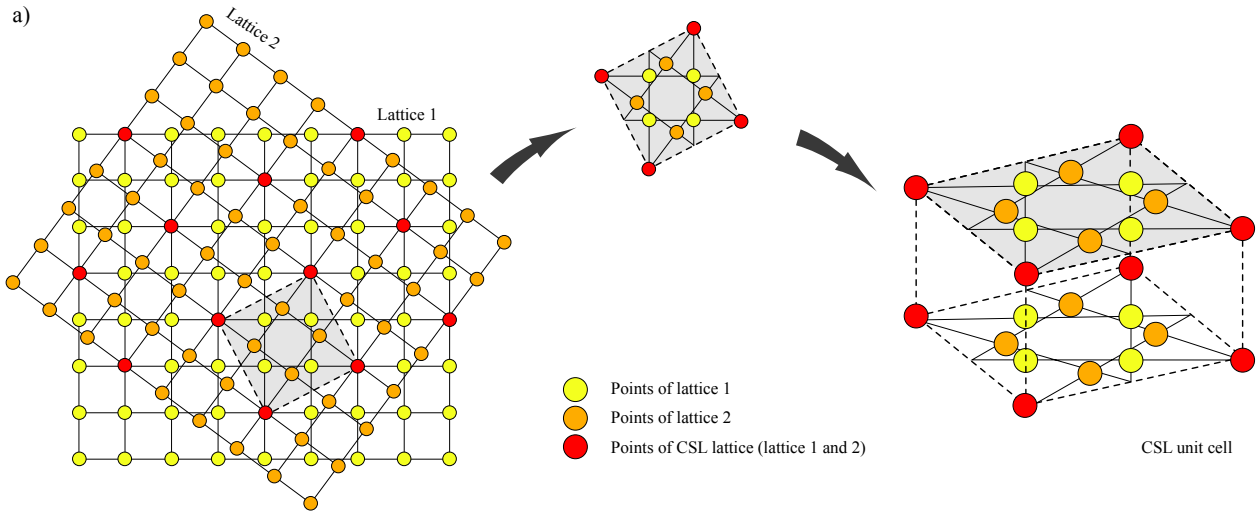
III.3 COINCIDENCE SITE LATTICE (CSL)

The fundamentals of the coincidence site lattice (CSL) model can be found in BOLLMANN (1970), WARRINGTON & BUFALINI (1971), RANDLE (1993, 1996) and HOWE (1997).

III.3.1 Principle

The coincidence site lattice (CSL) model is a technique allowing the quantification of the relative misorientation between two adjacent grains of the same phase in a microstructure. The misorientation is analyzed by overlapping the crystal lattices of both grains in their current orientation and by checking for coincidence lattice points. The coincidence lattice points themselves form a lattice, called coincidence site lattice, whose unit cell size is a measure of the matchability between both lattices.

The CSL is characterized by the multiplicity index  $\Sigma$ , which is defined as the ratio between the total number of sites and the number of CSL sites of the two interpenetrating lattices. The smaller the  $\Sigma$  value the better the matchability between both lattices. In the  $\Sigma$  value calculation, the unit cell of the CSL lattice serves as reference volume. CSL lattice points



b)

$$\Sigma = \frac{\text{Sum of the CSL lattice points (lattice 1 and 2) + points of lattice 1 + points of lattice 2}}{\text{Sum of the CSL lattice points (lattice 1 and 2)}} = \frac{2 \times 8 \times 1/8 + 8 \times 1/2 + 8 \times 1/2}{2 \times 8 \times 1/8} = 5 \quad (\text{Eq. III.4})$$

Fig. III.16 (a) Schematic representation illustrating the coincidence lattice resulting from the superposition of two adjacent grain lattices. The  $\Sigma$  value is calculated on the basis of Eq. III.4 (b). The points of lattice 1 (in yellow) and of lattice 2 (in orange) are part of two neighboring unit cells and count for one-half, whereas the CSL lattice points (in red) belong to eight neighboring cells and count each for one-eighth. The CSL lattice points are counted double as they belong to both lattices 1 and 2.

belong to both individual lattices and count therefore double. However, because they are shared with seven neighboring unit cells, their final weight is 2 x one-eighth. On the other hand, points of the individual lattices which are located on the faces of the CSL unit cell are shared with the adjacent unit cell and count only half (Fig. III.16). Generally, the complete CSL notation also includes the angle/axis pair describing the misorientation (s. Section 2.3.4) and the Miller indices of the GB plane. If similar  $\Sigma$  values originate from different misorientations, an index is added for differentiation, such as e.g.  $\Sigma = 13_1$  ( $22.6^\circ/[100]$ ) and  $\Sigma = 13_2$  ( $27.8^\circ/[111]$ ).

In cubic systems, misorientation has been associated with GB energy, and low-energy misorientations are linked with a high density, short-period-coincidence site lattice, i.e. a GB with low  $\Sigma$  value. However, there is no simple correlation between the GB energy and  $\Sigma$  (SUTTON & BALLUFFI 1987). The reason for this is that the energy of GB's not only depends on GB geometry, but also on other parameters like local defect structure, chemistry and electronic bonding. The CSL model is thus only a geometrical indicator that a GB has the potential for special characteristics.

### III.3.2 Deviation from exact CSL

In polycrystals there is little chance of a GB misorientation to be exactly that of a CSL. However, the special properties which may be associated with low CSL's can occur in GB's which are close to, but not exactly, CSL misorientations. An important feature of GB's which are close to CSL's is that, for small angular deviations, the CSL is preserved by dislocation arrays known as secondary intrinsic GB dislocations. It is generally admitted that the maximum angular deviation  $\Delta\theta$  corresponds to the highest density (i.e. smallest spacing) of dislocations possible in the GB's, which is itself interlinked with the multiplicity index  $\Sigma$ . The relationship between the maximum angular deviation  $\Delta\theta$  and the multiplicity index  $\Sigma$  is given by the so-called Brandon criterion (BRANDON 1966):

$$\Delta\theta = v_0 \Sigma^{-0.5} \quad (\text{Eq. III.5})$$

where  $v_0$  is a proportionality constant equal to the angular limit for a low angle GB, i.e.  $15^\circ$ . It is thus possible to calculate for each  $\Sigma$  the maximum angular deviation from the exact CSL misorientations. A listing of the maximum angular deviation calculated using the Brandon criterion for  $\Sigma$  up to 28 (alumina)

and for  $\Sigma$  up to 49 (zirconia) can be found in Table 5.2 in Chapter 5.

### III.3.3 Constrained CSL

In order to evaluate all possible coincidence orientations for non-cubic crystals, it is necessary to take into account the axial ratio of the CSL unit cell. For hexametric minerals, such as alumina, it has been shown that exact CSL's can be obtained only for rational values of the square of the crystallographic axes, i.e.  $c^2/a^2$  ratios (BRUGGEMANN et al. 1972). In practice, however, real crystals rarely conform to these stringent requirements and the irrational ratios of the real material must be constrained to the closest rational value, resulting in a so-called Constrained CSL (SINGH et al. 1990), also known as near-CSL (BONNET et al. 1981). The basic idea is that any small deviation from a rational  $c^2/a^2$  ratio can be accommodated by an array of dislocations.

The coincidence rotations for alumina were selected for a  $c/a$  ratio ranging from 2.699 to 2.763 (corresponding to  $c^2/a^2$  ratios ranging from 7.25 to 7.65), following the recommendations of GRIMMER (1989). For a complete listing of the Constrained CSL misorientations used for alumina, see Table 5.2.

### III.3.4 Fractions of CSL grain boundaries

The fractions of CSL GB's were calculated for alumina and zirconia samples based on GB counting in EBSD scans 2, 3 and 4 (Table III.3 and III.4). The fractions of the average samples for both sintering temperatures, as well as for the simulated 2D spatial models are shown in Table III.5.

### III.3.5 Triple junction character

The connectivity among GB's was assessed through studies of the triple junction distribution of GB's. Triple junctions were classified by the number of CSL GB's that coordinate them, giving four different triple junction fractions  $J_n$ , where  $n$  is the number of CSL GB's ( $n = 0, 1, 2, 3$ ). As these data make sense for FCC materials only, triple junction fractions are presented exclusively for zirconia (Table III.6).

$\Sigma$	A1 ( $n_{GB's} = 4665$ )						A2 ( $n_{GB's} = 4538$ )						A3 ( $n_{GB's} = 1986$ )						A4 ( $n_{GB's} = 1892$ )					
	2	3	4	Sum	$f_{M\Sigma A1}^*$	$f_{M\Sigma A1}^{**}$	2	3	4	Sum	$f_{M\Sigma A2}^*$	$f_{M\Sigma A2}^{**}$	2	3	4	Sum	$f_{M\Sigma A3}^*$	$f_{M\Sigma A3}^{**}$	2	3	4	Sum	$f_{M\Sigma A4}^*$	$f_{M\Sigma A4}^{**}$
3	7	6	10	23	0.49	13.14	15	9	12	36	0.79	18.85	6	4	3	13	0.65	15.12	6	3	4	13	0.69	15.12
7 <sub>1</sub>	2	0	1	3	0.06	1.71	0	2	0	2	0.04	1.05	0	1	0	1	0.05	1.16	0	2	1	3	0.16	3.49
7 <sub>2</sub>	1	0	1	2	0.04	1.14	2	0	1	3	0.07	1.57	1	0	0	1	0.05	1.16	0	2	0	2	0.11	2.33
7 <sub>3</sub>	4	6	9	19	0.41	10.86	5	3	6	14	0.31	7.33	5	1	8	14	0.70	16.28	4	4	3	11	0.58	12.79
8	2	3	1	6	0.13	3.43	2	4	4	10	0.22	5.24	1	2	4	7	0.35	8.14	0	0	1	1	0.05	1.16
11 <sub>1</sub>	3	1	3	7	0.15	4.00	1	2	0	3	0.07	1.57	0	0	0	0	0.00	0.00	1	1	0	2	0.11	2.33
11 <sub>2</sub>	4	2	2	8	0.17	4.57	2	5	3	10	0.22	5.24	1	0	2	3	0.15	3.49	1	4	1	6	0.32	6.98
11 <sub>3</sub>	3	1	2	6	0.13	3.43	3	4	5	12	0.26	6.28	0	0	2	2	0.10	2.33	1	2	0	3	0.16	3.49
12	0	0	0	0	0.00	0.00	0	0	1	1	0.02	0.52	0	0	0	0	0.00	0.00	0	0	0	0	0.00	0.00
13 <sub>1</sub>	1	1	1	3	0.06	1.71	0	2	1	3	0.07	1.57	0	0	0	0	0.00	0.00	0	0	0	0	0.00	0.00
13 <sub>2</sub>	1	3	3	7	0.15	4.00	2	3	3	8	0.18	4.19	0	1	1	2	0.10	2.33	0	1	1	2	0.11	2.33
13 <sub>3</sub>	0	1	2	3	0.06	1.71	0	1	0	1	0.02	0.52	0	0	1	1	0.05	1.16	1	0	0	1	0.05	1.16
13 <sub>4</sub>	0	3	3	6	0.13	3.43	3	1	3	7	0.15	3.66	2	1	2	5	0.25	5.81	0	1	1	2	0.11	2.33
13 <sub>5</sub>	1	1	0	2	0.04	1.14	0	0	0	0	0.00	0.00	0	0	1	1	0.05	1.16	0	1	0	1	0.05	1.16
14 <sub>1</sub>	1	2	2	5	0.11	2.86	1	3	1	5	0.11	2.62	3	1	1	5	0.25	5.81	1	2	2	5	0.26	5.81
14 <sub>2</sub>	0	0	0	0	0.00	0.00	0	0	0	0	0.00	0.00	0	0	0	0	0.00	0.00	1	0	0	1	0.05	1.16
15 <sub>1</sub>	1	0	4	5	0.11	2.86	1	0	3	4	0.09	2.09	0	0	1	1	0.05	1.16	4	0	0	4	0.21	4.65
15 <sub>2</sub>	0	0	0	0	0.00	0.00	1	0	1	2	0.04	1.05	0	0	0	0	0.00	0.00	0	0	1	1	0.05	1.16
17 <sub>1</sub>	2	2	4	8	0.17	4.57	1	0	2	3	0.07	1.57	0	1	1	2	0.10	2.33	0	1	0	1	0.05	1.16
17 <sub>2</sub>	0	1	1	2	0.04	1.14	2	1	1	4	0.09	2.09	1	0	0	1	0.05	1.16	0	0	1	1	0.05	1.16
17 <sub>3</sub>	1	2	2	5	0.11	2.86	2	2	0	4	0.09	2.09	0	2	0	2	0.10	2.33	0	1	3	4	0.21	4.65
17 <sub>4</sub>	0	0	0	0	0.00	0.00	0	0	1	1	0.02	0.52	0	0	0	0	0.00	0.00	0	0	0	0	0.00	0.00
18	0	0	0	0	0.00	0.00	1	0	0	1	0.02	0.52	1	0	0	1	0.05	1.16	0	0	0	0	0.00	0.00
19 <sub>1</sub>	0	0	0	0	0.00	0.00	0	0	0	0	0.00	0.00	0	0	1	1	0.05	1.16	0	0	0	0	0.00	0.00
19 <sub>2</sub>	2	1	2	5	0.11	2.86	1	3	2	6	0.13	3.14	2	0	0	2	0.10	2.33	0	0	1	1	0.05	1.16
19 <sub>3</sub>	0	0	0	0	0.00	0.00	2	0	0	2	0.04	1.05	2	0	1	3	0.15	3.49	0	0	1	1	0.05	1.16
19 <sub>4</sub>	1	1	1	3	0.06	1.71	1	0	0	1	0.02	0.52	1	0	0	1	0.05	1.16	0	1	0	1	0.05	1.16
20 <sub>1</sub>	2	0	3	5	0.11	2.86	3	2	3	8	0.18	4.19	0	1	0	1	0.05	1.16	0	2	0	2	0.11	2.33
20 <sub>2</sub>	0	0	0	0	0.00	0.00	1	0	0	1	0.02	0.52	0	0	0	0	0.00	0.00	0	0	0	0	0.00	0.00
21 <sub>1</sub>	2	0	0	2	0.04	1.14	0	0	0	0	0.00	0.00	0	0	1	1	0.05	1.16	0	1	0	1	0.05	1.16
21 <sub>2</sub>	0	1	5	6	0.13	3.43	1	0	0	1	0.02	0.52	0	1	1	2	0.10	2.33	0	0	1	1	0.05	1.16
21 <sub>3</sub>	0	0	0	0	0.00	0.00	0	1	0	1	0.02	0.52	0	0	0	0	0.00	0.00	0	0	0	0	0.00	0.00
22 <sub>1</sub>	0	1	2	3	0.06	1.71	1	0	2	3	0.07	1.57	3	2	1	6	0.30	6.98	0	0	1	1	0.05	1.16
22 <sub>2</sub>	0	0	0	0	0.00	0.00	0	0	0	0	0.00	0.00	0	0	0	0	0.00	0.00	0	0	0	0	0.00	0.00
23 <sub>1</sub>	1	0	0	1	0.02	0.57	0	0	0	0	0.00	0.00	0	0	0	0	0.00	0.00	0	0	1	1	0.05	1.16
23 <sub>2</sub>	1	0	1	2	0.04	1.14	0	1	2	3	0.07	1.57	0	0	1	1	0.05	1.16	0	0	0	0	0.00	0.00
23 <sub>3</sub>	1	0	0	1	0.02	0.57	0	0	2	2	0.04	1.05	0	1	0	1	0.05	1.16	0	1	0	1	0.05	1.16
23 <sub>4</sub>	0	3	1	4	0.09	2.29	0	3	1	4	0.09	2.09	1	0	0	1	0.05	1.16	2	0	1	3	0.16	3.49
23 <sub>5</sub>	2	0	2	4	0.09	2.29	0	1	1	2	0.04	1.05	0	0	0	0	0.00	0.00	0	2	0	2	0.11	2.33
24	0	2	1	3	0.06	1.71	0	0	0	0	0.00	0.00	0	0	0	0	0.00	0.00	0	0	0	0	0.00	0.00
25 <sub>1</sub>	0	2	0	2	0.04	1.14	0	0	0	0	0.00	0.00	0	0	0	0	0.00	0.00	0	0	0	0	0.00	0.00
25 <sub>2</sub>	2	1	1	4	0.09	2.29	3	2	1	6	0.13	3.14	1	0	0	1	0.05	1.16	1	0	1	2	0.11	2.33
25 <sub>3</sub>	0	1	0	1	0.02	0.57	0	0	1	1	0.02	0.52	0	0	0	0	0.00	0.00	1	0	0	1	0.05	1.16
26	0	0	0	0	0.00	0.00	1	2	0	3	0.07	1.57	0	0	0	0	0.00	0.00	0	1	0	1	0.05	1.16
27 <sub>1</sub>	0	0	0	0	0.00	0.00	1	2	1	4	0.09	2.09	1	0	0	1	0.05	1.16	0	0	0	0	0.00	0.00
27 <sub>2</sub>	0	0	0	0	0.00	0.00	2	0	1	3	0.07	1.57	0	1	1	2	0.10	2.33	0	0	0	0	0.00	0.00
27 <sub>3</sub>	1	0	2	3	0.06	1.71	0	0	0	0	0.00	0.00	0	0	0	0	0.00	0.00	1	1	1	3	0.16	3.49
28 <sub>1</sub>	3	0	0	3	0.06	1.71	1	2	1	4	0.09	2.09	0	0	0	0	0.00	0.00	0	0	0	0	0.00	0.00
28 <sub>2</sub>	2	1	0	3	0.06	1.71	0	1	1	2	0.04	1.05	0	0	0	0	0.00	0.00	0	0	0	0	0.00	0.00
Total	54	49	72	175	3.75	100.00	62	62	67	191	4.21	100.00	32	20	34	86	4.33	100.00	25	34	27	86	4.55	100.00

\* normalized over total GB's

\*\* normalized over CSL GB's

**Table III.3**  $\Sigma$  number fractions  $f_{M\Sigma}$  of GB's (%) in alumina samples A1, A2, A3 and A4.

$\Sigma$	Z1 ( $n_{GB's} = 1273$ )						Z2 ( $n_{GB's} = 2644$ )						Z3 ( $n_{GB's} = 1264$ )						Z4 ( $n_{GB's} = 1203$ )					
	2	3	4	Sum	$f_M \Sigma_{Z1}^*$	$f_M \Sigma_{Z1}^{**}$	2	3	4	Sum	$f_M \Sigma_{Z2}^*$	$f_M \Sigma_{Z2}^{**}$	2	3	4	Sum	$f_M \Sigma_{Z3}^*$	$f_M \Sigma_{Z3}^{**}$	2	3	4	Sum	$f_M \Sigma_{Z4}^*$	$f_M \Sigma_{Z4}^{**}$
3	9	9	6	24	1.89	10.62	16	15	22	53	2.00	11.23	6	6	10	22	1.74	10.78	6	4	13	23	1.91	10.75
5	7	5	7	19	1.49	8.41	14	15	13	42	1.59	8.90	5	6	2	13	1.03	6.37	6	8	7	21	1.75	9.81
7	3	3	5	11	0.86	4.87	6	6	10	22	0.83	4.66	5	3	6	14	1.11	6.86	2	3	2	7	0.58	3.27
9	6	4	4	14	1.10	6.19	9	8	12	29	1.10	6.14	3	3	4	10	0.79	4.90	5	3	5	13	1.08	6.07
11	5	5	8	18	1.41	7.96	9	11	7	27	1.02	5.72	7	7	2	16	1.27	7.84	4	4	10	18	1.50	8.41
13 <sub>1</sub>	2	1	1	4	0.31	1.77	0	4	4	8	0.30	1.69	2	1	2	5	0.40	2.45	4	3	5	12	1.00	5.61
13 <sub>2</sub>	4	3	2	9	0.71	3.98	3	4	1	8	0.30	1.69	1	4	0	5	0.40	2.45	0	2	1	3	0.25	1.40
15	2	6	7	15	1.18	6.64	7	12	11	30	1.13	6.36	3	5	5	13	1.03	6.37	1	0	1	2	0.17	0.93
17 <sub>1</sub>	3	2	0	5	0.39	2.21	3	0	4	7	0.26	1.48	0	1	0	1	0.08	0.49	3	0	1	4	0.33	1.87
17 <sub>2</sub>	6	3	1	10	0.79	4.42	10	2	5	17	0.64	3.60	1	3	1	5	0.40	2.45	3	1	1	5	0.42	2.34
19 <sub>1</sub>	2	2	1	5	0.39	2.21	1	3	3	7	0.26	1.48	1	0	1	2	0.16	0.98	2	0	4	6	0.50	2.80
19 <sub>2</sub>	1	2	0	3	0.24	1.33	1	4	1	6	0.23	1.27	0	1	1	2	0.16	0.98	2	0	1	3	0.25	1.40
21 <sub>1</sub>	0	1	1	2	0.16	0.88	3	2	2	7	0.26	1.48	0	0	1	1	0.08	0.49	0	2	2	4	0.33	1.87
21 <sub>2</sub>	1	2	0	3	0.24	1.33	1	2	6	9	0.34	1.91	3	2	4	9	0.71	4.41	3	0	3	6	0.50	2.80
23	1	2	0	3	0.24	1.33	5	5	4	14	0.53	2.97	4	3	3	10	0.79	4.90	4	3	1	8	0.67	3.74
25 <sub>1</sub>	0	1	1	2	0.16	0.88	2	2	1	5	0.19	1.06	0	1	1	2	0.16	0.98	1	0	1	2	0.17	0.93
25 <sub>2</sub>	0	2	0	2	0.16	0.88	7	5	4	16	0.61	3.39	1	2	0	3	0.24	1.47	2	0	3	5	0.42	2.34
27 <sub>1</sub>	0	2	2	4	0.31	1.77	0	4	1	5	0.19	1.06	2	2	0	4	0.32	1.96	0	1	2	3	0.25	1.40
27 <sub>2</sub>	3	2	1	6	0.47	2.65	8	2	4	14	0.53	2.97	3	2	1	6	0.47	2.94	1	1	2	4	0.33	1.87
29 <sub>1</sub>	1	1	0	2	0.16	0.88	1	2	0	3	0.11	0.64	0	2	0	2	0.16	0.98	0	1	0	1	0.08	0.47
29 <sub>2</sub>	0	0	0	0	0.00	0.00	4	5	2	11	0.42	2.33	4	1	1	6	0.47	2.94	0	3	1	4	0.33	1.87
31 <sub>1</sub>	0	0	2	2	0.16	0.88	3	2	1	6	0.23	1.27	1	1	0	2	0.16	0.98	1	0	0	1	0.08	0.47
31 <sub>2</sub>	2	1	4	7	0.55	3.10	5	5	1	11	0.42	2.33	1	2	3	6	0.47	2.94	1	0	1	2	0.17	0.93
33 <sub>1</sub>	0	0	1	1	0.08	0.44	2	0	1	3	0.11	0.64	0	1	2	3	0.24	1.47	3	2	4	9	0.75	4.21
33 <sub>2</sub>	4	0	1	5	0.39	2.21	2	2	4	8	0.30	1.69	2	1	2	5	0.40	2.45	0	0	4	4	0.33	1.87
33 <sub>3</sub>	0	2	3	5	0.39	2.21	2	0	0	2	0.08	0.42	0	1	0	1	0.08	0.49	1	0	1	2	0.17	0.93
35 <sub>1</sub>	3	1	0	4	0.31	1.77	3	3	2	8	0.30	1.69	2	1	1	4	0.32	1.96	1	1	1	3	0.25	1.40
35 <sub>2</sub>	1	2	1	4	0.31	1.77	3	4	3	10	0.38	2.12	1	0	0	1	0.08	0.49	1	0	2	3	0.25	1.40
37 <sub>1</sub>	0	2	0	2	0.16	0.88	0	1	1	2	0.08	0.42	0	1	0	1	0.08	0.49	0	1	0	1	0.08	0.47
37 <sub>2</sub>	2	0	2	4	0.31	1.77	0	1	2	3	0.11	0.64	0	0	2	2	0.16	0.98	1	1	1	3	0.25	1.40
37 <sub>3</sub>	3	2	0	5	0.39	2.21	1	3	1	5	0.19	1.06	1	0	0	1	0.08	0.49	1	1	1	3	0.25	1.40
39 <sub>1</sub>	1	0	0	1	0.08	0.44	1	1	2	4	0.15	0.85	1	0	1	2	0.16	0.98	1	0	0	1	0.08	0.47
39 <sub>2</sub>	2	1	1	4	0.31	1.77	3	6	4	13	0.49	2.75	1	0	4	5	0.40	2.45	1	2	0	3	0.25	1.40
41 <sub>1</sub>	0	1	0	1	0.08	0.44	0	1	0	1	0.04	0.21	0	1	0	1	0.08	0.49	2	0	0	2	0.17	0.93
41 <sub>2</sub>	3	0	1	4	0.31	1.77	2	0	3	5	0.19	1.06	2	1	1	4	0.32	1.96	0	0	1	1	0.08	0.47
41 <sub>3</sub>	0	0	0	0	0.00	0.00	0	0	1	1	0.04	0.21	0	0	0	0	0.00	0.00	1	0	2	3	0.25	1.40
43 <sub>1</sub>	0	0	0	0	0.00	0.00	0	1	1	2	0.08	0.42	0	0	0	0	0.00	0.00	0	0	0	0	0.00	0.00
43 <sub>2</sub>	0	1	2	3	0.24	1.33	5	0	1	6	0.23	1.27	0	0	1	1	0.08	0.49	2	0	0	2	0.17	0.93
43 <sub>3</sub>	0	1	0	1	0.08	0.44	3	0	0	3	0.11	0.64	0	1	1	2	0.16	0.98	0	1	2	3	0.25	1.40
45 <sub>1</sub>	0	0	0	0	0.00	0.00	2	1	2	5	0.19	1.06	0	1	1	2	0.16	0.98	0	0	1	1	0.08	0.47
45 <sub>2</sub>	2	1	1	4	0.31	1.77	2	0	4	6	0.23	1.27	1	1	1	3	0.24	1.47	1	0	0	1	0.08	0.47
45 <sub>3</sub>	0	2	0	2	0.16	0.88	1	2	0	3	0.11	0.64	3	0	0	3	0.24	1.47	2	2	1	5	0.42	2.34
47 <sub>1</sub>	1	0	0	1	0.08	0.44	1	1	1	3	0.11	0.64	0	0	1	1	0.08	0.49	1	1	1	3	0.25	1.40
47 <sub>2</sub>	1	0	0	1	0.08	0.44	0	3	1	4	0.15	0.85	0	0	0	0	0.00	0.00	0	0	0	0	0.00	0.00
49 <sub>1</sub>	0	1	0	1	0.08	0.44	1	1	0	2	0.08	0.42	0	0	0	0	0.00	0.00	0	0	0	0	0.00	0.00
49 <sub>2</sub>	0	0	1	1	0.08	0.44	4	2	1	7	0.26	1.48	1	0	2	3	0.24	1.47	0	1	0	1	0.08	0.47
49 <sub>3</sub>	1	1	0	2	0.16	0.88	3	3	3	9	0.34	1.91	0	0	0	0	0.00	0.00	1	0	2	3	0.25	1.40
Total	82	77	67	226	17.75	100.00	159	156	157	472	17.85	100.00	68	68	68	204	16.14	100.00	71	52	91	214	17.79	100.00

\* normalized over total GB's

\*\* normalized over CSL GB's

Table III.4  $\Sigma$  number fractions  $f_M \Sigma$  of GB's (%) in zirconia samples Z1, Z2, Z3 and Z4.

$\Sigma$	Alumina 1550 [°C]			Alumina 1700 [°C]			Alumina model***			$\Sigma$	Zirconia 1550 [°C]			Zirconia 1700 [°C]			Zirconia model***		
	Sum	$f_M \Sigma_{1550}^*$	$f_M \Sigma_{1550}^{**}$	Sum	$f_M \Sigma_{1700}^*$	$f_M \Sigma_{1700}^{**}$	Sum	$f_S \Sigma^*$	$f_S \Sigma^{**}$		Sum	$f_M \Sigma_{1550}^*$	$f_M \Sigma_{1550}^{**}$	Sum	$f_M \Sigma_{1700}^*$	$f_M \Sigma_{1700}^{**}$	Sum	$f_S \Sigma^*$	$f_S \Sigma^{**}$
3	59	0.64	16.12	26	0.67	15.12	150	0.09	3.26	3	77	1.97	11.03	45	1.82	10.77	2647	1.54	11.60
7 <sub>1</sub>	5	0.05	1.37	4	0.10	2.33	85	0.05	1.85	5	61	1.56	8.74	34	1.38	8.13	1867	1.08	8.18
7 <sub>2</sub>	5	0.05	1.37	3	0.08	1.74	98	0.06	2.13	7	33	0.84	4.73	21	0.85	5.02	1470	0.85	6.44
7 <sub>3</sub>	33	0.36	9.02	25	0.64	14.53	533	0.31	11.59	9	43	1.10	6.16	23	0.93	5.50	1508	0.87	6.61
8	16	0.17	4.37	8	0.21	4.65	209	0.12	4.54	11	45	1.15	6.45	34	1.38	8.13	1150	0.67	5.04
11 <sub>1</sub>	10	0.11	2.73	2	0.05	1.16	164	0.10	3.57	13 <sub>1</sub>	12	0.31	1.72	17	0.69	4.07	437	0.25	1.92
11 <sub>2</sub>	18	0.20	4.92	9	0.23	5.23	267	0.15	5.81	13 <sub>2</sub>	17	0.43	2.44	8	0.32	1.91	544	0.32	2.38
11 <sub>3</sub>	18	0.20	4.92	5	0.13	2.91	254	0.15	5.52	15	45	1.15	6.45	15	0.61	3.59	1369	0.79	6.00
12	1	0.01	0.27	0	0.00	0.00	32	0.02	0.70	17 <sub>1</sub>	12	0.31	1.72	5	0.20	1.20	232	0.13	1.02
13 <sub>1</sub>	6	0.07	1.64	0	0.00	0.00	27	0.02	0.59	17 <sub>2</sub>	27	0.69	3.87	10	0.41	2.39	593	0.34	2.60
13 <sub>2</sub>	15	0.16	4.10	4	0.10	2.33	201	0.12	4.37	19 <sub>1</sub>	12	0.31	1.72	8	0.32	1.91	456	0.26	2.00
13 <sub>3</sub>	4	0.04	1.09	2	0.05	1.16	19	0.01	0.41	19 <sub>2</sub>	9	0.23	1.29	5	0.20	1.20	304	0.18	1.33
13 <sub>4</sub>	13	0.14	3.55	7	0.18	4.07	211	0.12	4.59	21 <sub>1</sub>	9	0.23	1.29	5	0.20	1.20	265	0.15	1.16
13 <sub>5</sub>	2	0.02	0.55	2	0.05	1.16	43	0.02	0.93	21 <sub>2</sub>	12	0.31	1.72	15	0.61	3.59	853	0.49	3.74
14 <sub>1</sub>	10	0.11	2.73	10	0.26	5.81	186	0.11	4.04	23	17	0.43	2.44	18	0.73	4.31	712	0.41	3.12
14 <sub>2</sub>	0	0.00	0.00	1	0.03	0.58	14	0.01	0.30	25 <sub>1</sub>	7	0.18	1.00	4	0.16	0.96	157	0.09	0.69
15 <sub>1</sub>	9	0.10	2.46	5	0.13	2.91	90	0.05	1.96	25 <sub>2</sub>	18	0.46	2.58	8	0.32	1.91	643	0.37	2.82
15 <sub>2</sub>	2	0.02	0.55	1	0.03	0.58	80	0.05	1.74	27 <sub>1</sub>	9	0.23	1.29	7	0.28	1.67	264	0.15	1.16
17 <sub>1</sub>	11	0.12	3.01	3	0.08	1.74	137	0.08	2.98	27 <sub>2</sub>	20	0.51	2.87	10	0.41	2.39	577	0.33	2.53
17 <sub>2</sub>	6	0.07	1.64	2	0.05	1.16	63	0.04	1.37	29 <sub>1</sub>	5	0.13	0.72	3	0.12	0.72	62	0.04	0.27
17 <sub>3</sub>	9	0.10	2.46	6	0.15	3.49	121	0.07	2.63	29 <sub>2</sub>	11	0.28	1.58	10	0.41	2.39	496	0.29	2.17
17 <sub>4</sub>	1	0.01	0.27	0	0.00	0.00	36	0.02	0.78	31 <sub>1</sub>	8	0.20	1.15	3	0.12	0.72	120	0.07	0.53
18	1	0.01	0.27	1	0.03	0.58	50	0.03	1.09	31 <sub>2</sub>	18	0.46	2.58	8	0.32	1.91	489	0.28	2.14
19 <sub>1</sub>	0	0.00	0.00	1	0.03	0.58	22	0.01	0.48	33 <sub>1</sub>	4	0.10	0.57	12	0.49	2.87	235	0.14	1.03
19 <sub>2</sub>	11	0.12	3.01	3	0.08	1.74	110	0.06	2.39	33 <sub>2</sub>	13	0.33	1.86	9	0.36	2.15	425	0.25	1.86
19 <sub>3</sub>	2	0.02	0.55	4	0.10	2.33	34	0.02	0.74	33 <sub>3</sub>	7	0.18	1.00	3	0.12	0.72	206	0.12	0.90
19 <sub>4</sub>	4	0.04	1.09	2	0.05	1.16	56	0.03	1.22	35 <sub>1</sub>	12	0.31	1.72	7	0.28	1.67	388	0.23	1.70
20 <sub>1</sub>	13	0.14	3.55	3	0.08	1.74	116	0.07	2.52	35 <sub>2</sub>	14	0.36	2.01	4	0.16	0.96	413	0.24	1.81
20 <sub>2</sub>	1	0.01	0.27	0	0.00	0.00	16	0.01	0.35	37 <sub>1</sub>	4	0.10	0.57	2	0.08	0.48	10	0.01	0.04
21 <sub>1</sub>	2	0.02	0.55	2	0.05	1.16	19	0.01	0.41	37 <sub>2</sub>	7	0.18	1.00	5	0.20	1.20	361	0.21	1.58
21 <sub>2</sub>	7	0.08	1.91	3	0.08	1.74	102	0.06	2.22	37 <sub>3</sub>	10	0.26	1.43	4	0.16	0.96	54	0.03	0.24
21 <sub>3</sub>	1	0.01	0.27	0	0.00	0.00	10	0.01	0.22	39 <sub>1</sub>	5	0.13	0.72	3	0.12	0.72	35	0.02	0.15
22 <sub>1</sub>	6	0.07	1.64	7	0.18	4.07	109	0.06	2.37	39 <sub>2</sub>	17	0.43	2.44	8	0.32	1.91	677	0.39	2.97
22 <sub>2</sub>	0	0.00	0.00	0	0.00	0.00	4	0.00	0.09	41 <sub>1</sub>	2	0.05	0.29	3	0.12	0.72	67	0.04	0.29
23 <sub>1</sub>	1	0.01	0.27	1	0.03	0.58	19	0.01	0.41	41 <sub>2</sub>	9	0.23	1.29	5	0.20	1.20	300	0.17	1.32
23 <sub>2</sub>	5	0.05	1.37	1	0.03	0.58	40	0.02	0.87	41 <sub>3</sub>	1	0.03	0.14	3	0.12	0.72	84	0.05	0.37
23 <sub>3</sub>	3	0.03	0.82	2	0.05	1.16	105	0.06	2.28	43 <sub>1</sub>	2	0.05	0.29	0	0.00	0.00	60	0.03	0.26
23 <sub>4</sub>	8	0.09	2.19	4	0.10	2.33	71	0.04	1.54	43 <sub>2</sub>	9	0.23	1.29	3	0.12	0.72	291	0.17	1.28
23 <sub>5</sub>	6	0.07	1.64	2	0.05	1.16	95	0.06	2.07	43 <sub>3</sub>	4	0.10	0.57	5	0.20	1.20	156	0.09	0.68
24	3	0.03	0.82	0	0.00	0.00	53	0.03	1.15	45 <sub>1</sub>	5	0.13	0.72	3	0.12	0.72	304	0.18	1.33
25 <sub>1</sub>	2	0.02	0.55	0	0.00	0.00	11	0.01	0.24	45 <sub>2</sub>	10	0.26	1.43	4	0.16	0.96	276	0.16	1.21
25 <sub>2</sub>	10	0.11	2.73	3	0.08	1.74	80	0.05	1.74	45 <sub>3</sub>	5	0.13	0.72	8	0.32	1.91	288	0.17	1.26
25 <sub>3</sub>	2	0.02	0.55	1	0.03	0.58	18	0.01	0.39	47 <sub>1</sub>	4	0.10	0.57	4	0.16	0.96	268	0.16	1.17
26	3	0.03	0.82	1	0.03	0.58	86	0.05	1.87	47 <sub>2</sub>	5	0.13	0.72	0	0.00	0.00	237	0.14	1.04
27 <sub>1</sub>	4	0.04	1.09	1	0.03	0.58	79	0.05	1.72	49 <sub>1</sub>	3	0.08	0.43	0	0.00	0.00	3	0.00	0.01
27 <sub>2</sub>	3	0.03	0.82	2	0.05	1.16	71	0.04	1.54	49 <sub>2</sub>	8	0.20	1.15	4	0.16	0.96	230	0.13	1.01
27 <sub>3</sub>	3	0.03	0.82	3	0.08	1.74	64	0.04	1.39	49 <sub>3</sub>	11	0.28	1.58	3	0.12	0.72	228	0.13	1.00
28 <sub>1</sub>	7	0.08	1.91	0	0.00	0.00	71	0.04	1.54										
28 <sub>2</sub>	5	0.05	1.37	0	0.00	0.00	68	0.04	1.48										
Total	366	3.98	100.00	172	4.44	100.00	4599	2.67	100.00		698	17.82	100.00	418	16.94	100.00	22811	13.23	100.00

\* normalized over total GB's  
\*\* normalized over CSL GB's  
\*\*\* simulated for 50000 grains ( $n_{GB's} = 172378$ )

**Table III.5**  $\Sigma$  number fractions of GB's (%) for alumina and zirconia average samples sintered at 1550°C ( $f_M \Sigma_{1550}$ ) and 1700°C ( $f_M \Sigma_{1700}$ ), as well as for the simulated 2D spatial models ( $f_S \Sigma$ ).

	Z1				Z2				Z3				Z4				1550 [°C]		1700 [°C]		Model
	2	3	4	Sum	2	3	4	Sum	2	3	4	Sum	2	3	4	Sum	Sum	[%]	Sum	[%]	[%]
J <sub>0</sub>	206	154	162	522	321	324	328	973	159	179	187	525	155	164	145	464	1495	55.13	989	59.15	60.25
J <sub>1</sub>	141	125	102	368	199	204	203	606	85	109	89	283	85	77	120	282	974	35.91	565	33.79	32.95
J <sub>2</sub>	29	34	33	96	43	41	41	125	22	11	21	54	19	13	28	60	221	8.15	114	6.82	6.70
J <sub>3</sub>	3	4	2	9	7	3	3	13	0	0	2	2	1	1	0	2	22	0.81	4	0.24	0.10
Total	379	317	299	995	570	572	575	1717	266	299	299	864	260	255	293	808	2712	100.00	1672	100.00	100.00

**Table III.6** Triple junction fractions  $J_n$  (%) with  $n$  the number of CSL GB's. Values for both zirconia average samples and for the simulated 2D random model were obtained from GB counting in EBSD scan 2, 3 and 4 of samples Z1, Z2, Z3 and Z4.

## III.4 EBSD DATA

### III.4.1 Crystallographic files used for indexing

The crystallographic files for alumina and zirconia were generated according to the procedure described in Section 2.2.3. Lattice constants and reflectors are shown in Table III.7.

### III.4.2 List of EBSD runs

The list of EBSD runs for the eight ceramic samples is shown in Table III.8

### III.4.3 Maps and texture plots

Four EBSD scans were performed for each of the eight ceramic samples. Scan 1 was performed over large areas and was used to calculate the LPO. As it is generally the case in material sciences, the texture plots represent *upper* hemisphere equal area projections, contrary to the standard habit in earth sciences. Contours are multiples of uniform distribution, assuming 0.025 intervals. The maximum densities of the LPO were calculated using the EDAX<sup>®</sup> (TSL) OIM Analysis 3.08. Because of the fixed scanning direction of our system in beam scan mode (opposite to TD and RD settings), all scan images were rotated 180° to match the TD and RD directions (s. Section 2.2.6.2). Spherical harmonics truncated at an expansion of 22 with a Gaussian half width of 15° were used for calculations. The scans 2, 3 and 4 focused on restricted areas of the material surface and were aimed at highlighting a sufficient number of CSL

GB's. Crystallographic orientation and CSL maps, as well as SEM images captured by secondary or fore-scatter electrons are shown for both alumina and zirconia samples. As GB's can only be identified when the points of adjacent grains are in contact, a smooth cleaning up of CSL maps was performed. The legend and the layout applied to EBSD data for ceramics are shown in Fig. III.17 and III.18. Maps and texture plots are presented in Fig. III.19.

	Alumina	Zirconia
Space group	R-3c	Fm3m
Lattice constants		
a [nm]	4.76	18.241
c [nm]	12.99	/
$\alpha$ [°]	90.0	90.0
$\gamma$ [°]	120.0	/
Reflectors (hk(i)l)		
	-1 1 0 4	1 1 1
	-1 -1 2 0	0 0 2
	-2 1 1 3	2 0 2
	2 -2 0 4	1 1 3
	-1 2 -1 6	3 1 3
	0 1 -1 8	2 0 4
	1 -3 2 4	2 2 4
	3 0 -3 0	1 1 5
	0 -1 1 10	3 1 5
	1 -2 1 9	
	4 -2 -2 3	
	-1 -3 4 2	
	0 2 -2 10	
	0 0 0 12	
	-1 4 -3 4	
	4 -4 0 2	
	1 -3 2 10	
	2 -4 2 9	
	-2 -3 5 4	
	-1 0 1 14	

**Table III.7** Lattice constants and reflectors used for indexing alumina and zirconia.

Sample	Scan	Scan mode	Step size [ $\mu\text{m}$ ]	Area [ $\mu\text{m}^2$ ]	Measurements	Measurements with CI $\geq 0.2$	Average CI*	Number of grains	Average grain diameter** [ $\mu\text{m}$ ]	LPO (J index***)
A1	1	beam scan	5	500x500	11658	5195 (44.6%)	0.25 (0.48)	5195	/	1.05
	2	beam scan	0.4	50x50	18198	11851 (65.1%)	0.37 (0.53)	556	/	/
	3	beam scan	0.4	50x50	18198	12243 (67.3%)	0.38 (0.53)	549	2.1	/
	4	beam scan	0.4	50x50	18198	13559 (75.4%)	0.43 (0.56)	730	/	/
A2	1	beam scan	5	500x500	11658	5233 (44.9%)	0.25 (0.48)	5233	/	1.04
	2	beam scan	0.4	50x50	18198	13672 (75.1%)	0.44 (0.56)	639	/	/
	3	beam scan	0.4	50x50	18198	11829 (65.0%)	0.36 (0.52)	613	2.1	/
	4	beam scan	0.4	50x50	18198	11876 (65.3%)	0.37 (0.52)	575	/	/
A3	1	beam scan	15	1500x1500	11658	6495 (55.7%)	0.31 (0.50)	6495	/	1.03
	2	beam scan	0.8	100x100	18198	15052 (82.7%)	0.48 (0.57)	281	/	/
	3	beam scan	0.8	100x100	18198	15057 (82.7%)	0.49 (0.57)	260	6.2	/
	4	beam scan	0.8	100x100	18198	14838 (81.5%)	0.49 (0.58)	284	/	/
A4	1	beam scan	15	1500x1500	11658	6164 (52.9%)	0.29 (0.49)	6164	/	1.03
	2	beam scan	0.8	100x100	18198	14378 (79.0%)	0.45 (0.55)	264	/	/
	3	beam scan	0.8	100x100	18198	14927 (82.0%)	0.48 (0.57)	265	6.4	/
	4	beam scan	0.8	100x100	18198	14709 (80.8%)	0.48 (0.57)	250	/	/
Z1	1	beam scan	5	500x500	11658	8475 (72.7%)	0.43 (0.57)	8475	/	1.00
	2	beam scan	0.4	50x50	18198	17162 (94.3%)	0.59 (0.62)	251	/	/
	3	beam scan	0.4	50x50	18198	17264 (94.9%)	0.59 (0.62)	210	3.5	/
	4	beam scan	0.4	50x50	18198	17213 (94.6%)	0.59 (0.62)	194	/	/
Z2	1	beam scan	15	1500x1500	11658	7408 (63.5%)	0.37 (0.53)	7408	/	1.00
	2	beam scan	0.8	100x100	18198	16881 (92.8%)	0.57 (0.60)	344	/	/
	3	beam scan	0.8	100x100	18198	16799 (92.3%)	0.57 (0.61)	336	5.8	/
	4	beam scan	0.8	100x100	18198	16462 (90.5%)	0.55 (0.60)	332	/	/
Z3	1	beam scan	15	1500x1500	11658	7187 (61.6%)	0.36 (0.53)	7187	/	1.01
	2	beam scan	0.8	100x100	18198	16856 (92.6%)	0.56 (0.60)	157	/	/
	3	beam scan	0.8	100x100	18198	16840 (92.5%)	0.56 (0.60)	181	7.8	/
	4	beam scan	0.8	100x100	18198	16881 (92.8%)	0.55 (0.59)	181	/	/
Z4	1	beam scan	15	1500x1500	11658	8507 (73.0%)	0.43 (0.56)	8507	/	1.00
	2	beam scan	0.8	100x100	18198	17359 (95.4%)	0.58 (0.60)	160	/	/
	3	beam scan	0.8	100x100	18198	17382 (95.5%)	0.60 (0.62)	158	8.3	/
	4	beam scan	0.8	100x100	18198	17423 (95.7%)	0.61 (0.63)	172	/	/

\* in brackets the average CI considering only the values  $\geq 0.2$

\*\* calculated from the scans 2, 3 and 4 using the equivalent disc diameter method

\*\*\* calculated from scan 1 using EDAX<sup>®</sup> (TSL) OIM Analysis 3.08 algorithms for an expansion coefficient of 22 and a Gaussian half width of 15°

Table III.8 EBSD data for the eight ceramic samples.

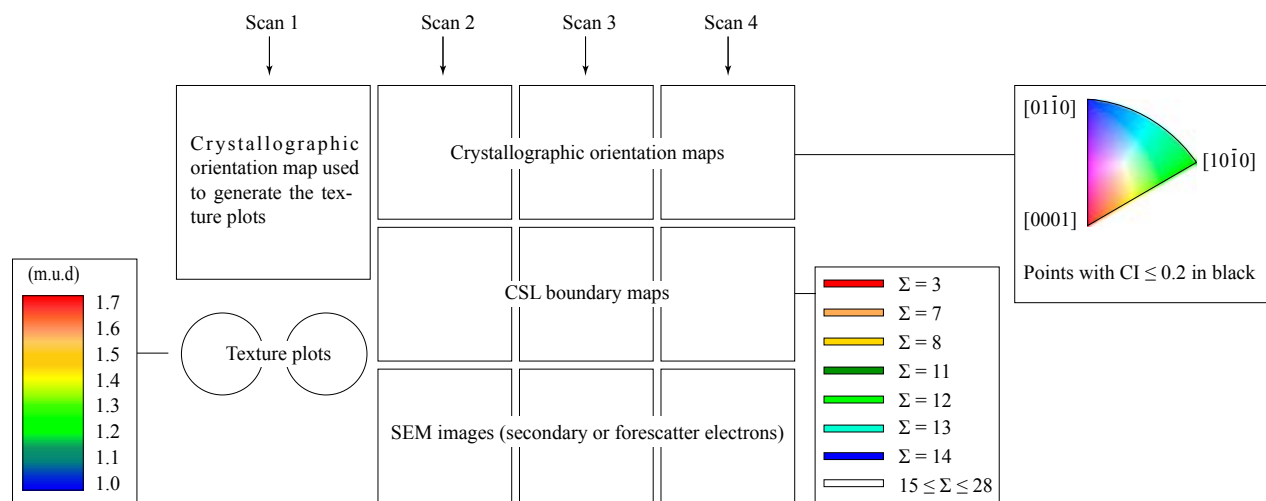


Fig. III.17 Legend and layout for the alumina maps and plots displayed in Fig. III.19.

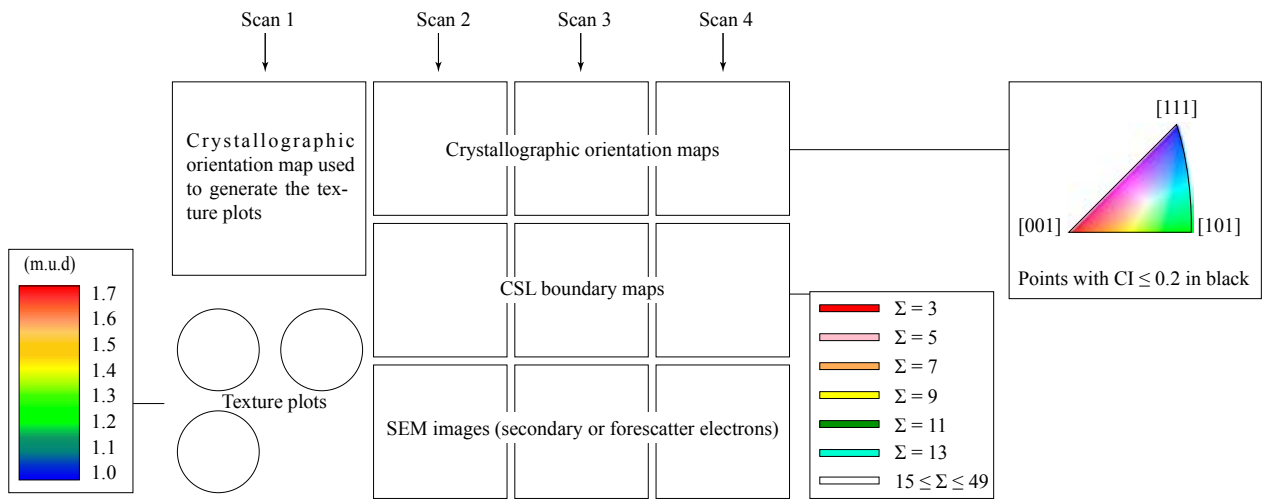


Fig. III.18 Legend and layout for the zirconia maps and plots displayed in Fig. III.19.

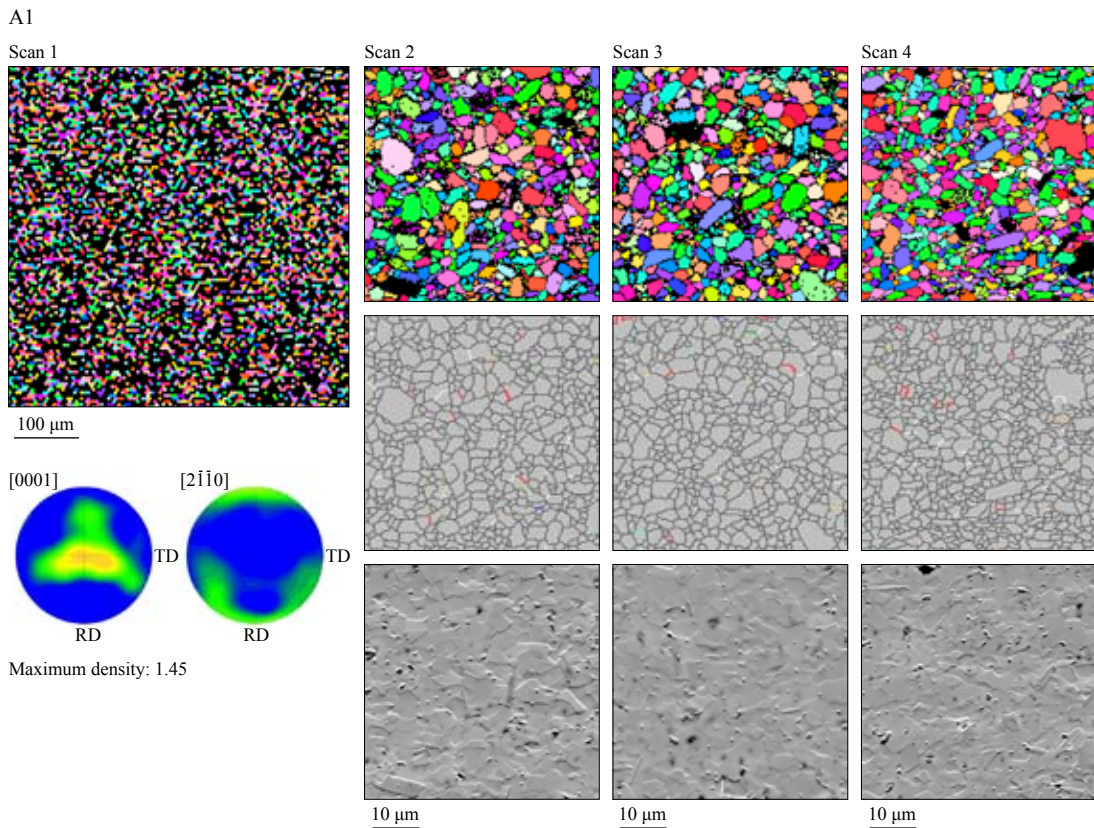


Fig. III.19 Phase maps, crystallographic orientation maps and texture plots for alumina and zirconia ceramics (s. also next pages).

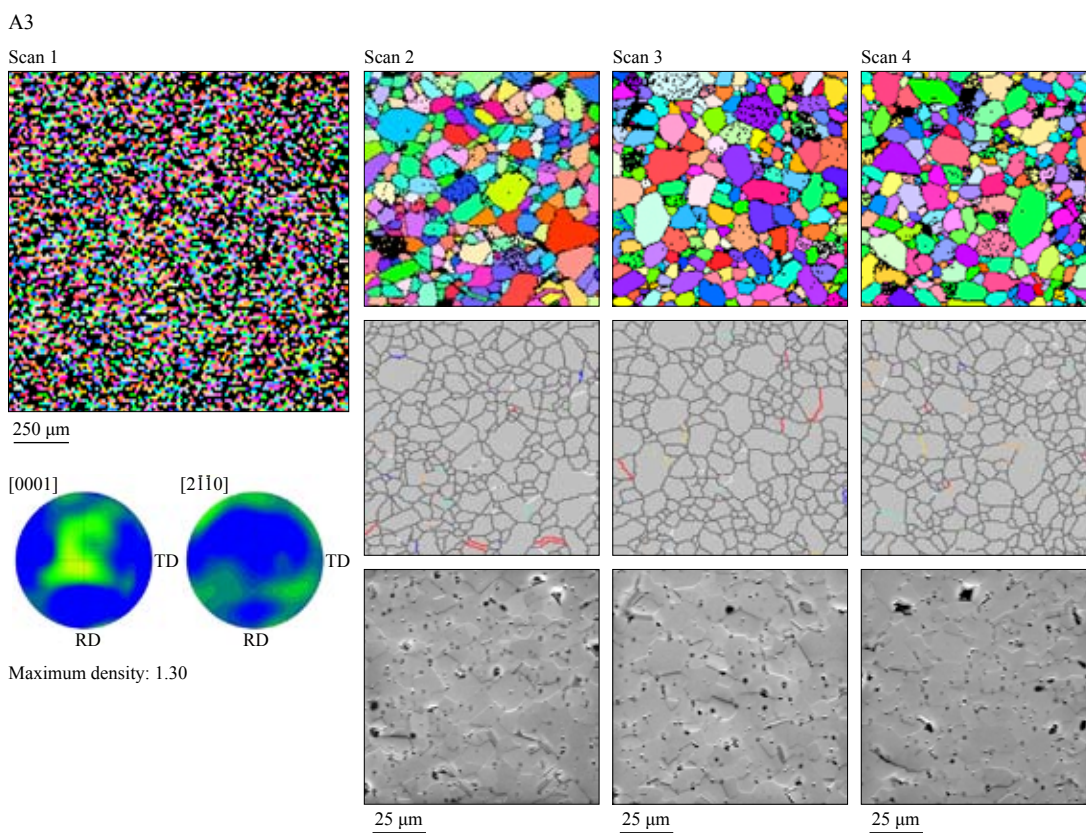
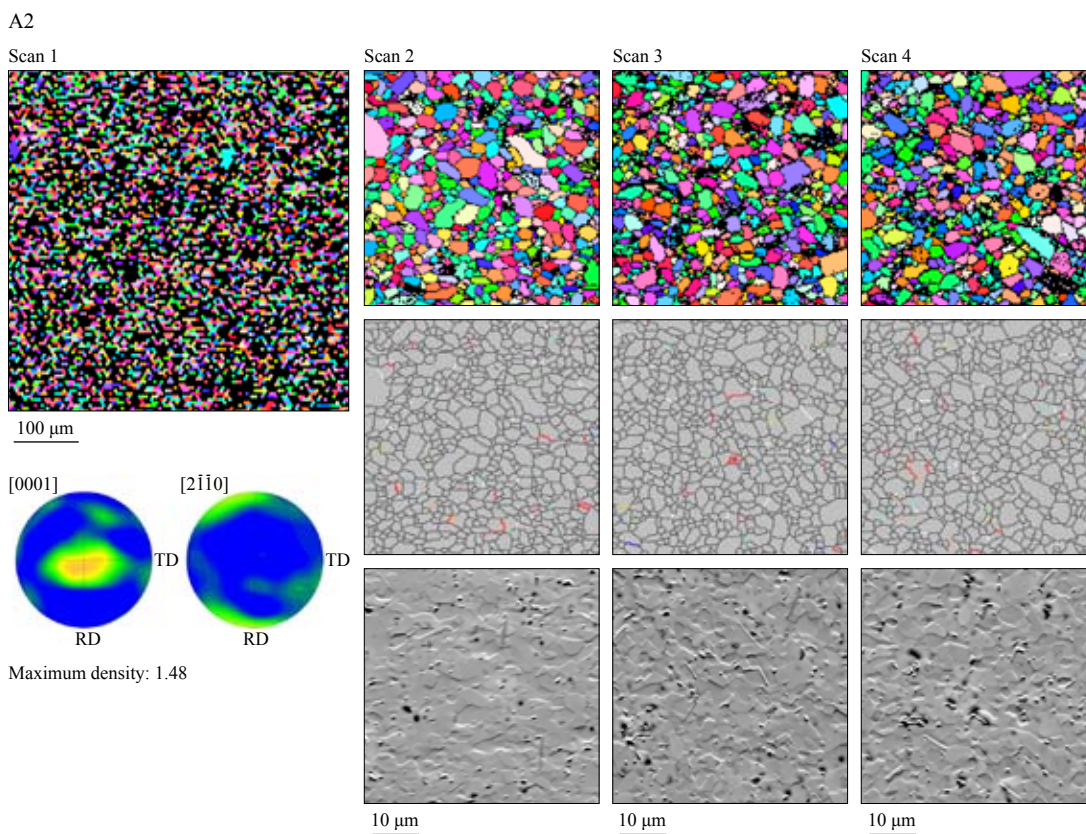


Fig. III.19 (continued).

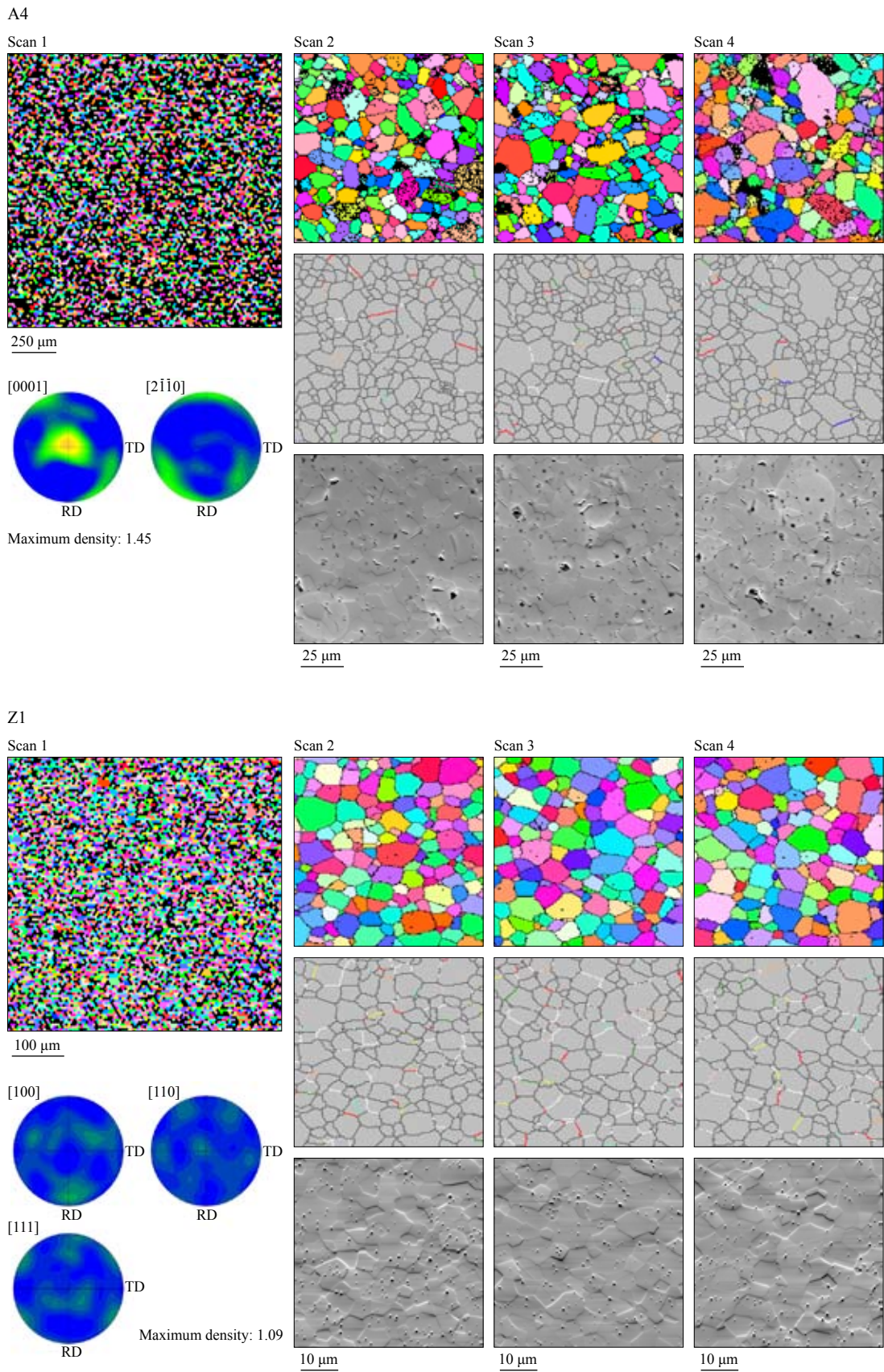
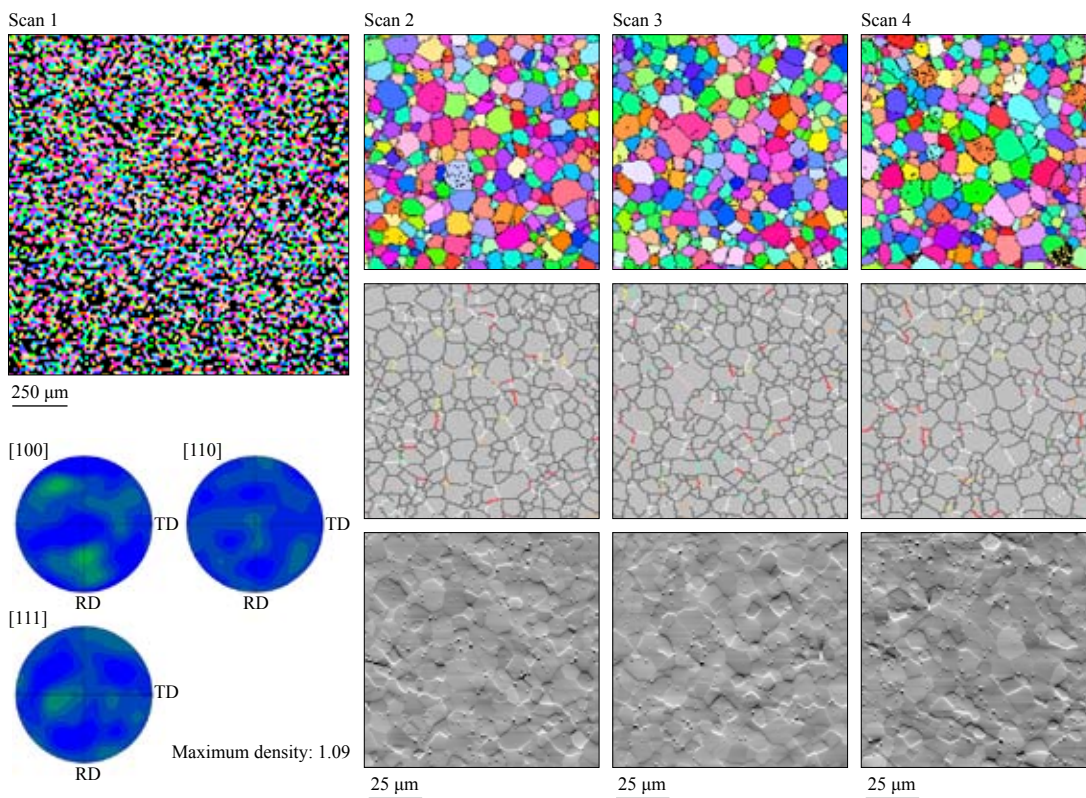


Fig. III.19 (continued).

Z2



Z3

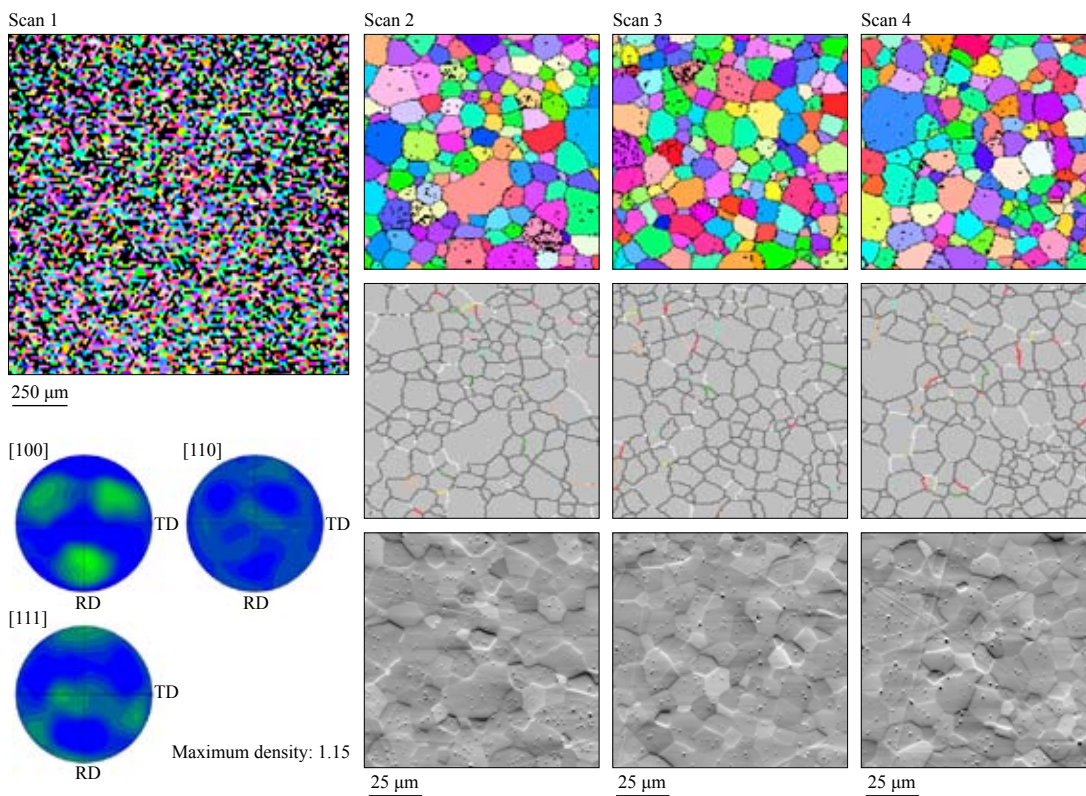
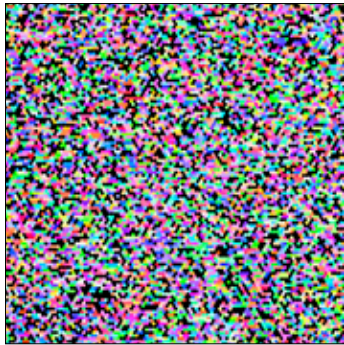


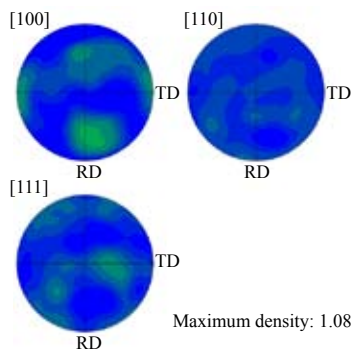
Fig. III.19 (continued).

Z4

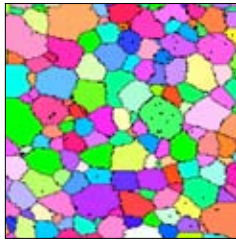
Scan 1



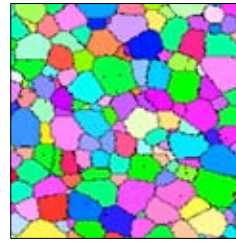
250 μm



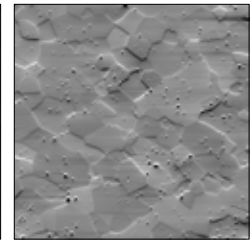
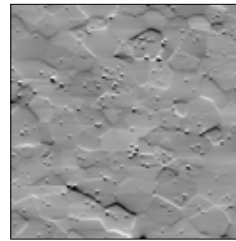
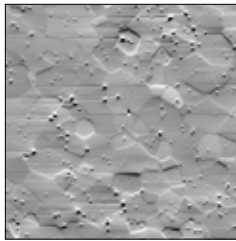
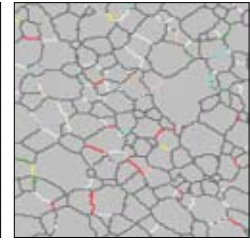
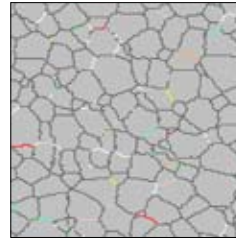
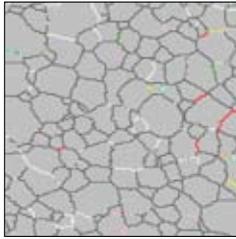
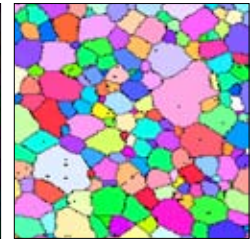
Scan 2



Scan 3



Scan 4



25 μm

25 μm

25 μm

Fig. III.19 (continued).

\*\*\*\*\*



## REFERENCES

- ABDEL MONEM A., WATKINS N.D. & GAST P.W. 1971. Potassium-argon ages, volcanic stratigraphy, and geomagnetic polarity history of the Canary Islands: Lanzarote, Fuerteventura, Gran Canaria, La Gomera. *American Journal of Science* 271, 490-521.
- ABRAMSON E.H., BROWN J.M., SLUTSKY L.J. & ZAUG J. 1997. The elastic constants of San Carlos olivine to 17 GPa. *Journal of Geophysical Research* 102, 12253-12263.
- ADAMS B.L., WRIGHT S.I. & KUNZE K. 1993. Orientation imaging: the emergence of a new microscopy. *Metallurgical Transactions A* 24, 819-831.
- ALCOA WORLD CHEMICALS. 2000. Product data - Reactive and calcined aluminas for the ceramic industry. <http://www.alcoa.com>.
- ALLÈGRE C.J., HAMELIN B. & DUPRÉ B. 1984. Statistical analysis of isotopic ratios in MORB: the mantle blob cluster and the convective regime of the mantle. *Earth and Planetary Science Letters* 71, 71-84.
- ANGUITA F. & HERNÁN F. 1975. A propagating fracture model versus a hot spot in the Canary Islands. *Earth and Planetary Science Letters* 27, 11-19.
- ANGUITA F. & HERNÁN F. 2000. The Canary Islands origin: a unifying model. *Journal of Volcanology and Geothermal Research* 103, 1-26.
- ARAÑA V. & ORTIZ R. 1986. Marco geodinámico del volcanismo canario. *Anales de Física* 82, 202-231.
- BANDA E., DAÑOBEITIA J.J., SURIÑACH E. & ANSORGE J. 1981. Features of crustal structure under the Canary Islands. *Earth and Planetary Science Letters* 55, 11-24.
- BARRUOL G. & KERN H. 1996. Seismic anisotropy and shear-wave splitting in the lower-crustal and upper-mantle rocks from the Ivrea Zone - Experimental and calculated data. *Physics of the Earth and Planetary Interiors* 95, 175-194.
- BARSOUM M.W. 1997. *Fundamentals of Ceramics*. McGraw-Hill, Singapore, 669 pp.
- BELL T.H., JOHNSON S.E., DAVIS B., FORDE A., HAYWARD N. & WILKINS C. 1992. Porphyroblast inclusion-trail orientation data; eppure non son girate! *Journal of Metamorphic Geology* 10, 295-307.
- BEN ISMAIL W. & MAINPRICE D. 1998. An olivine fabric database: an overview of upper mantle fabrics and seismic anisotropy. *Tectonophysics* 296, 145-157.
- BENNISON S.J. & HARMER M.P. 1990. A history of the role of MgO in the sintering of  $\alpha$ -Al<sub>2</sub>O<sub>3</sub>. *Ceramic Transactions* 7, 13-49.
- BERNACHE-ASSOLANT D. 1993. *Chimie-Physique du Frittage*. Hermès, Paris, 348 pp.
- BLACKMAN D.K., KENDALL J.M., DAWSON P.R., WENK H.R., BOYCE D. & MORGAN J.P. 1996. Teleseismic imaging of subaxial flow at mid-ocean ridges: travelttime effects of anisotropic mineral texture in the mantle. *Geophysical Journal International* 127, 415-426.
- BLACKMAN D.K., ILDEFONSE B., JOHN B.E., OHARA Y., MILLER D.J. & MACLEOD C.J. 2006. Expedition 304/305 reports. *Proceedings of the Integrated Ocean Drilling Program 304/305*.
- BOLLMANN W. 1970. *Crystal Defects and Crystalline Interfaces*. Springer Verlag, Berlin, 600 pp.
- BONATTI E. 1990. Subcontinental mantle exposed in the Atlantic Ocean on St Peter-Paul islets. *Nature* 345, 800-802.
- BONNET R., COUSINEAU E. & WARRINGTON D.H. 1981. Determination of near-coincident cells in hexagonal crystals - related DSC lattices. *Acta Crystallographica A* 37, 184-189.
- BOSSHARD E. & MACFARLANE D.J. 1970. Crustal structure of the western Canary Islands from seismic refraction and gravity data. *Journal of Geophysical Research* 75, 4901-4918.
- BOULLIER A.M. & NICOLAS A. 1975. Classification of textures and fabrics of peridotite xenoliths from South African kimberlites. *Physics and Chemistry of the Earth* 9, 467-475.
- BRAGG W.L. & BROWN G.B. 1926. The structure of olivine. *Zeitschrift für Kristallographie* 63, 538-556.
- BRANDON D.G. 1966. Structure of high-angle grain boundaries. *Acta Metallurgica* 14, 1479-1484.
- BROCKHOUSE B.N. 1953. The initial magnetization of nickel under tension. *Canadian Journal of Physics* 31, 339-355.

- BROTHERS R.N. & RODGERS K.A. 1969. Petrofabric studies of ultramafic nodules from Auckland, New Zealand. *Journal of Geology* 77, 452-465.
- BRUGGEMANN G.A., BISHOP G.H. & HARTT W.H. 1972. The Nature and Behavior of Grain Boundaries. In: Plenum Press, New York, 83-110.
- BÜCHI LABORTECHNIK AG. 2000. Büchi B-190 mini spray dryer - Operating Instruction.
- BUNGE H.J. 1965. Zur Darstellung allgemeiner Texturen. *Zeitschrift für Metallkunde* 56, 872-874.
- BUNGE H.J. 1982. *Texture Analysis in Materials Science*. Butterworth, London, 559 pp.
- BURKE K. & WILSON J.T. 1972. Is the African plate stationary? *Nature* 239, 387-390.
- BYSTRICKY M., KUNZE K., BURLINI L. & BURG J.P. 2000. High shear strain of olivine aggregates: rheological and seismic consequences. *Science* 290, 1564-1567.
- CAMACHO A.G. & VIEIRA R. 1991. Gravimetric study of Lanzarote island. *Cahiers du Centre Européen de Géodynamique et de Séismologie* 4, 339-351.
- CANNON R.M., RHODES W.H. & HEUER A.H. 1980. Plastic deformation of fine-grained alumina ( $\text{Al}_2\text{O}_3$ ). 1. Interface-controlled diffusional creep. *Journal of the American Ceramic Society* 63, 46-53.
- CARLSON W.D. 1989. The significance of intergranular diffusion to the mechanism and kinetics of porphyroblast crystallization. *Contributions to Mineralogy and Petrology* 103, 1-24.
- CARLSON W.D. 1991. Competitive diffusion-controlled growth of porphyroblasts. *Mineralogical Magazine* 55, 317-330.
- CARRACEDO J.C., DAY S., GUILLOU H., RODRÍGUEZ BADIOLA E., CANAS J.A. & PÉREZ TORRADO F.J. 1998. Hotspot volcanism close to a passive continental margin: the Canary Islands. *Geological Magazine* 135, 591-604.
- CARRY C. & MOCELLIN A. 1987. Structural superplasticity in single-phase crystalline ceramics. *Ceramics International* 13, 89-98.
- CARTER C.B. & AVÉ LALLEMANT H.G. 1970. High temperature flow of dunite and peridotite. *Geological Society of America Bulletin* 81, 2181-2202.
- CHADWICK B. 1968. Deformation and metamorphism in the Lukmanier region, central Switzerland. *Geological Society of America Bulletin* 79, 1123-1149.
- CHAI M., BROWN J.M. & SLUTSKY L.J. 1997. The elastic constants of an aluminous orthopyroxene to 12.5 GPa. *Journal of Geophysical Research* 102, 14779-14785.
- CHO J., CHAN H.M., HARMER M.P. & RICKMAN J.M. 1998. Influence of yttrium doping on grain misorientation in aluminum oxide. *Journal of the American Ceramic Society* 81, 3001-3004.
- CHO J., WANG C.M., CHAN H.M., RICKMAN J.M. & HARMER M.P. 2002. A study of grain-boundary structure in rare-earth doped aluminas using an EBSD technique. *Journal of Materials Science* 37, 59-64.
- CHOPRA P.N. & PATERSON M.S. 1981. The experimental deformation of dunite. *Tectonophysics* 78, 453-473.
- CHRISTENSEN N.I. & SALISBURY M.H. 1979. Seismic anisotropy of the oceanic upper mantle: evidence from the Bay of Islands Ophiolite Complex. *Journal of Geophysical Research* 84, 4601-4610.
- CHRISTENSEN N.I. 1984. The magnitude, symmetry and origin of upper mantle anisotropy based on fabric analyses of ultramafic tectonites. *Geophysical Journal of the Royal Astronomical Society* 76, 89-111.
- COATES D.G. 1967. Kikuchi-like reflection patterns obtained with scanning electron microscope. *Philosophical Magazine* 16, 1179-1184.
- COBLE R.L. 1961. Sintering crystalline solids. 2. Experimental test of diffusion model in powder compacts. *Journal of Applied Physics* 32, 793-799.
- COE R.S. & KIRBY S.H. 1975. The orthoenstatite to clinoenstatite transformation by shearing and reversion by annealing: mechanism and potential applications. *Contributions to Mineralogy and Petrology* 52, 29-55.
- COELLO J., CANTAGREL J.M., HERNÁN F., FÚSTER J.M., IBARROLA E., ANCOCHEA E., CASQUET C., JAMOND C., DÍAZ DE TÉRAN J.R. & CENDRERO A. 1992. Evolution of the eastern volcanic ridge of the Canary Islands based on new K-Ar data. *Journal of Volcanology and Geothermal Research* 53, 251-274.
- COISY P. 1977. Structure et chimisme des péridotites en enclaves dans les basaltes du Massif Central. Modèles géodynamiques du manteau supérieur. PhD Thesis, Nantes.
- COLLINS M.D. & BROWN J.M. 1998. Elasticity of an upper mantle clinopyroxene. *Physics and Chemistry of Minerals* 26, 7-13.
- CONTRUCCI I., KLINGELHÖFER F., PERROT J., BARTOLOME R., GUTSCHER M.A., SAHABI M., MALOD J. & REHAULT J.P. 2004. The crustal structure of the NW Moroccan continental margin from wide-angle and reflection seismic data. *Geophysical Journal International* 159, 117-128.
- DANOBEITIA J.J. & CANALES J.P. 2000. Magmatic underplating in the Canary Archipelago. *Journal of Volcanology and Geothermal Research* 103, 27-41.
- DASH B.P. & BOSSHARD E. 1969. Seismic and gravity investigations around the western Canary Islands. *Earth and Planetary Science Letters* 7, 169-177.
- DEER W.A., HOWIE R.A. & ZUSSMAN J. 1992. *An Introduction to Rock-forming Minerals*. Longman, 696 pp.
- DELFOSE D. & AEBERHARD M. 1997. Tiefenprofilanalysen von technischen Schichten und Oberflächen. Teil 1: Grundlagen des GD-OES und Beispiele aus der Galvanik. In: *Oberflächen-Polysurfaces*, 7-10.
- DIMOS D., CHAUDHARI P., MANNHART J. & LEGOUES F.K. 1988. Orientation dependence of grain boundary critical currents in  $\text{YBa}_2\text{Cu}_3\text{O}_{7-\delta}$  bicrystals. *Physical Review Letters* 61, 219-222.

- DINGLEY D.J. & STEEDS J.W. 1974. Application of Kossel X-ray diffraction in the SEM. In: Quantitative Scanning Electron Microscopy, Academic Press, London, 487-516.
- DINGLEY D.J. & RANDLE V. 1992. Microstructure determination by electron backscatter diffraction. *Journal of Materials Science* 27, 4545-4566.
- DINGLEY D.J. 2000. The development of automated diffraction in scanning and transmission electron microscopy. In: *Electron Backscatter Diffraction in Materials Science*, Kluwer Academic/Plenum Publishers, New York, 1-16.
- ENGI M., TODD C.S. & SCHMATZ D.R. 1995. Tertiary metamorphic conditions in the eastern Lepontine Alps. *Schweizerische Mineralogische und Petrographische Mitteilungen* 75, 347-369.
- ESTEY L.H. & DOUGLAS B.J. 1986. Upper mantle anisotropy: a preliminary model. *Journal of Geophysical Research* 91, 11393-11406.
- FARYNA M., JURA J. & SZTWIERTNIA K. 2000. Orientation imaging microscopy applied to zirconia ceramics. *Mikrochimica Acta* 132, 517-520.
- FARYNA M., BISCHOFF E. & SZTWIERTNIA K. 2002. Crystal orientation mapping applied to the Y-TZP/WC composite. *Mikrochimica Acta* 139, 55-59.
- FINGER L.W. & OHASHI Y. 1976. The thermal expansion of diopside to 800°C and a refinement of the crystal structure at 700°C. *American Mineralogist* 61, 303-310.
- FISCHMEISTER H.F. 1985. Structure and properties of high angle grain boundaries. *Journal de Physique* 46, 3-23.
- FORSYTH D.W. 1975. The early structural evolution and anisotropy of the oceanic upper mantle. *Geophysical Journal of the Royal Astronomical Society* 43, 103-162.
- FOX J.S. 1975. Three-dimensional isograds from the Lukmanier Pass, Switzerland, and their tectonic significance. *Geological Magazine* 112, 547-564.
- FRESE K., TROMMSDORFF V. & KUNZE K. 2003. Olivine [100] normal to foliation: lattice preferred orientation in prograde garnet peridotite formed at high H<sub>2</sub>O activity, Cima di Gagnone (Central Alps). *Contributions to Mineralogy and Petrology* 145, 76-85.
- FRISILLO A.L. & BARSCH G.R. 1972. Measurement of single-crystal elastic constants of bronzite as a function of pressure and temperature. *Journal of Geophysical Research* 77, 6360-6385.
- FÚSTER J.M. & AGUILAR M. 1965. Nota brevia sobre la geología del macizo de Betancuria, Fuerteventura. *Estudios Geológicos* 21, 181-198.
- FÚSTER J.M., FERNÁNDEZ SANTIN S. & SAGREDO J. 1968. Geology and volcanology of the Canary Islands, Lanzarote. Instituto Lucas Mallada, Madrid, 177 pp.
- FÚSTER J.M. 1975. Las Islas Canarias: un ejemplo de evolución temporal y especial del vulcanismo oceánico. *Estudios Geológicos* 31, 439-463.
- FYNN G.W. & POWELL W.J.A. 1979. The Cutting and Polishing of Electro-Optic Materials. Adams Hilger, London, 216 pp.
- GAHERTY J.B. 2001. Seismic evidence for hotspot-induced buoyant flow beneath the Reykjanes Ridge. *Science* 293, 1645-1647.
- GAHERTY J.B., LIZZARRALDE D., COLLINS J.A., HIRTH G. & KIM S. 2004. Mantle deformation during slow seafloor spreading constrained by observations of seismic anisotropy in the western Atlantic. *Earth and Planetary Science Letters* 228, 255-265.
- GARBACZ A. & GRABSKI M.W. 1993. The relationship between texture and CSL boundaries distribution in polycrystalline materials. I. The grain-boundary misorientation distribution in random polycrystal. *Acta Metallurgica et Materialia* 41, 469-473.
- GERTSMAN V.Y. & TANGRI K. 1995. Computer-simulation study of grain-boundary and triple junction distributions in microstructures formed by multiple twinning. *Acta Metallurgica et Materialia* 43, 2317-2324.
- GLASS S.J., MICHAEL J.R., READEY M.J., WRIGHT S.I. & FIELD D.P. 1998. Characterization of microstructure and crack propagation in alumina using Orientation Imaging Microscopy (OIM). In: *Ceramic Microstructures: Control at the Atomic Level*, Plenum Press, New York, 803-813.
- GOLDSTEIN J.I., NEWBURY D.E., ECHLIN P., JOY D.C., ROMING A.D., LYMAN C.E., FIORI C. & LIFSHIN E. 1992. *Scanning Electron Microscopy and X-Ray Microanalysis*. Plenum Press, New York, 820 pp.
- GRIMMER H. 1989. Coincidence orientations of grains in rhombohedral materials. *Acta Crystallographica A* 45, 505-523.
- GRUNAU H.R., LEHNER P., CLEINTUAR M.R., ALLENBACH P. & BAKKER G. 1975. New radiometric ages and seismic data from Fuerteventura (Canary Islands), Maio (Cape Verde Islands), and Sao Tomé (Gulf of Guinea). In: *Progress in Geodynamics*, 90-108.
- HANSEN J., POSPIECH J. & LÜCKE K. 1978. *Tables for Textures Analysis of Cubic Crystals*. Springer Verlag, Berlin, 600 pp.
- HASSOLD G.N., HOLM E.A. & MIODOWNIK M.A. 2003. Accumulation of coincidence site lattice boundaries during grain growth. *Materials Science and Technology* 19, 683-687.
- HAZEN R.M. 1976. Effects of temperature and pressure on the crystal structure of forsterite. *American Mineralogist* 61, 1280-1293.
- HESS H.H. 1964. Seismic anisotropy of the uppermost mantle under oceans. *Nature* 203, 629-631.
- HEUER A.H. & RÜHLE M. 1984. Phase transformations in ZrO<sub>2</sub>-containing ceramics: I. The instability of c-ZrO<sub>2</sub> and the resulting diffusion-controlled reactions. In: *Advances in Ceramics 12: Science and Technology of Zirconia II*, The American Ceramic Society, 1-13.
- HINZ K., DOSTMANN H. & FRITSCH J. 1982. The continental margin of Morocco: seismic sequences, structural elements and geological development. In: *Geology of the Northwest African Continental Margin*, Springer Verlag, Berlin, 34-59.

- HJELEN J., ORSUND R., HOEL E., RUNDE P., FURU T. & NES E. 1993. EBSD, progress in technique and applications. *Textures and Microstructures* 20, 29-40.
- HOERNLE K. & SCHMINCKE H.U. 1993. The role of partial melting in the 15-Ma geochemical evolution of Gran Canaria: a blob model for the Canary hotspot. *Journal of Petrology* 34, 599-626.
- HOERNLE K., ZHANG Y.S. & GRAHAM D. 1995. Seismic and geochemical evidence for large-scale mantle upwelling beneath the eastern Atlantic and western and central Europe. *Nature* 374, 34-39.
- HOLIK J.S., RABINOWITZ P.D. & AUSTIN J.A. 1991. Effects of Canary hotspot volcanism on structure of oceanic crust off Morocco. *Journal of Geophysical Research* 96, 12039-12067.
- HOWE J.M. 1997. *Interfaces in Materials*. Wiley, New York, 516 pp.
- HUMPHREYS F.J., HUANG Y., BROUGH I. & HARRIS C. 1999. Electron diffraction of grain and subgrain structures - resolution considerations. *Journal of Microscopy* 195, 212-216.
- IBE G. & LÜCKE K. 1972. Description of orientation distributions of cubic crystals by means of 3D rotation coordinates. *Texture* 1, 87-98.
- IKEDA T., SHIMOBAYASHI N., WALLIS S.R. & TSUCHIYAMA A. 2002. Crystallographic orientation, chemical composition and three-dimensional geometry of sigmoidal garnet: evidence for rotation. *Journal of Structural Geology* 24, 1633-1646.
- ILLINGWORTH J. & KITTLER J. 1988. A survey of the Hough transform. *Computer Vision, Graphics and Image Processing* 44, 87-116.
- ISAAK D.G. 1992. High-temperature elasticity of iron-bearing olivine. *Journal of Geophysical Research* 97, 1871-1885.
- JACKSON J.M., PALKO J.W., ANDRAULT J.W., SINOGEIKIN S.V., LAKSHANOV D.L., WANG J., BASS J.D. & ZHAO C.S. 2003. Thermal expansion of natural orthoenstatite to 1473 K. *European Journal of Mineralogy* 15, 469-473.
- Ji S.C., ZHAO X.O. & FRANCIS D. 1994. Calibration of shear-wave splitting in the subcontinental upper-mantle beneath active orogenic belts using ultramafic xenoliths from the Canadian Cordillera and Alaska. *Tectonophysics* 239, 1-27.
- JOHNSON S.E. 1993. Testing models for the development of spiral-shaped inclusion trails in garnet porphyroblasts: to rotate or not to rotate, that is the question. *Journal of Metamorphic Geology* 11, 635-659.
- JUNG H. & KARATO S.I. 2001. Water-induced fabric transitions in olivine. *Science* 293, 1460-1463.
- JUUL JENSEN D. & SCHMIDT N.H. 1990. An automatic on-line technique for determination of crystallographic orientation by EBSD. *Proceedings Recrystallization* 90, 219-224.
- KAUR I., MISHIN Y. & GUST W. 1995. *Fundamentals of Grain and Interphase Boundary Diffusion*. Wiley, Chichester, 512 pp.
- KERN H., BURLINI L. & ASHCHEPKOV I.V. 1996. Fabric-related seismic anisotropy in upper-mantle xenoliths: evidence from measurements and calculations. *Physics of the Earth and Planetary Interiors* 95, 195-209.
- KHAN M.A. 1974. Dynamic implications of mantle hotspots. *Nature* 251, 596-597.
- KIKUCHI S. 1928. Diffraction of cathode rays by mica. *Japanese Journal of Physics* 5, 83-96.
- KIM D.I., LEE F.H., KIM Y.W., OH K.H. & LEE H.C. 2002. EBSD analysis of grain boundary characteristics of abnormally grain grown alumina. *Materials Science Forum* 408, 1699-1704.
- KING A.H., SINGH A. & WANG J.Y. 1993. Principles of grain boundary geometry in noncubic materials, with applications to  $\text{YBa}_2\text{Cu}_3\text{O}_{7-\delta}$ . *Interface Science* 1, 347-359.
- KOCKS U.F. 1988. A symmetric set of Euler angles and oblique orientation space sections. *Proceedings of the 8th International Conference on Textures of Materials*, 31-36.
- KOCKS U.F. 1998. The representation of orientations and textures. In: *Texture and Anisotropy, Preferred Orientations in Polycrystals and their Effect on Materials Properties*, Cambridge University Press, Cambridge, 44-102.
- KOCKS U.F., TOMÉ C.N. & WENK H.R. 1998. *Texture and Anisotropy, Preferred Orientations in Polycrystals and their Effect on Materials Properties*. Cambridge University Press, Cambridge, 676 pp.
- KOHLSTEDT D.L. 1990. Chemical analysis of grain boundaries in an olivine-basalt aggregate using high-resolution, analytical electron microscopy. In: *The brittle-ductile Transition in Rocks*, American Geophysical Union, Washington, 211-218.
- KOSTOV I. 1968. *Mineralogy*. London, 587 pp.
- KRETZ R. 1973. Kinetics of the crystallization of garnet at two localities near Yellowknife. *The Canadian Mineralogist* 12, 1-20.
- KRIEGER LASSEN N.C., CONRADSEN K. & JUUL JENSEN D. 1992. Image processing procedures for analysis of electron backscattering patterns. *Scanning Electron Microscopy* 6, 115-121.
- KRONBERG M.L. 1957. Plastic deformation of single crystals of sapphire - basal slip and twinning. *Acta Metallurgica* 5, 507-524.
- KUMAZAWA M. & ANDERSON O.L. 1969. Elastic moduli, pressure derivatives, and temperature derivatives of single-crystal olivine and single crystal forsterite. *Journal of Geophysical Research* 74, 5961-5972.
- KUNZE F.R. & AVÉ LALLEMANT H.G. 1981. Non-coaxial experimental deformation of olivine. *Tectonophysics* 74, T1-T13.
- KUNZE K., WRIGHT S.I., ADAMS B.L. & DINGLEY D.J. 1993. Advances in automatic EBSD single orientation measurements. *Textures and Microstructures* 20, 41-54.

- LARTIGUE S. & PRIESTER L. 1988. Influence of doping elements on the grain boundary characteristics in alumina. *Journal de Physique C5-49*, 451-456.
- LAVAL J.Y. & SWIATNICKI W. 1994. Atomic structure of grain boundaries in  $\text{YBa}_2\text{Cu}_3\text{O}_{7-x}$ . *Physica C* 221, 11-19.
- LE BAS M.J., REX D.C. & STILLMAN C.J. 1986. The early magmatic chronology of Fuerteventura, Canary Islands. *Geological Magazine* 123, 287-298.
- LE PICHON X. & FOX P.J. 1971. Marginal offsets, fracture zones and the early opening of the North Atlantic. *Journal of Geophysical Research* 76, 6294-6308.
- LEE W.E. & RAINFORTH W.M. 1994. *Ceramic Microstructures - Property Control by Processing*. Chapman & Hall, London, 590 pp.
- LEVIEN L., WEIDNER D.J. & PREWITT C.T. 1979. Elasticity of diopside. *Physics and Chemistry of Minerals* 4, 105-113.
- LLOYD G. 1987. Backscattered electron techniques. *Mineralogical Magazine* 51, 3-19.
- MACFARLANE D.J. & RIDLEY W.I. 1969. An interpretation of gravity data for Lanzarote, Canary Islands. *Earth and Planetary Science Letters* 6, 431-436.
- MAINPRICE D. 1990. A Fortran program to calculate seismic anisotropy from the lattice preferred orientation of minerals. *Computers and Geosciences* 16, 385-393.
- MAINPRICE D. & SILVER P.G. 1993. Interpretation of SKS-waves using samples from the subcontinental lithosphere. *Physics of the Earth and Planetary Interiors* 78, 257-280.
- MAINPRICE D. & HUMBERT M. 1994. Methods of calculating petrophysical properties from lattice preferred orientation data. *Surveys in Geophysics* 15, 575-592.
- MAINPRICE D., BEN ISMAIL W. & WAGNER F. 1998. The relationship between olivine textures and seismic anisotropy in a database of upper mantle rocks. *Materials Science Forum* 273, 681-686.
- MAINPRICE D. 1999. The Unicef Careware software package. [ftp://saphir.dstu.univ-montp2.fr/TPHY/david/CareWare\\_Unicef\\_Programs/](ftp://saphir.dstu.univ-montp2.fr/TPHY/david/CareWare_Unicef_Programs/).
- MAINPRICE D., BARRUOL G. & BEN ISMAIL W. 2000. The seismic anisotropy of the Earth's mantle: from single crystal to polycrystal. In: *Earth's Deep Interior: Mineral Physics and Tomography from the Atomic to the Global Scale*, AGU, Washington, 237-264.
- MARINONI L. & PASQUARÉ G. 1994. Tectonic evolution of the emergent part of a volcanic ocean island: Lanzarote, Canary Islands. *Tectonophysics* 239, 111-137.
- MATSUI M. & BUSING W.R. 1984. Calculation of the elastic constants and high-pressure properties of diopside,  $\text{CaMgSi}_2\text{O}_6$ . *American Mineralogist* 69, 1090-1095.
- MATTHIES S., HELMING K. & KUNZE K. 1990. On the representation of orientation distributions in texture analysis in  $\sigma$ -sections. I. General properties of  $\sigma$ -sections. *Physica Status Solidi B* 157, 71-83.
- MAULER A., KUNZE K., BURG J.P. & PHILIPPOT P. 1998. Identification of electron backscatter diffraction patterns in a monoclinic solid-state solution series: example of omphacite. *Materials Science Forum* 273, 705-710.
- MAULER A., BYSTRICKY M., KUNZE K. & MACKWELL S.J. 2000. Microstructures and lattice preferred orientations in experimentally deformed clinopyroxene aggregates. *Journal of Structural Geology* 22, 1633-1648.
- McKIE C. & McKIE D. 1974. *Crystalline Solids*. Nelson, London, 600 pp.
- MERCIER J.C. & NICOLAS A. 1975. Textures and fabrics of upper-mantle peridotites as illustrated by xenoliths from basalts. *Journal of Petrology* 16, 454-487.
- MERCIER J.C. 1979. Peridotites xenoliths and the dynamic of kimberlite intrusion. In: *The Mantle Sample, Inclusions in Kimberlites and Other Volcanics*, American Geophysical Union, Washington, 197-212.
- MERCIER J.C. 1985. Olivine and pyroxene. In: *Preferred orientation in deformed metals and rocks: an introduction to modern texture analysis*, Academic Press, Orlando, 407-430.
- MINICH R.W., SCHUH C.A. & KUMAR M. 2002. Role of topological constraints on the statistical properties of grain boundary networks. *Physical Review B* 66, 052101.
- MISTLER R.E. & COBLE R.L. 1974. Grain boundary diffusion and boundary widths in metals and ceramics. *Journal of Applied Physics* 45, 1507-1509.
- MÖCKEL J.R. 1969. Structural petrology of the garnet peridotite of Alpe Arami (Ticino, Switzerland). *Leidse Geologische Mededelingen* 42, 61-130.
- MONTAGNER J.P. & TANIMOTO T. 1990. Global anisotropy in the upper mantle inferred from the regionalization of phase velocities. *Journal of Geophysical Research* 95, 4797-4819.
- MONTAGNER J.P. & TANIMOTO T. 1991. Global upper mantle tomography of seismic velocities and anisotropies. *Journal of Geophysical Research* 96, 20337-20351.
- MORAWIEC A., SZPUNAR J.A. & HINZ D.C. 1993. Texture influence on the frequency of occurrence of CSL-boundaries in polycrystalline materials. *Acta Metallurgica et Materialia* 41, 2825-2832.
- MORGAN W.J. 1971. Convection plume in the lower mantle. *Nature* 230, 42-44.
- MORGAN W.J. 1983. Hotspot tracks and the early rifting of the Atlantic. *Tectonophysics* 94, 123-139.
- MORIMOTO N. 1988. Nomenclature of pyroxenes. *Mineralogical Magazine* 52, 535-550.
- MORRIS W.G. 1976. Physical properties of electrical barriers in varistors. *Journal of Vacuum Science and Technology* 13, 926-931.
- MORRISON W.H. 1985. Stabilization of aqueous oxide pigment dispersions. *Journal of Coating Technology* 57, 55-65.

- MYERS D. 1999. Surfaces, Interfaces and Colloids. Wiley, New York, 502 pp.
- NATAF H.C., NAKANISHI I. & ANDERSON D.L. 1984. Anisotropy and shear-velocity heterogeneities in the upper mantle. *Geophysical Research Letters* 11, 109-112.
- NATAF H.C., NAKANISHI I. & ANDERSON D.L. 1986. Measurements of mantle wave velocities and inversion for lateral heterogeneities and anisotropy. *Journal of Geophysical Research* 91, 7261-7307.
- NEUMANN E.R., WULFF PEDERSEN E., JOHNSEN K., ANDERSEN T. & KROGH E. 1995. Petrogenesis of spinel harzburgite and dunite suite xenoliths from Lanzarote, eastern Canary Islands: Implication for the upper mantle. *Lithos* 35, 83-107.
- NEUMANN E.R., SORENSEN V.B., SIMONSEN S.L. & JOHNSEN K. 2000. Gabbroic xenoliths from La Palma, Tenerife and Lanzarote, Canary Islands: evidence for reactions between mafic alkaline Canary Islands melts and old oceanic crust. *Journal of Volcanology and Geothermal Research* 103, 313-342.
- NEUMANN E.R., GRIFFIN W.L., PEARSON N.J. & O'REILLY S.Y. 2004. The evolution of the upper mantle beneath the Canary Islands: information from trace elements and Sr isotope ratios in minerals in mantle xenoliths. *Journal of Petrology* 45, 2573-2612.
- NICOLAS A., BOUDIER F. & BOULLIER A.M. 1973. Mechanisms of flow in naturally and experimentally deformed peridotites. *American Journal of Science* 273, 853-876.
- NICOLAS A. & POIRIER J.P. 1976. Crystalline Plasticity and Solid State Flow in Metamorphic Rocks. Wiley, London, 444 pp.
- NICOLAS A. 1976. Flow in upper-mantle rocks: some geophysical and geodynamic consequences. *Tectonophysics* 32, 93-106.
- NOVAK G.A. & GIBBS G.V. 1971. The crystal chemistry of the silicate garnets. *American Mineralogist* 56, 791-825.
- ORTIZ R., ARAÑA V., ASTIZ M. & GARCÍA A. 1986. Magnetotelluric study of the Teide (Tenerife) and Timanfaya (Lanzarote) volcanic areas. *Journal of Volcanology and Geothermal Research* 30, 357-377.
- PALUMBO G., AUST K.T., ERB U., KING P.J., BRENNENSTUHL A.M. & LICHTENBERGER P.C. 1992. On annealing twins and CSL distributions in FCC polycrystals. *Physica Status Solidi A* 131, 425-428.
- PAN Y. & ADAMS B.L. 1994. On the grain boundary distribution in polycrystals. *Scripta Metallurgica et Materialia* 30, 1055-1060.
- PASSCHIER C.W., TROUW R.A.J., ZWART H.J. & VISSERS R.L.M. 1992. Porphyroblast rotation; eppur si muove? *Journal of Metamorphic Geology* 10, 283-294.
- PERA E., MAINPRICE D. & BURLINI L. 2003. Anisotropic seismic properties of the upper mantle beneath the Torre Alfina area (Northern Apennines, Central Italy). *Tectonophysics* 370, 11-30.
- POSPIECH J. 1972. Die Parameter der Drehung und die Orientierungsverteilungsfunktion. *Kristal und Technik* 7, 1057-1072.
- PRIESTER L. & LARTIGUE S. 1991. Description and role in the high-temperature deformation of grain boundaries in  $\alpha$ -alumina ceramics. *Journal of the European Ceramic Society* 8, 47-57.
- PRIOR D.J., BOYLE A.P., BRENKER F., CHEADLE M.C., DAY A., LOPEZ G., PERUZZO L., POTTS G.J., REDDY S.M., SPIESS R., TIMMS N.E., TRIMBY P.W., WHEELER J. & ZETTERSTRÖM L. 1999. The application of electron backscatter diffraction and orientation contrast imaging in the SEM to textural problems in rocks. *American Mineralogist* 84, 1741-1759.
- PRIOR D.J. & WHEELER J. 1999. A study of an albite mylonite using electron backscatter diffraction. *Tectonophysics* 303, 29-49.
- PUMPHREY P.H. & BOWKETT K.M. 1971. Angle/axis pair description of coincidence site lattice grain boundaries. *Scripta Metallurgica* 5, 365-369.
- RAHN M.K., STEINMANN M. & FREY M. 2002. Chloritoid composition and formation in the Central Alps: a comparison between Penninic and Helvetic occurrences. *Schweizerische Mineralogische und Petrographische Mitteilungen* 82, 409-426.
- RAITT R.W., SHOR G.G., FRANCIS T.J.G. & MORRIS G.B. 1969. Anisotropy of the Pacific upper mantle. *Journal of Geophysical Research* 74, 3095-3109.
- RALEIGH C.B. 1968. Mechanisms of plastic deformation of olivine. *Journal of Geophysical Research* 73, 5391-5406.
- RANDLE V. 1993. The Measurement of Grain Boundary Geometry. IOP Publishing, London, 169 pp.
- RANDLE V. 1996. The Role of the Coincidence Site Lattice in Grain Boundary Engineering. Cambridge University Press, Cambridge, 120 pp.
- RANDLE V. & ENGLER O. 2000. Introduction to Texture Analysis: Macrotexture, Microtexture and Orientation Mapping. Gordon and Breach, London, 408 pp.
- RANDLE V. 2000. Theoretical framework for electron backscatter diffraction. In: *Electron Backscatter Diffraction in Materials Science*, Kluwer Academic/Plenum Publishers, New York, 19-30.
- REED J.S. 1995. Principles of Ceramics Processing. Wiley, New York, 658 pp.
- RHODES M. & DAVIES J.H. 2001. Tomographic imaging of multiple mantle plumes in the uppermost lower mantle. *Geophysical Journal International* 147, 88-92.
- RING T.A. 1996. Fundamentals of Ceramic Powder Processing and Synthesis. Academic Press, San Diego, 961 pp.
- ROBERTSON A.H.F. & STILLMAN C.J. 1979. Submarine volcanic and associated sedimentary rocks of the Fuerteventura Basal Complex, Canary Islands. *Geological Magazine* 116, 203-214.

- ROBERTSON A.H.F. & BERNOULLI D. 1982. Stratigraphy, facies, and significance of late Mesozoic and Early Tertiary sedimentary rocks of Fuerteventura (Canary Islands) and Maio (Cape Verde Islands). In: *Geology of NW African Continental Margin*, Springer Verlag, Berlin, 498-525.
- RODEL J. & GLAESER A.M. 1990. Anisotropy of grains growth in alumina. *Journal of the American Ceramic Society* 73, 3292-3301.
- ROE R.J. 1965. Description of crystallite orientation in polycrystalline materials III, general solution to pole figure inversion. *Journal of Applied Physics* 36, 2024-2031.
- ROESER H.A. 1982. Magnetic anomalies in the magnetic quiet zone off Morocco. In: *Geology of the Northwest African Continental Margin*, Springer Verlag, Berlin, 60-68.
- ROEST W.R., DAÑOBEITIA J.J., VERHOEF J. & COLLETTE B.J. 1992. Magnetic anomalies in the Canary Basin and the Mesozoic evolution of the central north Atlantic. *Marine Geophysical Researches* 14, 1-24.
- SARUWATARI K., JI S.C., LONG C.X. & SALISBURY M.H. 2001. Seismic anisotropy of mantle xenoliths and constraints on upper mantle structure beneath the southern Canadian Cordillera. *Tectonophysics* 339, 403-426.
- SCHMINCKE H.U. 1973. Magmatic evolution and tectonic regime in the Canary, Madeira and Azores Island groups. *Geological Society of America Bulletin* 84, 633-648.
- SCHMINCKE H.U. 1982. Volcanic and chemical evolution of the Canary Islands. In: *Geology of the Northwest African Continental Margin*, Springer Verlag, Berlin, 273-306.
- SCHMINCKE H.U., KLÜGEL A., HANSTEEN T.H., HOERNLE K. & VAN DEN BOGAARD P. 1998. Samples from the Jurassic ocean crust beneath Gran Canaria, La Palma and Lanzarote. *Earth and Planetary Science Letters* 163, 343-360.
- SCHONEVELD C. 1977. A study of some typical inclusion patterns in strongly paracrystalline-rotated garnets. *Tectonophysics* 39, 453-471.
- SCHROEDER T.J. & JOHN B.E. 2004. Strain localization on an oceanic detachment fault system, Atlantis Massif, 30 degrees N, Mid-Atlantic Ridge. *Geochemistry, Geophysics, Geosystems* 5, Q11007.
- SCHUH C.A., KUMAR M. & KING W.E. 2005. Universal features of grain boundary networks in FCC materials. *Journal of Materials Science* 40, 847-852.
- SCHWARTZ A.J., KUMAR M. & ADAMS B.L. 2000. *Electron Backscatter Diffraction in Materials Science*. Kluwer Academic / Plenum Press, New York, 339 pp.
- SCHWARZER R.A. & WEILAND H. 1988. Texture analysis by the measurement of individual grain orientations. Electron microscopical methods and application to dual phase steel. *Textures and Microstructures* 8-9, 443-456.
- SCOTT C., KALISZEWSKI M., GRESKOVICH C. & LEVINSON L. 2002. Conversion of polycrystalline  $Al_2O_3$  into single-crystal sapphire by abnormal grain growth. *Journal of the American Ceramic Society* 85, 1275-1280.
- SCOTT H.G. 1975. Phase relationships in the zirconia-yttria system. *Journal of Materials Science* 10, 1527-1535.
- SERIER B., BERROUG A., JUVE D., TREHEUX D. & GONTIER MOYA E.G. 1993. Silver alumina solid-state bonding - Study of diffusion and toughness close to the interface. *Journal of the European Ceramic Society* 12, 385-390.
- SHEARER P.M. & ORCUTT J.A. 1986. Compressional and shear wave anisotropy in the oceanic lithosphere - the Ngendei seismic refraction experiment. *Geophysical Journal of the Royal Astronomical Society* 87, 967-1003.
- SIENA F., BECCALUVA L., COLTORTI M., MARCHESI S. & MORRA V. 1991. Ridge to hot-spot evolution of the Atlantic lithospheric mantle: evidence from Lanzarote peridotite xenoliths (Canary Islands). *Journal of Petrology Special Lherzolites Issue*, 271-290.
- SILVEIRA G., STUTZMANN E., GRIOT D.A., MONTAGNER J.P. & VICTOR L.M. 1998. Anisotropic tomography of the Atlantic Ocean from Rayleigh surface waves. *Physics of the Earth and Planetary Interiors* 106, 257-273.
- SILVER P.G. & CHAN W.W. 1991. Shear wave splitting and subcontinental mantle deformation. *Journal of Geophysical Research* 96, 16429-16454.
- SINGH A., CHANDRASEKHAR N. & KING A.H. 1990. Coincidence orientations of crystals in tetragonal systems, with applications to  $YBa_2Cu_3O_{7.8}$ . *Acta Crystallographica B* 46, 117-125.
- SOEDJATMIKO B. & CHRISTENSEN N.I. 2000. Seismic anisotropy under extended crust: evidence from upper mantle xenoliths, Cima Volcanic Fiels, California. *Tectonophysics* 321, 279-296.
- SPEAR F.S. 1993. Metamorphic phase equilibria and pressure-temperature-time paths. *Mineralogical Society of America Monograph*, 799 pp.
- SPEAR F.S. & DANIEL C.G. 1998. Three-dimensional imaging of garnet porphyroblast sizes and chemical zoning; nucleation and growth history in the garnet zone. *Geological Materials Research* 1, 1-43.
- STADELMANN P. 1987. A software package for electron-diffraction analysis and HREM image simulation in materials science. *Ultramicroscopy* 21, 131-145.
- STALLARD A. 2003. Comment on "Crystallographic orientation, chemical composition and three-dimensional geometry of sigmoidal garnet: evidence for rotation" by T. Ikeda, N. Shimobayashi, S. Wallis and A. Tsuchiyama. *Journal of Structural Geology* 25, 1337-1339.
- STILLMAN C.J., FÜSTER J.M., BENNELL-BAKER M.J., MUÑOZ M., SMEWING J.D. & SAGREDO J. 1975. Basal complex of Fuerteventura (Canary Islands) is an oceanic intrusive complex with rift-system affinities. *Nature* 257, 469-471.

- SUTTON A.P. & BALLUFFI R.W. 1987. On geometrical criteria for low interfacial energy. *Acta Metallurgica* 35, 2177-2201.
- SWIATNICKI W., LARTIGUE-KORINEK S. & LAVAL J.Y. 1995. Grain boundary structure and intergranular segregation in  $Al_2O_3$ . *Acta Metallurgica and Materialia* 43, 795-805.
- TANIMOTO T. & ANDERSON D.L. 1985. Lateral heterogeneity and azimuthal anisotropy of the upper mantle: Love and Rayleigh waves 100-250 s. *Journal of Geophysical Research* 90, 1842-1858.
- THOMAS L.E., HAWKESWORTH C.J., VAN CALSTEREN P., TURNER S.P. & RODGERS N.W. 1999. Melt generation beneath ocean islands: a U-Th-Ra isotope study from Lanzarote in the Canary Islands. *Geochimica and Cosmochimica Acta* 63, 4081-4099.
- TOMMASI A., TIKOFF B. & VAUCHEZ A. 1999. Upper mantle tectonics: three-dimensional deformation, olivine crystallographic fabrics and seismic properties. *Earth and Planetary Science Letters* 168, 173-186.
- TOSOH CORPORATION. 2000. Typical powder characteristics and properties. [http://www.tosoh.com/zirconia/bs%20basic2\\_grades.htm](http://www.tosoh.com/zirconia/bs%20basic2_grades.htm).
- VAN ROERMUND H.L.M. & BOLAND J.N. 1981. The dislocation substructures of naturally deformed omphacites. *Tectonophysics* 78, 403-418.
- VAUCHEZ A. & GARRIDO C.J. 2001. Seismic properties of an asthenospherized lithospheric mantle: constraints from lattice preferred orientations in peridotite from the Ronda massif. *Earth and Planetary Science Letters* 192, 235-249.
- VENABLES J.A. & HARLAND C.J. 1973. Electron back-scattering patterns - a new technique for obtaining crystallographic information in the scanning electron microscope. *Philosophical Magazine* 27, 1193-1200.
- VERMA R.K. 1960. Elasticity of some high-density crystals. *Journal of Geophysical Research* 65, 757-766.
- VOGT P.R. 1974. Volcano spacing fractures and thickness of the lithosphere. *Earth and Planetary Science Letters* 23, 337-348.
- VOLLMER F.W. 1990. An application of eigenvalues methods to structural strain domain analysis. *Geological Society of America Bulletin* 102, 786-791.
- WARRINGTON D.H. & BUFALINI P. 1971. Coincidence site lattice and grain boundaries. *Scripta Metallurgica* 5, 771-776.
- WATTS A.B. 1994. Crustal structure, gravity anomalies and flexure of the lithosphere in the vicinity of the Canary Islands. *Geophysical Journal International* 119, 648-666.
- WEI M., ZHI D. & BRANDON D.G. 2005. Microstructure and texture evolution in gel-cast  $\alpha$ -alumina/alumina platelet ceramic composites. *Scripta Materialia* 53, 1327-1332.
- WENK H.R. & BENNET K. 1991. Modelling plastic deformation of peridotite with the self-consistent theory. *Journal of Geophysical Research* 96, 8337-8349.
- WEVER F. 1924. The cylindrical structure of cubic crystallized metals. *Zeitschrift für Physik* 28, 69-90.
- WHEELER J., PRIOR D.J., ZIANG Z., SPIESS R. & TRIMBY P.W. 2001. The petrological significance of misorientations between grains. *Contributions to Mineralogy and Petrology* 141, 109-124.
- WILLIAMS P.F. & JIANG D. 1999. Rotating garnets. *Journal of Metamorphic Geology* 17, 367-378.
- WOODCOCK N.H. 1977. Signification of fabric shapes using an eigenvalues method. *Geological Society of America Bulletin* 88, 1231-1236.
- WRIGHT S.I. & ADAMS B.L. 1992. Automatic analysis of electron backscatter diffraction patterns. *Metallurgical Transactions A* 23, 759-767.
- WRIGHT S.I., ADAMS B.L. & KUNZE K. 1993. Application of a new automatic lattice orientation measurement technique to polycrystalline aluminium. *Materials Science and Engineering A* 160, 229-240.
- WRIGHT S.I. 1993. A review of automated orientation imaging microscopy (OIM). *Computer-Assisted Microscopy* 5, 207-221.
- WYNER E.F. 1979. Electrolysis of sodium through alumina arc tubes. *Journal of the Illuminating Engineering Society* 8, 166-173.
- ZDANIEWSKI W.A. & KIRCHNER H.P. 1987. Effect of grain boundary oxidation in fracture toughness of SiC. *Journal of the American Ceramic Society* 70, 548-552.
- ZEUCH D.H. & GREEN H.W. 1984. Experimental deformation of a synthetic dunite at high temperature and pressure. *Tectonophysics* 110, 233-262.
- ZHANG S. & KARATO S.I. 1995. Lattice preferred orientation of olivine aggregates deformed in simple shear. *Nature* 375, 774-777.
- ZHANG S., KARATO S.I., FITZ GERALD J.D., FAUL U.H. & ZHOU Y. 2000. Simple shear deformation of olivine aggregates. *Tectonophysics* 316, 133-152.
- ZUSSMAN J. 1968. Crystal chemistry of pyroxene and amphiboles. *Earth Science Reviews* 4, 39-67.

\*\*\*\*\*

# CURRICULUM VITAE

---

Born in Fribourg (Switzerland); 4<sup>th</sup> September 1975

## EDUCATIONAL BACKGROUND

- 1995            **High school graduation** (A-type), Collège St-Michel of Fribourg
- 1996 - 2000    **Diploma in Earth Sciences**, Department of Geosciences, University of Fribourg. Thesis title: *Géologie et Pétrographie du Schlappintal-E (Grisons, CH)*
- 2001            **Postgraduate diploma in analysis and management of geological risks** (CERG), University of Geneva and University of San José (Costa Rica). Thesis title: *Risk mitigation at Vesuvius (Italy)*
- 2003 - 2007    **PhD thesis**, Department of Geosciences, University of Fribourg. Thesis title: *EBSD-based investigations of upper mantle xenoliths, snowball garnets and advanced ceramics*

## PROFESSIONAL ACTIVITIES

- Since 1995     Civil parish of Hauterive: scrutineer at council, cantonal and federal ballots and elections
- 1995            Cantonal Hospital of Fribourg: archiving of medical records
- 1998            Department for Nature and Environment of Fribourg (civil service): maintenance and development of nature reserves
- 1998 - 1999    Water Laboratory of Neuchâtel (civil service): geological mapping, water quality check and development of environmental courses for teacher training college students
- 2001            Historical Museum of Yverdon-les-Bains (civil service): valuation of geological collection quality
- 2001 - 2002    Geological Museum of the Canton of Vaud, Lausanne (civil service): valuation of the Jura Mountains geotopes as potential nature reserves
- 2002            Federal Office for Water and Geology, Ittigen bei Bern (civil service): GIS data treatment, archiving and geological mapping
- 2002 - 2003    University of Geneva and University of Lausanne: assistant teacher in geophysics
- 2003 - 2007    University of Fribourg: assistant responsible for organizing and accompanying field trips

## PUBLICATIONS IN PEER-REVIEWED JOURNALS

- VONLANTHEN P., KUNZE K., BURLINI L. & GROBÉTY B. 2006. Seismic properties of the upper mantle beneath Lanzarote (Canary Islands): Model predictions based on texture measurements by EBSD. *Tectonophysics* 428, 65-85.

ROBYR M., VONLANTHEN P., BAUMGARTNER L. & GROBÉTY B. 2007. Growth mechanism of snowball garnets from the Lukmanier Pass area (Central Alps, Switzerland): a combined  $\mu$ CT/EPMA/EBSD study. Terra Nova, in press (accepted 17.11.06).

VONLANTHEN P. & GROBÉTY B. 2007. CSL grain boundary distribution in alumina and zirconia ceramics. Ceramics International, in press (accepted 15.03.07).

\*\*\*\*\*

## Already published:

- Vol. 1 **HILLGÄRTNER, Heiko** (1999) The evolution of the French Jura platform during the Late Berriasian to Early Valanginian: controlling factors and timing (203 pp.).
- Vol. 2 **DUPRAZ, Christophe** (1999) Paléontologie, paléocéologie et évolution des faciès récifaux de l'Oxfordien Moyen-Supérieur (Jura suisse et français) (247 pp.).
- Vol. 3 **BASSANT, Philip** (1999) The high-resolution stratigraphic architecture and evolution of the Burdigalian carbonate-siliciclastic sedimentary systems of the Mut Basin, Turkey (278 pp.).
- Vol. 4 **COLOMBIÉ, Claude** (2002) Sédimentologie, stratigraphie séquentielle et cyclostratigraphie du Kimméridgien du Jura suisse et du Bassin vocontien (France): relations plate-forme – bassin et facteurs déterminants (198 pp.).
- Vol. 5 **PICOT, Laurent** (2002) Le Paléogène des synclinaux du Jura et de la bordure sud-rhénane: paléontologie (Ostracodes), paléocéologie, biostratigraphie et paléogéographie (240 pp.).
- Vol. 6 **DAPPLES, Florence** (2002) Instabilités de terrain dans les Préalpes fribourgeoises (Suisse) au cours du Tardiglaciaire et de l'Holocène: influence des changements climatiques, des fluctuations de la végétation et de l'activité humaine (158 pp.).
- Vol. 7 **HUG, Wolfgang Alexander** (2003) Sequenzielle Faziesentwicklung der Karbonatplattform des Schweizer Jura im Oberoxford und unterstem Kimmeridge (154 pp.).
- Vol. 8 **OSWALD, Daniel** (2003) Analyse de l'activité de glissements de terrain et relation avec les conditions climatiques: Exemples dans les Préalpes fribourgeoises (Suisse) (147 pp.).
- Vol. 9 **BECKER, Damien** (2003) Paléocéologie et paléoclimats de la Molasse du Jura (Oligo-Miocène): apport des Rhinocerotidea (Mammalia) et des minéraux argileux (327 pp.).
- Vol. 10 **DELALOYE, Reynald** (2005) Contribution à l'étude du pergélisol de montagne en zone marginale (240 pp.).
- Vol. 11 **FREUDIGER-BONZON, Jeanne** (2005) Archaeometrical study (petrography, mineralogy and chemistry) of Neolithic Ceramics from Arbon Bleiche 3 (Canton of Thurgau, Switzerland) (187 pp.).
- Vol. 12 **STOFFEL, Markus** (2005) Spatio-temporal variations of rockfall activity into forests - results from tree-ring and tree analysis (188 pp.).
- Vol. 13 **RAMEIL, Niels** (2005) Carbonate sedimentology, sequence stratigraphy, and cyclostratigraphy of the Tithonian in the Swiss and French Jura Mountains – a high-resolution record of changes in sea level and climate (246 pp.).
- Vol. 14 **BRAILLARD, Luc** (2006) Morphogenèse des vallées sèches du Jura tabulaire d'Ajoie (Suisse): rôle de la fracturation et étude des remplissages quaternaires. (224 pp.).
- vol. 15 **GOYETTE-PERNOT, Jöelle** (2006) L'Ambroisie: analyse statistique et modélisation numérique de sa trajectoire aérobiologique (274 pp.).
- Vol. 16 **TRESCH, Jonas** (2007) History of a Middle Berriasian transgression (Switzerland, France, and southern England) (271 pp.).
- Vol. 17 **BONNET, Cécile** (2007) Interactions between tectonics and surface processes in the Alpine foreland: Insights from analogue model and analysis of recent faulting (189 pp.).

**GeoFocus** is the publication series of the Department of Geosciences, University of Fribourg, Switzerland, and can be ordered at:

Department of Geosciences - Geology and Paleontology  
University of Fribourg  
1700 Fribourg, Switzerland  
<http://www.unifr.ch/geoscience/geology>